Forward-Modelling the Hot Circumgalactic Medium in X-rays

Soumya Shreeram

München 2025

Forward-Modelling the Hot Circumgalactic Medium in X-rays

Soumya Shreeram

Dissertation
an der Fakultät für Physik
der Ludwig–Maximilians–Universität
München

vorgelegt von
Soumya Shreeram
aus Pune, India

München, den 02.10.2025

Erstgutachter: Prof. Dr. Kirpal Nandra
Zweitgutachter: Prof. Dr. Volker Springel
Tag der mündlichen Prüfung: 14.11.2025

To my family and dearest friends,
and to everything contributing to the little joys of everyday life.

Contents

List of Figures

List of Tables

Zusammenfassung

Die heiße Phase des zirkumgalaktischen Mediums (CGM) bietet einen einzigartigen Einblick in die Gasströme, die die Entwicklung von Galaxien bestimmen, da sie sowohl als Reservoir als auch als Kanal für Baryonen dient, die in die Galaxien hinein- und aus ihnen herausströmen. Das heiße CGM, wie es im Röntgenlicht beobachtet wird, ist eine Sonde für das diffuse baryonische Gas und trägt dazu bei, Rückkopplungsmechanismen und Galaxienentstehungsmodelle einzuschränken. Jüngste Fortschritte bei den Beobachtungsmöglichkeiten, insbesondere mit dem Röntgenteleskop eROSITA, haben neue Wege zur Untersuchung der Eigenschaften des heißen CGM um Galaxien mit der Masse der Milchstraße (MW) eröffnet und entscheidende Anhaltspunkte für kosmologische hydrodynamische Simulationen geliefert. Die Interpretation dieser Messungen ist jedoch aufgrund von Projektionseffekten, Beiträgen unaufgelöster Quellen und des komplexen Einflusses der großräumigen Umgebung einer Galaxie nach wie vor mit erheblichen Herausforderungen verbunden.

In dieser Arbeit erstellen wir ein vollständig selbstkonsistentes Vorwärtsmodell des heißen CGM unter Verwendung der kosmologischen hydrodynamischen Simulation TNG300. Wir konstruieren einen neuartigen Lichtkegel und generieren Schein-Röntgenbeobachtungen, die auf den intrinsischen Eigenschaften der Gaszellen basieren, sogenannte LC-TNGX, um direkte Vergleiche mit Beobachtungen zu ermöglichen. Unsere analytische Modellierung erfasst intrinsische Röntgen-Oberflächenhelligkeitsprofile über stellare und Halo-Massenbereiche hinweg. Wir stellen fest, dass höhere Sternmassenbereiche flacheren Steigungen der intrinsischen galaktozentrischen Profile entsprechen, was durch abnehmende Werte des Profilexponenten β quantifiziert wird. Wir bestimmen quantitativ den Effekt von Satellitengalaxien, die in Stacking-Experimenten fälschlicherweise als Zentralgalaxien identifiziert wurden, was die abgeleiteten Röntgenoberflächenhelligkeitsprofile des heißen CGM verzerrt. Für stellare Massenbereiche von $10^{10.5-11}$ $M_\odot$, $10^{11-11.25}$ $M_\odot$ und $10^{11.25-11.5}$ $M_\odot$ zeigen wir, dass selbst geringe Kontaminationsanteile (bis zu 1%) die gemessenen Röntgenoberflächenhelligkeitsprofile bei großen Radien dominieren können. Insbesondere im Bereich der MW-Masse dominieren falsch klassifizierte Zentrale, die 30%, 10% oder 1% einer gestapelten Probe ausmachen, das gemessene Oberflächenhelligkeitsprofil jenseits von Radien von $\geq 0.11\times R_{500c}$, $\geq 0.24\times R_{500c}$ bzw. $\geq 1.04\times R_{500c}$.

Darauf aufbauend entwickeln wir Vorwärtsmodelle, die auf die radialen Oberflächenhelligkeitsprofile von Galaxien mit großer Masse im eROSITA-Röntgenbereich zugeschnitten sind. Unser Modell umfasst zwei wichtige Emissionskomponenten: heißes Gas um Zentral- und Satellitengalaxien sowie punktförmige Quellenbeiträge von Röntgendoppelsternen (XRBs) und aktiven galaktischen Kernen (AGNs). Wir simulieren Scheinbeobachtungen unter Verwendung der

TNG300-basierten Gasprofile, wobei wir die Sternmassen- und Rotverschiebungsverteilungen aus den Beobachtungen sorgfältig abgleichen, und untersuchen, wie Variationen in der zugrunde liegenden Halomassenverteilung die Ergebnisse beeinflussen. Wir zeigen, dass eine Erhöhung der mittleren Halomasse um einen Faktor von ~ 2 zu einer $\sim 4 fachen$ Erhöhung der gestapelten Röntgenluminosität des heißen CGM führt. Durch die Einbeziehung empirischer Beschränkungen für AGN- und XRB-Leuchtkräfte identifizieren wir das Vorwärtsmodell, das am besten mit den eROSITA-Daten übereinstimmt. Im Bereich der MW-Sternmassen stimmt unser Modell gut mit der bisherigen Literatur überein. Wir stellen fest, dass innerhalb von etwa 40 kpc vom Galaxienzentrum das heiße CGM und die Punktquellenemission jeweils $\sim 40-50\%$ der gesamten Röntgenemission beitragen. Jenseits von ~ 40 kpc dominiert die heiße CGM-Emission von Satellitengalaxien, die massereichere Wirtshalos mit einer mittleren Größe von $M_{200m} \sim 10^{14}$ $M_\odot$ verfolgen, das gestapelte Signal. Dieser Ansatz bietet eine neuartige Methode, um die mittlere AGN-Röntgenleuchtkraft und die radiale Verteilung von heißem CGM-Gas in Galaxien mit großer Masse gemeinsam zu bestimmen, was Tests von AGN-Rückkopplungsvorschriften in hydrodynamischen Simulationen ermöglicht.

Zusätzlich zu den beobachteten Projektionseffekten untersuchen wir, wie die großräumige kosmische Umgebung die Röntgeneigenschaften des heißen CGM formt. Mithilfe des DisPerSE-Algorithmus zur Filamentfindung auf unserem TNG300-basierten Lichtkegel LC-TNGX, der sich über $0,03 \leq z \leq 0,3$ erstreckt, klassifizieren wir zentrale Galaxien in fünf verschiedene Kategorien der großräumigen Umgebung: Haufen und massereiche Gruppen, Haufenvororte, Filamente, Filament-Void-Übergangsregionen und Leerräume/Wände. Wir stellen fest, dass die Röntgenoberflächenhelligkeitsprofile zentraler Galaxien in Filamenten mit $M_{200\mathrm{m}} > 10^{12}$ $M_\odot$ im radialen Bereich von $(0,3-0,5)R_{200\mathrm{m}}$ um $20-45\%$ heller sind als die in Hohlräumen und Wänden. Dieser Überschuss ergibt sich aus höheren durchschnittlichen Gasdichten, Temperaturen und Metallizitäten in Filamentgalaxien, was einen deutlichen Einfluss des kosmischen Netzes auf die Eigenschaften heißen CGMs erkennen lässt. Unsere Ergebnisse unterstreichen, wie wichtig die Berücksichtigung der kosmischen Umgebung bei der Interpretation von Röntgen-CGM-Messungen ist, und zeigen vielversprechende Wege für zukünftige Studien auf, die untersuchen, wie die Geschichte des Zusammenbaus, die Gasakkretion und die Konnektivität im kosmischen Netz den Gehalt an heißem Gas in der Umgebung von Galaxien beeinflussen.

Insgesamt unterstreichen die in dieser Arbeit dargestellten Fortschritte, dass das vollständige Verständnis des heißen CGM einen integrierten Ansatz erfordert, der Röntgenbeobachtungen, sorgfältige Modellierung von Projektions- und Umgebungseffekten und robuste Vergleiche zwischen verschiedenen hydrodynamischen Simulationen kombiniert. Die hier entwickelten Methoden und Modelle bieten einen entscheidenden Rahmen für die Interpretation von Beobachtungen des heißen CGM, die durch aktuelle und zukünftige Röntgendurchmusterungen ermöglicht werden, und ermöglichen es uns, das komplexe Zusammenspiel von baryonischer Physik, AGN-Rückkopplung, Halo-Demographie und dem kosmischen Netz bei der Formung des heißen Gases um Galaxien zu entwirren. Da neue Daten von Missionen der nächsten Generation wie NewAthena und HUBS zusammen mit immer ausgefeilteren Simulationen eintreffen, stehen wir an der Schwelle, das heiße CGM als präzise kosmologische und astrophysikalische Sonde zu nutzen. Die vor uns liegenden Herausforderungen bei der Verknüpfung mikrophysikalischer Rückkopplungsprozesse mit großmaßstäblichen Beobachtungen, der Quantifizierung von Umge-

bungseinflüssen und der Eingrenzung der verschiedenen Mechanismen, die die Baryonenzyklen steuern, bieten einen spannenden Grenzbereich, in dem Theorie und Beobachtung konvergieren, um unsere Modelle der Galaxienbildung und -entwicklung zu verfeinern.

Abstract

The hot phase of the circumgalactic medium (CGM) offers a unique window into the gas flows that shape galaxy evolution, serving as both a reservoir and a conduit for baryons cycling in and out of galaxies. The hot CGM, as observed in X-rays, probes the diffuse baryonic gas, helping to constrain feedback mechanisms and galaxy formation models. Recent advances in observational capabilities, particularly from the X-ray telescope eROSITA, have opened new avenues to investigate the properties of the hot CGM around Milky Way (MW)-mass galaxies, yielding critical benchmarks for cosmological hydrodynamical simulations. Yet significant challenges remain in interpreting these measurements due to projection effects, contributions from unresolved sources, and the complex influence of a galaxy's large-scale environment.

In this thesis, we build a fully self-consistent forward model of the hot CGM using the TNG300 cosmological hydrodynamical simulation. We construct a novel lightcone and generate mock X-ray observations based on intrinsic gas cell properties, so-called LC-TNGX, to enable direct comparisons with observations. Our analytical modelling captures intrinsic X-ray surface brightness profiles across stellar and halo mass bins. We find that higher stellar mass bins correspond to shallower slopes of the intrinsic galactocentric profiles, quantified via decreasing values of the profile surface brightness exponent β. Critically, we quantify the effect of satellite galaxies incorrectly identified as centrals in stacking experiments, which biases the derived hot CGM X-ray surface brightness profiles. For stellar mass bins of $10^{10.5-11}$ $M_\odot$, $10^{11-11.25}$ $M_\odot$, and $10^{11.25-11.5}$ $M_\odot$, we demonstrate that even modest contamination fractions (as low as 1%) can dominate the measured X-ray surface brightness profiles at large radii. Specifically, in the MW-mass bin, misclassified centrals contributing 30%, 10%, or 1% of a stacked sample dominate the measured surface brightness profile beyond radii of $\geq 0.11 \times R_{500c}$, $\geq 0.24 \times R_{500c}$, and $\geq 1.04 \times R_{500c}$, respectively.

Building on this framework, we develop forward models tailored to the eROSITA stacked X-ray radial surface brightness profiles of MW-mass galaxies. Our model includes two key emission components: hot gas around both central and satellite galaxies, and point-source contributions from X-ray binaries (XRBs) and active galactic nuclei (AGN). We simulate mock observations using the TNG300-based gas profiles, carefully matching stellar mass and redshift distributions from the observations, and explore how variations in the underlying halo mass distribution affect the results. We show that for galaxy samples matched in stellar mass, increasing the mean halo mass by a factor of ~ 2 leads to a $\sim 4\times$ enhancement in the stacked X-ray luminosity of the hot CGM. By incorporating empirical constraints on AGN and XRB luminosities, we identify the model that best matches the eROSITA data. In the MW stellar mass bin, our model

agrees well with prior literature. We find that within approximately 40 kpc from the galaxy centre, the hot CGM and point-source emission each contribute $\sim 40 - 50\%$ of the total stacked X-ray emission. Beyond ~ 40 kpc, the hot CGM emission from satellite galaxies, tracing more massive host halos with mean $M_{200m} \sim 10^{14}$ $M_\odot$, dominates the stacked signal. This approach offers a novel method to jointly constrain the mean AGN X-ray luminosity and the radial hot CGM gas distribution in MW-mass galaxies, enabling tests of AGN feedback prescriptions in hydrodynamical simulations.

In addition to observational projection effects, we investigate how the large-scale cosmic environment shapes the hot CGM X-ray properties. Using the DisPerSE filament-finding algorithm on our TNG300-based lightcone spanning $0.03 \leq z \leq 0.3$, LC-TNGX, we classify central galaxies into five distinct large-scale environment categories: clusters and massive groups, cluster outskirts, filaments, filament-void transition regions, and voids/walls. We find that the X-ray surface brightness profiles of central galaxies in filaments with $M_{200\mathrm{m}} > 10^{12}$ $M_\odot$ are 20–45% brighter in the radial range of $(0.3\text{–}0.5) \times R_{200\mathrm{m}}$ compared to those in voids and walls. This excess arises from higher average gas densities, temperatures, and metallicities in filament galaxies, revealing a clear imprint of the cosmic web on hot CGM properties. Our findings highlight the importance of accounting for the cosmic environment in interpreting X-ray CGM measurements and suggest promising avenues for future studies exploring how the assembly history, gas accretion, and connectivity in the cosmic web shape the hot gas content around galaxies.

Taken together, the progress outlined in this thesis underscores that fully understanding the hot CGM requires an integrated approach, combining X-ray observations, careful modelling of projection and environmental effects, and robust comparisons across multiple hydrodynamical simulations. The methods and models developed here provide a critical framework for interpreting hot CGM observations enabled by current and future X-ray surveys, allowing us to disentangle the complex interplay of baryonic physics, AGN feedback, halo demographics, and the cosmic web in shaping the hot gas around galaxies. As new data arrives from next-generation missions like NewAthena and HUBS, alongside increasingly sophisticated simulations, we stand at the threshold of using the hot CGM as a precise cosmological and astrophysical probe. The challenges ahead in linking microphysical feedback processes to large-scale observables, quantifying environmental impacts, and constraining the diverse mechanisms governing baryon cycles offer an exciting frontier where theory and observation converge to refine our models of galaxy formation and evolution.

Chapter 1

Introduction

The Universe we reside in, smoothed over large scales, is governed by gravity and the cosmological principle. The cosmological principle states that the Universe is homogeneous and isotropic (Ellis & Harrison, 1974; Barrow & Matzner, 1977). Homogeneity implies that the entire Universe has the same average physical properties. Isotropy states that there is no preferential direction in the Universe. This principle allows us to derive significant results from local measurements, leading to the currently favoured concordance model that addresses the most important questions of cosmology, like the age, composition, and dynamics of the Universe. The concordance model describes the geometry of our Universe to be strikingly flat, whose energy budget at the present epoch is dominated by "cold dark matter" (CDM) and "dark energy", contributing to about 25% and 70%, respectively. The latter mysterious component, dark energy, is described by the cosmological constant Λ (for reviews see, e.g., Weinberg 1989; Carroll 2001; Padmanabhan 2003; Sahni 2004; Knobel 2012). The dominant contributions in the present-day Universe from dark energy and dark matter motivate the concordance model to also be called the ΛCDM model. Despite mounting evidence for the existence of these two components (Zwicky, 1933; Rubin et al., 1980), their exact properties and direct detections remain undiscovered to date (e.g., see Peebles & Ratra 2003; Arbey & Mahmoudi 2021; Oks 2021 for reviews).

With the advent of modern observational probes in astronomy, the constituents of the Universe in the ΛCDM framework are precisely measured up to $\lesssim 2\%$ (Planck Collaboration et al., 2020). One of the most powerful observational probes that provide us with impressively precise measurements of the cosmological parameters is the cosmic microwave background (CMB) anisotropies. The CMB, discovered by Penzias & Wilson (1979), is a footprint of photons that are emitted after the formation of the first baryons, 380,000 years after the Big Bang at redshift $z \sim 1000$. The anisotropies in the CMB spectrum are temperature differences at the scale of a few μK, which were generated by quantum density fluctuations in the early Universe. The CMB anisotropies have been measured by space missions like the Cosmic Background Explorer COBE (Kofman et al., 1993), WMAP (Hinshaw et al., 2013), and Planck Collaboration et al. (2020), with increasing precision, and they show good consistency with the ΛCDM model. Other observational probes include (i) Type 1a supernovae (SN1a, Riess et al. 1998; Perlmutter et al. 1999), providing evidence for the accelerated expansion of the Universe; (ii) baryon acoustic oscillations (BAO, Eisenstein et al. 2005; Cole et al. 2005; Percival et al. 2007; Alam

et al. 2021), measuring cosmic expansion by characterising features in the clustering of galaxies; (iii) weak gravitational lensing (Mellier, 1999; Munshi et al., 2008; Hoekstra & Jain, 2008; Kilbinger, 2015), probing the intervening dark matter distribution of the Universe; (iv) big bang nucleosynthesis measurements (Cooke et al., 2014; Cyburt et al., 2016), constraining baryonic matter the first seconds of the Universe; (v) abundance of galaxy clusters (e.g., Mantz et al. 2015; Bocquet et al. 2019; Ider Chitham et al. 2020; To et al. 2021; Garrel et al. 2022; Ghirardini et al. 2024; DES Collaboration et al. 2025), tracing the growth of structure in the Universe.

These combined cosmological probes provides broad support for the ΛCDM model, which is simply dependent on only six free parameters. These are the density parameters, the baryonic density Ω_b, and the dark matter density Ω_c, the Hubble constant, H_0[1], the amplitude of primordial perturbations, A_s, the power-law spectral index of the primordial density-field pertubations n_s, and the reioionization optical depth, τ. Another key derived quantity in the ΛCDM model is σ_8, the root-mean-square fluctuation amplitude of the matter power spectrum on $8h^{-1}$ Mpc scales[2]. While strong evidence exists in support of the ΛCDM model, there are discrepancies among key cosmological parameters between early-time (Planck Collaboration et al., 2020) and late-time cosmological probes (Riess et al., 2019, 2021).

Galaxies form through the gravitational collapse of matter perturbations, with the initial stages of galaxy formation depending on gas thermodynamics and associated physical processes, such as radiative cooling, condensation, and energetic feedback, which enable the formation of stars and galaxies (Rees & Ostriker, 1977; Silk, 1977; Somerville & Davé, 2015; Naab & Ostriker, 2017). The balance between different galaxy formation processes and initial conditions dictates the eventual formation of stars and their assembly into diverse galactic structures (Fall & Efstathiou, 1980; White & Rees, 1978). The Circumgalactic Medium (CGM) plays a crucial role in interfacing the gas between the interstellar medium (ISM) within galaxies and the external intergalactic medium (IGM) outside them, encompassing the fossil imprints of physical mechanisms that dictate the evolution of galaxies (Tumlinson et al., 2017). The CGM is a multiphase medium characterised by rich dynamics, complex ionisation states, and a range of temperatures and densities, acting both as a source of star-forming fuel and as a sink for outflowing gas from galaxies driven by stellar and Active Galactic Nuclei (AGN) feedback (Faucher-Giguère & Oh, 2023). The CGM can be probed by a variety of observational techniques, including absorption-line spectroscopy, emission-line studies, and stacking analysis, which have collectively advanced our understanding of the complex interplay between galaxies and their surroundings.

In summary, this thesis addresses three key questions in modelling the hot CGM by using a novel lightcone constructed using the IllustrisTNG cosmological simulation and generating mock X-ray observations. Chapt. 2 and the accompanying paper Shreeram et al. (2025a) details on the construction of the TNG-based lightcone and systematically investigates the projection effects—such as local correlated environment, misclassified central galaxies, and the offset between the X-ray centre and halo potential centre—that contaminate X-ray stacking observations of the hot CGM. By building an IllustrisTNG-based lightcone (LC-TNGX) and simulating how these effects arise in stacking experiments, this thesis provides a detailed framework to quantify

[1] H_0 is also parametrized by means of h as $H_0 = 100\ h$ km s^{-1} Mpc^{-1}

[2] σ_8 is related to A_s and n_s via the transfer of the primordial fluctuations to the matter power spectrum.

and mitigate them. In Chapt. 3 and accompanying paper Shreeram et al. (2025b), we demonstrate how to retrieve the intrinsic hot CGM physics from eROSITA data by developing a forward model of the stacked X-ray emissions from both hot gas and point sources (X-Ray binaries and AGN). This approach reveals a tight correlation between the underlying halo mass distribution and the resulting X-ray luminosity (with a factor $\sim 2\times$ increase in mean halo mass boosting the CGM's luminosity by $\sim 4\times$), and additionally allows constraining AGN X-ray luminosity jointly with the radial CGM profile. Finally, Chapt. 4 and the accompanying paper Shreeram et al. (2025c) explore how the cosmic web shapes the CGM by applying the filament finder DisPerSe to the LC-TNGX. This classification shows that the hot CGM of galaxies in filaments, cluster outskirts, and other environments each impart distinct imprints on X-ray profiles. E.g., galaxies in filaments with $M_{200\mathrm{m}} > 10^{12}$ $\mathrm{M}_{\odot}$ appear $20-45\%$ brighter at $(0.3-0.5)\times R_{200\mathrm{m}}$ than those in voids or walls. Together, these studies underscore both the importance of meticulous forward-modelling for reliable X-ray CGM measurements and the pivotal role of large-scale structure and environment in shaping the hot CGM. Lastly, Chapt. 5 summarises the main findings of this thesis and provides an overview of promising future directions to pursue with the tools developed and results obtained in this thesis.

In the current chapter, we describe on the history of the Universe in Sec. 1.1, walking through the evolution from the Big Bang (Sec. 1.1.1) and the formation of dark matter halos (Sec. 1.1.2) to galaxy formation (Sec. 1.1.3). Given our understanding of how galaxies form, we detail their key properties and scaling relations in Sec. 1.2. We then progress to the crucial question of how they evolve, in which the CGM, described in Sec. 1.3, plays a central role, and is the focus of this thesis. The CGM is the multi-phase complex gas hosted within the halo, bearing the imprint of numerous physical processes like gas inflows, outflows, and feedback. We summarise the main observational probes revealing different facets of the CGM in Sec. 1.3.1-1.3.3. In Sec. 1.4 we summarise the different ways the complex multi-scale, multi-physics CGM is modelled, with particular emphasis on using hydrodynamical simulations (Sec. 1.4.1). We also summarise the key physical processes that impact the CGM in Sec. 1.4.2. Lastly, Sec. 1.5 presents a summary of the objectives attained in this thesis.

1.1 The history of the Universe

While on large scales $\gtrsim$ 250 Mpc the Universe is homogeneous and isotropic (Laurent et al., 2016), on smaller scales we observe huge deviations from the mean matter density, resulting in the so-called cosmic web. These deviations from the cosmological principle are due to the tiny fluctuations in the primordial distribution of matter, which evolved under the influence of gravity, starting at ~0.1 Gyr, and have led to the present-day Universe at $t_0 \sim 13.7$ Gyr. The primordial fluctuations grew with time due to gravitational collapse, leading to the formation of high-density peaks that are the nodes of the cosmic web hosting today's galaxy clusters. The expansive network of bridges between these nodes forms a large-scale web dominated by filaments, which demarcate the underdense voids (Peebles, 2020). The existence and evolution of the cosmic web (Bond et al., 1996) has been modeled using large N-body simulations of structure formation in a ΛCDM Universe (e.g. Springel et al. 2006; Popping et al. 2009; Angulo et al.

2012; Habib et al. 2012; Poole et al. 2015). Although the existence of filaments, clusters and voids has been well predicted theoretically, advances in spectroscopic surveys with increasing resolution and depth have now allowed us to observationally map the cosmic web. The cosmic web, as traced by galaxies, has been studied up to redshift z $\approx$ 0.9 thanks to surveys such as the Center for Astrophysics (CfA) Redshift Survey (De Lapparent et al., 1986), Sloan Digital Sky Survey (SDSS, York et al., 2000), 2dF Galaxy Redshift Survey (2dFGRS, Colless et al., 2001), 6dF Galaxy Survey (6dFGS, Jones et al., 2009), Galaxy and Mass Assembly (GAMA, Driver et al., 2011), VIMOS Public Extragalactic Redshift Survey (VIPERS Guzzo et al., 2014), 2MASS (Huchra et al., 2012) and Cosmic Evolution Survey (COSMOS, Scoville et al., 2007). In Fig. 1.1, we show the cosmic web as observed by the SDSS out to redshift $z = 0.15$.

1.1.1 Evolution of the Universe from the Big Bang

Together with the cosmological principle, another fundamental assumption on which the standard cosmological theory relies is that on sufficiently large scales the Universe is governed by gravity and dark energy, as described by by the theory of General relativity (GR, Einstein, 1915). In GR, gravity is manifested as a curvature in spacetime, described by a metric. The most general, homogenous, and isotropic metric is called the Friedmann-Lemaître-Robertson-Walker (FLRW) metric

$$ds^2 = a(t)^2\mathbf{x}^2 - c^2dt^2, \tag{1.1}$$

where ds defines the infinitessimal line element, c is the speed of light, $\mathbf{x}$ is the spatial vector and $a(t)$ is the scale factor. The evolution of the primordial density fluctuations in an expanding Universe is described by $a(t)$; this function defines the dynamics of the Universe. At present time, t_0, the scale factor is defined to be unity, $a(t_0) \equiv a_0 = 1$. Additionally, $a(t)$ allows us to describe the position of any object in the Universe as $\mathbf{r} = a(t)\mathbf{x}$, where $\mathbf{x}$ is an arbitrary spatial vector for that object. Observations show that the recession velocity, $\mathbf{v}$, with which objects at a position, $\mathbf{r}$, move from the observer is related as follows: $\mathbf{v} = (\dot{a}/a)\mathbf{r}$ (Hubble, 1929; Riess et al., 1998)[4]. Therefore, $a(t)$ is continuously decreasing in the expanding Universe, i.e., $\dot{a}(t) > 0$. Here, $\dot{a}(t)/a(t) \equiv H(t)$ is the Hubble parameter describing the expansion rate of the Universe, and $H(t_0) \equiv H_0$ is a constant. The Planck Collaboration et al. (2020) measure $H_0 = (67.4 \pm 0.5)$ km/s/Mpc, which is obtained by combining information from the CMB temperature, polarization maps and the lensing data.

In angular coordinates, $\mathbf{x} = (r, \theta, \phi)$, and the FLRW metric from Eq. 1.1 can be written as

$$ds^2 = a(t)^2\left(\frac{dr^2}{1 - Kr^2} + r^2d\Omega\right) - c^2dt^2, \tag{1.2}$$

where K describes the geometry of the Universe, which assumes the value of 0, for a flat geometry, within the ΛCDM framework.

How the curvature of spacetime, as defined by the metric in Eq. 1.2, responds to the presence of mass, energy and momentum is encoded by Einstein's field equations. These are second-order

[3]Image credits: www.sdss4.org/science/orangepie/

[4]This relation is also called Hubble's law.

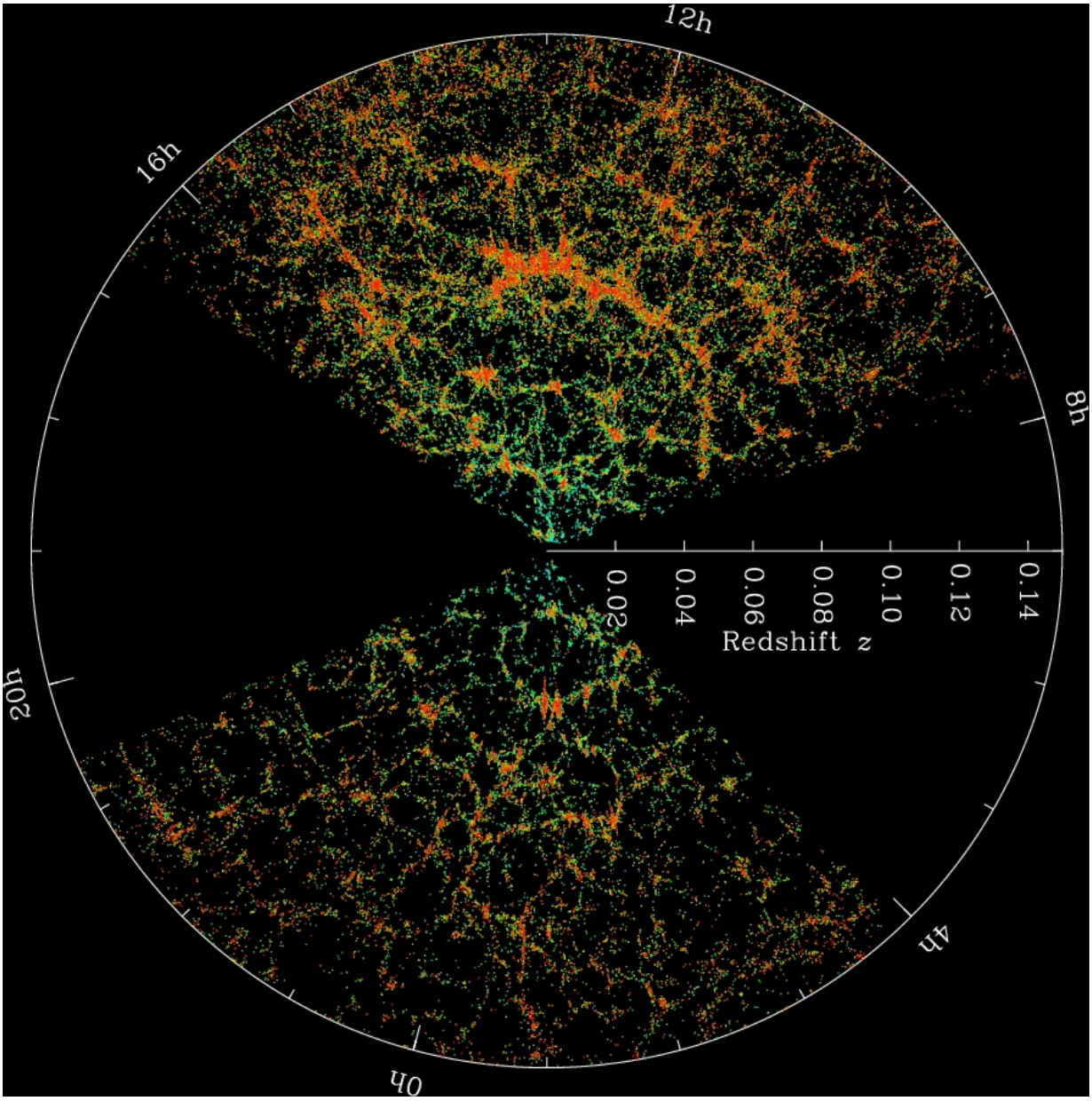

Figure 1.1: Two-dimensional map of the large-scale structure of the Universe as observed by the Sloan Digital Sky Survey (SDSS). The Milky Way galaxy is located at the center of the figure, and each point represents a galaxy. The redshift of a galaxy, which increases with distance from the Milky-Way observer, determines its radial position on the map. This image includes galaxies out to about 2 billion light-years, with the colors depicting the $g-r$ color of the galaxy. The striking web-like pattern that emerges is known as the cosmic web. It is a vast, interconnected network of filaments, clusters, and voids shaped by gravity and dark energy over cosmic time. The SDSS data provides a detailed view of the large-scale structure, revealing how galaxies trace the underlying distribution of dark matter across the Universe. Image Credits: M. Blanton and SDSS collaboration. [3]

non-linear differential equations, encapsulating six independent equations, that are written in the following form

$$G_{\mu\nu} + \Lambda g_{\mu\nu} = \frac{8\pi G}{c^4} T_{\mu\nu}, \tag{1.3}$$

where $G_{\mu\nu} \equiv R_{\mu\nu} - 1/2 g_{\mu\nu} R$ is the Einstein tensor, composed of $g_{\mu\nu}$, the metric tensor, and $R_{\mu\nu}$ the Ricci tensor. Additionally, R is the Ricci scalar, Λ is the cosmological constant, G is the gravitational constant, and $T_{\mu\nu}$ is the energy-momentum tensor. The left-hand side encapsulates the geometrical aspect of spacetime, and the right-hand side describes the sources (energy and momentum) that affect the curvature of spacetime. In a Universe without matter (i.e, vacuum only), the T^{μ}_{ν} term disappears. However, in our Universe, we assume T^{μ}_{ν} takes the form of a perfect fluid, and it is related to the energy, ρ, and pressure, P, densities as follows

$$T^{\mu}_{\nu} = (\rho + P) u^{\mu} u_{\nu} + P \delta^{\mu}_{\nu}, \tag{1.4}$$

where u^{μ} is the four-velocity, which for a particle of mass m is also called the four-momentum, $p^{\mu} = m u^{\mu}$. In the rest frame, $p^{\mu} = (1, 0, 0, 0)$, with the time-component, p^0, representing the energy.

In a homogenous and isotropic Universe, described by the FLRW metric (Eq. 1.2), the application of Einstein's equations (Eq. 1.3) with T^{μ}_{ν} assuming the form of a perfect fluid (Eq. 1.4), provides us with the Friedmann equations, which are as follows:

$$\frac{\dot{a}^2}{a^2} + \frac{K}{a^2} - \frac{\Lambda}{3} = \frac{8\pi G}{3}\rho, \text{ and} \tag{1.5}$$

$$2\frac{\ddot{a}}{a} + \frac{\dot{a}^2}{a^2} + \frac{K}{a^2} - \Lambda = -8\pi G \rho. \tag{1.6}$$

The main components of the Universe are non-relativistic matter, radiation, and dark energy. Assuming these different components comprising the Universe are adiabatic, they follow the equation of state

$$P = w \rho c^2, \tag{1.7}$$

where $w = 0$ for matter, $w = 1/3$ for radiation, and $w = -1$ for dark energy. By combining Eq. 1.5 and Eq. 1.6, with Eq. 1.7, we can show that the critical density of a Universe, ρ_c, is

$$\rho_c \equiv \frac{3H_0^2}{8\pi G} = 1.88 h^2 \times 10^{-29} \text{ g cm}^{-3}. \tag{1.8}$$

The $\Lambda/3$ and K terms in Eq. 1.5 can also be similarly used to define the dark energy density, $\rho_\Lambda = \Lambda c^2 / 8\pi G$, which is time independent, and the curvature density, $\rho_K = -3Kc^2/8\pi G$[5], which evolves as $\rho_K \propto a^{-2}$. By implementing energy conservation for matter and radiation, we find that the energy density of radiation evolves with time as $\rho_\gamma \propto a^{-4}$, while the energy density of matter evolves as $\rho_m \propto a^{-3}$. By defining the dimensionless density parameters, $\Omega_i = \rho_i / \rho_c$, we can then rewrite the Friedmann equation (Eq. 1.5) for our Univsere at the present time ($a_0 = 1$) as follows

$$\Omega_\Lambda + \Omega_m + \Omega_\gamma = 1. \tag{1.9}$$

[5]If the geometry of the Univserse is flat, i.e, $K = 0$, this component vanishes.

Cosmological probes (e.g., CMB anisotropies, SN1a, BAO, weak lensing, BBN, etc.) precisely measure the total matter density in the Universe today. By imposing Eq. 1.9 together with the evolution of each of these components with $a(t)$, we find that radiation dominated the Universe before $z \sim 3000$. This was followed by the matter-dominated era until $z \gtrsim 0.7$, after which dark energy took over.

1.1.2 Formation of dark matter halos

The fact that the Universe is homogeneous and isotropic at large scales allows us to define an average matter density $\langle \rho_m \rangle$. At smaller scales, under the influence of gravity, this average density is superposed with density fluctuations. The fractional density fluctuations are considered a realisation of random processes. A completely uniform Universe would not lead to the formation of all the inhomogeneous structures we see today, as also shown in Fig. 1.1. At any given random position in the sky (outside the Milky Way and local structures), the fractional fluctuations in mass (and energy) density, ρ, within a sphere of radius R decrease with R as a power-law. Due to gravity, these overdensities grow and attract increasingly more matter, resulting in the departure of structures from the background expansion; thereafter, they collapse to form halos. We compare these local (small-scale) perturbations to the average background density, $\langle \rho_m \rangle$, using the overdensity parameter defined as

$$\delta = \frac{\rho - \langle \rho_m \rangle}{\langle \rho_m \rangle}. \tag{1.10}$$

Let's consider the case of very small fluctuations, $\delta \ll 1$, where we can treat the growth of overdensities using linear structure formation theory. This holds for the very early Universe, where the fluctuations are of the order of $\delta \sim 10^{-5}$ as measured by the Planck Collaboration et al. (2020) using CMB anisotropies. However, at late times, these overdensities (and underdensities) follow highly non-linear evolution and are of the order of $\sim 10^2 - 10^3$.

The spatial density fluctuations $\delta(\mathbf{r})$ that grow linearly can be decomposed using the Fourier transform, $\delta_{\mathbf{k}}$, into harmonic waves with different amplitudes

$$\delta(\mathbf{r}) = \sum_{\mathbf{k}} \delta_{\mathbf{k}} e^{-i\mathbf{k}.\mathbf{r}}, \tag{1.11}$$

where $\mathbf{k}$ is the wave vector, whose magnitude, $k = |\mathbf{k}|$, is related to the wavelength of the wave $k = 2\pi/\lambda$. The square of the density waves, $|\delta_{\mathbf{k}}|^2$ probes the amount of structure at that given Fourier scale, k. By averaging over all the waves at a given wavenumber, we obtain the statistic defined as the matter power spectrum, $P(k) \equiv \langle |\delta_{\mathbf{k}}|^2 \rangle_k$. The evolving power per logarithmic band is also expressed as

$$\Delta_k^2 = \frac{k^3 P(k)}{2\pi^2}; \tag{1.12}$$

which is also related to the mean square density fluctuation. Given a smoothly varying power spectrum, we can associate $1/k$ with a scale $R \approx 1/k$. Therefore, the spatial density fluctuations represented at scale R are characterised by the power spectrum at any time $P(k, t)$.

The gravitational potential, ϕ, due to a density fluctuation, δ, in a region of size, R, is $\phi \propto \delta \langle \rho_m \rangle R^2$, which is independent of $a(t)$. In the early Universe, the density fluctuations that

were encoded in the potential must have been imprinted on the radiation field when radiation decoupled from matter. As the photos climb out of a potential $\phi/c^2 \approx \Delta\nu/\nu$, they are gravitationally redshifted due to loss of energy. We expect to see a temperature anisotropy in the CMB radiation $\Delta T/T \approx \phi/c^2$. The deepest potential wells of today's objects, i.e., galaxy clusters, require escape velocities of $v_{\rm esc} \sim 10^3$ km s^{-1}, corresponding to $\Delta T/T \approx O(10^{-5})$, which is exactly the scale measured in CMB anisotripies.

As the density fluctuations $\delta \rightarrow 1$, the amount of power per logarithmic band in Fourier space becomes non-linear (Peebles, 2020) and is better understood using N-body simulations. Additionally, the evolution of the density fluctuations is influenced by the expanding Universe, particularly $a(t)$, where the collapsing overdensities are damped by the expansion rate of the Universe. The maximum expansion of the density perturbation before collapsing, the so-called turnaround time, approaches when the density contrast $\delta \approx 1.06$. After the turnaround time, it can be shown that the perturbations eventually collapse to form bound objects, i.e., halos form above the critical threshold $\delta \equiv \delta_c \approx 1.686$. The corresponding redshift for the formation of structures goes up to $z \sim 20$ (Padmanabhan, 2002). As dark matter is the dominant component of matter, the halos that first formed were made up of dark matter. The distribution of dark matter then dictates the formation of objects with visible matter, like gaseous halos and stars, later forming galaxies (White & Rees, 1978). In the hierarchical CDM paradigm, smaller structures collapse first and then merge into larger systems, proceeding in a "bottom-up" fashion (Mo et al., 2010; Cole et al., 2000).

1.1.3 From dark matter halos to galaxy formation

While dark matter governs the large-scale scaffolding of the Universe, it is the baryonic matter, particularly in the form of stars and gas within galaxies, that traces and modifies the structure on smaller ($\sim$ kpc) scales (Blumenthal et al., 1984; Faucher-Giguère et al., 2011). Galaxies form within the gravitational potential wells of dark matter halos, representing collapsed, high-density regions within the cosmic web (Bond et al., 1996). They have characteristic stellar masses $\sim 10^{11}$ M$_\odot$, and are crucial tracers for understanding the Universe's evolution (Blanton & Moustakas, 2009; Naab & Ostriker, 2017).

Within the ΛCDM paradigm, cold dark matter is a collisionless fluid that collapses predominantly due to gravity, without experiencing shocks or significant free-streaming (Springel et al., 2006; Peebles, 2020). Contrarily, the infalling baryonic gas into the dark matter potential wells experiences pressure. It can cool and condense, losing energy primarily through two-body radiative processes such as bremsstrahlung emission, atomic excitation, and inverse Compton scattering (Rees & Ostriker, 1977; Silk, 1977; Böhringer & Werner, 2010). This enables the baryonic material to segregate from the dark matter and accumulate as dense, cold gas at the centre of the dark matter halo, forming stars that assemble into galaxies.

The initial stages of galaxy formation depend not only on the gravitational collapse of matter perturbations but also critically on gas thermodynamics and associated physical processes. Studies (e.g., Kereš et al. 2009; Dekel & Birnboim 2006) show that the gas accreting onto halos can follow distinct thermal pathways, which are critical for galaxy formation. If the cooling time of the gas is shorter than the dynamical time of the halo, rapid collapse and fragmentation

into stars can occur (Rees & Ostriker, 1977; Fardal et al., 2001; Dekel et al., 2009). In more massive halos, where radiative cooling may be inefficient, gas can shock-heat to the virial temperature and settle into a quasi-static equilibrium, forming a hot gaseous atmosphere. These hot atmospheres are prevalent at halo masses $\gtrsim 10^{12}$ $M_\odot$, i.e., at Milky-Way mass and more massive clusters and groups of galaxies today (e.g., Gunn & Gott 1972; Dekel & Birnboim 2006; Popesso et al. 2024c). In contrast, in low-mass halos or along dense filaments of the cosmic web, studies show that gas may avoid strong shock-heating and accrete directly in a "cold mode" (see e.g., Kereš et al. 2005; Birnboim & Dekel 2003). This cold flow occurs when the gas cools effectively as it falls in, or if its pressure support is negligible, allowing it to free-fall to the centre without developing an accretion shock. The transition between cold and hot mode accretion depends on halo mass and redshift, with halos $\ll 10^{12}$ $M_\odot$ typically accreting via the cold mode, while more massive halos (above $\gtrsim 10^{12}$ $M_\odot$) experience hot mode accretion (van de Voort et al., 2011; Kereš et al., 2009). These accretion modes, which depend on halo mass and redshift, fundamentally determine the gas supply available for star formation over cosmic time (Brinchmann et al., 2004; Ocvirk et al., 2008).

The balance between different galaxy formation processes and the initial conditions dictates the eventual formation of stars and their assembly into diverse galactic structures, such as whether a system forms an elliptical galaxy, if most gas turns into stars rapidly during collapse, or a spiral galaxy, if the gas remains gaseous and settles into a rotationally supported disk first (Fall & Efstathiou, 1980; White & Rees, 1978; Mo et al., 1998). The ability of gas to form molecular hydrogen and cool effectively is particularly important for the formation of the first stars in early, small halos at high redshifts (Tegmark et al., 1997; Abel et al., 2002; Bromm & Larson, 2004). The observable properties of galaxies (stellar mass, morphology, star formation rate, and internal structure) emerge from the complex interplay between cosmological accretion, star formation, and feedback processes (White & Frenk, 1991; Somerville & Davé, 2015), as further described in Sec. 1.2. Baryons can reach higher central densities than dark matter, enabling the formation of compact structures such as disks and bulges (Mo et al., 2010). However, energetic feedback from supernovae and AGN can heat and expel gas, reducing star formation and modifying the mass distribution within halos (Springel & Hernquist, 2005; Springel et al., 2005b; Velliscig et al., 2014). Studies linking star formation to gas surface density and pressure (see e.g., Kennicutt Jr 1998; Schaye & Dalla Vecchia 2008; Crain & van de Voort 2023) pave the way to understand the connections between interstellar gas properties and global galactic evolution. All these processes have an impact on the dark matter halos under certain conditions, contrary to naive expectations from dark matter-only models (Mashchenko et al., 2006, 2008; Governato et al., 2010; Pontzen & Governato, 2012; van Daalen et al., 2014).

Galaxy formation is a complex physical process governed by many effects acting simultaneously, e.g., gravitational dynamics, hydrodynamics, radiative cooling, and energetic feedback, all within dark matter halos (Somerville & Davé, 2015; Naab & Ostriker, 2017). The resulting galaxy populations vary widely in morphology and structure, shaped by complex formation histories and evolving intrinsic and extrinsic conditions (Conselice, 2014). Therefore, observational properties of galaxies serve as the most direct probes of their evolutionary pathways.

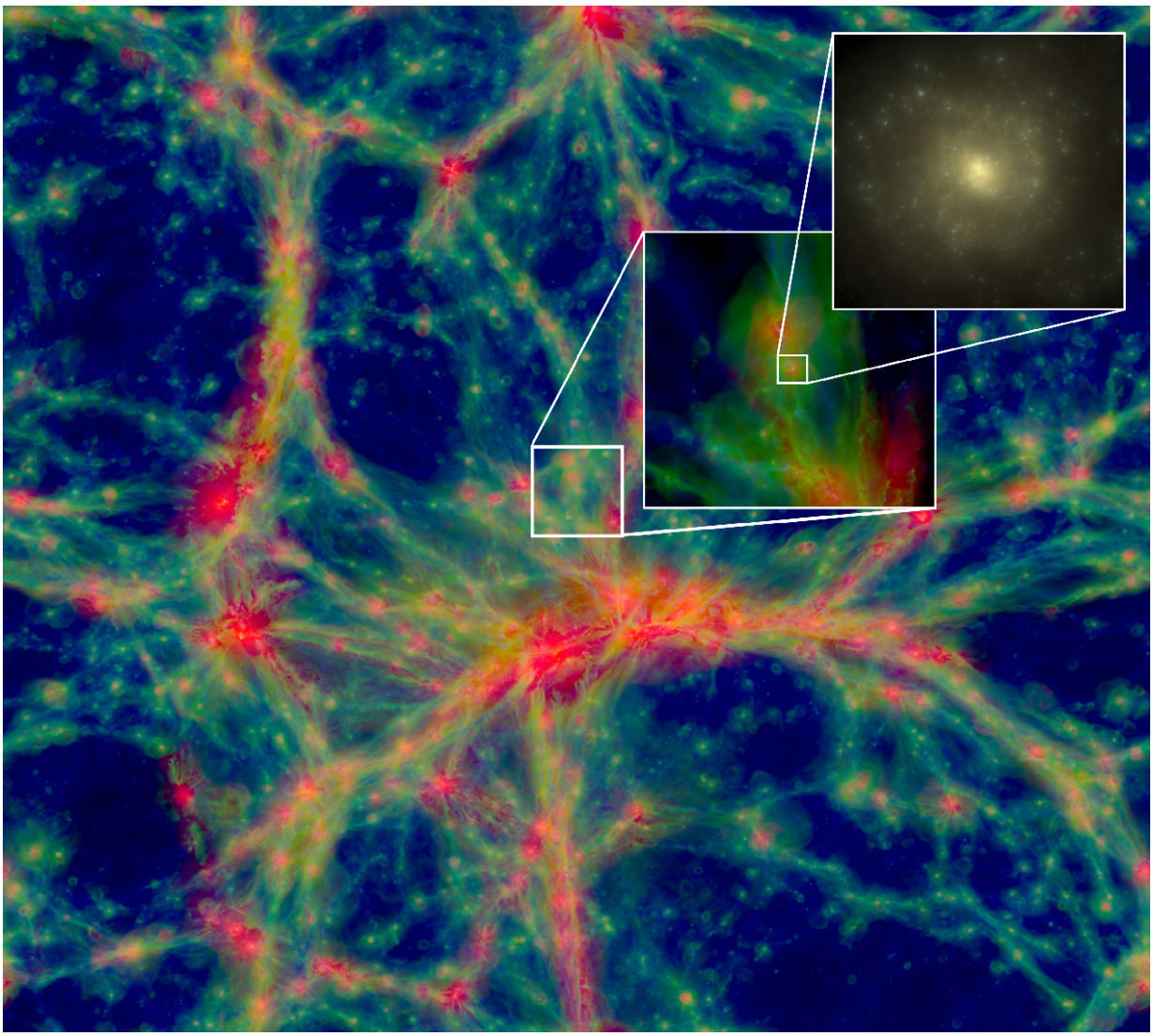

Figure 1.2: Visualisation of the multi-phase baryonic structure from the EAGLE (Schaye et al., 2015) Ref-L100N1504 simulation at $z = 0$, highlighting the interplay between gas dynamics and galaxy formation. The large panel displays a comoving $100 \times 100 \times 20$ Mpc slice in projection, where the gas density determines the brightness and gas temperature is color-coded: blue for cold gas ($T < 10^{4.5}$ K), green for warm gas ($10^{4.5}$ K $< T < 10^{5.5}$ K), and red for hot gas ($T > 10^{5.5}$ K). These temperature regimes trace distinct phases of the cosmic baryon cycle, such as cold filamentary inflows, shock-heated halo gas, and feedback-driven outflows, which are central to the thermodynamics of the CGM. The 10 cMpc and 60 ckpc insets zoom in on a galaxy with a stellar mass of $M_\star \sim 3 \times 10^{10}\, M_\odot$: the 10 cMpc view highlights its local cosmic web environment, while the 60 ckpc panel shows the distribution of starlight in optical bands. Together, these multiscale projections demonstrate how cosmological hydrodynamical simulations capture the emergence of galaxy populations from the evolving gas distribution within the large-scale structure. Figure taken from Schaye et al. (2015).

1.2 Galaxy properties

Historically, the structural and morphological diversity of galaxies was the key observational probe of physical processes inherent to galaxy formation and evolution. The Hubble sequence (Hubble, 1929; Sandage, 2005) and its later refinements (e.g., De Vaucouleurs 1959; van den Bergh 1976; Elmegreen & Elmegreen 1987) provide a taxonomy for galaxy types based on visual and structural characteristics such as spiral arms, bars, rings, and bulge-to-disk ratios. Hubble's terminology and classification of galaxies into "early-type" (ellipticals and lenticulars) and "late-type" (spirals) galaxies remains widely used, where galaxies are divided into smooth, dispersion-supported early-types and complex, rotation-supported late-types (see e.g., Blanton & Moustakas 2009; Mo et al. 2010). Spiral (late-type) galaxies are disk systems with ongoing star formation and typically blue in colour, often hosting central bulges (classical or pseudobulges), with bars that redistribute angular momentum, and distinct thin and thick disk components, e.g., Gilmore & Reid (1983); Kennicutt Jr (1998); Kormendy & Kennicutt Jr (2004). Lenticulars are disk galaxies with smooth, concentrated light profiles, low specific star formation rates, and little molecular gas; they lack spiral structure but retain disk-like features (Dressler, 1980; Van den Bergh, 2009; Blanton & Moustakas, 2009). Ellipticals (early-types) exhibit smooth, symmetric morphologies, old stellar populations, low cold-gas content, and predominantly red colours (e.g., Merritt 1999; Chiosi & Carraro 2002; Renzini 2006; Tojeiro et al. 2013; Cassisi & Salaris 2013). With the advent of recent surveys, which provide high quality galaxy spectra, galaxy light profiles, and robust bulge–disk decompositions, morphology can be better studied through quantitative structural parameters[6]. These advances allow us to move beyond purely visual classification and connect galaxy structure to formation pathways (e.g., Peletier & Balcells 1996; De Jong et al. 2004; Falcón-Barroso & Knapen 2013; Conselice 2014).

Galaxies grow and change through cosmic gas accretion, mergers, internal instabilities, and environmental interactions, which set the fuel for star formation and black hole growth and help trigger the transition from star-forming to quiescent states (quenching); e.g., Dekel & Birnboim (2006); Kereš et al. (2005); Martin et al. (2018); Peng et al. (2010). This evolution is tightly linked to feedback, the energy and momentum from stars and supermassive black holes, which acts in preventive (hindering fresh gas from reaching the ISM) and ejective (removing ISM gas) ways (see reviews by Somerville & Davé 2015; Naab & Ostriker 2017; Donahue & Voit 2022). Stellar feedback refers to outflows from massive stars and supernovae, while AGN feedback refers to energy and momentum transfer from central black holes of the galaxy (Dekel & Woo, 2003; Hopkins et al., 2012; Eckert et al., 2021). AGN feedback operates in two modes: a radiative (quasar) mode at high, radiatively efficient accretion, triggered by mergers or disk instabilities, which launches fast winds and expels cold gas to suppress star formation; and a kinetic jet (radio) mode at low, radiatively inefficient accretion from hot halos, where relativistic jets heat halo gas and prevent cooling flows (e.g., Croton et al. 2006; Hopkins & Elvis 2010; McNamara & Nulsen 2007; Heckman & Best 2014; Alexander & Hickox 2012; Brandt & Alexander 2015). In combination, stellar feedback regulates and can quench low-mass systems, while AGN feedback

[6]Morphology is parameterised by the bulge-to-disk ratio (B/T) and the Sérsic index n as a proxy for light concentration, where disks are well described by $n \sim 1$ (exponential profiles), whereas ellipticals and classical bulges typically have $n \sim 4$ (de Vaucouleurs-like profiles); e.g., see review by Blanton & Moustakas 2009.

is key to regulating quiescence in massive ($\gtrsim 10^{12}$ $M_\odot$) halos (e.g., Donahue & Voit 2022).

Statistical comparisons of galaxy populations across cosmic time provide key insights into their evolutionary pathways. Despite their diversity in mass, size, and morphology, galaxies also reveal a striking degree of regularity, following a number of remarkably tight scaling relations (see e.g., Mo et al. 2010). One of the most fundamental manifestations of this regularity is the bimodal distribution of galaxies in color–magnitude space. Galaxies display a pronounced separation into a 'blue cloud' and a 'red sequence' (Strateva et al., 2001; Baldry et al., 2004; Blanton & Moustakas, 2009). The red sequence is primarily made up of quiescent systems, dominated by old stellar populations with little or no ongoing star formation (e.g., Van Den Bosch et al. 2008; Graves et al. 2009; Williams et al. 2009). In contrast, the blue cloud contains star-forming galaxies, which host younger stellar populations and exhibit active star formation (Brinchmann et al., 2004; Asari et al., 2007; Whitaker et al., 2012). This bimodality persists at least to $z \sim 1$, and can be traced spectroscopically using the 4000-Å break, a robust indicator of stellar population age (Kauffmann et al., 2003; Bell et al., 2004; Kriek et al., 2006; Wu et al., 2018). Observationally, the comoving number and stellar mass density of quiescent galaxies has risen significantly since $z \sim 2$, indicating that many galaxies once in the blue cloud have transitioned to the red sequence through quenching processes (Vulcani et al., 2014; Sampaio et al., 2022). These trends highlight how statistical relations provide a powerful framework for linking galaxy properties to their evolutionary states, as discussed in the following subsection on the statistical properties of galaxies

1.2.1 Statistical properties of galaxies

Key statistical properties of galaxies encapsulate crucial information about the underlying physical processes and must be explained by any successful simulation or theory of galaxy formation (see review by Primack 2024). This requires determining marginal distribution functions, allowing us to grasp the properties intrinsic to a galaxy population. Here we discuss the Galaxy Stellar Mass Function (GSMF), Luminosity Function (LF), the Stellar Mass-to-Halo Mass Relation (SMHR), Star-Forming Main Sequence (SFMS), and Mass-Metallicity Relation (MZR).

A fundamental property of a galaxy is its luminosity, which broadly traces its stellar content and correlates with stellar mass via mass-to-light relations, but evolves as stars form and age (Conroy, 2013; Bell & de Jong, 2001). As a result, the distribution of luminosities encodes key aspects of how the galaxy population evolves across cosmic time (Binggeli et al., 1988; Blanton et al., 2003). This evolution is typically quantified using the LF, $\phi(L)$, and the GSMF, $\phi(M_\star)$, which give the comoving number density as a function of luminosity and stellar mass, respectively. Both are commonly parameterized by a functional form called the Schechter function described by a normalization ϕ^*, a characteristic scale (L^* or M^*), and a slope α (Schechter, 1976; Baldry et al., 2012). Connecting these functions to the galaxy assembly histories, observations show that massive galaxies assembled the bulk of their stars earlier ($z \gtrsim 2$), while low-mass systems built up more gradually over extended timescales, a trend often termed "downsizing" (see e.g., Cowie et al. 1996; Neistein et al. 2006; Fontanot et al. 2009). These statistical descriptions not only capture the evolution of the galaxy population but also reveal how different galaxy types and physical processes dominate in different regimes; e.g., in the local Universe, the bright end

of the LF is dominated by early-type systems, whereas the faint population is largely late-type and star-forming (see e.g., Blanton & Moustakas 2009; Driver et al. 2022). Similarly, the sharp cutoff of the GSMF at the high-mass end is shaped by AGN feedback, which is key in maintaining quiescence in massive halos ($\gtrsim 10^{12}$ $M_\odot$); see e.g., Pillepich et al. 2018b; Oppenheimer et al. 2021; Crain & van de Voort 2023.

Another key property with which galaxies are associated is their underlying dark matter halos, as discussed in Sec. 1.1.3. Consequently, characterizing the galaxy population typically requires connecting its observable properties to those of the host dark matter halos (Berlind & Weinberg, 2002; Cooray & Sheth, 2002; Wechsler & Tinker, 2018). The SMHR links galaxy stellar mass to host halo mass and is a key benchmark for galaxy formation models and for interpreting survey data, because it encodes how efficiently halos turn baryons into stars and thereby ties galaxy statistics to the underlying dark matter halo population (Behroozi et al., 2013; Moster et al., 2013). Empirically, the ratio $M_\star/M_\mathrm{h}$ peaks at ~ 0.03 in halos of $M_\mathrm{h} \sim 10^{12}$ $M_\odot$ (Milky Way halo mass scale), implying that even at peak efficiency only $\lesssim 20\%$ of the available baryons are converted into stars by $z \simeq 0$ (Fukugita & Peebles, 2004; Moster et al., 2010; Peebles & Ratra, 2003). The stellar fraction declines toward both lower and higher halo masses, pointing to stellar feedback suppressing star formation in low-mass halos and AGN feedback doing so at high masses (Dekel & Silk, 1986; Benson et al., 2003; Croton et al., 2006; Somerville & Davé, 2015). This relation is tightly constrained by joint analyses of abundances, clustering, lensing, and group catalogs, shows $\lesssim 0.2$ dex intrinsic scatter above the pivot mass, and indicates that the bulk of cosmic star formation over time occurs in a narrow band around $M_\mathrm{h} \sim 10^{12}\,M_\odot$ (Yang et al., 2009; Leauthaud et al., 2012; Behroozi et al., 2013; Wechsler & Tinker, 2018).

Among star-forming galaxies, the star formation rate (SFR) correlates tightly with stellar mass, defining the star-forming main sequence (SFMS), whose overall normalization has declined steadily since $z \sim 2$ (Brinchmann et al., 2004; Noeske et al., 2007; Whitaker et al., 2012; Speagle et al., 2014). A second key scaling is the mass–metallicity relation (MZR), which shows that more massive galaxies are typically more metal-rich, with a slope that is steep below $M_\star \sim 10^{10.5}$ $M_\odot$ and flattens at higher masses (e.g., Tremonti et al. 2004; Baldry et al. 2008; Zahid et al. 2014; Wu et al. 2016; Maiolino & Mannucci 2019 and references therein). At a fixed stellar mass, galaxies at higher redshift have lower gas-phase metallicities (Zahid et al., 2014; Erb et al., 2006; Curti et al., 2020; Sanders et al., 2021). This flattening at the high-mass end has been interpreted as the combined result of efficient metal removal through galactic winds in low-mass systems, saturation of chemical yields in more massive galaxies, reduced star formation in low-mass galaxies due to stellar feedback, and possible variations in the integrated stellar initial mass function (e.g., Dekel & Silk 1986; Köppen et al. 2007; Finlator & Davé 2008; Zahid et al. 2014). Together, the SFMS and MZR trace how galaxies assemble mass, accrete gas, and are regulated by feedback (Lilly et al., 2013; Somerville & Davé, 2015; Primack, 2024).

Simulations aim to model this intricate interplay of different processes shaping these galaxy properties and scaling relations (Crain & van de Voort, 2023). An illustration of these coupled processes across cosmic scales is provided in Fig. 1.2, which shows multi-scale projections from the EAGLE simulation (Schaye et al., 2015). The figure demonstrates how gas density and temperature trace cosmic web filaments and the dark matter halos. It also shows halos hosting hot gaseous atmospheres and the impacts on baryons due to feedback-driven processes. The zoom-

ins reveal how a typical Milky Way-mass galaxy emerges from this complex environment. Such visualisations emphasise the essential role of simulations in linking the large-scale distribution of baryons to the internal properties of galaxies. Because these processes are multi-scale, non-linear, and coupled across large dynamical ranges, analytic treatments alone are insufficient, and cosmological hydrodynamical simulations have become an indispensable tool to study galaxy formation and evolution (Vogelsberger et al., 2020). They capture detailed gas evolution, its multi-phase nature, and feedback effects, crucially tracing the bidirectional coupling between galaxies and the vast circumgalactic medium (Tumlinson et al., 2017; Faucher-Giguère & Oh, 2023), forming the self-consistent framework for galaxy growth and the baryonic cycle (Péroux & Howk, 2020).

1.3 The Circumgalactic Medium (CGM)

The CGM plays a crucial role in interfacing the gas between the interstellar medium (ISM) within galaxies and the external intergalactic medium (IGM) outside them. It is defined as the gas within the virial radius of the galaxy but outside its stellar disk. This surrounding gas reservoir is gravitationally bound to the halo and encompasses the fossil imprints of physical mechanisms—such as outflows, inflows, and feedback processes—that dictate the evolution of galaxies (see Tumlinson et al. 2017 for a review). In recent years, this component has assumed a central role in our understanding of galaxy evolution, owing to rapid observational advances in probing this diffuse, nearly invisible material. Observations and simulations alike reveal that the CGM is a multiphase medium characterised by rich dynamics, complex ionisation states, and a range of temperatures and densities. It acts both as a source of star-forming fuel through cosmic web accretion and as a sink for outflowing gas from galaxies driven by stellar and AGN feedback (Faucher-Giguère & Oh, 2023).

Gas inflows from the cosmic web are vital to sustain star formation, while feedback processes and galactic winds play an essential role in regulating SFRs. Therefore, studies of the CGM help to constrain the mass distribution, kinematics, thermodynamics, and chemical abundances of the gas flows that regulate galaxy formation. These mechanisms are sensitive to the galaxy's environment and its dark matter halo properties, as shown by the SHMR (see Sec. 1.2.1); see review from Wechsler & Tinker (2018). According to most models, the SHMR indicates that the low-halo-mass end is sensitive to stellar and supernova (SN) driven feedback (Dekel & Woo, 2003; Benson et al., 2003), which causes gas heating, hot bubble formation (McKee & Ostriker, 1977), galactic-scale wind outflows (Dekel & Silk, 1986), and turbulence (Ostriker & Shetty, 2011; Strickland & Heckman, 2009). In contrast, AGN are expected to dominate the feedback in high-halo-mass systems (Silk & Rees, 1998; Fabian, 2012; Eckert et al., 2021). Of particular interest is the peak of the SHMR relation at the pivotal halo mass $M_{\rm h} \sim 10^{12}$ $M_\odot$, which corresponds to the mass scale of Milky Way (MW)-like galaxies and marks the maximum in star formation efficiency. The hot, volume-filling phase of the CGM at this mass scale encapsulates a rich range of physical processes and is therefore a key testbed for galaxy formation models (Faucher-Giguère & Oh, 2023).

The CGM is empirically observed to be multiphase, exhibiting a complex gas structure at

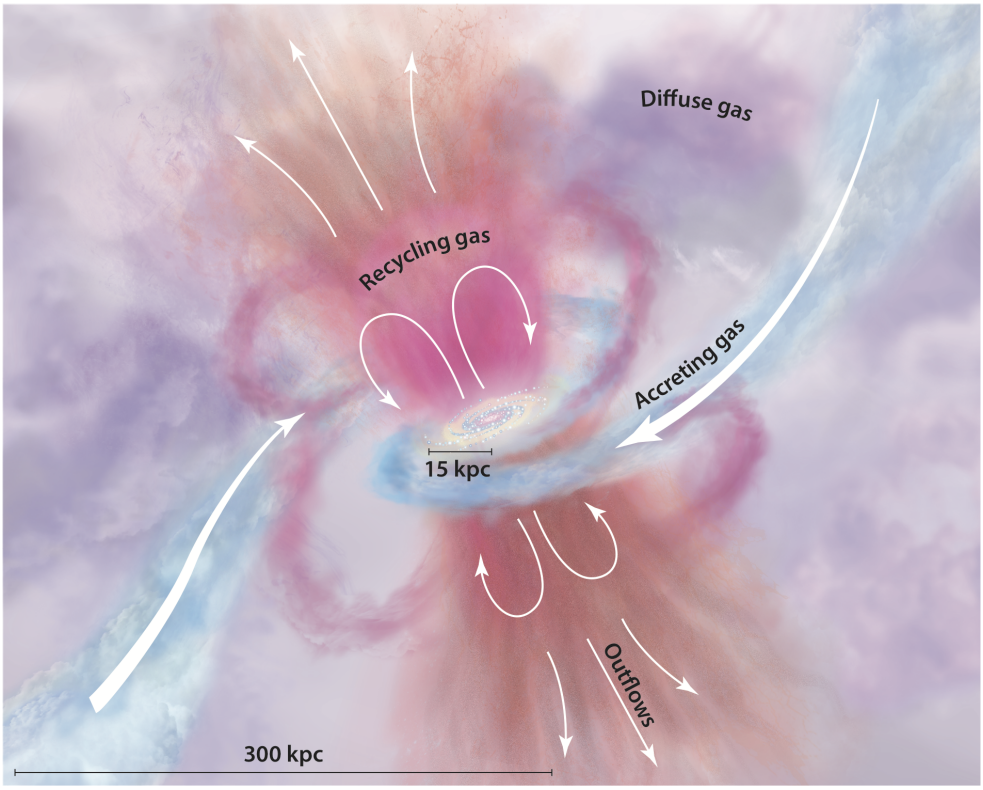

Figure 1.3: Illustration of the CGM taken from Tumlinson et al. (2017). The central galaxy, shown with a red stellar bulge and blue gaseous disk, is embedded within a halo of diffuse, multiphase gas, hosted by the CGM. Cold gas is accreted onto the galaxy through filamentary inflows from the intergalactic medium (IGM), shown in blue, while energetic outflows, driven by stellar and AGN feedback, emerge from the disk in pink and orange. Some of this ejected material eventually recycles back into the halo. The surrounding CGM, shown in varying shades of purple, represents a dynamically evolving reservoir that contains a mixture of gas contributed by inflows, outflows, and recycled material. This diffuse halo is empirically observed to be multiphase, containing cool ($T \sim 10^4$ K), warm-hot ($T \sim 10^{4-5.5}$ K), and hot ($T \gtrsim 10^{5.5}$ K) gas. These phases arise from a combination of cooling flows, shock heating, and turbulent mixing, resulting in a complex structure that is continuously reshaped through gas dynamics and feedback, and is probed observationally across the electromagnetic spectrum.

various temperatures and ionisation states (Tumlinson et al., 2017; Mo & Miralda-Escudé, 1996; Maller & Bullock, 2004). It contains a mixture of cool ($T \sim 10^4$ K), warm-hot ($T \sim 10^{4-5.5}$ K) and hot ($T \gtrsim 10^{5.5}$ K) gas, which are associated with processes such as infall of cooling flows (e.g., McCourt et al. 2012), shock heating and mixing of the diffuse gas during galactic outflows (e.g., Fielding et al. 2017; Thompson et al. 2016), contact layers between infalling cool gas and the ambient hot medium (Begelman & Fabian, 1990). This complex CGM structure can be probed through a variety of observational techniques across the electromagnetic spectrum, which are detailed in the following sections.

1.3.1 Absorption Line Studies

Absorption-line spectroscopy is one of the primary observational techniques for probing low-column-density CGM gas. This technique analyses the absorption features due to intervening gas imprinted on the continuum spectra of bright background sources such as quasars (see e.g., Prochaska et al. 2011; Tumlinson et al. 2013; Werk et al. 2014; Rubin 2017). Absorption lines from the CGM of halos span a wide range of ionized metal transitions, tracing gas at both high and low column densities. These studies can infer the chemical composition, ionisation conditions, kinematics, gas surface density, and thermodynamic structure of gas in the halos of the foreground galaxies (see e.g., Oppenheimer et al. 2012; Lan & Mo 2018; Lan 2020; Anand et al. 2021; Fumagalli 2024; Ng et al. 2025; Wu et al. 2025). Several major surveys have systematically characterised the CGM through these techniques (Tumlinson et al., 2013; Bordoloi et al., 2014; Lehner et al., 2022).

Absorption features span across wavelengths, ranging from soft X-rays to UV and optical/NIR bands all the way to radio 21 cm lines; each probing different temperature regimes and redshift windows (e.g., see Fig. 6 in Tumlinson et al. 2017). Different ions trace distinct phases of the CGM: e.g., neutral hydrogen (H I), Mg II, C II, and Si II trace cooler gas ($T \sim 10^4$ K) while C IV and Si IV probe intermediate-temperature gas. At the highest temperatures ($T > 10^{5.5}$ K), X-ray absorption lines from ions like O VI, O VII Kα or Ne VIII become prominent (see e.g., Wang et al. 2005; Nicastro et al. 2005; Galeazzi et al. 2007; Bhattacharyya et al. 2023; Mathur et al. 2023).

Despite their advantages, absorption-line studies face challenges (see e.g., Churchill et al. 2015; Marra et al. 2021; Fumagalli 2024); they are generally limited to one sightline per galaxy due to the rarity of bright background quasars (e.g., Lehner et al., 2015; Bowen et al., 2016; Rauch & Haehnelt, 2011; Zhu & Ménard, 2013). In soft X-rays, the major challenge is constructing statistical samples and mapping the large-scale extent of the CGM, which will improve with future X-ray telescopes with microcalorimeters (Wijers et al., 2020; Bogdán et al., 2023). Additionally, line saturation and the blending of narrow line components can introduce ambiguities in the measurements (Tumlinson et al., 2017). The interpretation of observed lines often relies on complex photoionisation equilibrium (PIE) or collisional ionisation equilibrium (CIE) models, which can be affected by uncertainties in relative elemental abundances and the extragalactic ultraviolet background (Kollmeier et al., 2014).

1.3.2 Emission Studies

Emission, and especially emission line, observations serve as a complementary method to absorption line studies for investigations the CGM by directly detecting photons emitted from the gas. These studies are particularly effective at probing denser regions of the CGM as the emission measure scales as density squared (n^2)[7]. Therefore, it poses a challenge to probe the lower

[7]For Lyα nebulae, the emission is further affected by scattering since it is a resonant line. For recombination lines, it depends on the densities of the ions and electrons. For emission due to collisionally-excited HI regions, in addition to the dependence on the ion density, there is also influence due to the UV radiation field (see e.g., Cantalupo et al. 2005; Dijkstra 2014; Hennawi & Prochaska 2013)

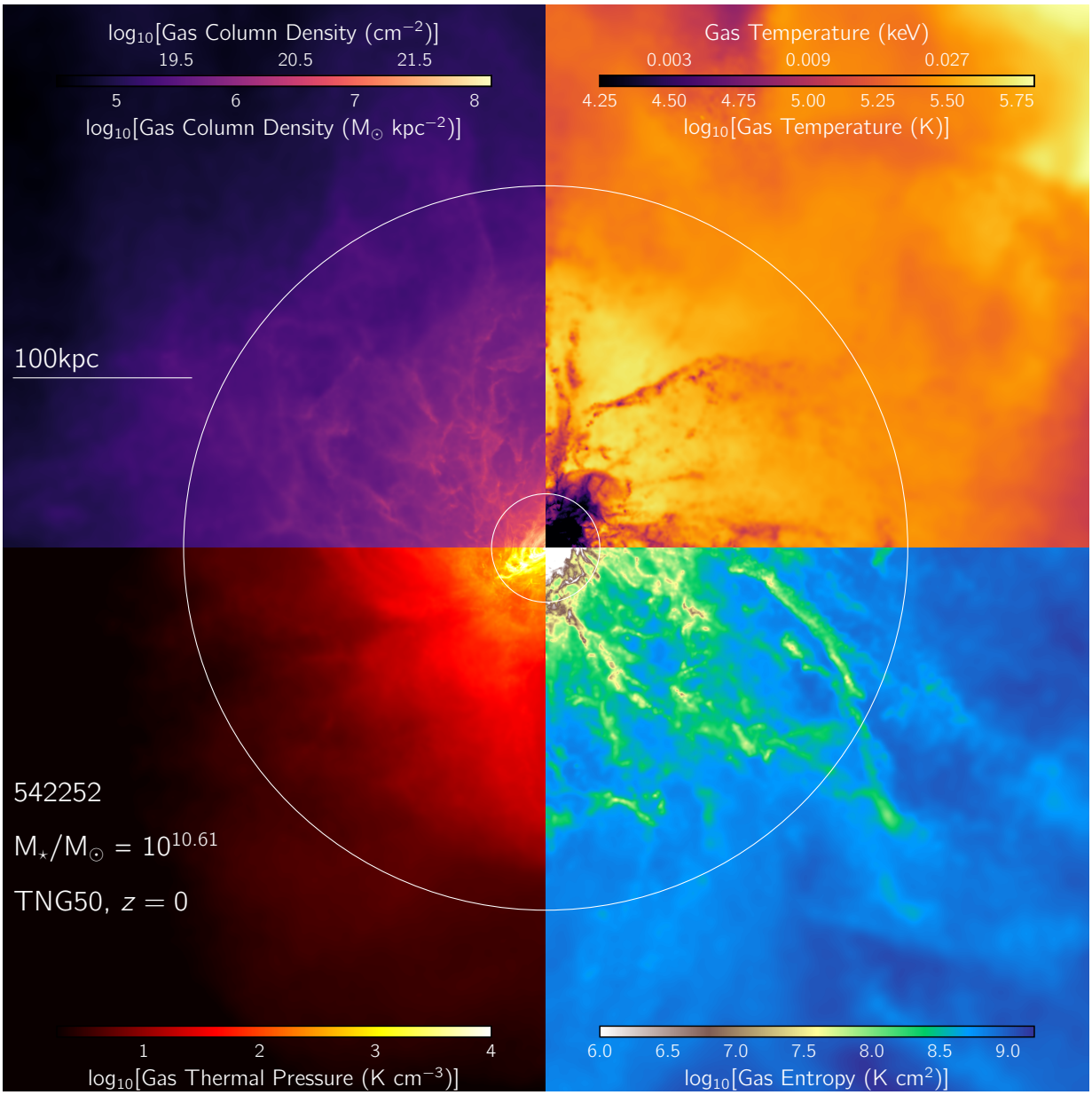

Figure 1.4: Visualisation of CGM gas properties around a Milky Way-like galaxy at $z = 0$ in the TNG50 simulation, taken from Ramesh et al. (2023b). The panels project the quantities within $\pm 1.5 R_{200c}$ and the white circle marks the R_{200c} of the halo. The four quadrants show the gas column density (upper left), gas temperature (upper right), pressure (lower left), and entropy (lower right). Temperature and entropy trace thermal structure and the shock-heated gas in the halo. They highlight the multi-phase nature of the CGM, where the central galaxy is dominated by dense, cold gas, while the outer regions host hotter gas. The entropy panel also highlights inhomogeneities within the CGM, appearing as overdense, cool, low-entropy regions. The gas column density map is useful for comparison with observations probing the CGM in absorption and emission line studies, as further detailed in Sec. 1.3.1 and 1.3.2.

density regions, which are better accessed in absorption line studies. The current state of emission line measurements is advancing across different wavelengths. In the radio band, the Milky Way's halo has been extensively mapped for High-Velocity Clouds (HVCs) via 21 cm H I line emission (Wakker & van Woerden, 1997), although applying this technique to external galaxies typically yields detections limited to within 10-20 kpc from the galactic center (Putman et al., 2012). In the UV wavelengths, Hayes et al. (2016) measured an extended O VI halo around a low-redshift starburst galaxy, and extended Lyα emission has been observed out to about 100 kpc from z $\sim$ 2.5 – 6.4 galaxies and quasars (e.g., Cantalupo et al. 2014; Prescott et al. 2015; Swinbank et al. 2015; Wisotzki et al. 2018; Farina et al. 2019; Leclercq et al. 2020; Li et al. 2023). However, complexities in Lyα radiative transfer hinder simple interpretation of Lyα emission maps (Dijkstra, 2014). Additionally, in optical wavelengths, Hα emission is found at 30-100 kpc around low-redshift galaxies by stacking spectra (e.g., Zhang et al. 2016, 2018, 2020; Tacchella et al. 2022; Zhang & Zaritsky 2024).

In the soft X-ray band, studies probe hot gas with temperatures exceeding $\gtrsim 10^{5.5}$ K, where highly ionized species such as O VII and O VIII exhibit strong transitions. For fully ionized gas, X-ray emission allows for more direct mass inferences, circumventing the uncertain ionization corrections common in absorption-line measurements. It is possible to probe the hot CGM using both narrow-band and broad-band contributions (Koutroumpa et al., 2007; Bertone et al., 2010; van de Voort, 2013; Bogdán et al., 2013b,a; Miller & Bregman, 2015; Anderson et al., 2016; Li & Bregman, 2017; Bogdán et al., 2017; Li et al., 2017; Bregman et al., 2018; Das et al., 2019; Gupta et al., 2023; Zheng et al., 2024a; Ponti et al., 2023a; Locatelli et al., 2024; Zheng et al., 2024b). The narrow-band emission comprising O VII and O VIII metal lines dominates the lower halo mass regime $10^{12} - 10^{13}$ $M_\odot$ (Bertone et al., 2010; van de Voort, 2013; Wijers, 2022) and is well-studied within our MW (Koutroumpa et al., 2007; Ponti et al., 2023a; Zheng et al., 2024a; Locatelli et al., 2024). The broad-band contributions in X-ray emission studies probe the thermal bremsstrahlung (free-free) continuum emission together with the weaker radiative recombination emission (see e.g., Böhringer & Werner 2010; Lovisari et al. 2021), allowing us to probe the plasma beyond line emission alone in stacking analyses.

Despite these advancements, due to the n^2 scaling of emission measure, the extremely low surface brightness of CGM gas beyond $\gtrsim$ 100 kpc, and the steep increase of surface brightness dimming ($\propto 1/(1+z)^4$) with redshift, emission lines observations are technically challenging and expensive for extragalactic and distant objects. Specifically in soft X-rays, this motivates the need for future high-spectral resolution instruments to distinguish the extragalactic emission from that of the MW foreground (Nelson et al., 2023; Truong et al., 2023; Schellenberger et al., 2024; ZuHone et al., 2024). Currently, extragalactic emission line studies are limited to single-object direct imaging or small sample sizes, highlighting the importance of complementary broadband stacking/averaging analysis, as further detailed in the next section. Nevertheless, by implementing forward models (Sec. 1.4), we can access buried hot CGM information, probed by current X-ray observations, demonstrating that we do not need to wait until missions like NewAthena (Nandra et al., 2013; Barret et al., 2020; Cruise et al., 2025), and HUBS (Cui et al., 2020) to gain valuable insights about the CGM.

1.3.3 CGM observations using large optical galaxy samples

A common technique employed to obtain higher signal-to-noise measurements to map the large-scale CGM out to the virial radius is averaging over numerous objects, also called stacking. This technique is a powerful way to extract faint signals by grouping objects in redshift and stellar or halo mass bins. With the advent of large-area optical surveys, it has now become possible to obtain redshifts and stellar mass catalogues of the order $\gtrsim 10^6$ galaxies, e.g., with SDSS[8] (Comparat et al., 2017); DESI[9] Legacy Survey (Zou et al., 2019). Observational probes studying the CGM are thus made possible with stacking techniques that use large area optical surveys. Due to detection limits, these probes are especially powerful at the MW-stellar mass ($\sim 5 \times 10^{10}$ $M_\odot$) scale and the more massive galaxy groups mass scale. They are as follows:

Thermal Sunyaev–Zeldovich effect (tSZ)

The thermal Sunyaev–Zel'dovich effect (Sunyaev & Zeldovich, 1972, tSZ) at mm-wavelengths originates from the Compton scattering of CMB photons travelling through hot ionized gas along the line of sight. These photons undergo inverse Compton scattering with the free electrons prevailing in the CGM, IGM and other intervening ionised media, causing secondary CMB anisotropies. The tSZ signal is an excellent tool for accessing the hot baryonic gas. This technique has been successfully applied together with stacking, probing the hot CGM around MW-mass galaxies and groups (Planck Collaboration et al., 2013; Lim et al., 2018, 2021; Schaan et al., 2021; Bregman et al., 2022; Das et al., 2023; Oren et al., 2024; Di Mascolo et al., 2024).

Fast radio bursts (FRBs)

A new approach involves using FRBs to measure the Dispersion Measure (DM), which traces the total column density of free electrons along the line of sight. FRBs are mysterious millisecond-duration events detected with radio telescopes, which appear to be orders of magnitude more luminous than pulsars, originating from cosmological distances (Petroff et al., 2019). While there are many open questions regarding their physical origin and mechanisms (Zhang, 2023), they are proving to be a powerful probe for accessing the electron column densities in galactic halos (McQuinn, 2013; Ravi et al., 2019; Prochaska & Zheng, 2019; Wu & McQuinn, 2023; Ocker et al., 2025) and for computing the low-z baryon fraction[10] (Muñoz & Loeb, 2018; Lee et al., 2022; Macquart et al., 2020). As the majority of the CGM gas is ionised, foreground galactic halos cause a significant excess in the measured DM. For FRB DM measurements of the CGM of halos, precise localisation of the host galaxy is required to confidently measure the contribution from the foreground halos (e.g., see Medlock et al. 2024). Distinguishing between different CGM models using FRBs would necessitate tens of thousands of bursts, which will become possible with upcoming facilities (Hallinan et al., 2019; Vanderlinde et al., 2019; Leung et al., 2021; Bhandari & Flynn, 2021).

[8] https://www.sdss4.org/dr12/spectro/galaxy/

[9] https://www.legacysurvey.org/dr10/description/

[10] The baryon fraction in the local Universe, f_b, corresponds to the fraction of "baryonic mass" within halos.

Soft X-ray stacking

X-ray broadband emission maps, when combined with stacking, allow us to map the large-scale extent of the hot CGM to the halo's virial radius. Given the advent of the eROSITA telescope (Predehl et al., 2010; Merloni et al., 2024), with high sensitivity in the soft X-ray band, i.e., $0.5 - 2$ keV, and large-area optical surveys (e.g., SDSS, DESI), it is possible to exploit the unprecedented statistics to stack the X-ray emission at the position of optically selected galaxies (Comparat et al., 2022; Chadayammuri et al., 2022; Zhang et al., 2024a). The recent work, by Zhang et al. (2024a), represents the state-of-the-art hot CGM measurements for MW-mass galaxies, which combines largest optical galaxy sample with the German half-sky eROSITA coverage in X-rays. They stack $415,627$ galaxies with photometric redshifts from the DESI Legacy Survey DR 9 (Dey et al., 2019; Zou et al., 2019) and $30,825$ central galaxies with spectroscopic redshifts from the SDSS DR7 Main Galaxy Sample (Strauss et al., 2002; Abazajian et al., 2009). These measurements provide powerful constraints on the hot CGM of Milky-Way mass and M31-mass galaxies.

While X-ray stacking with eROSITA currently represents the most sensitive means of probing the hot CGM, its interpretation remains challenged by various observational effects that can contaminate the intrinsic CGM signal. To disentangle this signal from observational systematics, a comprehensive theoretical framework for modelling the intrinsic X-ray emission from the hot CGM is essential. More precisely, projection effects have emerged as a significant yet previously underexplored source of contamination in stacking experiments. These projection effects include contributions from the large-scale structure (LSS) surrounding halos, the misclassification of satellite galaxies as centrals due to photometric redshift uncertainties in wide-area surveys, offsets between the observed X-ray centre and the true centre of the gravitational potential, and the line-of-sight projection of unrelated foreground and background X-ray emission. In this context, it becomes crucial to quantify all such influences to enable robust tests of theoretical and numerical predictions of the hot CGM against observational data, and doing so is the main topic of this thesis. In the following Section 1.4, we provide a overview of the scopes of modelling the hot CGM, while Chapter 2 and 3 addresses the specific questions regarding X-ray stacking using the technique developed in this thesis, providing a comprehensive analysis and understanding of the contaminating projection effects that affect X-ray stacking measurements of the hot CGM.

1.4 Modelling the CGM

Modelling the multi-phase, multi-scale, multi-process CGM described in Sec. 1.3, and comparing it with observations, is vital to further our understanding of galaxy formation and evolution. More precisely, CGM models encapsulate the distribution of baryons around the galaxy, probing complex gas flows that fuel star formation, which are regulated by stellar and AGN feedback. In addition to hydrodynamical simulations, which are described in Sec. 1.4.1, alternative approaches to model the CGM include (i) semi-analytic models (SAMs), and (ii) analytical and equilibrium models. Together, SAMs, analytical, and equilibrium models form useful tools for computationally inexpensive predictions and aiding in the interpretation of observational results.

SAMs use analytic or phenomenological recipes to model baryonic processes atop merger trees derived from dark matter N-body simulations (Lacey & Silk, 1991; White & Frenk, 1991; Somerville & Primack, 1999; Cole et al., 2000; Springel et al., 2001; Croton et al., 2006; Guo et al., 2011; Somerville & Davé, 2015). They predict gas infall, cooling, star formation, and feedback, enabling broad parameter exploration across cosmological volumes (e.g., Henriques et al. 2015; Hirschmann et al. 2016; Lagos et al. 2018; Ayromlou et al. 2021b; Yates et al. 2024). Despite their computational efficiency for population studies, SAMs lack the capacity required to capture the detailed, multiphase structure observed in the CGM (e.g., Mitchell et al. 2018; Ayromlou et al. 2021a; Vani et al. 2025).

Various analytical and equilibrium models are implemented to describe the intrinsic properties of the hot CGM using simplified assumptions. These models often assume a generic force balance (e.g., hydrostatic equilibrium) in hot halos, maintained by feedback-driven heating or by a balance between gravitational forces and cooling losses (Faerman et al., 2017; Voit et al., 2019; Pal Choudhury et al., 2019; Stern et al., 2024; Singh et al., 2021; Pandya et al., 2023; Faerman & Werk, 2023). Common frameworks include precipitation models (Voit et al., 2017, 2018; Singh et al., 2021), isentropic configurations (Faerman et al., 2020, 2022), cooling flow models (Stern et al., 2019, 2024; Sultan et al., 2025), and baryon pasting approaches (Osato & Nagai, 2023). While these models can predict thermodynamic profiles of the CGM, significant divergence amongst them at both small and large radial scales highlights shortcomings in pressure support mechanisms and equilibrium assumptions (Pandya et al., 2023; Singh et al., 2024). This divergence underlines the limitations of these models in replicating the dynamic complexity and the self-consistent evolution inherent in real cosmic environments.

In contrast, hydrodynamical simulations offer a more comprehensive approach by resolving the spatially and kinematically complex structures observed in the CGM and capturing the full range of interactions between baryons and dark matter (e.g., Naab & Ostriker 2017). Such simulations incorporate detailed physics without relying on oversimplified assumptions, allowing for realistic modelling of multiphase gas dynamics, star formation, and feedback processes in a self-consistent manner. Thus, while SAMs and analytical models provide useful insights, hydrodynamical simulations remain the most powerful and versatile tool for accurately modelling the CGM and linking theoretical predictions with observational data. The different approaches to modelling the CGM are discussed in Sec. 1.4.1. The combined strengths of modelling approaches aid in understanding the CGM's multifaceted processes and provide a comprehensive framework for linking theory with observations. Sec. 1.4.2 summarises the key physical processes currently modelled to describe the CGM.

1.4.1 Hydrodynamical simulations

Historically, the emergence of hydrodynamical cosmological simulations as a tool was motivated by their early success in interpreting physical effects (see e.g., Holmberg 1941; Toomre & Toomre 1972; Aarseth 2003), such as the structure of the Lyman-α forest, the distribution of cosmic baryons in the Universe (e.g., Cen & Ostriker 1992; Hernquist et al. 1996; Cen & Ostriker 1999; Zhang et al. 1995), producing realistic galaxy populations (Springel et al., 2018; Schaye et al., 2015; Vogelsberger et al., 2014; Kaviraj et al., 2017), the impact of baryonic physics on the

matter power spectrum (see e.g., Jing et al. 2006; Rudd et al. 2008; van Daalen et al. 2020; Giri & Schneider 2021), the generation of late-type disc galaxies by including stellar feedback (Guedes et al., 2011; Stinson et al., 2013; Hopkins et al., 2014; Wang et al., 2015; Grand et al., 2017; Okamoto et al., 2005) and the influence of AGN feedback in higher-mass ($\gtrsim 10^{12}$ $M_\odot$) galaxies (see reviews by Brandt & Alexander 2015; Eckert et al. 2021; Harrison & Ramos Almeida 2024 and e.g., Springel et al. 2005a; Di Matteo et al. 2005; Vogelsberger et al. 2014). All these successes underpin the development of modern cosmological hydrodynamic simulations, which have since become one of the preferred methods for tackling the complex, multiscale, and multiphysics challenges inherent in galaxy formation (Vogelsberger et al., 2020; Faucher-Giguère & Oh, 2023).

Hydrodynamical simulations explicitly track baryonic matter (gas and stars), which brings into play a vast array of additional nonlinear processes that shape galaxies and their halos. Modern cosmological simulations evolve dark matter and baryons typically within a ΛCDM framework, starting from inflationary initial conditions and imprinting perturbations on a homogeneous Universe. The dynamics and evolution of the contents of the Universe are governed by the Friedmann equations (Somerville & Davé, 2015; Crain & van de Voort, 2023), as also detailed in Sec. 1.1.1. Dark matter dynamics are modelled using the collisionless Boltzmann and Poisson equations in an expanding Universe, solved via N-body techniques such as Particle-Mesh (PM), TreePM, and Fast Multipole methods, implemented by key codes like ART (Kravtsov et al., 1997), RAMSES (Teyssier, 2002), GADGET-2/3 (Springel, 2005), Arepo (Springel, 2010b), Enzo (Bryan et al., 2014), ChaNGa (Jetley et al., 2008), GIZMO (Hopkins, 2015), HACC (Habib et al., 2016), PKDGRAV3 (Potter et al., 2017), Gasoline2 (Wadsley et al., 2017), and SWIFT (Schaller et al., 2024). Baryonic matter, treated as an inviscid ideal gas, is evolved using hydrodynamic solvers that fall into Lagrangian (e.g., Smooth Particle Hydrodynamics (SPH); Springel 2010a), Eulerian (e.g., adaptive-mesh-refinement; Berger & Oliger 1984), or Arbitrary Lagrangian-Eulerian (e.g., moving-mesh; Springel 2010b) schemes. Due to finite resolution in simulations, sub-resolution models are employed to represent unresolved physical processes at $\lesssim$ kpc-scale, such as gas cooling, star formation (typically from dense, neutral gas following a two-phase ISM prescription; Springel & Hernquist 2003), and feedback from stars and black holes. Stellar feedback injects thermal or kinetic energy and regulates star formation, often through decoupled wind particles (Vogelsberger et al., 2020). Black hole growth is modelled through gas accretion and mergers, with AGN feedback implemented in thermal or kinetic modes, as mentioned in Sec. 1.1.3 and later in Sec. 1.4.2; in simulations like IllustrisTNG, kinetic AGN feedback at low accretion rates drives super-virial outflows and suppresses star formation in massive halos (Weinberger et al., 2018). Additional physics that are also modelled in some simulations include magnetic fields, cosmic rays, and radiation hydrodynamics, which alter gas properties, as discussed further in Sec. 1.4.2.

Broadly, the results of hydrodynamical simulations can be categorised into two domains: those that describe global statistical properties of the galaxy population and those that focus on the detailed physical properties of individual galaxies. The former are best studied using large-volume simulations ($\geq 50^3$ Mpc^3), which provide the statistical power necessary for comparison with galaxy surveys, while the latter are better probed by zoom-in simulations. Groundbreaking large-volume hydrodynamical simulations, such as, BAHAMAS (McCarthy

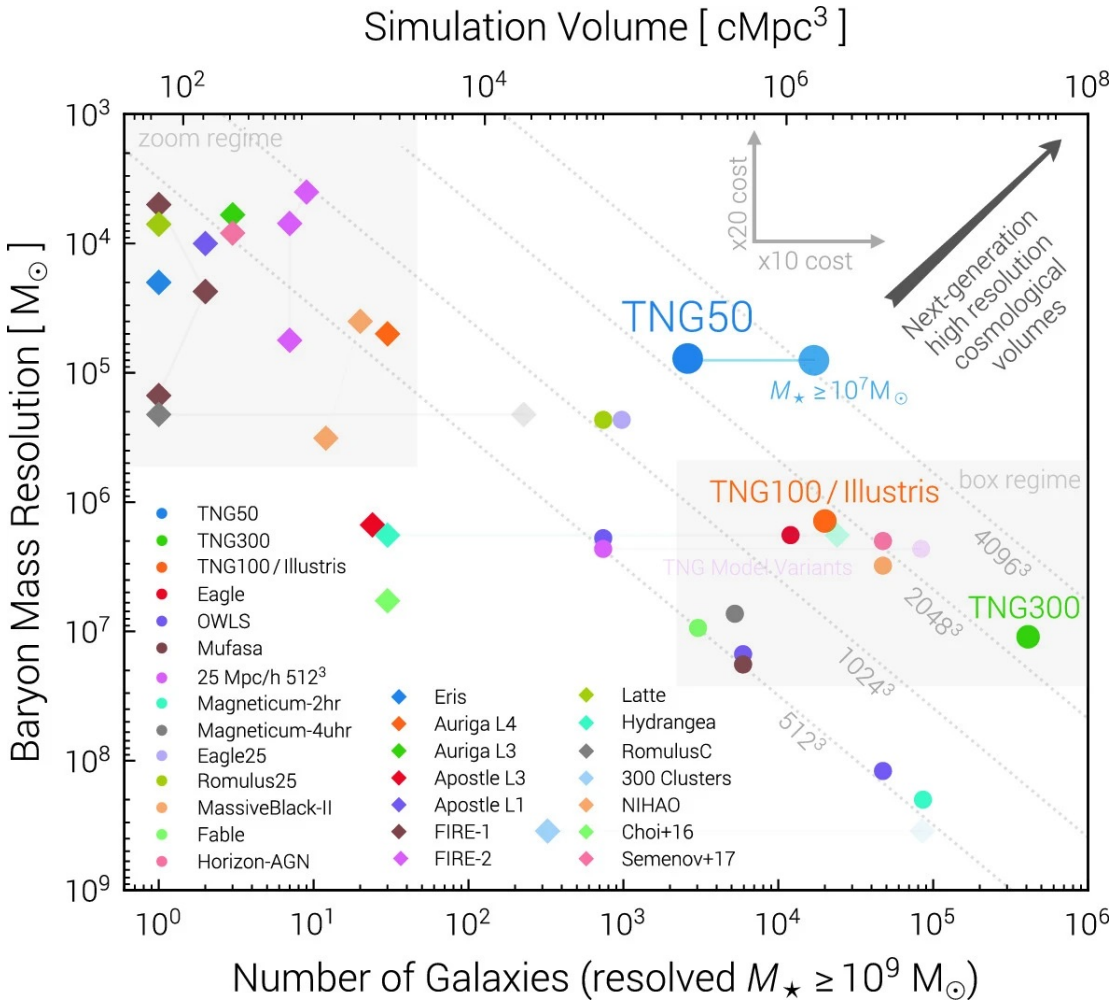

Figure 1.5: Comparison of various cosmological hydrodynamical simulations at $z \sim 0$, including both large-volume runs (shown as circles) with box sizes exceeding 25 Mpc and zoom-in simulation projects (shown as diamonds). The x-axis represents the effective simulation volume, which is a proxy for the total number of resolved galaxies with stellar masses $> 10^9$ $M_\odot$ and the total galaxy statistics. The y-axis indicates the mass resolution, expressed by the lowest baryonic mass element. Progressing toward the upper right corner of the plot marks the frontier of next-generation, high-resolution cosmological simulations, which require significant computational resources and access to some of the world's largest supercomputing facilities. Here the IllustrisTNG suite of simulations are highlighted with three box sizes (50 Mpc/h, 100 Mpc/h, and 300 Mpc/h), of which this thesis utilises the 300 Mpc/h TNG box. This figure is taken from Pillepich et al. (2021).

et al., 2016), BlueTides (Feng et al., 2016), EAGLE (Schaye et al., 2015), Fable (Henden et al., 2018), FLAMINGO (Schaye et al., 2023b), Horizon-AGN (Dubois et al., 2014), Illustris (Vogelsberger et al., 2014; Genel et al., 2014; Sijacki et al., 2015), IllustrisTNG (The Next Generation) (Pillepich et al., 2018b; Springel et al., 2018; Nelson et al., 2018; Marinacci et al., 2018; Naiman et al., 2018), Magneticum (Dolag, 2015; Dolag et al., 2025), MTNG - Mil-

lenniumTNG (Pakmor et al., 2023), MassiveBlack-II (Khandai et al., 2015), MUFASA (Davé et al., 2016), OWLS (Schaye et al., 2010) and SIMBA (Davé et al., 2019), form the benchmark for theoretical galaxy and CGM studies. Additionally, high-resolution and zoom-in projects, such as Apostle (Sawala et al., 2016), Auriga (Grand et al., 2017), Aquarius (Springel et al., 2008), Eris (Guedes et al., 2011), FIRE-1 (Hopkins et al., 2014), Fire-2 (Hopkins et al., 2018), FLARES (Lovell et al., 2021), FOGGIE (Peeples et al., 2019), Hydrangea (Bahé et al., 2017), The Three Hundred project (Cui et al., 2018b), NIHAO (Wang et al., 2015), Agertz & Kravtsov (2016), and smaller-volume projects (25 Mpc)^3 e.g., Romulus25 (Tremmel et al., 2017), CAMELS (Villaescusa-Navarro et al., 2021a), further complement these efforts, probing the fine physical detail of gas flows on smaller scales (see also Tab. 2 in Vogelsberger et al. 2020 for a summary of simulation properties).

Each simulation suite brings a different balance of box size, mass resolution, baryonic physics, and scientific aims, but together they provide a vast repository of realisations to be used to interpret observational campaigns and understand the baryon cycle (e.g., Wright et al. 2024). We show a summary plot from Pillepich et al. (2021) of the resolved baryonic mass element (proxy for the resolution of the simulation) as a function of the simulation volume (proxy for galaxy statistics) for some key simulations in Fig. 1.5. We note that more recently, there exist new suites of next-generation cosmological simulations such as MTNG and FLAMINGO, which offer Gpc-scale box sizes, however, with poorer mass resolutions compared to TNG300 (see Fig. 1 in Schaye et al. 2023a). To construct a forward model that replicates observational X-ray stacking experiments, we require a simulation that combines large galaxy statistics, capturing the effects of cosmological large-scale structure, together with the smaller-scale complex physics of feedback and cooling in the hot CGM. At the time of starting this thesis, the TNG300 run of the IllustrisTNG cosmological hydrodynamical simulation offers the optimal compromise between volume (302.6 Mpc box size) and mass resolution (1.1×10^7 $M_\odot$), enabling the detailed study of the hot CGM gas hosted by MW-mass galaxies together with a statistically robust sample of galaxies.

The IllustrisTNG project, comprising a suite of publicly available simulations with three box sizes TNG50, TNG100, and TNG300, utilises the AREPO code. AREPO employs a moving-mesh finite volume method on an unstructured, dynamic Voronoi tessellation to solve equations of ideal magnetohydrodynamics (MHD) and self-gravity, with gravity calculated via a Tree-PM scheme. IllustrisTNG accounts for many physical processes, of which the most notable ones are star formation regulated by a subgrid ISM model (Springel & Hernquist, 2003), metal enrichment (Naiman et al., 2018), radiative gas cooling, galactic wind outflows (Pillepich et al., 2018a), magnetic fields and diffuse radio emission (Marinacci et al., 2018), supermassive black hole growth with Bondi accretion and mergers, thermal and kinetic modes for black hole feedback (Weinberger et al., 2018). TNG300 contains 2500^3 dark matter particles, with a baryonic mass resolution of 1.1×10^7 $M_\odot$, a comoving value of the adaptive gas gravitational softening length for gas cells of 370 comoving parsec, gravitational softening of the collisionless component of 1.48 kpc, and dark matter mass resolution of 5.9×10^7 $M_\odot$. The TNG simulations adopt the Planck Collaboration XIII 2016 cosmological parameters, with the matter density parameter $\Omega_\mathrm{m} = \Omega_\mathrm{dm} + \Omega_\mathrm{b} = 0.3089$, baryonic density parameter $\Omega_b = 0.0486$, Hubble constant $\mathrm{H}_0 = 100h$ km/s/Mpc with $h = 0.6774$, and $\Omega_\Lambda = 0.6911$. The TNG model is calibrated to match key

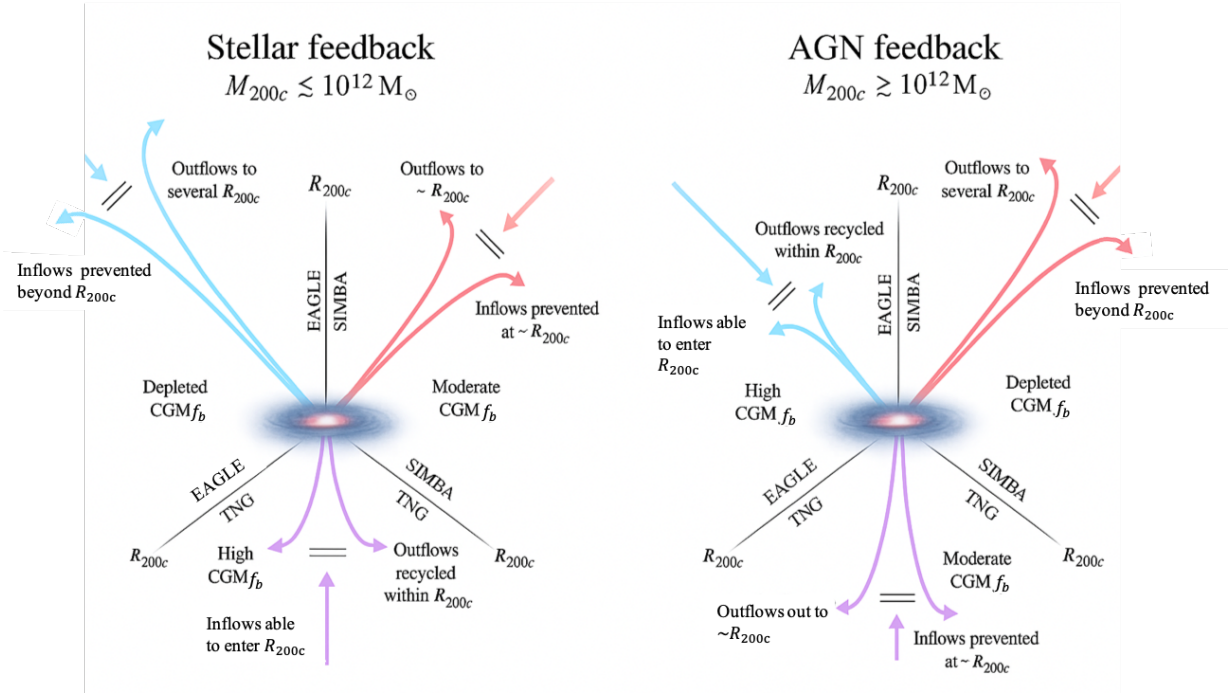

Figure 1.6: Schematic diagram adapted from Wright et al. (2024) summarising the differences between three key simulations, EAGLE, TNG and SIMBA, on the gas flows inherent to the CGM. They split the galaxy sample into low mass haloes (left) and higher mass haloes (right), where stellar and AGN feedback dominate, respectively. They find that stellar feedback-driven outflows in EAGLE (upper left) and SIMBA (upper right) can reach 2–3 $\times$ R_{200c} at low halo masses ($M_{200c} \lesssim 10^{12}$ $M_\odot$), while TNG (bottom) predicts outflows that remain largely confined within the halo. For AGN-driven outflows, SIMBA produces powerful winds extending several times R_{200c} even in halos up to $M_{200c} \approx 10^{13.5}$ $M_\odot$, whereas TNG and EAGLE show more limited gas ejection beyond 2–3 $\times$ R_{200c}. Consequently, feedback also impacts the baryon fraction in the CGM, as also depicted in the illustration.

observational constraints at $z = 0$, such as the cosmic star formation rate density, the galaxy stellar mass function, and the stellar-to-halo mass relation, correlation functions and power spectra, aiming to produce a realistic and diverse galaxy population (Weinberger et al., 2018; Pillepich et al., 2018a,b; Springel et al., 2018).

Accurately modelling the hot CGM is challenging due to its complex, multiphase, and multi-scale structure, and its properties are highly sensitive to subgrid feedback models in cosmological simulations (see e.g., Lau et al. 2024). Wright et al. (2024) find significant differences between simulations like EAGLE, IllustrisTNG (TNG), and SIMBA as shown in Fig. 1.6, due to different feedback schemes. Other key findings on the CGM from hydrodynamical simulations include a split in X-ray properties between star-forming and quiescent galaxies in the Milky Way mass range, driven by black hole feedback that affects hot gas content, temperature, and X-ray brightness (Truong et al., 2023; Oppenheimer et al., 2020). Simulations also predict anisotropic CGM outflows (Truong et al., 2021b), complex multiphase gas (Ramesh et al., 2023b), significant magnetic field effects (Tumlinson et al., 2017; Ramesh et al., 2023a), additional pressure

support from cosmic rays (Ji et al., 2020; Werhahn et al., 2021; Ruszkowski & Pfrommer, 2023; Girichidis et al., 2024), and varying baryon fraction distribution (e.g., Davies et al. 2020a; Medlock et al. 2024). All these findings highlight that while the CGM properties remain sensitive to feedback prescriptions and unresolved sub-grid models, accurate comparisons with observational benchmarks of the hot CGM offer promising avenues to better inform and calibrate simulation models, as also highlighted in Fig. 1.6. Indeed, this is one of the primary aims of this thesis, which I will come back to in Sec. 1.5.

1.4.2 Key physical processes shaping the hot CGM

The CGM is shaped by a complex interplay of physical processes that drive its evolution and impact its observable properties. These processes are incorporated into hydrodynamical simulations, which progress towards describing the observed multiphase structure and dynamics (Tumlinson et al., 2017). The combined effects of the key processes offer a comprehensive framework for investigating the CGM's structural evolution, and they aid in comparing theoretical predictions with observations (Faucher-Giguère & Oh, 2023). The complete list of all the processes is vast and still being explored with improving data and modelling; here, we expand on the key mechanisms which have been topics of active investigation in the last decades.

Thermal instabilities

Thermal instabilities lead to the condensation of hot gas into cooler clumps, seeding diverse phases within the CGM, as seen in both absorption and emission studies (McCourt et al., 2012; Voit, 2021; Donahue & Voit, 2022). These instabilities are driven by an imbalance between heating and cooling and contribute to the rich, multiphase structure that characterises the CGM (Field, 1965). Radiative cooling is critical for governing the thermal state and evolution of the CGM, particularly in its ability to transition gas between phases. Efficient cooling can lead to the condensation of gas into denser structures, contributing to the formation of cold clumps and clouds within the hotter halo environment. It directly influences the density and temperature distributions by allowing energy loss via emission lines and continuum processes (Sutherland & Dopita, 1993; Wiersma et al., 2009).

Stellar Feedback and Galactic Winds

Feedback from stars primarily impacts lower-mass systems and includes mechanisms like supernova explosions, stellar winds, and radiation pressure (Dekel & Woo, 2003; Benson et al., 2003; Faucher-Giguère & Oh, 2023), as also introduced in Sec. 1.2. These processes inject energy and momentum into the CGM, heating the gas and propelling metals outward, which aids in redistributing baryons and in maintaining a multiphase state (see e.g., Kay et al. 2002; Ceverino & Klypin 2009; Katz et al. 2024). Stellar feedback is crucial for regulating star formation within galaxies and affecting the thermal balance of their surrounding halos (e.g., Muratov et al. 2015; Agertz & Kravtsov 2016).

AGN Feedback

AGN feedback exerts a significant influence on the CGM, particularly in massive ($\gtrsim 10^{12}$ $M_\odot$) halos dominated by supermassive black holes (see Sec. 1.2 and reviews by Brandt & Alexander 2015; Eckert et al. 2021). AGNs release large amounts of energy via jets, winds, and radiation, driving outflows that redistribute metals and thermal energy throughout the CGM (Kormendy & Ho, 2013). This feedback includes thermal and kinetic components, both critical for maintaining hot atmospheres, suppressing cooling flows, and modifying star formation rates (e.g., Springel et al. 2005a; Di Matteo et al. 2005). By heating the surrounding gas, AGN feedback prevents excessive cooling that could otherwise trigger star formation, aligning with observed X-ray luminosities and CGM thermal profiles (Kereš et al., 2009; Choi et al., 2015; Donahue & Voit, 2022). By accurately modelling AGN feedback, simulations can more precisely mirror the complex interplay between galaxies and their circumgalactic environments (Harrison & Ramos Almeida, 2024; Vogelsberger et al., 2014).

Cosmological environment

The broader large-scale cosmological environment, i.e., the location of the galaxy in the cosmic web, also influences the CGM. For instance, galaxies infalling into clusters via cosmic filaments are systematically more quenched than their counterparts from other isotropic directions (see e.g. Martínez et al. 2016; Einasto et al. 2018; Salerno et al. 2019; Gouin et al. 2020). Simulations show that the gas content of galaxies located as far as 3× virial radius (Cen et al., 2014; Arthur et al., 2019; Mostoghiu et al., 2021) to 5× the virial radius (Bahé et al., 2013) of the groups and clusters centre is gas-depleted compared to their counterparts in the field, as also reaffirmed by observations (e.g., Tanaka et al. 2004; Catinella et al. 2013; Cortese et al. 2011). Similar trends of higher gas depletion, higher quiescent fraction, and stellar mass also hold for galaxies closer to the cosmic filament spines (Malavasi et al., 2017; Laigle et al., 2018; Sarron et al., 2019; Bonjean et al., 2020; Winkel et al., 2021; Hoosain et al., 2024). Furthermore, the large-scale structure can collimate cold streams, guiding gas into halos, and imparting angular momentum to the infalling gas (van de Voort & Schaye, 2012; Zinger et al., 2016; Nuza et al., 2014). This aspect is the focus of Chapt. 4 of this thesis.

Turbulence and ram pressure

Turbulence and ram pressure in the CGM are caused by large-scale inflows, energetic feedback, and accretion onto dense clumps and clouds within the CGM, representing a kinetic energy-dominated CGM (e.g., McCourt et al. 2011; Faucher-Giguère & Quataert 2012). Turbulent motions play a vital role in sustaining a stable, multiphase CGM by mediating mixing and assisting in pressure support, shaping the distribution of gas phases in halos (Ocker et al., 2025), particularly in the inner regions of the CGM (e.g., Schmidt et al. 2021). While the $\gtrsim 10^{11.5}$ $M_\odot$ halos are mostly thermally supported against gravitational infall, the contributions from ram pressure and turbulence become increasingly important in lower halo mass objects (see e.g., Fielding et al. 2017; Lochhaas et al. 2020; Kakoly et al. 2025).

Magnetic Fields

The presence of magnetic fields (see e.g., Pakmor et al. 2014; Rieder & Teyssier 2016) introduces nonthermal pressure support in the CGM. Studies show that magnetic fields can impact the stability of cold, dense clouds (Nelson et al., 2020), alter gas inflow velocities, temperatures, and pressures (van de Voort et al., 2021), affect the evolution and dynamics of the gas (Pakmor et al., 2020) and suppress fluid instabilities (e.g. Berlok & Pfrommer 2019; Sparre et al. 2020). This effect is found to be important in the central regions (e.g., $\lesssim 0.3\ R_{200c}$) of the CGM (e.g., Ramesh et al. 2023a), and is also shown to impact the propagation of cosmic rays (e.g., Yang & Ji 2023; Beck 2009; Pakmor et al. 2014; Butsky & Quinn 2018). Quantitative predictions for magnetic field properties in the CGM still vary significantly between different simulation codes due to differences in feedback models, numerical techniques, and resolution (Pakmor & Springel, 2013; Su et al., 2017; Vogelsberger et al., 2020); however, future comparisons with observations (e.g., Prochaska et al. 2019) offer crucial constraints to inform simulation models.

Cosmic Rays

Cosmic rays (CR) are high-energy particles originating from processes like supernovae and AGN activity. As they propagate through the CGM they can exert pressure, drive winds, and modulate cooling rates, influencing both the multiphase structure and dynamics of the CGM (see review by Owen et al. 2023). Recent studies (Ji et al., 2020; Werhahn et al., 2021; Ruszkowski & Pfrommer, 2023; Girichidis et al., 2024) suggest that cosmic rays are integral in providing additional pressure support to the observed hot phase against collapse and energising outflows (e.g., see also Trapp et al. 2022; Chan et al. 2022). Ponnada et al. (2022, 2024) highlight cosmic rays' ability to couple with magnetic fields, amplifying their impact through increased pressure support and energy transport. Additionally, cosmic rays may facilitate metal mixing and alter thermal stability thresholds, especially for the cold gas phases, further shaping the CGM as probed in UV-absorption lines (e.g., Salem et al. 2016; Buck et al. 2020; Butsky et al. 2022). Current limitations in accurately modelling CR transport are self-consistent treatment of magnetic fields, anisotropic diffusion, and streaming related challenges that demand advanced numerical techniques to prevent instabilities (e.g., Vogelsberger et al. 2020).

1.5 This Thesis

The hot component of the CGM, as probed in X-rays, is the most massive and volume-filling among the multiphase gas hosted by halos $\gtrsim 10^{11.5}\ M_\odot$. With the advent of eROSITA, we have the highest signal-to-noise X-ray data available at the time of writing this thesis, as presented in Zhang et al. (2024a,b). They conduct X-ray stacking experiments with the eROSITA data and detect the hot CGM out to the virial radius of Milky-Way and M31-like galaxies. X-ray stacking analysis provides the most sensitive state-of-the-art observations of the hot CGM in the current observational landscape. Still, they are subject to observational effects that affect the interpretation of the hot CGM. Consequently, we need a complete theoretical framework

to describe the hot CGM emission to disentangle the intrinsic signal from other observational effects.

To interpret the X-ray radial profiles probing the hot CGM, modelling the projection effects affecting the measurements is of utmost importance. We are interested in constructing a forward model with large statistics of galaxies to mimic observational X-ray stacking experiments. In other words, we require a simulation that contains a large enough box size to encompass the effects of the cosmological LSS and also accounts for the complexities introduced by feedback and cooling, inherent to the hot CGM. Therefore, we use cosmological hydrodynamical simulations that self-consistently predict the LSS and its impact on gas dynamics within a halo. We use the IllustrisTNG cosmological hydrodynamical simulation with the box of side length 302.6 Mpc (TNG300; Nelson et al., 2019)[11], as introduced in Sec. 1.4.1 and will be further described in Chapt 2. Using TNG300, we construct a lightcone, so-called LC-TNGX, and generate mock X-ray observations by self-consistently using the gas cell information. The LC-TNGX is a novel tool that forms the basis for the various aspects of the hot CGM studied in this thesis.

In summary, this thesis answers three important questions in the field of modelling the hot CGM, in the following three Chapters 2, 3, and 4 and accompanying publications Shreeram et al. (2025c,a,b):

1. **How do projection effects that impact the hot CGM as measured in X-rays?** In order to test theoretical and numerical predictions of the hot CGM against X-ray observations, we must quantify all the effects that influence observations in stacking experiments. Among the primary sources of contamination in X-ray stacking experiments are the projection effects affecting the hot gas emission. These projection effects, which have not been explored in detail before, include the contribution from the LSS halo environment (locally correlated X-ray emission), the effect of satellite galaxies being misclassified as central due to limitations in the (photometric) redshift accuracy for the galaxies in large surveys, the offset between the X-ray centre and the centre defined by the minimum of the halo potential, and the Line-of sight (LoS) projection of uncorrelated X-ray emission of fore- and background structures. Chapt. 2 explores these effects using LC-TNGX to provide a complete description and full understanding of the contaminating projection effects in X-ray stacking experiments of the hot CGM.

2. **Can we retrieve the hot CGM physics from the X-ray stack of galaxies from eROSITA data?** With our knowledge of projection effects in Chapt. 2, we proceed in Chapt. 3 and embark on the challenge of developing a forward model for the stacked X-ray radial surface brightness profile measured by eROSITA around MW-mass galaxies. Our model contains two emitting components: hot gas (around central galaxies and around satellite galaxies hosted by more massive halos) and X-ray point sources (X-ray binaries and Active Galactic Nuclei). In Chapt. 3, we show that for the same mean stellar mass, a factor $\sim 2\times$ increase in the mean value of the underlying halo mass distribution results in $\sim 4\times$ increase in the stacked X-ray luminosity from the hot CGM. Here, we find that the gas physics driving the shape of the observed hot CGM (in stellar-mass-selected X-ray stacking experiments)

[11] http://www.tng-project.org

is tightly correlated with the underlying halo-mass distribution. Additionally, this chapter provides a novel technique to constrain the average AGN X-ray luminosity jointly with the radial hot CGM gas distribution within the halo using measurements from X-ray galaxy stacking experiments.

3. **How does the large-scale cosmic web impact the X-ray emitting CGM?** While key physical processes of the hot CGM have been widely studied, the influence of a galaxy's large-scale cosmic environment on the hot gas content remains less explored. In Chapt. 4, we investigate how the large-scale cosmic web affects the X-ray surface brightness (XSB) profiles of galaxies in the context of cosmological simulations. Again, using our novel IllustrisTNG-based lightcone, spanning $0.03 \leq z \leq 0.3$, first developed in Chapt. 2, we apply the filament finder DisPerSE on the galaxy distributions to identify the cosmic filaments within the lightcone. We classify central galaxies into five distinct large-scale environment (LSE) categories: clusters and massive groups, cluster outskirts, filaments, filament-void transition regions, and voids/walls. We find that the X-ray surface brightness profiles (XSB) of central galaxies of dark matter haloes in filaments with $M_{200\mathrm{m}} > 10^{12}\,\mathrm{M}_{\odot}$ are X-ray brighter than those in voids and walls, with $20-45\%$ deviations in the radial range of $(0.3-0.5)\times R_{200\mathrm{m}}$. Our results demonstrate that the impact of the large-scale cosmic environment is imprinted on the hot CGM's X-ray emission.

Chapter 2

Quantifying Observational Projection Effects with a Simulation-based hot CGM model

The results presented in this chapter were published in Astronomy & Astrophysics, 697, A22, titled "*Quantifying observational projection effects with a simulation-based hot CGM model*" **Shreeram, S.**, Comparat, J., Merloni, A., Zhang, Y., Ponti, G., Nandra, K., ... & Sorini, D. (2025a).

2.1 Summary

In this chapter, we take the first step toward a self-consistent framework for modelling the hot CGM by constructing a cosmological lightcone from the TNG300 hydrodynamical simulation. This lightcone is initially employed to study projection effects that bias stacked X-ray measurements of the CGM, but it also forms the foundation for the subsequent chapters. More precisely, in Chapt. 3, it is implemented for forward modelling of eROSITA observations, and in Chapt. 4, it is combined with large-scale structure classifications to explore environmental dependencies. In order to build a fully self-consistent forward model for the hot CGM, we construct a lightcone and generate mock X-ray observations of the large-scale structure. We quantify the main projection effects impacting CGM measurements, namely the locally correlated large-scale structure in X-rays and the effect due to satellite galaxies misclassified as centrals, which affect the measured hot CGM galactocentric profiles in stacking experiments. We present an analytical model that describes the intrinsic X-ray surface brightness profiles of haloes across the stellar and halo mass bins. The increasing stellar mass bins result in decreasing values of β, the exponent quantifying the slope of the intrinsic galactocentric profiles. We measure the effect of misclassified centrals in stacking experiments for three stellar mass bins: $10^{10.5-11}\mathrm{M}_{\odot}$, $10^{11-11.25}\mathrm{M}_{\odot}$, and $10^{11.25-11.5}\mathrm{M}_{\odot}$. We find that the contaminating effect of the misclassified centrals on the stacked profiles increases when the stellar mass decreases. When stacking galaxies of Milky-Way-like stellar mass, this effect is dominant already at a low level of contamination: in particular, misclassified centrals

contributing 30%, 10%, or 1% of a sample dominate the measured surface brightness profile at radii $\geq 0.11 \times R_{500c}$, $\geq 0.24 \times R_{500c}$, and $\geq 1.04 \times R_{500c}$, respectively.

2.2 Motivation for this work

Several extragalactic studies have reported single-object broad-band X-ray detections of hot gas around galaxies (Bogdán et al., 2013b,a; Anderson et al., 2016; Bogdán et al., 2017; Li et al., 2017; Das et al., 2019). Owing to the density-squared dependence of X-ray emissivity, however, these detections are confined to the densest regions of the CGM, typically within 40–150 kpc of the galaxy centre. To extend measurements out to the halo virial radius, $R_{\rm vir}$ (i.e., $\gtrsim$ 200 kpc), Anderson et al. (2015) stacked the all-sky X-ray data from ROSAT at the positions of the SDSS galaxies. With the launch of SRG/eROSITA, we have unprecedented statistics to extend the study of the hot CGM in X-rays with stacking analysis. E.g., Oppenheimer et al. (2020) first demonstrated the promise of this approach using mock observations from the IllustrisTNG and EAGLE simulations, while subsequent works (Comparat et al., 2022; Chadayammuri et al., 2022), and more recently Zhang et al. (2024a, hereafter Z+24), have applied it directly to eROSITA data, detecting the hot CGM out to $R_{\rm vir}$ around Milky Way– and M31–like systems. Today, stacking represents the most sensitive technique available for probing the hot CGM in X-rays. Yet, its interpretation remains complicated by a variety of observational effects, motivating the need for a comprehensive theoretical framework to isolate the intrinsic hot CGM signal from other observational effects.

A plethora of theoretical models (e.g., Faerman et al. 2017; Voit et al. 2019; Pal Choudhury et al. 2019; Stern et al. 2024; Singh et al. 2021; Pandya et al. 2023; Faerman & Werk 2023) have been used to describe and predict the intrinsic properties of the hot CGM; Singh et al. (2024) discuss the comparison of some idealised cases. Similarly, Oppenheimer et al. (2020); Vladutescu-Zopp et al. (2024) made explicit predictions of the intrinsic hot CGM profiles obtained by assigning mock X-ray emission to the hot halos found in cosmological hydrodynamical simulations. However, before testing theoretical and numerical predictions of the hot CGM against state-of-the-art observations, we must quantify all the effects that influence the hot CGM observations in stacking experiments. Among the primary sources of contamination in X-ray stacking experiments, inhibiting us from retrieving the physical properties of the detected CGM emission, are (1) unresolved AGN and X-ray binaries (XRB) population of galaxies (Biffi et al., 2018b; Vladutescu-Zopp et al., 2023), and (2) projection effects within the hot gas emission of the cosmic web. These projection effects include the contribution from the Large-Scale Structure (LSS) halo environment (locally correlated X-ray emission), the effect of satellite galaxies being misclassified as central due to limitations in the (photometric) redshift accuracy for galaxies in large surveys (see e.g., Weng et al. 2024), the offset between the X-ray centre and the centre defined by the minimum of the halo potential, and the Line-of sight (LoS) projection of uncorrelated X-ray emission of fore- and background structures. Z24 tried to model these effects empirically for the first time; however, we need forward models based on cosmological hydrodynamical simulations for a complete description and full understanding of these contaminating effects.

Table 2.1: For every stellar mass bin, we present the mean stellar mass within twice the stellar half mass radius, the total number of central galaxies, the total number of satellite galaxies, mean halo mass, the minimum and maximum values of halo masses for the given stellar mass bin, the mean R_{200m}, and the mean R_{500c}.

$\log_{10}\left(\frac{M_\star}{M_\odot}\right)$ min-max	$\log_{10}\frac{M_\star}{M_\odot}$ mean	$N_{\rm centrals}$ $\texttt{CEN}^{\rm sim}$	$N_{\rm satellites}$ $\texttt{SAT}^{\rm sim}$	$\log_{10}\frac{M_{200m}}{M_\odot}$ mean	$\log_{10}\left(\frac{M_{200m}}{M_\odot}\right)$ min-max	$R_{\rm 200m}$ kpc	$R_{\rm 500c}$ kpc
10.5 – 11	10.7	5109	2719	12.7	[11.9, 13.7]	525.02	242.75
11 – 11.25	11.1	680	220	13.3	[12.6, 14.0]	816.05	369.01
11.25 – 11.5	11.4	305	60	13.6	[13.2, 14.2]	1077.71	484.52

Table 2.2: For every halo mass bin used to generate the X-ray surface brightness profiles, we present the mean halo mass, the total number of distinct halos, the mean stellar mass, the mean $R_{\rm 200m}$ and the mean $R_{\rm 500c}$, for every halo mass bin.

$\log_{10}\frac{\rm M_{200m}}{\rm M_\odot}$ min-max	$\log_{10}\frac{\rm M_{200m}}{\rm M_\odot}$	$N_{\rm Distinct\ halos}$ $\texttt{CEN}^{\rm sim}_{\rm halo}$	$\log_{10}\frac{\rm M_{\star,<2\times R_\star}}{\rm M_\odot}$	$R_{\rm 200m}$ kpc	$R_{\rm 500c}$ kpc
12.5 – 13.0	12.7	3,677	10.7	375.54	246.35
13.0 – 13.5	13.2	1,113	11.0	549.27	353.35
13.5 – 14.0	13.7	382	11.4	810.09	519.34

In this chapter, we analyse numerical simulations to empirically quantify the effects of the locally correlated X-ray emission and the misclassified centrals, also called the satellite-boost effect, relevant for measuring the hot CGM in stacking experiments. To do this, we use the TNG300 hydrodynamical simulations (Pillepich et al., 2018b; Marinacci et al., 2018; Naiman et al., 2018; Nelson et al., 2015; Springel et al., 2018) to construct a lightcone and generate mock X-ray observations. We focus here on the projection effects of hot gas affecting the X-ray surface brightness profiles. The structure of the chapter is as follows. Sec. 2.3 details the construction of the TNG300 lightcone (LC-TNG300) used for modelling the hot CGM in this study. We explain all the projection effects in detail in Sec. 2.3.1. In Sec. 2.4, we describe the process for generating mock X-ray observations that mimic observational data and provide the machinery for computing the surface brightness profiles. Sec. 2.5 presents the main results of this work done with the TNG300 lightcone. Lastly, Sec. 2.6 discusses the main findings and Sec. 2.7 provides an overview with prospects.

2.3 Simulated lightcone with IllustrisTNG: LC-TNG300

Since we are interested in studying the impact of the locally correlated X-ray emission within the LSS environment of the halo, we require a simulation that contains all the complexities introduced by feedback and cooling, which are imprinted in X-ray measurements. We also require a large box size to encompass the effects of the cosmological LSS itself. Therefore, we use cosmo-

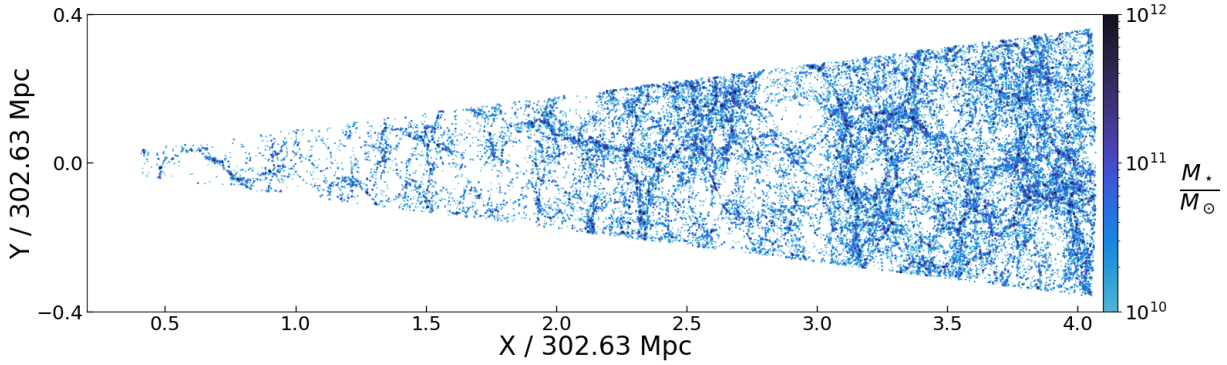

Figure 2.1: Illustration of the lightcone built using TNG300 in the x-y plane. The figure shows the subhalos within LC-TNG300 at $0.03 \leq z \leq 0.3$ remapped using `boxremap` (Carlson & White, 2010). The observer is set at the $(0, 0, 0)$ location. The lightcone goes out to 1231 cMpc along the x-axis, subtending an area of 47.28 deg^2 on the sky in the y-z plane. The subhalos are colour-coded with their stellar masses.

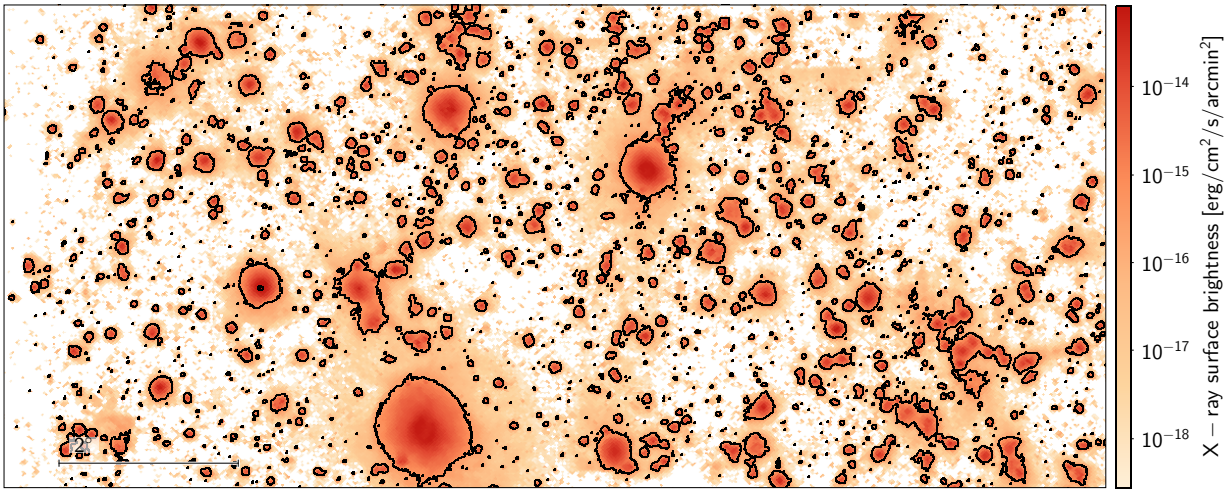

Figure 2.2: The projected rest-frame X-ray events from the TNG300 ligthcone in the 0.5 − 2.0 keV band for a telescope with energy-independent collecting area 1000 cm^2 and exposure time of 1000 ks. The events are generated using the hot gas cells within the TNG300 lightcone at redshifts 0.03 − 0.3 using `pyXsim` (ZuHone & Hallman, 2016). The centre for the projection onto the sky is chosen as R.A., Dec.≡ (0., 0.) degrees. The contours represent the two X-ray surface brightness levels of 5×10^{-14} erg s^{-1} cm^{-2} arcmin^{-2} and 2×10^{-16} erg s^{-1} cm^{-2} arcmin^{-2}.

logical hydrodynamical simulations that self-consistently predict the LSS and its impact on gas dynamics within a halo. We use the IllustrisTNG cosmological hydrodynamical simulation with the a of side length 302.6 Mpc (TNG300; Nelson et al., 2019)[1]. IllustrisTNG accounts for many physical processes, among of the most notable which are star formation regulated by a subgrid ISM model (Springel & Hernquist, 2003), metal enrichment (Naiman et al., 2018), radiative gas cooling, galactic wind outflows (Pillepich et al., 2018a), magnetic fields and diffuse radio emis-

[1] `http://www.tng-project.org`

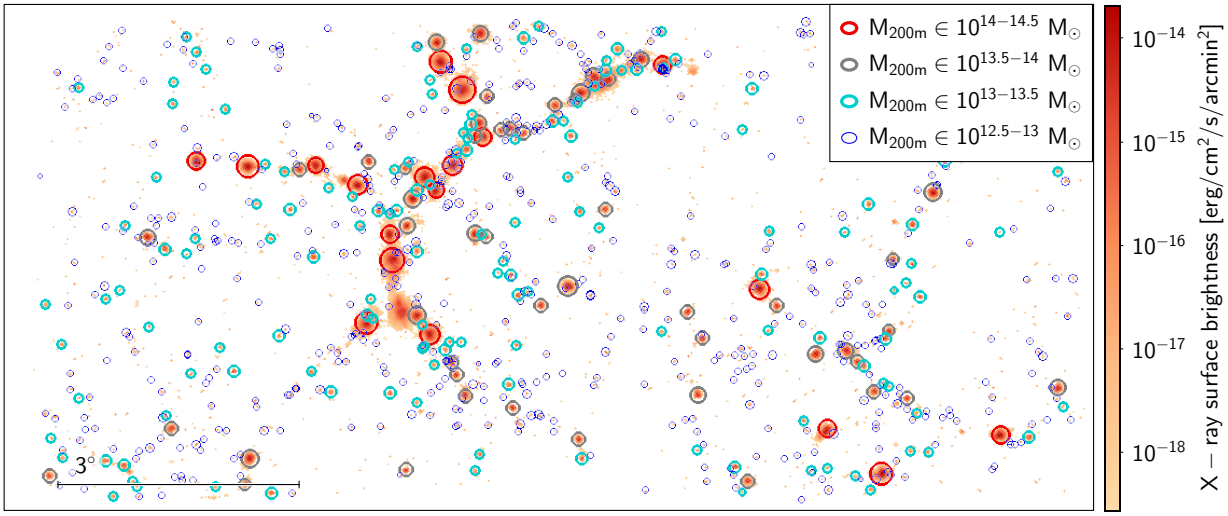

Figure 2.3: The projected halos (*centrals*) are overplotted with their corresponding scaled R_{500c} at $z = 0.3$; the R_{500c} of the halos are represented by the size of the circles. We also show the projected rest-frame X-ray events from the TNG300 ligthcone in the 0.5 − 2.0 keV band for a telescope with energy-independent collecting area 1000 cm^2 and exposure time of 1000 ks at the redshift slice of $0.284 \leq z \leq 0.3$. The halos with $M_{200m} \in 10^{14-14.5}$ $M_\odot$ are shown in red, $M_{200m} \in 10^{13.5-14}$ $M_\odot$ in grey, $M_{200m} \in 10^{13-13.5}$ $M_\odot$ in cyan, and $M_{200m} \in 10^{12.5-13}$ $M_\odot$ in blue.

sions (Marinacci et al., 2018), supermassive black hole growth with Bondi accretion and mergers, thermal and kinetic modes for black hole feedback (Weinberger et al., 2018). IllustrisTNG also reproduces correlation functions and power spectra of particles and halos (Springel et al., 2018). TNG300 contains 2500^3 dark matter particles, with a baryonic mass resolution of 1.1×10^7 $M_\odot$, a comoving value of the adaptive gas gravitational softening length for gas cells of 370 comoving parsec, gravitational softening of the collisionless component of 1.48 kpc, and dark matter mass resolution of 5.9×10^7 $M_\odot$. The TNG simulations adopt the Planck Collaboration XIII 2016 cosmological parameters, with the matter density parameter $\Omega_m = \Omega_{dm} + \Omega_b = 0.3089$, baryonic density parameter $\Omega_b = 0.0486$, Hubble constant $H_0 = 100h$ km s^{-1} Mpc^{-1} with $h = 0.6774$, and $\Omega_\Lambda = 0.6911$.

The Friends-of-Friends (FoF) algorithm is applied to the dark matter particles with linking length $b = 0.2$ to obtain the halos. The subhalos are retrieved with SUBFIND (Springel et al., 2001; Dolag et al., 2009) that detects gravitationally bound substructures, which are equivalent to galaxies in observations. Additionally, SUBFIND classifies the subhalos into centrals and satellites, where centrals are the most massive substructure within a distinct halo.

To model the hot gas emission in the redshift range $0.03 \lesssim z \lesssim 0.3$, as in observations (e.g. Comparat et al. 2022; Chadayammuri et al. 2022; Zhang et al. 2024a), we need four boxes lined up behind each other to arrive at the comoving distance, $d_C(z = 0.3)$, of 1231 Mpc. For a full-sky lightcone going up to $z = 0.3$, we must replicate and stack 512 boxes; however, such replication causes large-scale projection effects that cannot be estimated properly; see Merson et al. (2013).

Therefore, we box remap[2] all snapshots into a configuration where the longest length of one of the sides is $\sim 4\times$ the original length (Carlson & White, 2010). This technique ensures that the new elongated box has a one-to-one remapping, remains volume-preserving, and keeps local structures intact. For a box whose original dimensions are normalized to $(1, 1, 1)$, the unique solution for the transformed box sides is $(4.1231, 0.7276, 0.3333)$, respectively. We remap the coordinates of particles (gas, dark matter, and stars) and the halo and their subhalo catalogues. There are 22 snapshots within the observationally motivated redshift range of $0.03 \leq z \leq 0.3$. Therefore, we obtain 22 remapped particle cuboids and 22 remapped galaxy catalogue cuboids at redshift $z < 0.3$. We define the observer's position as being at a corner of the smallest face. The opening angles for the observer are $(\theta_{\rm LC\ obs}, \phi_{\rm LC\ obs}) = (10.16,\ 4.64)$ degrees. The area subtended on the sky for a given observer is 47.28 deg^2. We illustrate the lightcone constructed with the box remap technique in Fig. 2.1. We also publicly release `LightGen`, the code used for generating the lightcone in this work.

The distinct halos, $\texttt{CEN}^{\rm sim}_{\rm halo}$, and subhalos within the LC-TNG300 are catalogued with their physical properties and binned in stellar mass and halo mass bins, as shown in Tab. 2.1 and Tab. 2.2. We have 5,109 centrals and 2,719 satellites of stellar mass in the Milky-Way range ($\rm M_\star = 10^{10.5-11} M_\odot$), which is sufficient to statistically model the projection effects in these halos.

This chapter defines the stellar mass used from TNG300 as the mass within twice the stellar half-mass radius. We present quantities relative to both critical and mean densities because R_{500c}[3] is the radius most commonly used by X-ray astronomers (see e.g., Lyskova et al. (2023) and references therein), and R_{200m}[4] represents the halo's viral radius and is theoretically more relevant as it presents quantities within the virialized halo. The galaxy catalogue is divided into central, $\texttt{CEN}^{\rm sim}$, and satellites, $\texttt{SAT}^{\rm sim}$ for the concerned stellar mass bins. To construct the $\texttt{SAT}^{\rm sim}$ catalogue, we refer to the halo/subhalo classification, where we match all the central galaxies with the distinct halos, thereby leaving behind all the secondary subhalos or satellites.

2.3.1 Contributions to observed X-ray surface brightness profiles

The main objective of this study is to model the various sources of contamination that come into play when measuring the hot gas component of the CGM. Here, we list all the components contributing to the observed X-ray surface brightness profile.

1. Intrinsic emission from the halo. This corresponds to the emission within the radius, $R_{\rm 200m}$, of the central halo in 3D. We associate this X-ray emission with being intrinsic to the galaxy's CGM. It must be noted that the definition of a halo boundary at which the gas is bound is non-trivial; we refer to Diemer et al. (2017) and references therein for more details.

[2] http://mwhite.berkeley.edu/BoxRemap/

[3] $R_{\rm 500c}$ is the radius at which the density of the halo is 500× the critical density of the universe.

[4] $R_{\rm 200m}$ is the radius at which the density of the halo is 200× the mean matter density (cold dark matter and baryons).

2. Locally correlated environment. This component encapsulates the surrounding emission of the galaxy with the LSS in which it resides. Also known as the 2-halo term (Cooray & Sheth, 2002; Kravtsov et al., 2004), this corresponds to the contribution arising due to the local background changing with the size of the halo. This effect is explored in tSZE studies, where Vikram et al. (2017), Lim et al. (2021) show the impact of the two-halo component, where the one-halo contribution at mass scales $M_{200} \leq 10^{13-13.5}$ h^{-1} $M_\odot$ is swamped by the two-halo term due to nearby massive systems dominating the measured signal. Given our focus on MW-size halos, modelling the contribution from the locally-correlated background is crucial for disentangling intrinsic hot CGM emission from the local background.

3. Intrinsic emission from satellites. The X-ray emission from the satellite galaxy contributes to the total observed CGM emission in projection. As the host galaxy is more massive, with a deeper potential well, the contribution of this effect is negligible in stacking experiments (see Rohr et al. (2024) for further insight into the detectability of the satellite emission).

4. Contamination from misclassified centrals. In observations that use photometric surveys, classifications between centrals and satellites are inhibited due to limitations in the redshift accuracy. This effect is large and unavoidable for photometric surveys ($\sim$ 30% contaminants for MW-like galaxies; Sec 3.5 in Z24) and significantly mitigated for spectroscopic surveys ($\sim$ 1% contaminants for MW-like galaxies; Sec 3.7 in Z24), but not completely removed due to survey incompleteness or residual uncertainty in the central/satellite classification for systems with a low number of galaxies (see also Weng et al. 2024 who quantify the effect for absorbers in cold gas with TNG50). This implies that the measured X-ray surface brightness profiles in stacked samples of galaxies classified as centrals contain the intrinsic emission around truly central galaxies but are contaminated by the emission measured around satellites (off-centred) misclassified as centrals. In conclusion, including the emission around satellites in the stacking analysis alters the recovered profiles and, therefore, must be modelled.

5. The X-ray to true centre offset. The theoretically defined centre of a halo, which is the minimum of the dark matter potential well, could be offset from the observationally defined centres, e.g., the peak of the SZ signal or the X-ray emission, or the optical/infrared centre inferred from the stellar distribution (Zitrin et al., 2012; Lauer et al., 2014; Saro et al., 2015; Cui et al., 2016; Seppi et al., 2023). This offset is associated with physical effects such as galaxy mergers (Martel et al., 2014), misidentification of the brightest halo galaxy (Hoshino et al., 2015; Hikage et al., 2018; Oguri et al., 2018; Zhang et al., 2019) or failure of the brightest halo galaxy being a proxy for the minimum of the halo potential in optical studies (Skibba et al., 2011). Overall, miscentering causes a smoothing effect in stacking studies (Oguri & Takada, 2011), and therefore, must be calibrated and modelled. This effect of miscentring correlates with halo mass; hence, it is well-studied at the cluster and group scales. As we simulate X-ray emission around lower mass, MW-like halos in this work, we extend the discussion of miscentering of the X-ray emission from the minimum of the host halo potential to MW mass scales. We return to the implications

of such X-ray–potential offsets for stacked CGM measurements in Sec. 2.6.3, where we assess how miscentering can bias inferred profiles.

6. Contamination from other X-ray sources. Other X-ray emitting sources, like XRB and AGN, contaminate the measured hot CGM. The XRB emission is distributed on the scale of the stellar body of a galaxy; however, for an instrument with a Point Spread Function (PSF) like eROSITA, it is unresolved and appears as a point source. Z24 take special precautions to account for this by masking the eROSITA-detected point sources within the X-ray data. They also model additional contributions from the unresolved XRB and AGN. While this chapter does not address this effect, Chapt. 3 provides further details on the modelling of the AGN and XRB resolved/unresolved emissions for eROSITA observations.

7. Line of Sight (LoS) projection. Objects along the line of sight that do not reside near the galaxy also contaminate the detected signal. Nevertheless, this uncorrelated contamination is well-modelled as the large-scale background and foreground in observations and, therefore, is not discussed further in this work.

8. Other X-ray background components. The local background is a combination of (1) the Soft X-ray background (SXRB; Henley & Shelton 2010, 2012, 2013; Nakashima et al. 2018; Gupta et al. 2023; Pan et al. 2024; Yeung et al. 2024), which is composed of emission from the local hot bubble, the MW CGM, other intervening galactic structure and the time variable solar-wind charge exchange, (2) the Cosmic X-ray background (De Luca & Molendi, 2004; Gilli et al., 2007; Luo et al., 2016; Cappelluti et al., 2017), which is dominated by AGN, and (3) the instrumental effects. In this study, we simulate intrinsic X-ray events from hot gas alone; therefore, this study does not quantify the impacts of these other well-studied X-ray background components.

In summary, this chapter focuses on modelling the locally correlated environment and the effect due to misclassified-centrals (the satellite-boost effect). We also quantify the effect of the X-ray to true centre offset for the halo mass bins considered here.

2.4 Method

We detail the process to create mock X-ray observations in Sec. 2.4.1 and introduce the formalism used to fit the X-ray surface brightness profiles in Sec. 2.4.2. We detail the data products generated to study the projection effects in Sec. 2.4.3.

2.4.1 Mock X-ray observation

The photons are simulated in the 0.5 – 2.0 keV intrinsic band with `pyXsim` (ZuHone & Hallman, 2016), which is based on PHOX (Biffi et al., 2013; Biffi et al., 2018a), by assuming an input emission model where the hot X-ray emitting gas is in collisional ionization equilibrium. The spectral model computations of hot plasma use the Astrophysical Plasma Emission Code, APEC[5]

[5]APEC link https://heasarc.gsfc.nasa.gov/xanadu/xspec/manual/node134.html

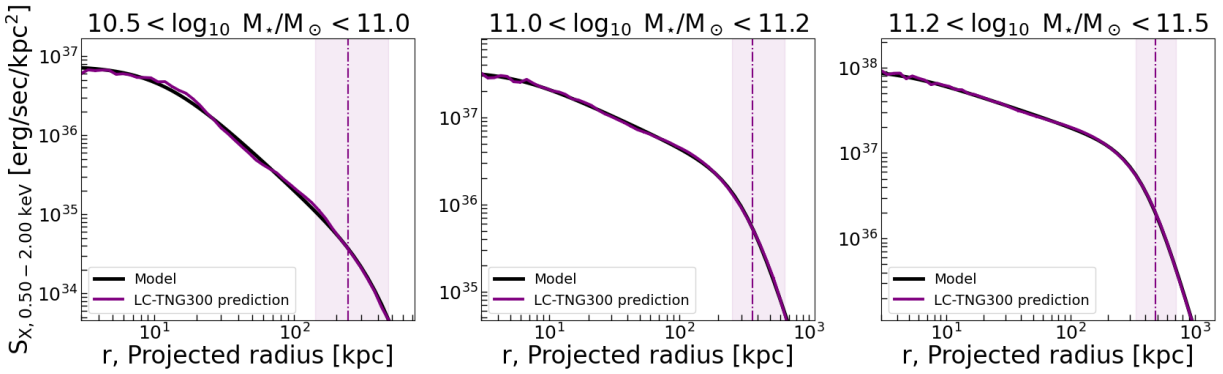

Figure 2.4: Mean X-ray surface brightness profiles in the stellar mass bins: $M_\star = 10^{10.5-11}$ $M_\odot$, corresponding to MW-like galaxies (*left*), $M_\star = 10^{11-11.25}$ $M_\odot$ (*centre*), and $M_\star = 10^{11.25-11.5}$ $M_\odot$ (*right*). The vertical dashed line is the mean R_{500c} at 242.75 kpc (*left*), 369.01 kpc (*centre*), and 484.52 kpc (*right*) of the respective galaxy stellar mass bin, with the shaded area corresponding to the minimum and maximum values. The black line is the analytical model, shown in Eq. 2.7, fit to the LC-TNG300 mean X-ray surface brightness profiles. The best-fitting parameters for the model are given in Tab. 2.3. We find decreasing values for the slope, β, with increasing stellar mass bins.

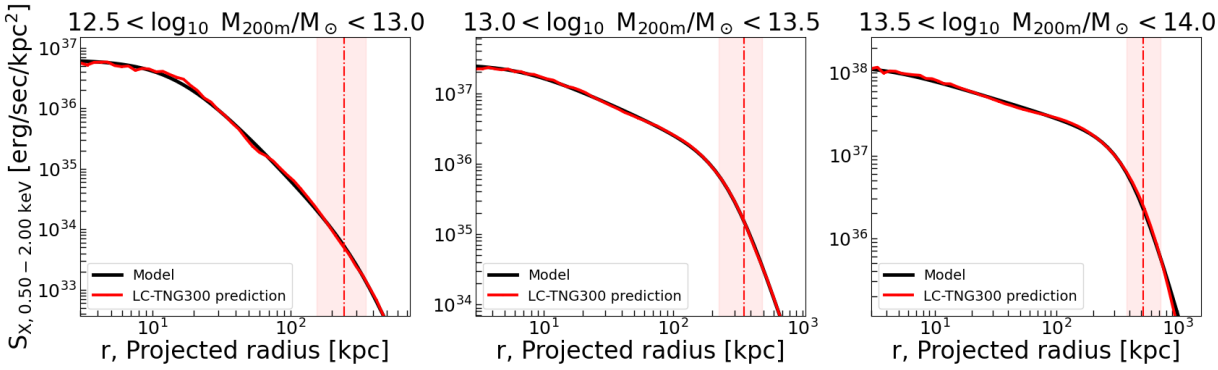

Figure 2.5: Mean X-ray surface brightness profiles in the halo mass bins: $M_{200\mathrm{m}} = 10^{12.5-13}$ $M_\odot$, corresponding to MW-like galaxies (*left*), $M_{200\mathrm{m}} = 10^{13-13.5}$ $M_\odot$ (*centre*), and $M_{200\mathrm{m}} = 10^{13.5-14}$ $M_\odot$ (*right*). The vertical dashed line is the mean R_{500c} at 246.35 kpc (*left*), 353.35 kpc (*centre*), and 519.34 kpc (*right*) of the respective halo mass bin with the shaded area corresponding to the minimum and maximum values. The black line is the analytical model, shown in Eq. 2.7, that fits the LC-TNG300 mean X-ray surface brightness profiles. The best-fitting parameters for the model are given in Tab. 2.4. We find decreasing values for the slope, β, with increasing halo mass bins.

code (Smith et al., 2001) with atomic data from ATOMDB v3.0.9 (Foster et al., 2012). The APEC model requires the plasma temperature of the gas cells (in keV), the metal abundances, the redshift z, and the normalization, N, which is defined as follows.

$$N = \frac{10^{-14}}{4\pi[D_\mathrm{A}(1+z)]^2} \int n_\mathrm{e} n_\mathrm{H} \mathrm{dV}, \tag{2.1}$$

Table 2.3: For every stellar mass bin, we present the best-fitting parameters of the model (see Eq. 2.7): S_0,:the central surface brightness; r_c, the core radius; β, the exponent quantifying the slope of the profile; r_s, the scale radius at which the slope changes to ϵ.

$\log_{10} M_\star/M_\odot$ min max	$\log_{10} S_0$	r_c [kpc]	β	r_s [kpc]	ϵ
10.5 - 11	$36.963^{+0.001}_{-0.001}$	$11.37^{+0.05}_{-0.05}$	$0.443^{+0.000}_{-0.001}$	441^{+4}_{-6}	$4.5^{+0.1}_{-0.1}$
11 - 11.25	$37.631^{+0.002}_{-0.002}$	$5.39^{+0.06}_{-0.07}$	$0.283^{+0.001}_{-0.001}$	328^{+2}_{-2}	$4.24^{+0.05}_{-0.05}$
11.25 - 11.5	$38.080^{+0.003}_{-0.003}$	$4.00^{+0.08}_{-0.07}$	$0.249^{+0.001}_{-0.001}$	407^{+2}_{-2}	$4.70^{+0.03}_{-0.03}$

Table 2.4: For every halo mass bin, we present the best-fitting parameters of the model (see Eq. 2.7): S_0, the central surface brightness; r_c, the core radius; β, the exponent quantifying the slope of the profile; r_s, the scale radius at which the slope changes to ϵ.

$\log_{10} M_{200m}/M_\odot$ min max	$\log_{10} S_0$	r_c [kpc]	β	r_s	ϵ
12.5 - 13	$36.804^{+0.001}_{-0.001}$	$15.4^{+0.2}_{-0.2}$	$0.575^{+0.001}_{-0.001}$	322^{+33}_{-31}	$3.0^{+0.6}_{-0.4}$
13 - 13.5	$37.414^{+0.002}_{-0.002}$	$7.05^{+0.08}_{-0.07}$	$0.307^{+0.001}_{-0.001}$	$276.0^{+0.9}_{-0.9}$	$4.80^{+0.02}_{-0.03}$
13.5 - 14	$38.085^{+0.002}_{-0.002}$	$4.08^{+0.07}_{-0.06}$	$0.242^{+0.001}_{-0.001}$	$412.7^{+0.5}_{-0.5}$	$4.894^{+0.002}_{-0.002}$

where D_A is the angular diameter distance to the source (cm), dV is the volume element (cm^3), n_e and n_H are the electron and hydrogen densities (cm^{-3}), respectively. The temperature is calculated from the internal energy u and the electron abundance $x_e (= n_e/n_H)$ of the gas cells[6]. The temperature T for every gas cell is defined as

$$T = (\gamma - 1)\frac{u}{k_B}\mu \tag{2.2}$$

where k_B is Boltzmann's constant in CGS units and $\gamma = 5/3$ is the adiabatic index. The mean molecular weight μ is given as

$$\mu = \frac{4}{1 + 3X_H + 4X_H x_e} m_p \tag{2.3}$$

where $X_H = 0.76$ is the hydrogen mass fraction and m_p is the proton mass in grams. The metal abundances within TNG are provided for the snapshots at redshift intervals of every 0.1. As a result, 19 of the 22 snapshots within the lightcone constructed in this work lack metallicity information. Given the lack of metallicity information and the inaccuracies introduced by interpolation of metallicity values between the 0.1 redshift intervals due to the evolution of gas particles, we assume a constant metallicity of 0.3 $Z_\odot$; this is consistent with measurements for our MW (Miller & Bregman, 2015; Bregman et al., 2018; Kaaret et al., 2020; Ponti et al., 2023b). This work uses the solar abundance values from Anders & Grevesse (1989).

The TNG star formation model is based on the subgrid two-phase model proposed by Springel & Hernquist (2003), with some modifications (see Pillepich et al., 2018b, and references therein). The gas cells that emit efficiently in the soft X-ray band (i.e. [0.3–5] keV) are due

[6]See FAQ here: https://www.tng-project.org/data/docs/faq/

to the SN-driven kinetic decoupled winds, which ultimately deposit energy into non-star-forming gas cells. Additionally, the hot component of this two-phase model exhibits typically high temperature ($> 10^5$ K). As further explained in Truong et al. (2020) (see Appendix B-C), because this multiphase structure within the TNG model is not resolved, and it is instead modelled by a simplistic two-phase structure with unrealistic assumptions, we cannot make a sensible estimate of the X-ray emission from the unresolved phases of the ISM. Therefore, by excluding the parameter space of the warm-neutral ISM (Le Brun et al., 2014; Rahmati et al., 2016; Wijers et al., 2019), namely: (1) excluding star-forming gas cells, (2) ignoring gas cells below 10^5 K, and (3) ignoring gas cells with densities above 10^{-25} g/cm^3, we ensure the gas particles used in this work are physically emitting X-rays.

Within `pyXSim`, the number of photons generated depends on the specified collecting area of the assumed X-ray telescope, its exposure time, and redshift. We generate sufficient photons by assuming a telescope with an energy-independent collecting area of 1000 cm^2 (about 3/4 of the eROSITA field-of-view-average effective area at 1 keV) and an exposure time of 1000 ks. The photon-list is generated in the observed frame of the X-ray emitting gas cells and is corrected to rest frame energies. The LoS direction determines the event's position in the sky. We define the LoS along the x-axis within the lightcone. By applying a $\theta_{\rm LC\ obs}/2 = 5.08$ deg rotation along the z-axis and $-\phi_{\rm LC\ obs}/2 = -2.32$ deg rotation along the y-axis, we centre the y-z plane at $(0, 0)$ degrees. The photons generated by the gas particles are projected onto the sky, with the resulting image shown in Fig. 2.2.

We also project the halo and subhalo positions on the sky, as shown in Fig. 2.3 for a redshift slice of $z = 0.3$. The X-ray events are then stacked around the projected halo/subhalo positions. The surface brightness profiles[7] $\mathcal{S}(r)$ are calculated as a function of the projected radius on the sky in the $0.5 - 2$ keV energy band. The centre is chosen as the location of the most bound particle within the halo/subhalo as found by the FoF/SUBFIND algorithm. The number of photons with rest frame energy E [erg] in each radially outward bin r, $N(E, r)$, is weighted by the area, $\mathcal{A}$ [kpc^2], of the 2D shell between r and $r + \mathrm{d}r$, the fraction of photons collected from the source, $f_{\rm A}$, and the exposure time, $t_{\rm exp}$ [seconds],

$$\mathcal{S}_{\rm X}(r) = \frac{\sum_{E_i=0.5\ \rm keV}^{2\ \rm keV} N(E_i, r)\ E_i}{f_{\rm A} t_{\rm exp} \mathcal{A}(r)} \left[\frac{\rm erg}{\rm sec\ kpc^2}\right]. \tag{2.4}$$

Here, $f_{\rm A}$ is the fraction of the source photons collected by the synthesized telescope that has a collecting area A:

$$f_{\rm A} = \frac{A}{4\pi d_{\rm L}(z)^2} \tag{2.5}$$

where $d_{\rm L}(z)$ is the luminosity distance to the source.

[7] We define the surface brightness profiles in this work in units of erg s$^-$1 kpc$^-$2, consistent with Z24, also called the luminosity profile.

2.4.2 X-ray surface brightness profiles and their analytic modelling

The hot CGM surface brightness profile can be analytically described by the β model (Cavaliere & Fusco-Femiano, 1976);

$$\bar{\mathcal{S}}_{\rm X,0.5-2.0\ keV}[r] = S_0 \left[1 + \left(\frac{r}{r_{\rm c}}\right)^2\right]^{-3\beta+\frac{1}{2}}, \tag{2.6}$$

where S_0 is the central surface brightness, $r_{\rm c}$ is the core radius at which the profile slope becomes steeper, and β is the exponent quantifying the slope of the profile. In cases where the outskirt steepens more than the slope defined for the inner radii by the $\beta-$model, following Vikhlinin et al. (2006), we introduce a new slope-parameter as follows:

$$\bar{\mathcal{S}}_{\rm X,0.5-2.0\ keV}[r] = S_0 \left[1 + \left(\frac{r}{r_{\rm c}}\right)^2\right]^{-3\beta+\frac{1}{2}} \times \left[1 + \left(\frac{r}{r_{\rm s}}\right)^{\gamma}\right]^{-\epsilon/\gamma}, \tag{2.7}$$

where r_s is the scale radius at which the slope changes to ϵ and γ defines the width of the transition region. We fix $\gamma = 3$ and restrict the priors on $r_s > r_c$ and $\epsilon < 5$, as suggested by Vikhlinin et al. (2006), in the fitting procedure.

2.4.3 Prerequisite data products for quantifying projection effects

To obtain contributions from the large-scale structure, i.e. the locally correlated X-ray emission, we generate cubes and profiles with the $\texttt{CEN}^{\rm sim}$ catalogue for two cases as follows:

1. $\rm R_{200m}$ cubes and profiles: every central galaxy within the halo catalogue is assigned X-ray events within $R_{\rm 200m}$ of the parent halo. We define these profiles as the intrinsic hot gas emission profiles.

2. $\rm R_{\pm 3Mpc}$, $\rm R_{\pm 9Mpc}$ and $\rm R_{\pm 27Mpc}$ cubes and profiles: all the X-ray events, intrinsic and locally extrinsic, irrespective of whether they belong to the galaxy but within 3 Mpc, 9 Mpc, and 27 Mpc of the source centre, are selected in 3D spherical comoving volumes. We construct the profiles and cubes to quantify the impact of contamination from the local vicinity on the intrinsic source emission.

To quantify contributions from the emission associated with misclassified centrals, we use the $\texttt{SAT}^{\rm sim}$ catalogue in the same stellar mass bin as the central galaxies. For galaxies in the three stellar mass bins ($10^{10.5-11}$ $\rm M_\odot$, $10^{11-11.25}$ $\rm M_\odot$, and $10^{11.25-11.5}$ $\rm M_\odot$) we construct a total galaxy samples containing $N_{\rm tot}$ galaxies, of which there are $N_{\rm cen}$ centrals and $N_{\rm sat}$ satellites. The number of satellites is defined as $N_{\rm sat} = f_{\rm sat} N_{\rm tot}$, where $f_{\rm sat}$, the fraction of satellites, is varied at the values 0.01, 0.1, and 0.3. The corresponding mean X-ray surface brightness profiles for a sample containing $f_{\rm sat}$ satellites are obtained as follows.

$$\bar{\mathcal{S}}_{\rm X,tot}[r] = \frac{\sum_{i=1}^{N_{\rm tot}} \mathcal{S}^{(i)}_{\rm X,tot}}{N_{\rm tot}}. \tag{2.8}$$

The mean X-ray surface brightness profile components from the central galaxies, $\bar{\mathcal{S}}_{\rm X,cen}[r]$ and satellite galaxies, $\bar{\mathcal{S}}_{\rm X,sat}[r]$ contributing to $\bar{\mathcal{S}}_{\rm X,tot}[r]$ are as follows:

$$\bar{\mathcal{S}}_{\rm X,cen}[r] = (1 - f_{\rm sat}) \times \frac{\sum_{i=1}^{N_{\rm cen}} \mathcal{S}^{(i)}_{\rm X,cen}}{N_{\rm cen}}, \tag{2.9}$$

and

$$\bar{\mathcal{S}}_{\rm X,sat}[r] = f_{\rm sat} \times \frac{\sum_{i=1}^{N_{\rm sat}} \mathcal{S}^{(i)}_{\rm X,sat}}{N_{\rm sat}}, \tag{2.10}$$

respectively. Therefore, $\bar{\mathcal{S}}_{\rm X,tot}[r] = (1 - f_{\rm sat})\ \bar{\mathcal{S}}_{\rm X,cen}[r] + f_{\rm sat}\ \bar{\mathcal{S}}_{\rm X,sat}[r]$. We calculate the uncertainties in the total surface brightness profile of the total, central, and satellite components by bootstrapping.

2.5 Results

Here, we present the main results of this work. In Sec. 2.5.1, we discuss the outcome of fitting the analytical model to the stacked LC-TNG300 intrinsic profiles. In Sec. 2.5.2, we carry forward the current state-of-the-art to understand the impact of the locally correlated environment on the intrinsic X-ray surface brightness profile. Lastly, in Sec. 2.5.3, we show the prominence of the effect due to misclassified centrals.

2.5.1 Fitting analytic models to the intrinsic X-ray surface brightness profiles

Fig. 2.4 and Fig. 2.5 show the mean X-ray surface brightness profiles in three stellar mass and halo mass bins, respectively. We fit the surface brightness profiles with the analytic model introduced in Eq. 2.7 and provide the best-fit parameters in Tab. 2.3 and Tab. 2.4 for the stellar and halo mass bins, respectively. A simple β model by Eq. 2.6, describes the lowest stellar and halo mass bins. However, the simple β model fails to describe the more massive stellar and halo mass bins. Therefore, we implement the modified–β model as described in Eq. 2.7, which successfully describes the LC-TNG300 profiles in the stellar and halo mass bins across all masses.

The latter model has two break radii, the core radius r_c and the scale radius r_s, where $r_c \ll r_s$. The scale radius r_s affects the profile at radii beyond $R_{\rm 500c}$, the mean $R_{\rm 500c}$ of the stacked mass bin. The model also introduces two slope parameters: β, which influences the X-ray surface brightness profile at radii $r < r_s$ and ϵ, the slope that affects the profile at $r > r_s$. As $R_{\rm 500c}$ is the radius used most commonly in observations, and β quantifies the shape of the profile at radii $\leq R_{\rm 500c}$, we discuss here the variations in β across the stellar and halo mass bins.

The increasing stellar mass bins $10^{10.5-11}$ $\rm M_\odot$, $10^{11.25-11.5}$ $\rm M_\odot$, and $10^{11.25-11.5}$ $\rm M_\odot$ result in decreasing values of β from 0.4, 0.28, and 0.25, respectively. The same trend holds for the halo mass bins, where increasing halo mass bins: $10^{12.5-13}$ $\rm M_\odot$, $10^{13-13.5}$ $\rm M_\odot$, and $10^{13.5-14}$ $\rm M_\odot$ have decreasing values of β from 0.57, 0.30, to 0.24, respectively. One of the reasons for the decrease

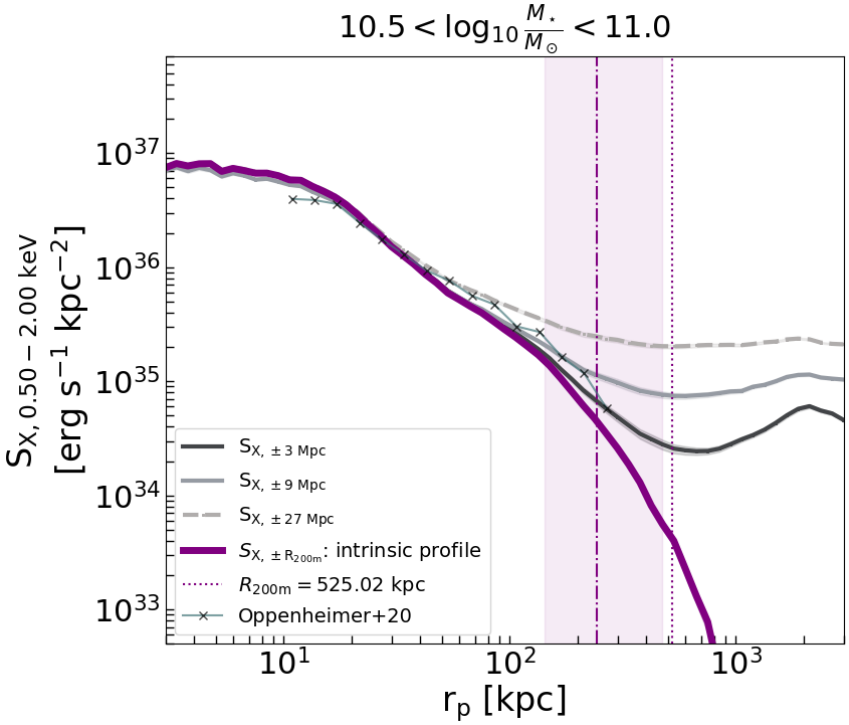

Figure 2.6: Mean X-ray surface brightness profiles in the stellar mass bin $M_\star = \left[10^{10.5}, 10^{11}\right]$ $M_\odot$, corresponding to MW-like galaxies. The locally correlated large-scale structure contributions are shown by comparing the profiles obtained with photons selected within $\pm R_{200m}$ (*purple*) and those obtained within ±3 Mpc (*solid black*), ±9 Mpc (*solid grey*), ±27 Mpc (*dashed grey*) away from the halo centre. The crosses are from previous work by Oppenheimer et al. (2020), who generate mock X-ray observations using TNG-100. The vertical dashed line at 242 kpc and the dotted line at 525 kpc are the mean R_{500c} and R_{200m}, respectively, of the 5,109 galaxies used in the mass bin with the shaded area corresponding to the minimum and maximum R_{500c} values. The shaded uncertainties on the profiles represent the variance obtained by bootstrapping.

is attributed to the mass-dependence of the feedback prescriptions in the TNG300 model, i.e., stellar mode dominating at lower masses, and the kinetic and thermal modes of energy injection by AGN dominating galaxies with $M_\star \geq 10^{10.5}$ $M_\odot$ (Weinberger et al., 2016). As discussed in Weinberger et al. (2018), the two AGN-related feedback channels depend on the black-hole (BH) accretion rates. For high accretion rates, the thermal mode causes the gas cells close to the galactic centre to heat, eventually releasing the energy radiatively in X-rays. However, for lower accretion rates, the kinetic mode kicks in, depositing energy through winds and jets in random directions away from the BH. This causes gas heating and, hence, X-ray emission via cooling at a larger distance away from the galaxy centre, overall causing a flattening of the radial X-ray surface brightness profile as shown by the slope β in Fig. 2.4 and 2.5. This reasoning is further consolidated with studies detailing the effects of the kinetic mode of BH feedback in the TNG model (Terrazas et al., 2020), its impact on the gas properties, i.e., temperature, entropy, density, and CGM fraction (Zinger et al., 2020; Davies et al., 2020a), and its correlations with

X-ray emission (Truong et al., 2020; Oppenheimer et al., 2020; Truong et al., 2021a; Ayromlou et al., 2023). Sorini et al. (2024) show a similar trend of decreasing slope for the gas density profiles with the SIMBA (Davé et al., 2019) suite of simulations. With simulation comparison projects like CAMELS simulations (Villaescusa-Navarro et al., 2021b), it is possible to study the correlation between X-ray emission around galaxies with different feedback implementations, the exploration of which we leave for a future study.

In the following two sections, we focus on how the projection effects result in deviations from the intrinsic profile. We discuss the effects on the stellar mass bins as it is an observationally available mass proxy.

2.5.2 Locally correlated environment

For the MW-mass bin, $M_\star = 10^{10.5-11}$ M$_\odot$, with mean $R_{200\mathrm{m}} = 525$ kpc, we generate cubes within ±3 Mpc, ±9 Mpc and ±27 Mpc from the galaxy center. This corresponds to photons selected within $\sim 5.7 \times R_{200\mathrm{m}}$, $\sim 17 \times R_{200\mathrm{m}}$, and $\sim 51.4 \times R_{200\mathrm{m}}$, respectively. Fig. 2.6 presents the impact of the locally correlated LSS for MW-like halos. We show the intrinsic profile that is obtained by selecting events within $\pm R_{200m}$ of the galaxy centre in purple. We compare our result with previous work from Oppenheimer et al. (2020), shown with the crosses in Fig. 2.6. They predict the profile between 10 – 242 kpc for a stellar mass sample in the mass range $10^{8.2-11.39}$M$_\odot$ containing ∼ 400 galaxies. Their stellar mass sample is divided into low sSFR and high sSFR. We take the mean of the low sSFR and high sSFR profiles generated in their work and compare them with ours. The halo mass range corresponding to their stellar mass bin is $10^{\sim 12.3-13}$ M$_\odot$, which entails the mean halo mass $M_{200\mathrm{m}} = 10^{12.7}$ M$_\odot$, same as that of the MW mass bin used in our work. Oppenheimer et al. (2020) use the TNG-100 simulation and synthesize mock X-ray observations for individual halos as opposed to this work that uses TNG300 and synthesizes mock X-ray observations within the lightcone. Despite these differences, this work's predicted X-ray intrinsic emission profiles are in good agreement with Oppenheimer et al. (2020).

We find that increasing the volume by $\frac{4\pi}{3}(5.7^3 - 1^3)R^3_{200m} = 771.5 \times R^3_{200m}$, i.e., by including events within ±3 Mpc, boosts the X-ray surface brightness profile at R_{200m} by a factor of 5.2. We show this with the thick black line in Fig. 2.6. We find deviations from the true intrinsic profile due to events selected within ±3 Mpc at ∼ 150 kpc, which corresponds to $\approx 0.6 \times R_{500c}$ and $\approx 0.3 \times R_{200m}$ for the MW-stellar mass bin.

When considering the events within ±9 Mpc, i.e., increasing the volume used to compute the X-ray surface brightness profiles by $\frac{4\pi}{3}(17^3 - 1^3)R^3_{200m} = (2.0 \times 10^4)\, R^3_{200m}$, we find that the X-ray surface brightness profile at R_{200m} is boosted by a factor of 16.8 This is shown by the grey curve in Fig. 2.6. We find deviations from the true intrinsic profile due to events selected within ±9 Mpc, at ∼ 100 kpc, which corresponds to $\approx 0.4 \times R_{500c}$ and $\approx 0.2 \times R_{200m}$ for the MW-stellar mass bin.

For events selected in ±27 Mpc or by including events in a volume of $(8.2 \times 10^4)\, R^3_{200m}$, the X-ray surface brightness profile at R_{200m} is boosted by 47.3. This is shown by the light grey dashed curve in Fig. 2.6. The profile, in this case, remains unchanged only at radii ≤ 40 kpc, which corresponds to $\approx 0.2 \times R_{500c}$ and $\approx 0.08 \times R_{200m}$ for the MW-stellar mass bin.

In conclusion, we show for the first time the effect of the local environment on the true

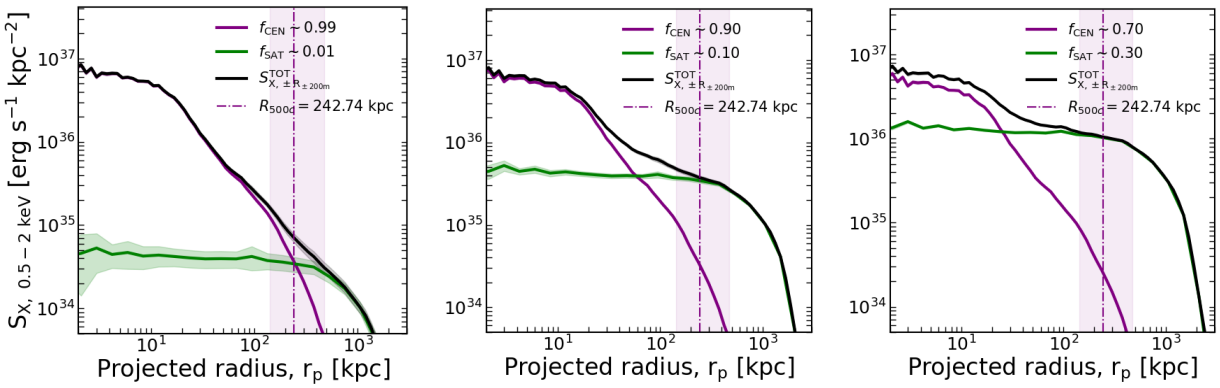

Figure 2.7: Effect of centrals (*purple*) and misclassified-centrals (*green*), in the stellar mass bin $M_\star = \left[10^{10.5}, 10^{11}\right]$ $M_\odot$, on the total X-ray surface brightness profiles (*black*). The total sample is constructed such that there are 1% satellites and 99% centrals (*left panel*), 10% satellites and 90% centrals (*middle panel*), and 30% satellites and 70% centrals (*right panel*). The vertical dashed line at 242 kpc is the mean R_{500c} of the 5109 galaxies used in the mass bin with the shaded area corresponding to the minimum and maximum values. The shaded regions on the profiles are the uncertainties obtained by bootstrapping.

intrinsic profile of a mean MW-like stacked X-ray surface brightness profile. Namely, we find deviations from the true profile at $\approx 0.3 \times R_{200m}$, $\approx 0.2 \times R_{200m}$, and $\approx 0.08 \times R_{200m}$ by including events out to $\sim 5.7 \times R_{200\mathrm{m}}$, $\sim 17 \times R_{200\mathrm{m}}$, and $\sim 51.4 \times R_{200\mathrm{m}}$, respectively. The black, grey, and dashed-grey curves in Fig. 2.6 show that increasing the integration volume swamps the features of the intrinsic profile at radii closer to the galaxy centre.

In observations, one is sensitive to the complete line of sight towards the observer. Therefore, this effect can be corrected by subtracting a background emission level determined empirically from the observed surface brightness at a large distance from the halos of interest (assuming spherical symmetry in the large-scale emission). We test the impact of a simple, conventional background subtraction, where we subtract the mean value of the surface brightness profile beyond the $R_{200\mathrm{m}}$ (vertical purple dotted line) from the respective grey, and dashed-grey curves in Fig. 2.6, as is most commonly done in observations. We find that the resulting profiles after background subtraction agree well with the intrinsic profile (solid purple line) out to $R_{500\mathrm{c}}$ (the vertical dashed-dotted line). Beyond $R_{500\mathrm{c}}$, such a subtraction underestimates the X-ray emission at the outskirts. However, this must be further tested with larger-volume lightcones than that used here (see further discussion in Sec. 2.6.1). Nevertheless, given the setup used in this work, we can, for the first time, probe this effect locally around the halo and show its impact in stacking experiments.

2.5.3 The Effect of Misclassified Centrals

In simulations, we completely and accurately classify central and satellite galaxies within a given stellar mass bin. Using this to our advantage, here, we make a precise prediction of the average emission arising from stacking around satellite galaxies by considering the following fraction of satellite (or misclassified centrals) contaminating the total galaxy sample: 0.01, 0.1 and 0.3.

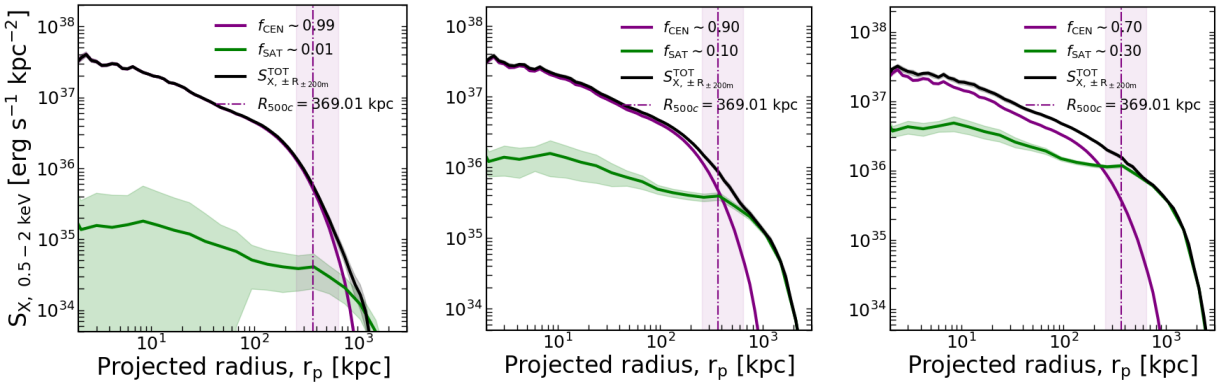

Figure 2.8: Effect of centrals (*purple*) and misclassified-centrals (*green*), in the stellar mass bin $M_\star = \left[10^{11}, 10^{11.25}\right]$ $M_\odot$, on the total X-ray surface brightness profiles (*black*). The total sample is constructed with 1% (*left panel*), 10% (*middle panel*), and 30% (*right panel*) satellites. The vertical dashed line at 369 kpc is the mean R_{500c} of the 680 galaxies used in the mass bin with the shaded area corresponding to the minimum and maximum values.

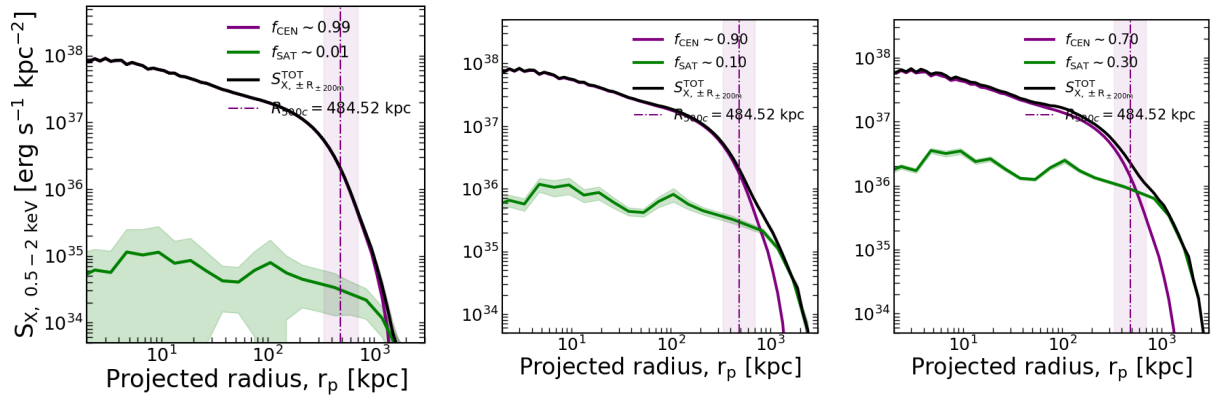

Figure 2.9: Effect of centrals (*purple*) and misclassified-centrals (*green*), in the stellar mass bin $M_\star = \left[10^{11.25}, 10^{11.5}\right]$ $M_\odot$, on the total X-ray surface brightness profiles (*black*). The total sample is constructed with 1% (*left panel*), 10% (*middle panel*), and 30% (*right panel*) satellites. The vertical dashed line at 484.5 kpc is the mean R_{500c} of the 305 galaxies used in the mass bin with the shaded area corresponding to the minimum and maximum values.

We select these contamination fractions of satellites by bootstrapping over the entire satellite galaxy sample. Tab. 2.1 details the number of centrals and satellites in the three stellar mass bins presented here. We show our findings in Fig. 2.7, 2.8, and 2.9, corresponding to stellar mass bins $10^{10.5-11}$ $M_\odot$, $10^{11-11.25}$ $M_\odot$, and $10^{11.25-11.5}$ $M_\odot$, respectively.

Fig. 2.7 quantifies the effect of misclassified centrals on the total surface brightness profile, shown with the solid black line, in the MW-stellar mass bin of $10^{10.5-11}$ $M_\odot$. We show the integrated profile obtained by stacking only the satellite galaxies misclassified as centrals in green and the intrinsic profile due to central galaxies in purple. The point at which the profile due to misclassified centrals (*green*) intersects the intrinsic central galaxy (*purple*) profile represents the

point at which the effect due to misclassified centrals contributes ∼ 50% to the total (centrals and satellites) emission. For a sample with 1% (*left panel*) and 10% (*central panel*) contaminating satellites, the effect due to misclassified centrals dominates over the intrinsic central galaxy emission at radii $\geq 1.04 \times R_{500c}$ (∼ 252 kpc) and $\geq 0.24 \times R_{500c}$ (∼ 59 kpc), respectively. In a sample with 30% satellites contaminants (*right panel*), the effect due to misclassified centrals dominates over the intrinsic central galaxy emission at radii $\geq 0.11 \times R_{500c}$ (∼ 27 kpc).

Analogously, Fig. 2.8 quantifies the effect of misclassified centrals on the total surface brightness profile, shown with the solid black line, for galaxies in the stellar mass bin $10^{11-11.25}$ $M_\odot$. For a sample with 1% (*left panel*) contaminating satellites, we find that the effect of misclassified centrals has negligible impact within radii $\leq R_{500c}$. For 10% satellite contamination (*central panel*), the effect due to misclassified centrals dominates over the intrinsic central galaxy emission at radii $\geq 1.1 \times R_{500c}$ (∼ 400 kpc) and for 30% satellites contamination (*right panel*), the effect due to misclassified centrals dominates over the intrinsic central galaxy emission at radii $\geq 0.63 \times R_{500c}$ (∼ 231 kpc).

Finally, Fig. 2.9 quantifies this effect for the largest mass bin we are considering, $10^{11.25-11.5}$ $M_\odot$. For a sample with 1% (*left panel*), 10% (*centre panel*) and 30% satellite contamination (*right panel*), the effect due to misclassified centrals remains negligible at all radii $\leq R_{500c}$. More precisely, the 1% satellite contamination has a negligible impact on the total surface brightness profile. The 10% and 30% satellite contamination dominate over the intrinsic central galaxy profile at $\geq 1.7 \times R_{500c}$ (∼ 804 kpc) and $\geq 1.2 \times R_{500c}$ (∼ 565 kpc), respectively.

As expected, we find from Fig. 2.7, 2.8, and 2.9 that the effect due to misclassified centrals becomes increasingly important as we probe lower stellar mass bins in stacking experiments. As we go to higher mass bins, the decreasing impact of the effect of misclassified centrals is attributed to the satellites - of the same stellar mass bin - residing in less massive parent halos (see further explanation in Sec. 2.6).

Fig. 2.10 presents the radial fraction of the X-ray emission from the intrinsic CGM - for four different levels of misclassified centrals contamination - in three stellar mass bins: $10^{10.5-11}$ $M_\odot$, $10^{11-11.25}$ $M_\odot$, and $10^{11.25-11.5}$ $M_\odot$, respectively. We complement the conclusions from Fig. 2.7, 2.8, and 2.9 by showing that for MW-like galaxies, the effect of misclassified centrals at the lowest contamination fraction of 0.01 results in the intrinsic central galaxy emission contributing only ∼ 51% of the total emission at R_{500c}. This further deteriorates with the increasing fraction of misclassified centrals in the galaxy sample, where fractions of 0.1, 0.3, or 0.5 result in the intrinsic emission contributing ∼ 9%, ∼ 3% and ∼ 1% of the total emission at R_{500c}, respectively. This effect is less pronounced for the intermediate and most massive stellar mass bins of $10^{11-11.25}$ $M_\odot$ and $10^{11.25-11.5}$ $M_\odot$ compared to the MW-like stellar mass bin. In the case of the $10^{11-11.25}$ $M_\odot$ mass bin, for a fraction of misclassified centrals of 0.01, 0.1, 0.3, or 0.5, the central intrinsic emission contributes ∼ 93%, ∼ 55%, ∼ 23% and ∼ 11% of the total emission at R_{500c}, respectively. Analogously, for the stellar mass bin of $10^{11.25-11.5}$ $M_\odot$, for a fraction of misclassified centrals of 0.01, 0.1, 0.3, or 0.5, the central intrinsic emission contributes ∼ 99%, ∼ 86%, ∼ 61% and ∼ 40% of the total emission at R_{500c}, respectively. Therefore, we present a clear trend of the increasing importance of the effect of misclassified centrals, not only due to the increasing fraction of satellite contamination in the galaxy sample but also due to the decreasing stellar mass bins.

2.6 Discussion

This chapter uses a TNG300-based forward model for the hot CGM emission and demonstrates, for the first time, the effect of locally correlated large-scale structure around a halo, the effect of misclassified centrals in stacked hot CGM galactocentric profiles and the effect of the choice of centre. Our findings are important for studies of the X-ray emission around lower mass galaxies with stacking experiments. We divide the discussion of our results by focusing on the projection effects due to the locally correlated environment, first, in Sec. 2.6.1, second, the effect of misclassified centrals in Sec. 2.6.2, and lastly, the effect of miscentering in Sec. 2.6.3.

2.6.1 Locally correlated environment

The locally correlated environment for MW-like stellar mass galaxies boosts the mean galactocentric X-ray emission at large radii less than R_{200m}. More precisely, at R_{200m} the X-ray emission is boosted 5.2×, 16.8× and 47.3× by including emission ±3 Mpc, ±9 Mpc, ±27 Mpc away from the halo centre, respectively.

Increasing the volume over which the intrinsic galactocentric profiles are measured also leads to increased X-ray emission at smaller radii. This increased X-ray emission, in projection, is attributed to the local environment in which the galaxy resides. The upturn in the black line in Fig. 2.6, corresponding to including events within ±3 Mpc ($\sim 5.7R_{200m}$) of the galaxy centre, signifies the presence of other X-ray emitting halos $\gtrsim$ 1 Mpc away from MW-like galaxies, i.e., $\approx 2 \times R_{200m}$ or $\approx 4 \times R_{500c}$. This "upturn" feature is washed out as we start including events in even larger volumes, as shown by the grey and dashed-grey lines (corresponding to events selected within ±9 Mpc and ±27 Mpc, respectively) in Fig. 2.6. This supports our finding that an observer starts probing the averaged hot gas emission from all galaxies in projection along the line of sight, drowning out the features due to the local environment when integrating events over larger volumes around a galaxy centre.

Further improvements to study this effect would involve including events to even larger radii around the galaxy. Given the limited area of the lightcone, 47.28 deg^2, we are constrained in studying this effect out to ±27 Mpc. To quantify the effects of the locally correlated large-scale environment to even larger distances than those explored here, we need larger-volume lightcones, which is possible with larger cosmological hydrodynamical simulations like Magneticum (Dolag, 2015), MillenniumTNG (Pakmor et al., 2023; Hernández-Aguayo et al., 2023), and FLAMINGO (Schaye et al., 2023a). Additionally, future studies could study how different simulation feedback prescriptions can impact the trend observed in the X-ray surface brightness profiles by including events in larger volumes. It is particularly interesting to understand how the physics implemented in hydrodynamical simulations impacts the baryon spread around galaxies, i.e., the radius at which all the emissions converge to the mean background level in X-rays. We leave the study of these aspects to future work, which is made possible with the advent of projects like the CAMELS simulations (Villaescusa-Navarro et al., 2021b); see, e.g., Gebhardt et al. (2024) and Sorini et al. (2022).

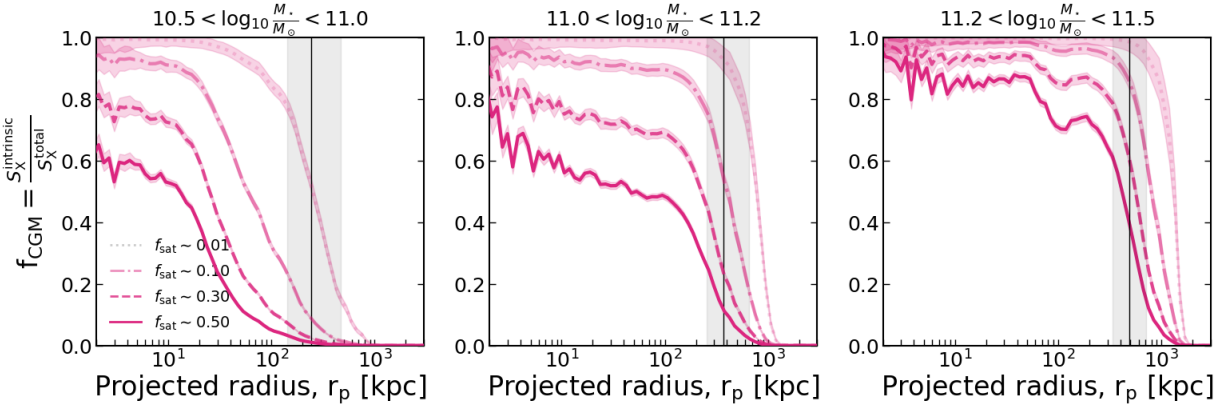

Figure 2.10: The fraction of X-ray emission from the intrinsic hot CGM for different levels of satellite contamination (misclassified centrals) in the total galaxy sample. The fraction of X-ray emission from the intrinsic hot CGM for misclassified central contamination fractions of 0.01 (dotted line), 0.1 (*dash-dotted line*), 0.3 (*dashed line*), and 0.5 (*solid line*) are shown for three different mass bins: MW-like galaxies with stellar-masses in $10^{10.5-11}$ $M_\odot$ (*left panel*), $10^{11-11.25}$ $M_\odot$ (*middle panel*), and $10^{11.25-11.5}$ $M_\odot$ (*right panel*). The shaded regions around each curve correspond to the uncertainty of the mean profile obtained by bootstrapping. The vertical black solid line at 242 kpc in the left panel, 369 kpc in the middle panel, and 484.5 kpc in the right panel corresponds to the mean R_{500c} of the respective mass bins with the shaded area signifying the minimum and maximum values. We find that the contaminating effect of the misclassified centrals on the stacked profiles increases when the stellar mass decreases.

2.6.2 The Effect of Misclassified Centrals

We next examine the impact of satellites that are misclassified as centrals ("satellite boost") on the stacked X-ray surface brightness profiles. Figure 2.7, 2.8, and 2.9 show this effect for stellar mass bins of $10^{10.5-11}$, $10^{11-11.25}$, and $10^{11.25-11.5}$, $M_\odot$, respectively.

For the MW-like stellar mass bin ($10^{10.5-11}$ $M_\odot$), the effect is strongest. Satellites in this mass range typically reside in group- or cluster-mass halos ($M_{200m} \sim 10^{12.3-15.1}$ $M_\odot$, with a mean of $10^{13.7}$ $M_\odot$), much more massive than the halos of the genuine centrals of the same stellar mass. The X-ray surface brightness of these satellites, misclassified as centrals, therefore reflects the extended emission of the host halo rather than their own CGM. When such satellites are stacked together with centrals, they add an off-centered, group- or cluster-scale component that flattens the overall profile slope. Even modest contamination fractions can dominate the stacked profile at large radii: for example, if only 10% of satellites are misclassified as centrals in the stacking sample, they already dominate over the central contribution beyond $\sim 0.2\ R_{500c}$.

By contrast, for the higher stellar mass bins ($10^{11-11.25}$ and $10^{11.25-11.5}$ $M_\odot$), the impact of misclassified centrals is much weaker. In these bins, both centrals and satellites occupy comparably massive halos, so the magnitude of the effect on the X-ray surface brightness profiles is weaker than in the MW-mass bin. As a result, the relative bias from contamination is reduced. This trend is summarized in Fig. 2.10, where the MW-like bin consistently shows the largest loss of intrinsic central emission at R_{500c} for all contamination levels, while the higher-mass bins remain much less affected.

To understand why the MW stellar-mass bin is most affected by misclassified centrals, we examine the host halo masses of satellites in the higher stellar-mass bins of $10^{11-11.25}$ $M_\odot$ and $10^{11.25-11.5}$ $M_\odot$. These satellites typically reside in halos with mean masses of $\sim 10^{14}$ $M_\odot$ and $\sim 10^{14.2}$ $M_\odot$, respectively, compared to the mean halo masses of $10^{13.3}$ $M_\odot$ and $10^{13.6}$ $M_\odot$ for the corresponding centrals. Because the halo masses of centrals and satellites in these more massive bins are closer in value than for the MW-mass bin[8], much larger levels of contamination are required for misclassified centrals to alter the stacked signal. Within the more realistic contamination levels considered here, the effect is therefore negligible for the higher stellar-mass bins. In summary, misclassified centrals can significantly bias stacked X-ray surface brightness profiles in the MW stellar-mass regime, but this effect is less prominent in higher stellar masses, where the halo masses of centrals and satellites are more comparable.

We now address whether this effect of satellites misclassified as centrals could be mitigated observationally using X-ray information. For this discussion, we assume that the galaxy sample has already been accurately classified into centrals and satellites. In that case, the residual impact of misclassified centrals arises primarily from instrumental resolution: satellites closer to their central than the instrument's angular resolution cannot be distinguished and may be misidentified as centrals. In principle, one could attempt to use X-ray detections of individual halos to exclude satellites near centrals. However, this approach is only feasible when the halo can be individually resolved in X-rays, which is not viable for MW-mass halos with survey instruments like eROSITA due to the faintness of their CGM emission (see also Sec. 2.6.3).

For more massive halos (M31-like), where detection is more likely, we explore whether removing satellites within a given angular separation of a central reduces contamination. We find that excluding M31-mass satellites within 15″ of a central lowers their mean contribution to the stacked X-ray surface brightness profile by $\sim 25\%$ at R_{500c}, compared to the case where all satellites are treated as misclassified centrals (see Fig. 2.11). Thus, this proximity-based selection mitigates the flattening of the stacked profile caused by satellites. A key caveat, however, is that such a procedure preferentially selects galaxies in isolated environments, biasing the inferred CGM signal.

Given these findings, we conclude that the contribution of satellites in MW-like galaxy samples must not be neglected in stacking analyses. Observationally, disentangling the contamination from misclassified centrals requires modelling the intrinsic central galaxy profile jointly with an additional component capturing the contribution of misclassified centrals for a given contamination fraction, as done in the following Chapt. 3. This effect is particularly severe for photometric surveys, where contamination levels can reach $\sim 30\%$ for MW-like galaxies (Sec. 3.5 in Z24). In spectroscopic surveys, the problem is significantly alleviated, with contamination reduced to $\sim 1\%$ (Sec. 3.7 in Z24), though not eliminated entirely due to survey incompleteness or residual uncertainties in central–satellite classification, especially in low-richness systems. Similar challenges have also been quantified in other tracers, such as absorbers in cold gas using TNG50 (Weng et al., 2024), underscoring that central–satellite misclassification remains a non-negligible systematic that must be accounted for in stacking analysis.

[8]This is a direct implication arising from the difference in the stellar-to-halo-mass relation for central and satellite galaxies (Shuntov et al., 2022)

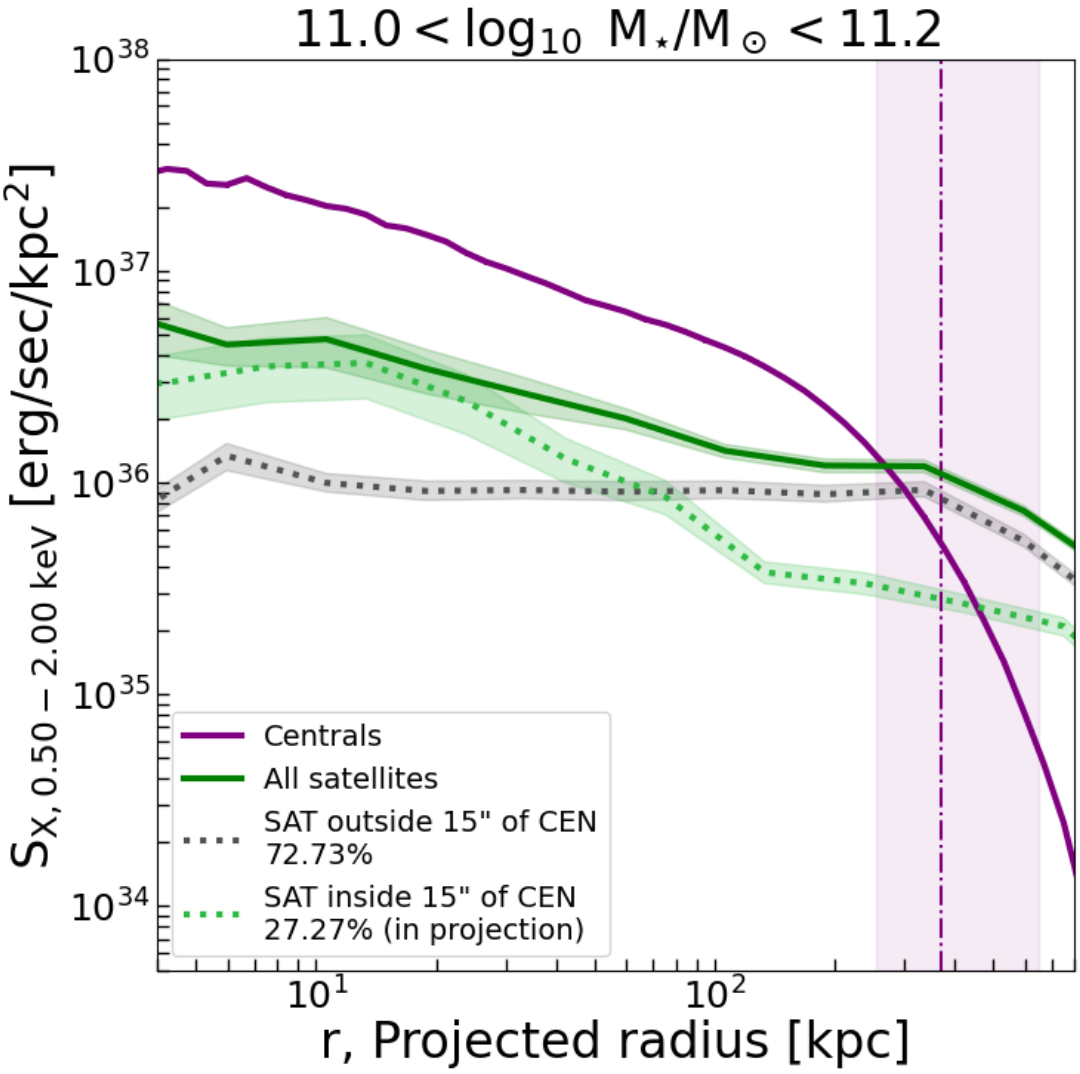

Figure 2.11: Effect of selectively removing satellites misclassified as centrals on the stacked X-ray surface brightness profile. The selection is based on the proximity of the satellite contaminant from the true central. The total population of satellites misclassified as centrals (*solid green line*) is divided into satellites within 15" of a central (*green dotted line*) and satellites farther than 15" from a central (*grey dotted line*) in projection on the sky. We show that satellites (misclassified as centrals) within 15" of a central galaxy have a steeper profile than the case where we consider all the satellites, thereby reducing the overall flattening of the X-ray surface brightness profile due to misclassified centrals. Contrarily, the satellites farther than 15" from a central have a constant surface brightness profile. The central galaxy profile is shown in purple. The vertical dashed line at 369 kpc is the mean R_{500c} of the 680 galaxies used in the M31 stellar mass bin, and the shaded area corresponds to the minimum and maximum R_{500c} value of the central galaxies in the M31-mass bin. The shaded uncertainties on the profiles represent the variance obtained by bootstrapping.

2.6.3 Offsets between the X-ray and the minimum of the dark matter potential centres: magnitude and implications

As first introduced in Sec. 2.3.1, we now return to study the effect of offsets between the observationally defined X-ray centre and the "true" centre defined by the minimum of the halo dark matter potential. The X-ray centre is computed as the luminosity-weighted mean of the counts within the spherical R_{200m} aperture of the central halo. In contrast, in our lightcone analysis we adopt as the input (true) centre the position of the most bound particle within the halo, as identified by the FoF/SUBFIND algorithm in TNG300. Offsets, $\Delta_{X-ray-input}$, are measured in projection on the sky and converted to physical distances using the halo redshift.

We find that the $\Delta_{X-ray-input}$ distribution has a mean of 70 kpc, with 16^{th}–84^{th} percentiles spanning 13–131 kpc, consistent with previous studies (Seppi et al., 2023; Popesso et al., 2024a). The halos in this sample have a mean $M_{200m} = 10^{13.3}$ $M_\odot$ (i.e. M31-like systems), with 16^{th}–84^{th} percentiles between $10^{12.4}$–$10^{13.5}$ $M_\odot$. Examining bins in halo mass, we find mean offsets of 52 kpc, 66 kpc, and 79 kpc for the $10^{12.5-13}$ $M_\odot$, $10^{13-13.5}$ $M_\odot$, and $10^{13.5-14}$ $M_\odot$ ranges, respectively, indicating that the offset between X-ray and true centres increases systematically with halo mass.

In a stacking analysis with an eROSITA-like instrument, using the halo potential minimum as the centre, such offsets would contribute to a miscentering effect. If the X-ray halo is individually detected, miscentering can only be corrected when the offset is larger than the eROSITA resolution of $\sim 30''$. In our lightcone, $\sim$ 13% of halos have such resolvable offsets, with the fraction remaining $\sim$ 13% in the $10^{12.5-13}$ $M_\odot$ and $10^{13-13.5}$ $M_\odot$ bins, and rising to 17% in the $10^{13.5-14}$ $M_\odot$ bin. However, we note that diffuse X-ray emission from individual MW-mass halos is below eROSITA's detection threshold. Detecting the X-ray peak in such systems is therefore not feasible at present, though it may become possible with future, higher-sensitivity observatories.

2.7 Conclusions

The main conclusions from this chapter are summarised as follows.

1. We present an analytical model (Eq. 2.7) that well-describes the intrinsic S_X-profile in LC-TNG300 across the stellar mass bins $10^{10.5-11}M_\odot$, $10^{11-11.25}M_\odot$, and $10^{11.25-11.5}M_\odot$ and halo mass bins of $10^{12.5-13}M_\odot$, $10^{13-13.5}M_\odot$, and $10^{13.5-14}M_\odot$. We provide the best-fitting parameters for the analytical model in Tab. 2.3 and Tab. 2.4 for the stellar and halo mass bins explored in this work.

2. We carry forward the current state-of-the-art modelling analysis presented in Oppenheimer et al. (2020) by also showing the impact of the locally correlated environment on the measured X-ray surface brightness profiles.

3. We present, for the first time, the effect of misclassified centrals in stacking experiments for three stellar mass bins: $10^{10.5-11}M_\odot$, $10^{11-11.25}M_\odot$, and $10^{11.25-11.5}M_\odot$. We find that the contaminating effect of the misclassified centrals on the stacked profiles increases when the stellar mass decreases.

4. For the MW-like galaxies, we conclude that the contribution of satellites (or misclassified centrals) can not be neglected in stacking analysis (see Fig. 2.10). In cases where 30%, 10%, or 1% of the satellites contribute to the total emission of MW-like galaxies, we have shown that they dominate the measured total S_X profile at radii $\geq 0.11 \times R_{500c}$, $\geq 0.24 \times R_{500c}$, and $\geq 1.04 \times R_{500c}$, respectively.

5. We report in Sec. 2.6.3 that the offsets between the X-ray peak and the halo potential centre are typically $\sim$ 70 kpc (increasing with halo mass), and while most of these offsets are below eROSITA's resolution, $\sim$ 10–20% are resolvable; such miscentering can bias stacked X-ray CGM profiles by artificially broadening the emission, and must be accounted, when possible, for when interpreting future direct detections or stacking analyses.

Modelling observed CGM profiles and comparing them with simulations is crucial to constrain the different galaxy formation models and to understand how the feedback and physics prescriptions affect the hot CGM profile. Current state-of-the-art cosmological hydrodynamical simulations are calibrated on the stellar mass function and successfully reproduce realistic galaxy populations. Despite this, Davies et al. (2020b) show that EAGLE and IllustrisTNG predict different total gas mass fractions, affecting the observed CGM properties at MW-masses. Similarly, Khrykin et al. (2024) shows how the hot gas is sensitive to the different feedback variants within SIMBA. The model and methodology presented here provide the machinery to compare the measured hot CGM profiles among current simulations in future works.

Future X-ray missions, on the observation side, like Athena (Nandra et al., 2013), AXIS (Mushotzky et al., 2019), HUBS (Cui et al., 2020) will push our current detection limits and provide us with (i) the spatial resolution to reach higher redshifts, (ii) better quantify point-like source contamination within the hot CGM, (iii) the spectral resolution to allow disentangling components via spectral fitting and (iv) the grasp to reach even fainter surface brightness levels. This chapter, focusing on modelling the projection effects, is a step towards exploiting the information provided by the next-generation telescopes to better understand the intrinsic hot CGM emission. The prospects of this framework would be to extend it to interpret hot X-ray CGM measurements in stacking experiments by accounting for all projection effects, i.e., not only the impact due to the local environment of the halo and the effect due to misclassified centrals but also the emission from other X-ray sources such as AGN and XRB.

Chapter 3

Retrieving the hot CGM physics from the X-ray radial profile from eROSITA with an IlustrisTNG-based forward model

The results presented in this chapter were published in Astronomy & Astrophysics, titled "*Retrieving the hot CGM physics from the X-ray radial profile from eROSITA with an IlustrisTNG-based forward model*" **Shreeram, S.**, Comparat, J., Merloni, ... (2025b)

3.1 Summary

In this chapter, we build on the IllustrisTNG lightcone framework developed in Chapt. 2, to construct a forward model for the stacked X-ray observations for interpreting eROSITA data. While the previous chapter focused on characterizing and mitigating projection effects inherent to CGM measurements done by stacking analysis, here, we utilize this information and use the same lightcone to carefully model the measured X-ray signal. More precisely, in this chapter, we develop forward models for the stacked X-ray radial surface brightness profile measured by eROSITA around MW-mass galaxies. Our model contains two emitting components: hot gas (around central galaxies and around satellite galaxies hosted by more massive halos) and X-ray point sources (XRB and AGN). We model the hot gas profile using the TNG300-based products. We generate mock observations with our TNG300-based model (matching stellar mass and redshift with observations) with different underlying halo mass distributions. Therefore, we test the CGM properties as a function of their host halo mass distribution. The point sources are described by a simple point-spread-function (PSF) of eROSITA, and we fit their normalization in this work. In total, we fit the X-ray surface brightness profile with two free parameters: the normalization of satellites in more massive host halos and the normalization of the mean point source emission. We show that for the same mean stellar mass, a factor $\sim 2\times$ increase in the mean value of the underlying halo mass distribution results in $\sim 4\times$ increase in the stacked X-ray luminosity from the hot CGM. Using empirical models to derive a permissible range of AGN and XRB luminosities in the MW-mass X-ray galaxy stack, we choose our forward model best

describing the hot CGM for the eROSITA observations. Our chosen model in the MW stellar mass bin is in good agreement with previous literature results. We find that at $\lesssim$ 40 kpc from the galaxy centre, the hot CGM of central galaxies and the X-ray point source emission (from XRB and AGN) each account for $\sim$ 50% of the total X-ray emission budget. Beyond $\sim$ 40 kpc, we find that the hot CGM around satellites (probing their more massive host halos with mean $M_{200\mathrm{m}} \sim 10^{14}$ $\mathrm{M}_{\odot}$) starts to dominate the stacked X-ray surface brightness profile. The gas physics driving the shape of the observed hot CGM (in stellar-mass-selected X-ray stacking experiments) is tightly correlated by the underlying halo-mass distribution. This chapter describes a novel technique to constrain the AGN X-ray luminosity jointly with the radial hot CGM gas distribution within the halo using measurements from X-ray galaxy stacking experiments. Implementing this technique on other state-of-the-art simulations will provide a new ground for testing different galaxy formation models with observations. Lastly, the modelling strategy developed here also motivates us to explore new directions, such as the environmental analysis done in Chapt. 4, where we study how the large-scale structure influences the hot CGM.

3.2 Motivation for this work

Given the advent of eROSITA (Merloni et al., 2024), there have been several studies exploiting the unprecedented statistics for stacking the X-ray emission at the position of optically selected galaxies, such as Comparat et al. (2022); Chadayammuri et al. (2022) and most recently, Zhang et al. (2024a, hereafter Z24). Z24 represent the state-of-the-art hot CGM measurements for MW-mass galaxies, combining the largest optical galaxy sample with the German half-sky eROSITA coverage in X-rays. They stack 415, 627 galaxies with photometric redshifts, $\mathrm{Full}_{\mathrm{phot}}$, from the DESI Legacy Survey DR 9 (Dey et al., 2019; Zou et al., 2019, 2022) and 30, 825 central galaxies with spectroscopic redshifts from the SDSS DR7 Main Galaxy Sample (Strauss et al., 2002; Abazajian et al., 2009). The latter, the SDSS-based central galaxy sample, is advantaged with spectroscopic information, allowing thr classification of galaxies into centrals and satellites with halo mass information (Tinker, 2021). Z24 retrieve the X-ray surface brightness profile from the hot CGM by empirically modelling the impact due to satellites, AGN and XRB emission. However, the former, the DESI Legacy survey-based galaxy sample, can not be classified into centrals and satellites, given the limitations in photometric redshift accuracy, making the modelling of this dataset challenging. To exploit the highest signal-to-noise ratio data (factor of 13.5 times more statistics than the spectroscopic sample) to date, in this chapter, we construct a forward model to disentangle the hot CGM radial profiles from the X-ray stack of optically selected galaxies.

Among the dominating sources of contamination in X-ray stacking experiments at MW-mass galaxies are *(1)* the AGN and X-ray binary (XRB) populations of galaxies (Biffi et al., 2018b; Vladutescu-Zopp et al., 2023), and *(2)* the effect of having satellite galaxies in the stacking sample, where these satellites contribute to the averaged X-ray stack with their more massive host galaxy within which they are embedded in the Large Scale Structure (see, e.g., Chapter 4, Weng et al. 2024). Given that we are modelling a photometric galaxy sample in this chapter, we do not have the classification of galaxies into centrals and satellites due to limitations in the (photomet-

ric) redshift accuracy for the galaxies in large optical surveys. Therefore, we use our TNG-based forward model to account for the satellite galaxy contribution by allowing the normalization of the surface brightness profile to be free when fitting to the data. The contaminating effect of the satellites was quantified in detail in Chapt. 2 (and accompanying paper Shreeram et al. 2025c), where we find that this effect becomes increasingly significant in the stacking sample as the stellar mass decreases. When conducting blind X-ray stacking analysis at the positions of optically selected galaxies, where centrals and satellites are unclassified, the inclusion of satellites implies that the total measured X-ray surface brightness profile comprises (i) the intrinsic hot gas emission around truly central galaxies and (ii) the contamination of hot gas emission measured around satellites. We emphasize that the latter does not correspond to the emission intrinsic to the satellites as the more massive host (central) galaxy in the vicinity of the satellite dominates the emission, resulting in a negligible contribution of the intrinsic satellite emission (see, e.g., Rohr et al. 2024).

This chapter presents a forward model for the stacked galaxy profile comprising the X-ray emitting gas and point source emission. We use the lightcone built with TNG300 in Chapt. 2 to construct mock galaxy catalogues representing the observations. From our TNG-based mock galaxy catalogue, we predict the hot gas CGM profile contribution to the X-ray galaxy stack from central and satellite galaxies. We parameterize the normalization of the hot gas contribution from satellites, $\mathcal{N}_{\rm sat}$. The hot gas prediction for central galaxies from our forward model with TNG is left unchanged. As for the point-like source contributions from AGN and XRB, we do not use the simulations, which are quite uncertain in their predicted instantaneous AGN activity, but rather we describe their contribution with a normalization parameter $\mathcal{N}_{\rm ps}$ and fix the radial shape using the PSF of eROSITA. This leaves us with two fitting parameters in our model: the contribution of point sources in the stack $\mathcal{N}_{\rm ps}$ and the normalization of the satellite X-ray surface brightness profile $\mathcal{N}_{\rm sat}$. We fit our forward model to the mean X-ray surface brightness profile reported Z24, obtained by stacking MW-mass galaxies. We obtain the point source luminosity obtained from our fitting analysis, and we interpret our results by comparing them with independent empirical models of AGN luminosity functions.

The chapter is organized as follows. Sec. 3.3 expands on the observational data used for modelling in this study. Sec. 3.4 describes the forward model built in this work; details on the point source and hot gas component are provided in Sec. 3.4.1 and Sec. 3.4.2, respectively, and generation of mock galaxy catalogues in Sec. 3.4.3. Sec. 3.5 interprets and discusses the results, and Sec. 3.6 summarizes the main findings of this chapter.

3.3 Data

This study uses the results from Z24, specifically the galaxy sample derived from optical data from the Legacy Survey Data release 9 (Dey et al. 2019), and X-ray data from the first four *SRG*/eROSITA All-Sky Surveys (eRASS:4) within the western galactic hemisphere (Merloni et al., 2024). Here, we summarize the relevant details from Z24 to motivate the forward-model setup, as described in Sec. 3.4.

The LS DR9 overlaps by $9,340$ deg^2 with the western Galactic hemisphere. Z24 define the

$\text{Full}_{\text{phot}}$ sample containing 1,677,909 galaxies, which is based on the LS DR9 galaxy catalog from Zou et al. (2019, 2022), who provide the galaxy properties. Stellar masses, $M_\star$, with uncertainties of $\sim$ 0.2 dex are provided in the range $9.5 < \log M_\star < 11.5$ and photometric redshifts, z_{phot}, with uncertainty $\Delta z_{\text{phot}} \lesssim 0.03$, span the range $0.01 < z_{\text{phot}} < 0.4$ (see Tab. 3 in Z24 for further classification into stellar mass bins). We focus here on the modelling of the X-ray emission from MW-like galaxies, defined by the stellar mass bin $10.5 < \log_{10} M_\star < 11.0$, and located in the redshift range $0.02 < z_{\text{phot}} < 0.17$. This sample contains 415,627 galaxies and median stellar mass and redshift of 5.5×10^{10} $M_\odot$ and $z_{\text{phot}} = 0.14$, respectively.

The details of the data analysis pipeline used to obtain the observed X-ray surface brightness profiles, based on the LS DR9 ($\text{Full}_{\text{phot}}$) galaxies, are provided in Z24. They stack the X-ray data in different stellar mass bins following the method from Comparat et al. (2022). The first step is to generate X-ray event cubes around every galaxy in the sample within 3 Mpc. The events within the cube are assigned a physical radial distance from the source, R_{kpc}, along with the exposure time, t_{exp}, effective collecting area, A_{eff}, and the rest frame energy of the event around the source E_{rest}. The X-ray surface brightness profile around the galaxy is obtained, with additional correction factors due to absorption and area loss if masking of sources is applied (see Eq. 1 in Z24). We use the background subtracted profiles in this work (for details of the background treatment in the data, see Appendix A in Z24).

3.4 Forward model built in this work

This section explains the forward model we built to fit the observed X-ray surface brightness profile reported in Z24. The mean X-ray surface brightness profile obtained from X-ray stacking of galaxies at their optically detected positions is expressed as

$$\mathbf{S}_{\text{X, total}}(r) = \mathbf{S}_{\text{X, hot gas}}(r) + \mathbf{S}_{\text{X, point-source}}(r), \tag{3.1}$$

where $\mathbf{S}_{\text{X, hot gas}}[r]$ is the X-ray contribution to $\mathbf{S}_{\text{X, total}}(r)$ from hot gas (further detailed in Sect. 3.4.2) and $\mathbf{S}_{\text{X, point-source}}[r]$ is the X-ray contribution from AGN and XRB (Sect. 3.4.1). We then introduce the forward models constructed in this work in Sec. 3.4.3.

3.4.1 The point source component

The $\mathbf{S}_{\text{X, point-source}}[r]$ component is expressed as

$$\mathbf{S}_{\text{X, point-source}}(r) = \mathcal{N}_{\text{ps}}\ \text{PSF}(z, r) \tag{3.2}$$

where $\mathcal{N}_{\text{ps}}$ is the normalization of the point-source component and $\text{PSF}[z, r]$ is the shape of the point-source component as defined by the survey-averaged eROSITA PSF. Here, the shape of the mean PSF is obtained by converting from angular to physical scale [kpc] using the redshifts of the galaxies in the stacking sample. We constrain $\mathcal{N}_{\text{ps}}$ by fitting the observations.

We do not use the TNG300 outputs to predict the contributions from AGN and XRB for the following reasons. As presented in Habouzit et al. (2019), the X-ray Luminosity Function

(XLF) for AGN in TNG shows an overproduction of faint AGN at $z = 0$, a common problem in hydrodynamical cosmological simulations due to poorly resolved sub-grid feedback prescriptions (Sijacki et al., 2015; Volonteri et al., 2016; Rosas-Guevara et al., 2016; Biffi et al., 2018b). Additionally, TNG underpredicts the bright end of the XLF compared with observations, due to the over-efficient kinetic mode of feedback prescriptions with TNG (Habouzit et al., 2019). Given these discrepancies between the hydrodynamical simulations and observations, using the TNG-based predictions for the X-ray AGN contribution would be unreliable for the purpose of this work. As for XRB, whose prediction depends on the star formation rates (SFR) of galaxies (more details in Sec. 3.5.1), using the TNG SFR values for the mock galaxies to represent observations requires extreme care, given how sensitive the SFR is to the definition of quenched galaxies, the physical apertures used for measurement of the SFR, and the mass resolution of the simulation (Donnari et al., 2019). Additionally, the quenched fraction of satellite galaxies is overestimated in the stellar mass range of $M_\star \in 10^{10-11}$ $M_\odot$ at $z = 0$ (Donnari et al., 2021), which entails the mass range of interest in this work. These caveats impede us from reliably predicting meaningful estimates for point source contributions intrinsic to the TNG model that can be directly compared with observations.

In this chapter, we use independent empirical estimates (Sec. 3.5.1 and Sec. 3.5.2) to predict the allowed range of the mean X-ray luminosity from XRB and AGN, respectively. Since the estimates from these empirical models are independent of TNG, we use them to inform our forward models for the permitted values of point source luminosities, as shown in Fig. 3.2.

3.4.2 The hot gas component

In this chapter, we model the hot gas emission using the TNG300 hydrodynamical simulations (Pillepich et al., 2018b; Marinacci et al., 2018; Naiman et al., 2018; Nelson et al., 2015; Springel et al., 2018); we use TNG300 to construct a lightcone and generate mock X-ray observations, as presented in Chapt. 2. Here, we summarize the most important features. We use the IllustrisTNG cosmological hydrodynamical simulation with the box of side length 302.6 Mpc (Nelson et al., 2019, TNG300;)[1]; this box size allows us to map the hot CGM around MW-mass analogues embedded in the large-scale structure. TNG300 contains 2500^3 dark matter particles, with a baryonic mass resolution of 1.1×10^7 $M_\odot$ (resulting in $\gtrsim 10^3$ particles at MW-mass galaxies), a comoving value of the adaptive gas gravitational softening length for gas cells of 370 comoving parsec (allowing us to resolve the X-ray gas from $\sim$ 5 kpc from the halo centre), gravitational softening of the collisionless component of 1.48 kpc, and dark matter mass resolution of 5.9×10^7 $M_\odot$. The TNG simulations adopt the Planck Collaboration XIII 2016 cosmological parameters. The TNG300 lightcone, LC-TNG300, is constructed with the box remap technique (Carlson & White, 2010), and spans across redshifts $0.03 \lesssim z \lesssim 0.3$; this range is motivated by observations (e.g. Comparat et al. 2022; Chadayammuri et al. 2022; Zhang et al. 2024a). It goes out to 1231 cMpc along the x-axis, subtending an area of 47.28 deg^2 on the sky in the y-z plane. The physical properties of the distinct halos and subhalos within the TNG300 lightcone are obtained by the SUBFIND algorithm (Springel et al., 2001; Dolag et al., 2009). SUB-

[1] http://www.tng-project.org

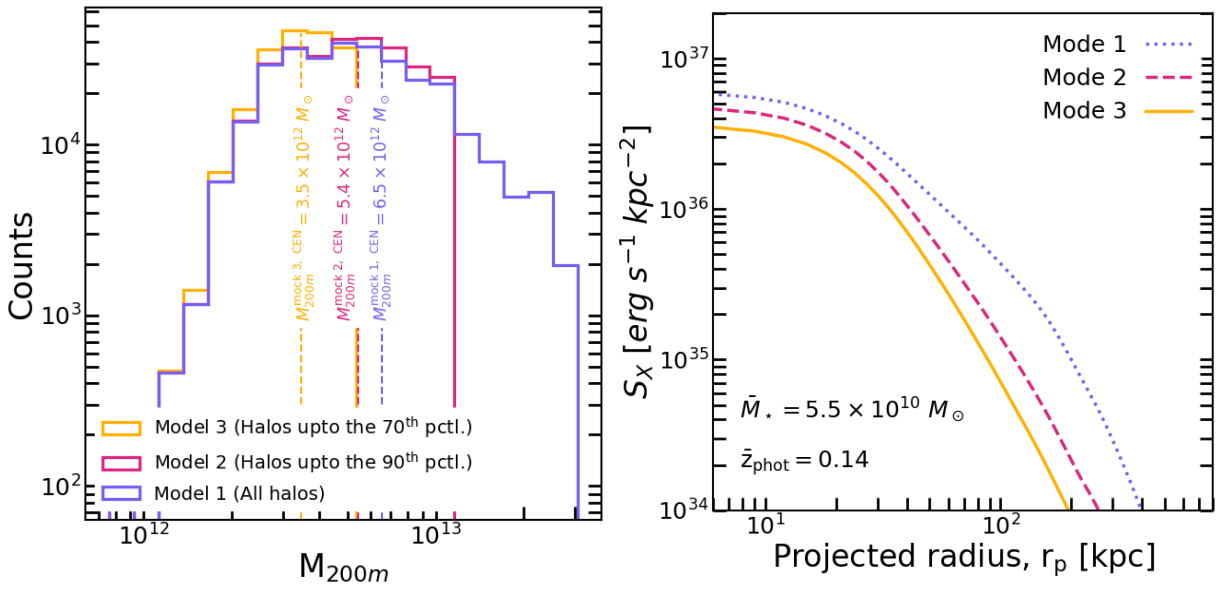

Figure 3.1: Forward models constructed for the hot CGM from central galaxies by varying the underlying halo mass distribution. *Left panel*: The purple halo mass distribution (Model 1) is obtained from the mock central galaxy catalogue - constructed with the TNG300 lightcone (LC-TNG300) from Chapt. 2 - for the X-ray stack from Zhang et al. (2024a) that uses optically detected galaxies with photometric redshifts ($\rm Full_{phot}$) from LS DR9 (Dey et al., 2019). Note that the mock galaxy catalogue is generated by matching LC-TNG300 to $\rm Full_{phot}$ in stellar mass and redshift (see details in Sec. 3.4.3); the median stellar mass and redshift of the $\rm Full_{phot}$ (and our mock catalogues) are 5.5×10^{10} $\rm M_\odot$ and 0.14, respectively. The underlying halo mass distribution of the $\rm Full_{phot}$ optical dataset is unknown. The pink distribution (Model 2; with mean $M_{\rm 200m} = 5.4 \times 10^{12}$ $\rm M_\odot$) discards the top 10% most massive halos before the generation of the mock galaxy catalogue. The yellow distribution (Model 3; with mean $M_{\rm 200m} = 3.5 \times 10^{12}$ $\rm M_\odot$) discards the top 30% most massive halos before the generation of the mock galaxy catalogue. *Right panel*: The corresponding X-ray surface brightness profiles in the $0.5 - 2$ kev energy band (for details on their generation see Sec. 3.4.2) for the three mock galaxy catalogues with different halo mass distributions, which are shown in the left panel. The profiles are convolved with the eROSITA PSF and they represent the $\rm Full_{phot}$ dataset in the stellar mass and redshift plane. Nevertheless, due to the impact of the underlying halo mass distribution, the shape and normalization of the hot CGM profiles are impacted, where discarding the most massive halos from the underlying halo distribution results in steeper profiles with lower normalizations.

FIND detects gravitationally bound substructures, equivalent to galaxies in observations, and also provides us with a classification of subhalos into centrals and satellites, where centrals are the most massive substructure within a distinct halo. For the MW-mass bin[2], $\rm M_\star = 10^{10.5-11} M_\odot$, we have 5, 109 centrals and 2, 719 satellites, resulting in a total simulated galaxy catalog with 7, 828 galaxies (subhalos).

The X-ray photons are simulated within the LC-TNG300 in the $0.5 - 2.0$ keV intrinsic band with `pyXsim` (ZuHone & Hallman, 2016), which is based on PHOX (Biffi et al., 2013; Biffi et al.,

[2]This chapter defines the stellar mass used from TNG300 as the mass within twice the stellar half-mass radius.

2018a), by assuming an input emission model where the hot X-ray emitting gas is in collisional ionization equilibrium. The spectral model computations of hot plasma use the Astrophysical Plasma Emission Code, APEC[3] code (Smith et al., 2001) with atomic data from ATOMDB v3.0.9 (Foster et al., 2012). This model uses the plasma temperature of the gas cells (in keV), the redshift z, and metallicity; Shreeram et al. (2025c) assume a constant metallicity of 0.3 $Z_{\odot}$ for the generation of X-ray events. The X-ray events use the solar abundance values from Anders & Grevesse (1989). The events are generated by assuming a telescope with an energy-independent collecting area of 1000 cm^2 and an exposure time of 1000 ks. The photon list is generated in the observed frame of the X-ray emitting gas cells and is corrected to rest frame energies. Finally, the photons generated by the gas cells are projected onto the sky.

We obtain X-ray radial surface brightness profiles in the 0.5 − 2.0 keV band for all galaxies. Given that SUBFIND provides us with an accurate classification of galaxies into centrals and satellites, we separate the hot gas component into X-ray emission around centrals and satellites. For central galaxies, the profiles represent the hot gas emission around them; however, for satellite galaxies, the profiles mostly probe the hot gas emission of the more massive host halo in the vicinity.

We convolve the individual X-ray surface brightness profiles from LC-TNG300-based mock galaxies catalogues with the eROSITA PSF (Merloni et al., 2024). The PSF convolved mean X-ray surface brightness profile from hot gas, $\mathbf{S}_{\rm X,\ hot\ gas}[r]$, is expressed as follows.

$$\mathbf{S}_{\rm X,\ hot\ gas}(r) = f_{\rm cen}\, S_{\rm X,\ cen} + \mathcal{N}_{\rm sat} \times f_{\rm sat}\, S_{\rm X,\ sat}, \tag{3.3}$$

where $S_{\rm X,\ cen}$ is the TNG-based prediction for the hot gas around central galaxies and $S_{\rm X,\ sat}$ corresponds to the hot gas around satellites. After matching LC-TNG300 with Full$_{\rm phot}$ in stellar mass and redshift, the mock galaxy catalogues fix the fraction of centrals, $f_{\rm cen}$, and satellites, $f_{\rm sat}$. $\mathcal{N}_{\rm sat}$ is the factor by which the mock prediction from $S_{\rm X,\ sat}$ is rescaled to match the observations, thereby renormalizes the $S_{\rm X,\ sat}$ of the TNG300-based prediction; $\mathcal{N}_{\rm sat}$ is the only free parameter in the hot gas emission component.

The motivation behind introducing the renormalization parameter, $\mathcal{N}_{\rm sat}$, for fitting the forward model prediction for $S_{\rm X,\ sat}$ with observations is as follows. The TNG-based prediction for $S_{\rm X,\ sat}$ from the mock catalogues (for a given $f_{\rm sat}$) is $\sim 5 - 7\times$ brighter than the Full$_{\rm phot}$ stack. Chapt. 2 and accompanying paper Shreeram et al. (2025c) find that the shape of the X-ray radial surface brightness profile from satellite galaxies (hosted by massive halos) is unaffected by $f_{\rm sat}$ in the galaxy sample. This is because the halo masses making up the average profile from satellite galaxies, whose $M_{\star} \in 10^{10.5-11}$ M$_{\odot}$, are dominated by host (central) halos with mean $M_{\rm 200m} \sim 10^{14}$ M$_{\odot}$. Therefore, by changing the normalization of the $S_{\rm X,\ sat}$, we effectively damp the normalization of the X-ray thermal gas contribution from the most massive clusters in the simulation. This is justified given that the hot gas fraction from TNG is overpredicted at halo masses above $M_{\rm 500c} \gtrsim 10^{13.5}$ M$_{\odot}$, as shown in Fig. 6 in Popesso et al. (2024b). This is also reflected in the $L_{\rm X} - M_{\rm 500c}$ relation shown in Zhang et al. (2024b) and Popesso et al. (2024c).

We emphasize that the X-ray surface brightness profile prediction from central galaxies, $S_{\rm X,\ cen}$, which represents the CGM physics of interest in this work, is untouched. We predict

[3]APEC link https://heasarc.gsfc.nasa.gov/xanadu/xspec/manual/node134.html

Table 3.1: Summary of the best-fit parameters (see Eq. 3.1-3.3) and derived quantities (luminosity values) obtained from fitting the three forward models from this work to the $\text{Full}_{\text{phot}}$ X-ray surface brightness profile. For every model, we present the best-fit $\mathcal{N}_{\text{sat}}$: renormalization of the $S_{\text{X, sat}}$ (of the TNG300-based prediction), f_{sat}: the fraction of satellites in the mock galaxy catalogue (see descriptions of the mock catalogues in Sec. 3.4.3), $\mathcal{N}_{\text{ps}}$: the normalization of the point-source component (see Eq. 3.2), $L_{X,\text{ PS}}$: the X-ray luminosity obtained by integrating the point source component, $L_{X,\text{ cenCGM}}$: the X-ray luminosity obtained by integrating the central galaxies hot CGM component, χ^2_{red}: the reduced χ^2 statistic for the model, obtained by using $21-2$ degrees of freedom.

	Best-fit $\mathcal{N}_{\text{sat}}$ $[10^{34}\ \frac{\text{ergs}}{\text{s kpc}^2}]$	f_{sat}	Best-fit $\mathcal{N}_{\text{ps}}$ $\frac{\text{ergs}}{\text{s kpc}^2}$	$L_{X,\text{ PS}}$ [ergs/s]	$L_{X,\text{ cenCGM}}$ [ergs/s]	χ^2_{red}
Model 1	$2.75^{+0.12}_{-0.12}$	0.31	$7.6^{+2.2}_{-1.6} \times 10^{36}$	$7.851^{+0.028}_{-0.274} \times 10^{39}$	$6.58^{+0.27}_{-0.94} \times 10^{40}$	0.44
Model 2	$2.95^{+0.14}_{-0.13}$	0.33	$1.1^{+0.2}_{-0.2} \times 10^{37}$	$1.195^{+0.003}_{-0.042} \times 10^{40}$	$2.76^{+0.06}_{-0.19} \times 10^{40}$	1.32
Model 3	$1.51^{+0.07}_{-0.073}$	0.56	$1.5^{+0.2}_{-0.2} \times 10^{37}$	$1.576^{+0.001}_{-0.063} \times 10^{40}$	$1.69^{+0.28}_{-0.91} \times 10^{40}$	1.89

multiple CGM profiles by changing the host halo mass distribution of the central galaxies and propagating it through our pipeline to generate mock galaxy catalogues for each halo distribution considered, as detailed in the following section. Note that the stellar mass and redshift distributions are the same for all three models.

We restrict our analysis to the MW-mass stellar bin due to both observational and modelling constraints. While comparisons across a broader stellar mass range are desirable, for lower-mass galaxies, there are currently no suitable X-ray stacking data available. For higher-mass galaxies, the existing stacked X-ray measurements (e.g., from Z24) extend to redshifts beyond the coverage of our lightcone. Extending the analysis to these massive galaxies would require constructing a new lightcone from a larger-volume simulation (e.g., FLAMINGO, MTNG), generating matched mock X-ray observations, and repeating the full forward-modelling pipeline introduced here, an effort that warrants a future study. In contrast, the MW-mass bin provides observational data within the redshift range of LC-TNG300, making it the optimal case for robust model–data comparison and the hot CGM signal retrieval.

3.4.3 Mock galaxy catalogues

We now use the LC-TNG300 galaxy catalogue to construct a mock galaxy sample for the LS DR9 $\text{Full}_{\text{phot}}$ galaxies. We match every one of the $415,627$ galaxies in the $\text{Full}_{\text{phot}}$ sample with a galaxy from LC-TNG300 in redshift and stellar mass. By construction, the simulated LC-TNG300 galaxies follow the same stellar mass and redshift distribution as the observational sample. The mock sample predicts the mean X-ray surface brightness profile for gas emitted around centrals and satellites.

In this work, we also test the impact of the underlying halo mass distribution on the CGM physics. Therefore, we additionally generate two other mock galaxy catalogues using LC-TNG300, matched in stellar mass and redshift, however, with different underlying halo mass distributions (see left panel of Fig. 3.1). Consequently, we also emulate the corresponding X-ray surface brightness profiles by varying the halo distributions (see right panel of Fig. 3.1). The differences between the three forward models are as follows:

- Model 1 leaves LC-TNG300 halo mass distribution unchanged (purple line in Fig. 3.2), resulting in a mean halo mass of $M_{200m} = 6.5 \times 10^{12} \mathrm{M}_{\odot}$.
- Model 2 changes the underlying central galaxy halo distribution by excluding the 10% most massive (central) halos from the original LC-TNG300 halo mass distribution (pink line in Fig. 3.1). This results in a mean halo mass of $M_{200m} = 5.4 \times 10^{12} \mathrm{M}_{\odot}$.
- Model 3 changes the underlying halo distribution by excluding the 30% most massive (central) halos from the original LC-TNG300 halo mass distribution (yellow line in Fig. 3.1). This results in a mean halo mass of $M_{200m} = 3.5 \times 10^{12} \mathrm{M}_{\odot}$.

By changing the underlying halo mass distributions for the fixed stellar mass bins, we are effectively altering the mean halo mass of our mock galaxy catalogue. We note that for model 3, the resulting mean halo mass lies within the range predicted by various observational and empirical works that constrain the stellar-to-halo-mass relation (SHMR) at low redshift. For the mean stellar mass of our three mock samples ($M_{\star} = 5.5 \times 10^{10}$ M$_{\odot}$), studies typically find $M_{\rm halo} \sim 5 \times 10^{11}$ M$_{\odot}$ (Taylor et al., 2020) to 1–3 $\times 10^{12}$ M$_{\odot}$ (Leauthaud et al., 2012; Coupon et al., 2015; Girelli et al., 2020; Behroozi et al., 2019). Importantly, different simulations predict different SHMRs (see e.g., Wright et al. 2024), and this variation can introduce systematic biases when comparing predicted CGM emission at fixed stellar mass. If the simulated halo mass distribution does not accurately reflect that of the observational sample, the predicted X-ray signal may be systematically over- or under-estimated. For instance, using a simulation that associates higher halo masses at fixed stellar mass than the true sample would yield artificially elevated CGM emission predictions, potentially leading to an erroneous conclusion about a simulation–observation mismatch. This underscores the motivation for our approach: rather than adopting a single SMHR, we forward-model the halo mass distribution consistently with the data, using observational constraints (further discussed in Sec. 3.5.1-3.5.3). Our framework thus enables posterior constraints on the halo mass distribution associated with the Full$_{\rm phot}$ dataset, based on the TNG-informed models developed in this work. Given the large scatter in halo mass at fixed stellar mass (e.g., Moster et al., 2020), and the strong dependence of CGM surface brightness profiles on this distribution (see right panel of Fig. 3.1), a rigorous treatment of halo demographics is essential for robust comparisons between simulations and stacked X-ray observations.

3.5 Results and discussion

We fit the data from Z24 with our three forward models, which contain the hot gas component and the point source component, as shown in Eq. 3.1-3.3. The three models emulate different X-ray surface brightness profiles for different halo mass distributions (Sec. 3.4.3 and Fig. 3.1). We implement Markov Chain Monte Carlo (Hastings, 1970, MCMC) to determine the posterior probability distributions of the two free parameters of our models: $\mathcal{N}_{\rm sat}$, and $\mathcal{N}_{\rm ps}$. The latter is obtained using the Affine-Invariant Ensemble Sampler algorithm in `emcee` (Foreman-Mackey et al., 2013). We assume a Gaussian likelihood function and uniform priors on $\mathcal{N}_{\rm sat} \in (0.005, 1000) \times 10^{35}$,

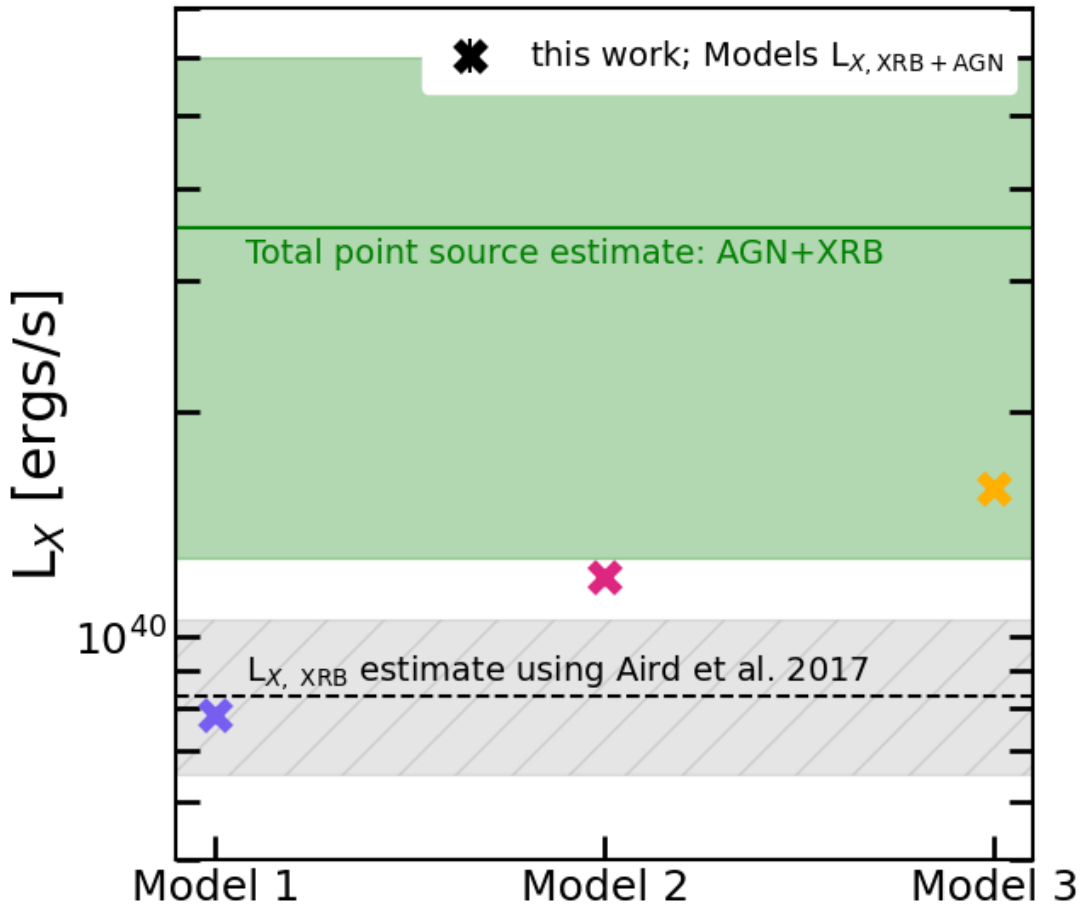

Figure 3.2: Comparison of the mean point source (AGN and XRB) luminosities from our three forward models (crosses, based on the different halo distributions shown in Fig. 3.1) with the empirically allowed range of XRB and total point source luminosities, shown as the grey hatched region and the green shaded region, respectively. We estimate the contribution due to XRB emission using the Aird et al. (2017) model. For estimating the AGN luminosity budget, $L_{X,\,\mathrm{AGN}}$, we use the Aird et al. (2013) model for the incidence rate distribution as a function of the $L_{X,\,\mathrm{AGN}}^{2-10\,\mathrm{keV}}$ keV. To convert the $2-10$ keV luminosity distribution to the $0.5-2$ keV band, we use an empirical obscuration model from Comparat et al. (2019). For more details, see the text of Sec. 3.5.1 and 3.5.2. This comparison favours model 3, shown by the yellow cross, where the hot CGM component allows for a point source component with luminosity that agrees with empirical estimates from the low redshift universe.

and $\mathcal{N}_{\mathrm{ps}} \in (0.5,\ 550) \times 10^{35}\mathrm{erg\ s^{-1}\ kpc^{-2}}$. For the three forward models constructed in this work, we show the most likely values of the free parameters in Tab. 3.1. We compute the luminosities from the hot gas around centrals, satellites and point sources within R_{500c}. Fig. 3.2 shows the mean point source luminosities we obtain for the three models implemented in this work (purple, pink, and yellow crosses). We compare our results with independent predictions of the expected luminosity from XRB and AGN around MW-mass galaxies using current empirical models in the literature. Sec. 3.5.1 and Sec. 3.5.2 describe how we obtain these estimates shown in Fig. 3.2

for the expected luminosity from XRB and AGN around MW-mass galaxies.

3.5.1 Predicting the X-ray emission from XRB

The XRB component is divided into High-mass X-ray Binaries (HXRB) and Low-mass X-ray Binaries (LXRB); see review by Fabbiano (2006). The average XRB emission from a normal galaxy is characterized by scaling laws, where the former HXRB population scales with the recent star formation rate (SFR) in the galaxy (Grimm et al., 2003; Shtykovskiy & Gilfanov, 2005; Mineo et al., 2012). In contrast, LXRB emission spans longer timescales, tracing the stellar mass of the galaxy (Gilfanov, 2004; Boroson et al., 2011; Zhang et al., 2012; Lehmer et al., 2019). The total XRB emission from extragalactic objects is distributed on the scale of the stellar body; however, for an instrument with a 30 arcsec PSF like eROSITA, it is effectively unresolved and appears as a point source. Aird et al. (2017) and Lehmer et al. (2016) provide simple empirical recipes by parameterizing the total X-ray luminosity from XRB as a function of both the SFR and stellar mass, $M_\star$, of the galaxy,

$$L_{X,\,\mathrm{XRB}} = L_{X,\,\mathrm{LXRB}} + L_{X,\,\mathrm{HXRB}} = \alpha(1+z)^{\gamma} M_\star + \beta(1+z)^{\delta}\mathrm{SFR}^{\theta}, \tag{3.4}$$

where α, β, γ, δ, and θ are fitting constants. Aird et al. (2017) report the following best-fitting values: $\log\alpha = 28.81 \pm 0.08$, $\gamma = 3.90 \pm 0.36$, $\log\beta = 39.50 \pm 0.06$, $\delta = 0.67 \pm 0.31$ and $\theta = 0.86 \pm 0.05$.

We quantify the contribution of the total $L_{X,\,\mathrm{XRB}}$ in the LS DR9 $\mathrm{Full_{phot}}$ galaxy catalogue using the model from Aird et al. (2017). Since we will later use these estimates to inform our forward models for the allowed range of point source luminosities, we adopt a TNG-independent method to predict $L_{X,\,\mathrm{XRB}}$ unbiasedly (other reasons for not using TNG also detailed in Sec. 3.4.1). We use UCHUU, a suite of ultra-large cosmological N-body simulations (Ishiyama et al., 2021), with the galaxy catalogue from UNIVERSEMACHINE (Behroozi et al., 2019) to construct a mock for the $\mathrm{Full_{phot}}$ galaxy sample. The SFRs from UNIVERSEMACHINE are calibrated to reproduce observations. We use the half-sky lightcone, constructed in the procedure as detailed in Comparat et al. (2020), for building the mock galaxy catalogue. The mocks are generated similarly to Z24, ensuring the galaxy stellar mass function of the LS DR9 $\mathrm{Full_{phot}}$ galaxy catalogue is reproduced. Therefore, they can be reliably used for the purpose of this study. We apply Eq. 3.4 on the mocks to estimate the contribution of XRB in the galaxy stack, given the stellar masses and SFR of the mock galaxies. With these ingredients, we predict that the contribution from XRB alone to be $L_{X,\,\mathrm{XRB}} = (8.2^{+2.2}_{-1.7}) \times 10^{39}$ ergs s-1, represented by the grey hatched region in Fig. 3.2[4].

[4]We note that the X-ray scaling relation from Lehmer et al. (2019) predicts $L_{X,\mathrm{XRB}} = (5.1^{+1.6}_{-0.9}) \times 10^{39}$ erg/s for the $\mathrm{Full_{phot}}$ galaxy catalogue. Nevertheless, the predictions from using the Aird et al. (2017) and Lehmer et al. (2019) scaling relations are consistent with each other, and we have verified that adopting the Lehmer relation would not change our conclusions.

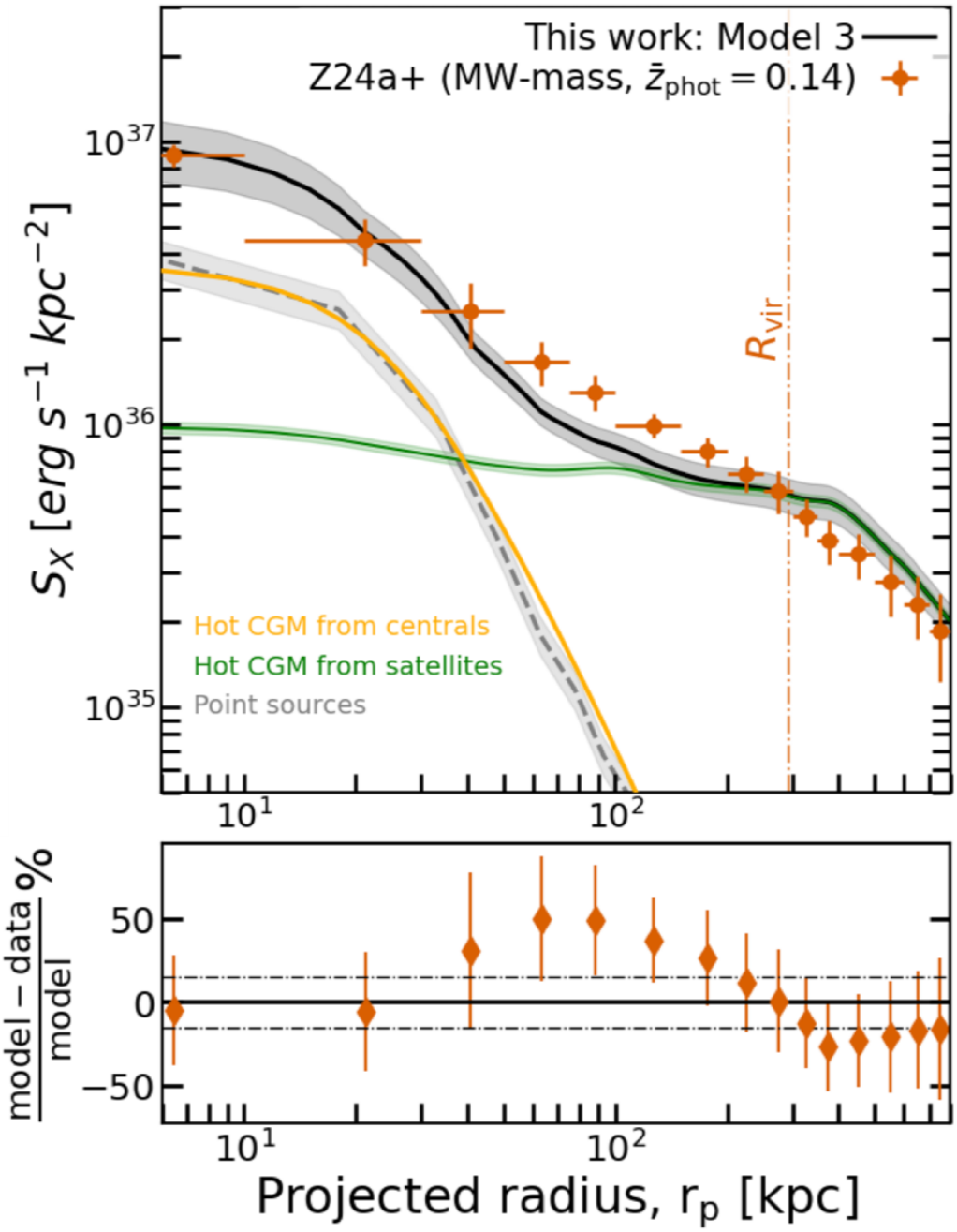

Figure 3.3: Decomposition of the X-ray stack of the galaxies in the photometric sample, $\text{Full}_{\text{phot}}$, into contributions from hot gas (centrals and satellites hosted by more massive host halos) and point sources (AGN and XRB). The orange data points from Z24 are described with the model from this work (shown by the black solid line). The orange dashed-dotted line at 292 kpc corresponds to the virial radius of the observational sample. The model is composed of the following: the hot CGM from central galaxies (yellow), the events around satellites probing the hot gas of their more massive host halos (green), and X-ray events from unresolved and resolved point-like sources comprising AGN and XRB (grey). The bottom panel shows the percentage deviation of the best-fit forward model from the data. The dashed-dotted lines show the 15% level.

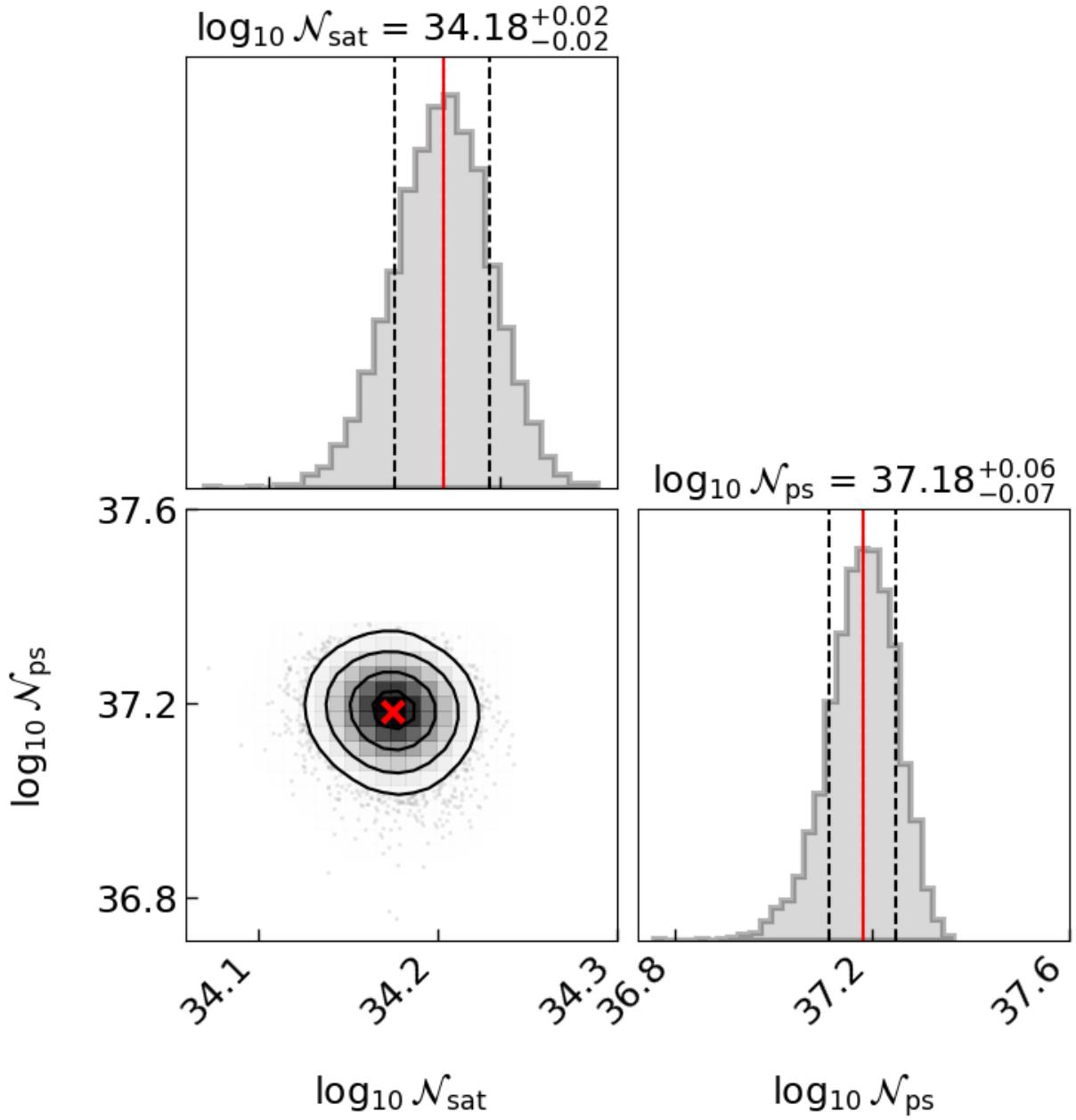

Figure 3.4: Posterior probability distributions of the renormalization factor of the $S_{\rm X,\ sat}$ profile: $\mathcal{N}_{\rm sat}$, and the normalization of the point source component: $\mathcal{N}_{\rm ps}$, which are obtained by fitting the forward-model 3 from this work to the $\rm Full_{phot}$ data points from Z24 shown in Fig. 3.3. The vertical red lines in the diagonal plots correspond to the most likely value; the respective values are shown in the titles (refer to Tab. 3.1). The black dashed lines are the 68% confidence interval of the marginalized distribution of the free parameters. The contour plot marks the most likely values with the red cross, and the contours correspond to the 68%, 95% and 99.7% confidence intervals.

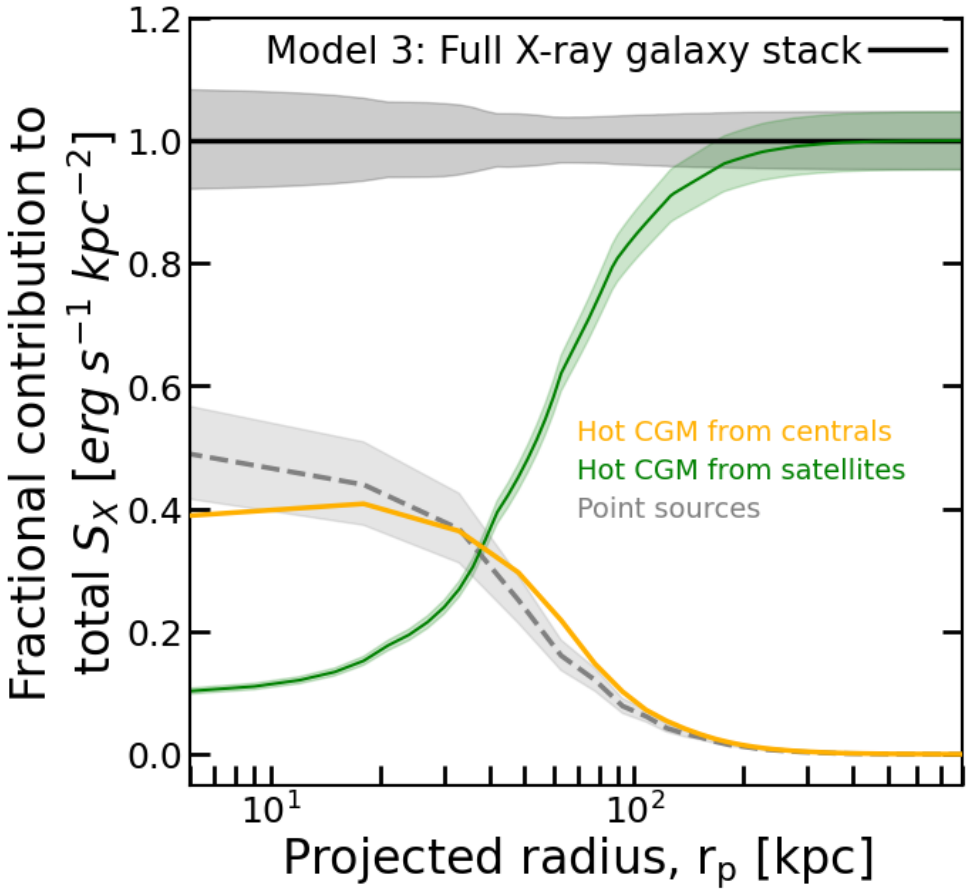

Figure 3.5: The fractional contribution to the total X-ray surface brightness profile of the hot CGM from central galaxies (yellow), the events around satellites arising mainly from the hot gas of their more massive host halos (green), and X-ray events from unresolved and resolved point-like sources comprising AGN and XRB (dashed grey line). The errors on the profiles are obtained from the posterior distributions of the MCMC fitting analysis.

3.5.2 Predicting the expected $L_{X,\ \mathrm{AGN}}$ for MW-mass galaxies using an empirical model for the low-redshift universe

X-ray emission from AGN originates around an accreting supermassive black hole (see Brandt & Alexander 2015 for a review), appearing as a point-like X-ray source with eROSITA.

We to use the empirical model from Aird et al. (2013, hereafter A13) to estimate the $L_{X,\ \mathrm{AGN}}$ for a mean stellar mass $M_\star = 10^{10.7}\ \mathrm{M}_\odot$. A13 provide a model for the probability of a galaxy hosting an AGN for a given stellar mass, $M_\star$, and redshift, z as a function of the specific black hole accretion rate, λ [erg s^{-1} $\mathrm{M}_\odot^{-1}$]; also called the incidence rate distribution, $\mathcal{P}(\lambda \mid M_\star, z)$. The specific accretion rate, λ, of an AGN is the ratio of $L_{\mathrm{bol}}/M_{\mathrm{M}_\odot}$, where L_{bol} is the bolometric luminosity. The model C from A13 successfully predicts the XLF and its evolution at $0.2 < z <$

1.0. The specific accretion rate, λ, is related to the X-ray luminosity,

$$L_{X,\,\mathrm{AGN}}^{2-10\ \mathrm{keV}} = \frac{1}{25}\lambda \times 1.26 \times 10^{38} \times 0.002\ M_\star\ [\mathrm{ergs\ s^{-1}}], \tag{3.5}$$

where the $0.002\ M_\star$ factor represents the mass of the black hole, $M_\bullet$, and assumes correlation between $M_\bullet$ and the mass of the bulge, M_{bulge} (Marconi & Hunt, 2003). Additionally, we also assume $M_\star \approx M_{\mathrm{bulge}}$ (A13). For the mean of our $\mathrm{Full_{phot}}$, $M_\star = 10^{10.7}\ \mathrm{M_\odot}$ and at the median redshift, $\langle z \rangle = 0.14$, we obtain the incidence rate distribution, $\mathcal{P}(\lambda \mid L_X,\ M_\star, z)$, as a function of $L_{X,\,\mathrm{AGN}}^{2-10\ \mathrm{keV}}$ using Eq. 3.5. To obtain the $0.5-2$ keV mean observed X-ray luminosity, which is required to compare with the estimate from this work, we further need to convert the incidence rate distribution from $L_{X,\,\mathrm{AGN}}^{2-10\ \mathrm{keV}}$ to $L_{X,\,\mathrm{AGN}}^{0.5-2\ \mathrm{keV}}$.

An important factor that comes into play when performing a conversion from $2-10$ keV (Hard X-ray band; HXB) to the $0.5-2$ keV (Soft X-ray Band; SXB) luminosity is the intrinsic obscuration of the AGN. Our estimate of $L_{X,\,\mathrm{AGN}}$ represents the contribution from the obscured AGN and the observed unobscured Type 1 AGN, the dominating component in the energy range under concern (see e.g. Hasinger 2008). We use the Comparat et al. (2019) empirical obscuration model to obtain the observed HXB to SXB luminosity conversion; they self-consistently build an obscuration model based on observational work (Ricci et al., 2017; Buchner & Bauer, 2017; Ueda et al., 2014; Aird et al., 2015; Buchner et al., 2015). The Comparat et al. (2019) model is implemented on the UCHUU simulations (introduced in Sec. 3.5.1), and we obtain the HXB to SXB conversion as a function of $L_{X,\,\mathrm{AGN}}^{2-10\ \mathrm{keV}}$. Finally, we obtain the desired A13-based $\mathcal{P}(\lambda \mid L_X,\ M_\star, z)$ distribution as a function of the $L_{X,\,\mathrm{AGN}}^{0.5-2\ \mathrm{keV}}$. The expectation value is obtained as follows: $\langle L_{X,\,\mathrm{AGN}}^{0.5-2\ \mathrm{keV}} \rangle = \int \mathcal{P}(\lambda \mid L_X,\ M_\star, z) L_{X,\,\mathrm{AGN}}^{0.5-2\ \mathrm{keV}} d\lambda$.

An additional consideration is that the optical sample used for X-ray stacking in Z24 excludes objects classified as point sources in the optical. This effectively excludes optically bright quasars, where point-like emission strongly dominates over the host galaxy contribution. An open question is how such optical selection criteria for AGN modify the X-ray luminosity distribution in X-rays, and addressing this is beyond the scope of this work. Nonetheless, we compute a conservative X-ray luminosity threshold to account for this exclusion of optical quasars as follows. We convert the optical r-band luminosity distribution of the $\mathrm{Full_{phot}}$ galaxy sample to the $2-10$ keV luminosity distribution using a bolometric correction factor of 2.5 (Collin et al., 2002; Duras et al., 2020; Buchner et al., 2024). We use $10\times$ the mean of the HXB luminosity distribution as the threshold above which the object is classified as a bright point source in the optical LS DR9 catalogue. This conservative limit excludes objects with $L_{X,\,\mathrm{AGN}}^{2-10\ \mathrm{keV}} > 8 \times 10^{43}$ ergs s^{-1}. We adopt this cut in the $\mathcal{P}(\lambda \mid L_X,\ M_\star, z)$ distribution as a function of the $L_{X,\,\mathrm{AGN}}^{2-10\ \mathrm{keV}}$ from A13. After applying the obscuration model from Comparat et al. (2019), we obtain $\langle L_{X,\,\mathrm{AGN}}^{0.5-2\ \mathrm{keV}} \rangle = 2.7^{+2.2}_{-2.0} \times 10^{40}$ ergs s^{-1}. The sum of $L_{X,\,\mathrm{AGN}}$ computed here and $L_{X,\,\mathrm{XRB}}$ computed in the previous Sec. 3.5.1 is represented with the green shaded region in Fig. 3.2.

The large error bars on our estimate of $L_{X,\,\mathrm{AGN}}$ using the methodology described here are due to the uncertainties in the empirical obscuration model and the uncertainties in the incidence rate distribution, which is poorly constrained for the low-redshift universe. The estimates here can be further improved with future work that strengthens the connection between the low luminosity X-

ray AGN population and the host galaxy properties, proper knowledge mapping AGN selection functions from optical to X-ray luminosities, and better constrained obscuration models.

3.5.3 Using Model 3 for interpreting the $\text{Full}_{\text{phot}}$ data

In the light of the empirical estimates we obtain from Sec. 3.5.1 and 3.5.2, we compare the prediction for point source luminosities from our three forward models (based on the different halo distribution shown in Fig. 3.1) with the empirically constrained range of point source luminosities as shown in Fig. 3.2. This comparison favours model three, which has a mean $M_{200\text{m}} = 3.5 \times 10^{12}$ $\text{M}_\odot$, for which the hot CGM component allows for a point source component with a luminosity that agrees with empirical estimates from the low redshift universe. We focus our results on model three for all the following discussions of the hot CGM.

The results of fitting model 3 to the X-ray surface brightness profile obtained by stacking on the $\text{Full}_{\text{phot}}$ galaxies is shown in Fig. 3.3, with the posterior distribution of the best-fit parameters shown in Fig. 3.4.

3.5.4 X-ray emission from the hot CGM

The contribution of the hot CGM component from central galaxies is shown with the yellow line in Fig. 3.3 for forward-model 3. By integrating the area under the mean X-ray surface brightness profile from the central galaxy hot CGM component within R_{500c}, we obtain an X-ray luminosity, $L_{X,\,\text{CGM}} = 1.69^{+0.28}_{-0.91} \times 10^{40}$ ergs s-1. We also show the residual plot of the per cent deviation of the data from our model, where the discrepancies are within 15%.

We show the fractional contribution of the various emission components in our forward model 3 to the mean X-ray surface brightness profile upon stacking galaxies in Fig. 3.5. We note that at mean redshifts of 0.14 and the underlying halo mass distribution for model 3, the hot CGM is unresolved with an eROSITA-like PSF. At $\lesssim 40$ kpc, the hot CGM from central galaxies and the X-ray point sources emission from XRB and AGN each account for up to $40 - 50\%$ of the total X-ray emission budget, respectively.

We compare our results with the other hot CGM measurements presented in Z24, based on a different optical galaxy catalogue, namely from the SDSS spectroscopic survey. Given the spectroscopic optical information, the galaxy sample is classified into centrals and satellites (Tinker, 2021), which makes it possible to empirically model the hot CGM profile from other contaminating effects (point sources and satellites). They selected 30, 825 central galaxies with spectroscopic redshifts < 0.2 and MW-like stellar masses of $10.5 < \log(M_\star/\text{M}_\odot) < 11$. In Z24, this SDSS-based spectroscopic sample is called the CEN sample. The resulting profile, as shown by the data points in Fig. 3.6, is compared with the hot CGM component (model 3) we obtain here (solid yellow line). Our TNG-based forward model of the hot CGM prediction is in excellent agreement with the hot CGM measurement from Z24 at $\gtrsim 60$ kpc. At the inner radii ($\lesssim 60$ kpc), our TNG-based model 3 overpredicts the X-ray emission. We note that the halo mass distributions of the two samples have similar mean values, where the mean $M_{200\text{m}} = 3.5{\times}10^{12}$ $\text{M}_\odot$ for our forward model 3 and the mean $M^{\text{CEN}}_{200\text{m}} \sim 3{\times}10^{12}$ $\text{M}_\odot$. However, the median $M^{\text{CEN}}_{200\text{m}} \sim 1.3{\times}10^{12}$ $\text{M}_\odot$,

highlighting the spread in the halo mass distribution. This result further emphasizes the importance of the underlying halo mass distribution and the impact of the halo mass scatter introduced in stellar-mass selections when comparing hot CGM profiles across different observations and simulation-based models. For reference, we also show the forward models 1 and 2, which we exclude because their hot CGM component does not allow for a sufficient contribution of point source luminosity in the X-ray galaxy stack (see Sec. 3.5.3). In addition to this shortcoming, we find that models 1 and 2 are discrepant with the CEN sample measurement of the hot CGM, further favouring model 3.

3.5.5 X-ray emission from satellite's host halos

At larger radii ($\gtrsim$ 40 kpc), the contribution from the emission around satellites dominates the total X-ray signal, thereby explaining the flattening observed in the measurements, as also found by Comparat et al. (2025). This emission originates from the massive host halos in which the satellite galaxies reside; we find the mean host halo mass of these satellites to be $M_{200\mathrm{m}} \sim 10^{14}$ M$_\odot$. We emphasize that this component is not intended to probe the intrinsic CGM of the satellites themselves, but rather captures the background X-ray emission associated with their host halos. Since the Full$_{\mathrm{phot}}$ galaxy catalogue includes both central and satellite galaxies without classification, any observational stacking analysis based on such samples unavoidably includes this contribution. We quantify the X-ray luminosity from satellite host halos as $L_{X,\,\mathrm{SAT}} = 3^{+3}_{-2} \times 10^{41}$ erg/s, obtained by integrating the area under the predicted surface brightness profile $S_{\mathrm{X,\,sat}}$. Interestingly, Zhang et al. (2018) also find an inflection point at $\sim$ 50 kpc due to the satellite's host halos in the stacked Hα+N[II] radial emission profile (see Fig. 8 therein), which traces the cool component of the CGM. The findings from Zhang et al. (2018) on the cool CGM is complementary to our results presented here on forward-modelling the hot CGM probed by X-ray stacking.

Upon fitting our forward model to the Full$_{\mathrm{phot}}$ stack, we introduce a renormalization parameter, $\mathcal{N}_{\mathrm{sat}}$, which rescales the $S_{\mathrm{X,\,sat}}$ contribution to match the observations. This scaling is necessary due to the known overprediction of hot gas fractions in TNG300 for halos above $10^{13.5}$ M$_\odot$ (Popesso et al., 2024b), leading to an overly bright $S_{\mathrm{X,\,sat}}$ component (see Sec. 3.4.2). Importantly, the shape of this satellite-related emission component is independent of the satellite fraction, as demonstrated in Fig. 2.7, 2.8, and 2.9 in Chapt. 2. From our fitting analysis for model 3, we find that the TNG-based fiducial $S_{\mathrm{X,\,sat}}$ normalisation of the hot CGM must be rescaled by 0.15 to provide an observationally consistent contribution for the Full$_{\mathrm{phot}}$ galaxy catalogue based X-ray stack. We highlight that this renormalisation does not affect the hot CGM contribution from centrals, which remains unchanged. Therefore, $\mathcal{N}_{\mathrm{sat}}$ effectively provides a quantitative correction factor, illustrating how the overabundance of hot gas in massive halos biases the observable MW-mass stacked X-ray profiles. We conclude that the inclusion and forward-modelling of the satellite's host halo component is crucial to physically interpret the Full$_{\mathrm{phot}}$ data.

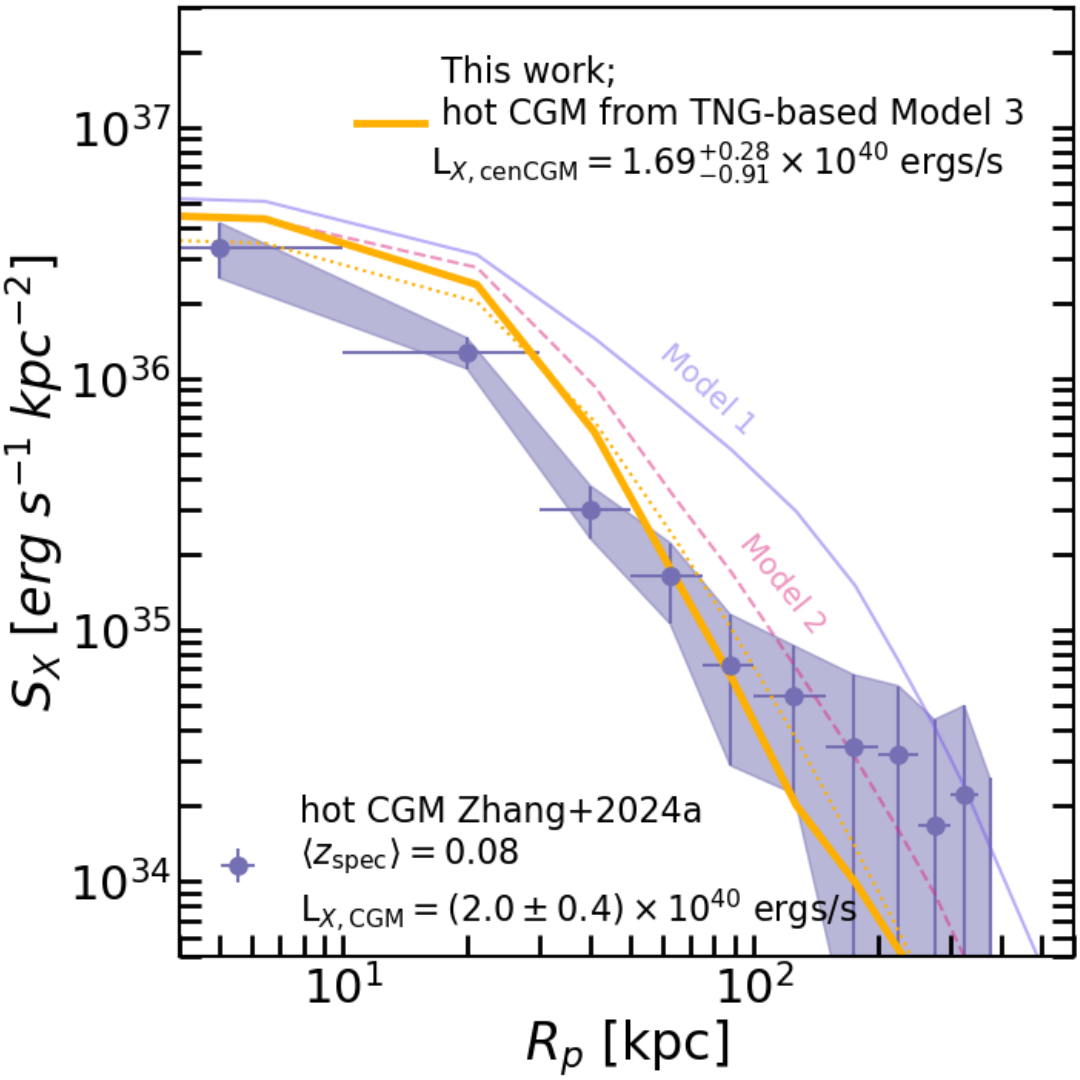

Figure 3.6: Comparison of the hot gas CGM profile from our TNG-based model 3 (solid yellow line) with the hot CGM measurement from Z24 based on X-ray stacking at the optical positions of galaxies from the SDSS spectroscopic galaxy catalogue (CEN sample). The CEN sample has a mean redshift $\langle z_{\mathrm{spec}} \rangle = 0.08$, which is lower than that for the $\mathrm{Full_{phot}}$ galaxy sample, $\langle z_{\mathrm{phot}} \rangle = 0.14$, modelled here. Therefore, our models (solid yellow, dashed pink, and solid purple) are convolved with the eROSITA PSF representing $z = 0.08$ to enable comparison with the CEN sample profile from Z24. Our $\mathrm{Full_{phot}}$-based model 3 convolved with the $\langle z_{\mathrm{phot}} \rangle = 0.14$ PSF in shown by the dotted-yellow line. For reference, we also show the other two models, 1 and 2, with different underlying halo distributions (see text in Sec. 3.4.3), which we excluded in this work (see Fig. 3.2) as the hot CGM component did not allow for a point source component with a luminosity consistent with empirical estimates from the low redshift universe. Our model 3 is in good agreement with the CEN sample hot CGM profile from Z24.

3.6 Conclusions

In this work, we forward model the measurements of the X-ray surface brightness profiles obtained by stacking at the optical galaxy positions of the LS DR9 photometric ($\text{Full}_{\text{phot}}$) galaxy catalogue, reported by Z24. We retrieve the contribution of the hot CGM from central galaxies from that of point sources and satellite galaxies. Our hot CGM forward model is based on TNG300 hydrodynamical simulations. The main results are summarized as follows:

1. We test the impact of the underlying halo mass distribution on the TNG-based prediction for corresponding X-ray surface brightness profiles. We do so by generating multiple mock galaxy catalogues using the LC-TNG300, matched in stellar mass and redshift to the $\text{Full}_{\text{phot}}$ galaxy catalogue, however, with different underlying halo mass distributions (Sec. 3.4.3; Fig. 3.1). Namely, the three models obtained by varying the halo mass distribution are as follows: model 1 leaves LC-TNG300 halo mass distribution unchanged, models 2 and 3 change the underlying halo distribution by excluding the 10% and 30% most massive halos from the original LC-TNG300 halo mass distribution, respectively. We show that the shape and normalization of the hot CGM X-ray surface brightness profiles are impacted by varying the halo mass distributions, where discarding the most massive halos from the underlying halo distribution results in steeper profiles with lower normalization. More precisely, we find that a factor $\sim 2\times$ increase in the mean value of the underlying halo mass distribution results in $\sim 4\times$ increase in the X-ray luminosity from the hot CGM.

2. We fit for the stacked X-ray radial surface brightness profile observed by eROSITA around MW-mass galaxies from Zhang et al. (2024a) with our forward models. Our model contains two main emitting components (Eq. 3.1-3.3): hot gas (around central galaxies and around satellite galaxies hosted by more massive halos) and X-ray point sources (X-ray binaries and Active Galactic Nuclei). For three forward models, we compute the X-ray luminosity from point sources, $L_{X,\,\text{PS}}$, and the CGM (see results in Tab. 3.1). Using the empirical estimates for the expected luminosity from XRB (Sec. 3.5.1) and AGN (Sec. 3.5.2) for MW-mass galaxies, we put constraints on the permissible values of $L_{X,\,\text{PS}}$ contribution to the X-ray stack (see Fig. 3.1). This analysis favours model three, which has a mean $M_{200\text{m}} = 3.5 \times 10^{12}\ \text{M}_{\odot}$, implying that the hot CGM component allows for a point source component with a mean AGN luminosity that agrees with empirical estimates from the low redshift universe. We therefore focus on model three.

3. By integrating the area under the mean X-ray surface brightness profile from the central galaxy hot CGM component within R_{500c}, we obtain an X-ray luminosity, $L_{X,\,\text{CGM}} = 1.69^{+0.28}_{-0.91} \times 10^{40}$ ergs s-1. We also show the residual plot of the per cent deviation of the data from our model, where the discrepancies within the $50 - 105$ kpc range are within 15% (Fig. 3.3). We find that at $\lesssim 40$ kpc, the hot CGM from central galaxies and the X-ray point sources emission from XRB and AGN each account for $40 - 50\%$

of the total X-ray emission budget, respectively (Fig. 3.5). At larger radii > 40 kpc, the contribution from the emission around satellites dominates the total X-ray emission, thereby explaining the overall flattening in the measurements.

4. We compare our results with the hot CGM measurements presented in Z24, based on a different optical galaxy catalogue, namely from the SDSS spectroscopic survey (see comparison in Fig. 3.6). Our TNG-based forward model of the hot CGM prediction broadly agrees with the hot CGM measurement from Z24. The $L_{X,\,\mathrm{CGM}}$ measured between the two works are consistent. We note that the halo mass distributions of the two samples are similar mean values, where the mean $M_{200\mathrm{m}} = 3.5 \times 10^{12}$ $\mathrm{M}_{\odot}$ for our forward model 3 and the mean $M_{200\mathrm{m}}^{\mathrm{CEN}} \sim 3 \times 10^{12}$ $\mathrm{M}_{\odot}$. This result further emphasizes the importance of the underlying halo mass distribution when comparing hot CGM profiles across different observations and simulation-based models.

This work provides a novel technique to constrain the mean AGN X-ray luminosity of a galaxy sample jointly with the radial hot CGM gas distribution within the halo using the X-ray hot CGM (stacking) measurements as a new benchmark. Alongside the progress in our understanding of how various stellar and AGN feedback prescriptions impact the hot CGM's properties (Lau et al., 2024; Medlock et al., 2025), here, we emphasize another vital ingredient when comparing simulations with X-ray observations: the sensitivity of the X-ray CGM properties to the underlying halo mass distribution, stellar mass, and redshift. One of the outstanding challenges in the current paradigm of galaxy formation and evolution models implemented in hydrodynamical simulations is to jointly constrain the microscopic scales (e.g., subgrid model physics) and their impact on the diffuse gas within the halo (Crain & van de Voort, 2023). Future work implementing the data-comparison strategy developed here on other state-of-the-art simulations, like EAGLE (Crain et al., 2015; Schaye et al., 2015), FLAMINGO (Schaye et al., 2023b), Magneticum (Dolag et al., 2005; Beck et al., 2016), SIMBA (Davé et al., 2019), will provide observationally motivated ranges for the allowed X-ray AGN luminosity for the MW-mass scales. Comparing the AGN X-ray luminosity predictions retrieved from the methodology developed here (informed by hot CGM X-ray observations) with those predicted by the simulation itself will provide a new ground for recalibrating and improving the current landscape of sub-grid AGN modes (e.g., see Alexander & Hickox 2012 for a review). Additionally, future X-ray missions on the observation side, like Athena (Nandra et al., 2013), AXIS (Mushotzky et al., 2019), HUBS (Cui et al., 2020) will push our current detection limits to resolve the hot CGM at higher redshifts in X-rays. This would further our understanding of how observations compare to the spatially resolved hot gas distribution at MW-mass scales in simulations.

Chapter 4

Effect of the large-scale cosmic web environment on the X-ray emitting Circumgalactic medium

*The results presented in this chapter are submitted to A&A as "Effect of the large-scale cosmic web environment on the X-ray emitting Circumgalactic medium " **Shreeram, S.**, Galárraga-Espinosa, D., Comparat, J., Merloni, ...*

4.1 Summary

In this chapter, we bring together the main findings of this thesis and place them in the broader context of hot CGM studies. Building on the lightcone framework first developed in Chapt. 2, which was subsequently applied to forward model eROSITA data in Chapt. 3, we now explore the impact of the large-scale structure on the hot CGM in this chapter. These chapters put together collectively advance our ability to interpret stacked X-ray observations of the CGM. The results presented here demonstrate that accurate modelling of projection effects, contaminants, and environmental influences is essential to extract robust constraints on the hot CGM from current and future X-ray surveys.

This chapter studies the hot CGM in the context of the large-scale cosmic web, investigating how the galaxy's large-scale environment shapes its X-ray surface brightness (XSB) profiles and the implications for interpreting stacked observations. We use our novel IllustrisTNG-based lightcone, spanning $0.03 \leq z \leq 0.3$, first developed in Chapt. 2, to generate self-consistent mock X-ray observations, using intrinsic gas cell information. We apply the filament finder DisPerSE on the galaxy distributions to identify the cosmic filaments within the lightcone. We classify central galaxies into five distinct large-scale environment (LSE) categories: clusters and massive groups, cluster outskirts, filaments, filament-void transition regions, and voids/walls. We find that the X-ray surface brightness profiles (XSB) of central galaxies of dark matter haloes in filaments with $M_{200\mathrm{m}} > 10^{12}$ $\mathrm{M}_{\odot}$ are X-ray brighter than those in voids and walls, with $20-45\%$ deviations in the radial range of $(0.3 - 0.5) \times R_{200\mathrm{m}}$. We investigate the source of this enhancement and

find that the filament galaxies show higher average gas densities, temperatures, and metallicities compared to voids/walls galaxies. Our results demonstrate that the impact of the large-scale cosmic environment is imprinted on the hot CGM's X-ray emission. Future theoretical work on studying the effect of assembly history, connectivity, and gas accretion on galaxies in filaments and voids would help to further our understanding of the impact of the environment on X-ray observations.

4.2 Motivation for this work

Observational and theoretical studies show that galaxy properties, such as stellar mass, star formation rate, and gas content, vary across different LSE. The galaxies close to groups and clusters, which form the nodes of the cosmic web, are more likely to be elliptical, red, and have suppressed star formation, compared to their less crowded "field" counterparts that tend to be spiral, blue, and actively forming stars (Dressler, 1980; Butcher & Oemler, 1984; Dressler et al., 1997; Lewis et al., 2002; Blanton et al., 2005; Alpaslan et al., 2015; Pasquali & Nachname, 2015; Shimakawa et al., 2021). Additionally, galaxies infalling into clusters via cosmic filaments are systematically more quenched than their counterparts from other isotropic directions (see e.g. Martínez et al. 2016; Einasto et al. 2018; Salerno et al. 2019; Gouin et al. 2020). Simulations show that the gas within galaxies as far as within 3× virial radius (Cen et al., 2014; Arthur et al., 2019; Mostoghiu et al., 2021) to 5× the virial radius (Bahé et al., 2013) of the groups and clusters centre is gas-depleted compared to their counterparts in the field, as also consistently found by observations (e.g., Tanaka et al. 2004; Catinella et al. 2013; Cortese et al. 2011). Similar trends of higher gas depletion, higher quiescent fraction, and stellar mass also hold in observations of galaxies closer to the cosmic filament spines (Malavasi et al., 2017; Laigle et al., 2018; Sarron et al., 2019; Bonjean et al., 2020; Winkel et al., 2021; Hoosain et al., 2024).

As discussed in Chapt. 1, the hot CGM, which is the diffuse gas that surrounds galaxies, plays a crucial role in regulating the growth and evolution of the galaxy (see Tumlinson et al. 2017 and Faucher-Giguère & Oh 2023 for a review). The hot gas ($T \gtrsim 10^6$ K) reservoir hosted by the CGM is crucial for replenishing the cold gas consumed for star formation (Fox & Davé, 2017; Wang et al., 2022). The ability of the halos to retain or deplete their cold gas in an intrafilamentary environment has been shown to be correlated with the stellar mass in HI studies, see e.g., Kleiner et al. 2017; Odekon et al. 2018; Hoosain et al. 2024. From these HI studies, the emerging picture is that mass plays a crucial role in determining whether a galaxy can retain/further accrete gas from the cosmic web, or is more vulnerable to stripping and supply truncation. More massive galaxies ($M_\star > 10^{11}$ M$_\odot$) retain and accrete the gas from the surrounding filament due to their deeper gravitational potentials; however, the lower-mass ($M_\star < 10^{10.5}$ M$_\odot$) galaxies are more subject to gas-depleting processes like stripping and detachment. However, there is a lack of understanding of how the hot gas content around galaxies, as probed by the CGM, is impacted by their presence in filaments, voids, and nodes. At present, such an analysis is not feasible with existing X-ray and optical large-area datasets, but the framework developed here with simulations sets a precedent for future observational studies once suitable data become available. This motivates the need to explore how the hot CGM, as traced through X-ray emission, is affected

by the large-scale cosmic web environment.

In the ΛCDM Universe, the existence of the cosmic web follows from the initial fluctuations in the primordial density field, whose evolution is dictated by gravity in an expanding Universe. The anisotropic nature of gravitational collapse leads to the formation of high-density peaks that are the nodes that host today's galaxy clusters, and the expansive network of bridges between these nodes forms a large-scale web dominated by filaments, which demarcate the underdense voids (Peebles, 2020). The theoretical formulation of the existence and evolution of the cosmic web (Bond et al., 1996) has been confirmed by all large N-body simulations of structure formation in a ΛCDM Universe (e.g. Klypin & Shandarin 1983; Springel et al. 2006; Popping et al. 2009; Angulo et al. 2012; Habib et al. 2012; Poole et al. 2015). Similarly, advances in spectroscopic surveys, with increasing resolution and depth, have enabled observational mapping of the cosmic web, providing strong support for the presence of filaments, clusters, and voids. A unified approach to jointly study cosmic web, as traced by galaxies, is possible with exquisite detail up to redshift $z \approx 0.9$ with surveys such as the CfA Redshift Survey (De Lapparent et al., 1986), SDSS (York et al., 2000), 2dFGRS (Colless et al., 2001), 6dFGS (Jones et al., 2009), GAMA Driver et al. (2011), Vipers (Guzzo et al., 2014), 2MASS (Huchra et al., 2012) and COSMOS (Scoville et al., 2007). This is being further pushed to higher redshifts of about $z \approx 2$, close to the peak epoch of star formation with ongoing and upcoming stage-4 surveys such as Euclid (Laureijs et al., 2011), PFS (Takada et al., 2014), and 4MOST (De Jong et al., 2012).

Studies using simulations find that cosmic filaments dominate the mass budget of the Universe, occupying 50% of the total mass of the cosmic web, with mean overdensities $\delta \sim 10$ (Cautun et al., 2014), while the underdense voids, $\delta \sim -0.8$, are the most voluminous component of the cosmic web (Sheth & Van De Weygaert, 2004). Cui et al. (2018a) show that the gas component is the dominant tracer of baryonic matter in cosmic filaments, hosting the warm-hot intergalactic medium (WHIM) gas phase (Galárraga-Espinosa et al., 2021). The WHIM gas can be accreted onto the halos resulting in the denser circumgalactic medium (CGM) gas phase ($n_{\rm H} \gtrsim 10^{-4}$ cm^{-3}; see categorisation in Martizzi et al. 2019), and inversely, CGM gas around halos might be ejected due to feedback effects or undergo stripping due to ram-pressure inside filaments (Benítez-Llambay et al., 2013; Winkel et al., 2021). Liao & Gao (2019) show that up to 30% of the gas accreting onto galaxies residing in filaments is pre-processed, and they also have higher baryon fractions compared to the field galaxies (e.g., see also Singh et al. 2020). The CGM, as probed in X-rays, is thus an interesting avenue to test for these environment-driven gas processes.

In this work, we use an IllustrisTNG-based lightcone from Chapt. 2 and the accompanying paper Shreeram et al. (2025c), LC-TNGX, to study the impact of the LSE on the hot gas properties of galaxies. Isolating the impact of the LSE is complicated by the fact that various mechanisms, both gravitational and hydrodynamic, act simultaneously on galaxies. Particularly, local overdensity and galaxy hierarchy (central vs satellite) also impact galaxy properties (Pasquali & Nachname, 2015; O'Kane et al., 2024; Rodríguez-Medrano et al., 2024). The latter effect can be accounted for by separately studying central/satellite galaxy trends of galaxy properties (Yu et al., 2025). The former effect of local overdensity (or crowdedness of the environment) is related to different cosmic web environments having degeneracies between their local and global overdensities (Hahn et al., 2007; Cautun et al., 2014; O'Kane et al., 2024). As the local overden-

sity correlates with the halo mass function, where massive halos reside in high-density regions (Tinker et al., 2011; Wang et al., 2018; Wechsler & Tinker, 2018), in this chapter, we account for the local density effects by studying the impact of the LSE in halo mass bins. In this way, we can distinguish the effect of the stellar-to-halo-mass relation (SHMR) from that of the LSE (e.g, see Wechsler & Tinker 2018).

The chapter is organised as follows. We describe the LC-TNGX and how we self-consistently generate mock X-ray observations within the LC-TNGX, using the gas cell information in Sec. 4.3.1. We apply DisPerSe on the galaxy distribution to identify the cosmic filaments within LC-TNGX, as detailed in Sec. 4.3.2. We classify the central galaxies in different LSE: clusters and groups, galaxies in clusters and group outskirts, galaxies in filaments, galaxies in the filament-void transition region, and galaxies in voids and walls in Sec. 4.3.3. Sec. 4.4 presents the main results of this work on how the XSB profiles are affected by the physical processes in galaxies that depend on different LSE. We also present the thermodynamic properties that are the primary drivers of the X-ray emission in Sec. 4.5. Finally, we discuss our findings in Sec. 4.6 and report our conclusions in Sec. 4.7.

4.3 Methods

This section details the data products used for studying the impact of the LSE on the hot CGM. More precisely, Sec. 4.3.1 describes the TNG300 X-ray lightcone (LC-TNGX), Sec. 4.3.2 describes the filament catalogue obtained within the LC-TNGX using DisPerSE, and lastly, Sec. 4.3.3 describes the classifications of the LC-TNGX halos into their LSE categories.

4.3.1 The TNG300 X-ray lightcone: LC-TNGX

In this work, we model the hot gas emission using the TNG300 hydrodynamical simulations (Pillepich et al., 2018b; Marinacci et al., 2018; Naiman et al., 2018; Nelson et al., 2015; Springel et al., 2018); we use TNG300[1] to construct a lightcone, using the `LightGen` code[2], and generate mock X-ray observations (LC-TNGX), which is presented in Shreeram et al. (2025c) and applied to eROSITA data in Shreeram et al. (2025a). Here, we summarise the most important features. Using the IllustrisTNG cosmological hydrodynamical simulation, with the box of side length 302.6 Mpc (Nelson et al., 2019, TNG300), we determine the hot CGM properties of galaxies in LC-TNGX around a wide range of halo masses embedded in the LSS. TNG300 contains 2500^3 dark matter particles, with a baryonic mass resolution of 1.1×10^7 $M_\odot$, a comoving value of the adaptive gas gravitational softening length for gas cells of 370 comoving parsec, gravitational softening of the collisionless component of 1.48 kpc, and dark matter mass resolution of 5.9×10^7 $M_\odot$. The TNG simulations adopt the Planck Collaboration XIII 2016 cosmological parameters. LC-TNGX is constructed with the box remap technique (Carlson & White, 2010), and spans across redshifts $0.03 \lesssim z \lesssim 0.3$; this range was motivated by initial MW-mass scale

[1] http://www.tng-project.org

[2] The code to generate ligthcones from TNG is publically available at https://github.com/SoumyaShreeram/LightGen/

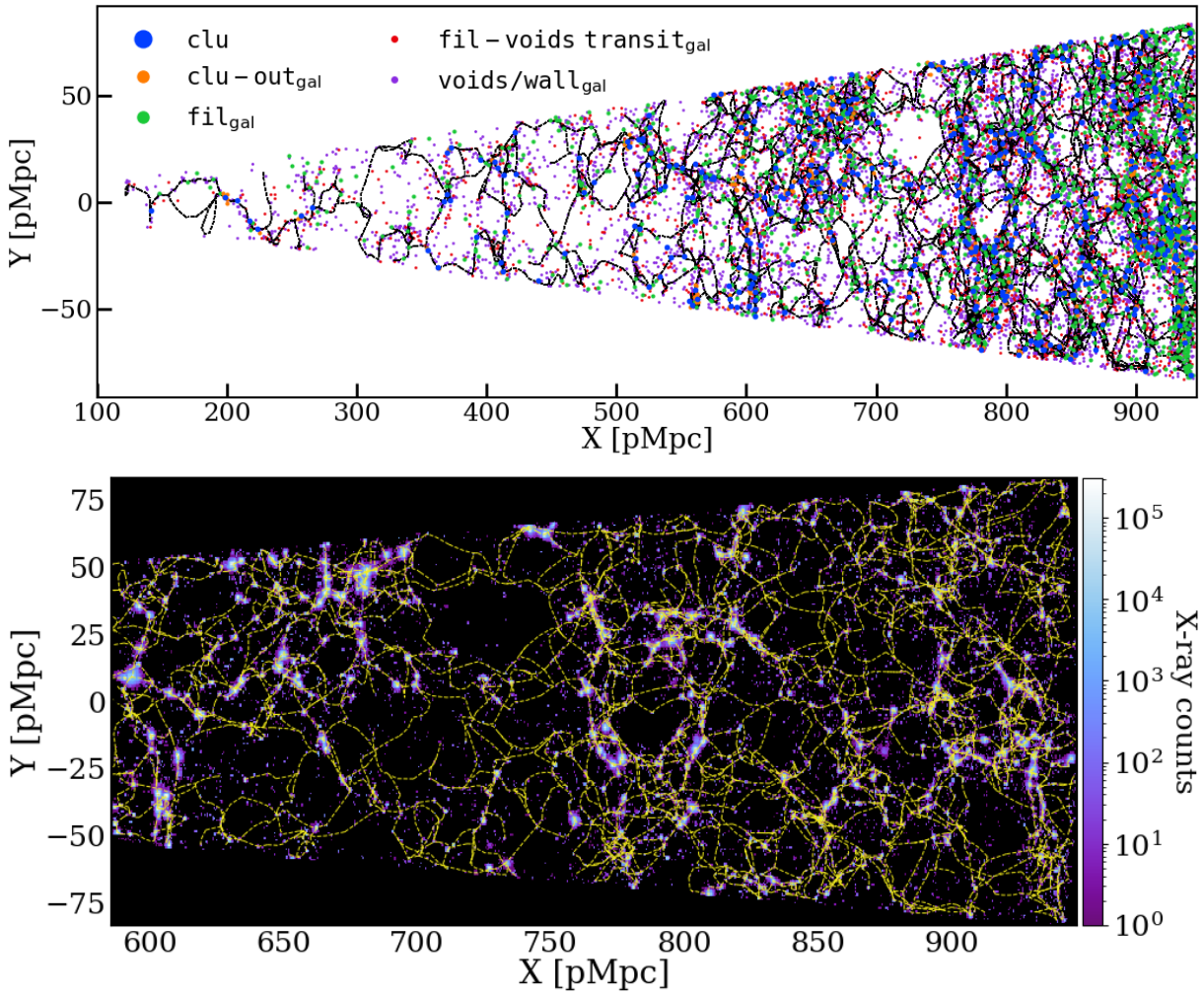

Figure 4.1: The TNG300 lightcone (LC-TNGX) built in Shreeram et al. (2025c) overplotted with the filaments identified using the DisPerSe algorithm (Sec . 4.3.2). The top panel shows the central galaxies in LC-TNGX that are classified into five distinct large-scale environments categories: (1) clusters in blue, (2) cluster outskirts in orange, (3) filaments in green, (4) filament-void transition region in red, and (5) voids/walls in purple, defined in Sec. 4.3.3. The bottom panel zooms into the lightcone, showing the X-ray events generated with `pyXsim` in the 0.5 − 2.0 keV energy band with the filaments depicted by the yellow-dashed lines. While the filaments are identified using the galaxy distribution, we show that the hot gas emitting X-ray events trace the cosmic web. This alignment validates the full pipeline used here and in Chapt. 2, from the lightcone construction and X-ray map generation to filament identification.

of the hot CGM observations (e.g. Comparat et al. 2022; Chadayammuri et al. 2022; Zhang et al. 2024a). It goes out to 1231 comoving Mpc (cMpc) along the x-axis, subtending an area of 47.28 deg^2 on the sky in the y-z plane. There are 22 snapshots within the observationally motivated redshift range of $0.03 \leq z \leq 0.3$.

The physical properties of the distinct halos and subhalos within the TNG300 lightcone are obtained by the Friend-of-Friend (FoF) and SUBFIND algorithm (Springel et al., 2001; Dolag et al.,

2009). SUBFIND detects gravitationally bound substructures, equivalent to galaxies in observations, and also provides us with a classification of subhalos into centrals and satellites, where centrals are the most massive substructure within a distinct FoF halo.

This chapter focuses on the average XSB profiles of central galaxies in halo mass bins. We identify centrals using FoF groups, where the group centre is defined as the most bound particle within the central subhalo as found by the SUBFIND algorithm. We exclude satellite galaxies, since their stacked XSB profiles are dominated by the hot gas emission of their more massive host halos rather than by the intrinsic CGM of the satellites themselves. Segregating satellites by environment would therefore not directly probe their own hot gas content, but instead that of their nearby massive companions. As quantified in Shreeram et al. (2025c), including satellites primarily adds a flat background component at large radii, driven by group- and cluster-mass hosts. Since the aim of this work is to study the XSB of galaxies as a function of environment, we focus exclusively on centrals, for which the measured signal can be directly attributed to their own halo gas content.

The X-ray photons are simulated within the LC-TNGX in the 0.5 – 2.0 keV intrinsic band with `pyXsim` (ZuHone & Hallman, 2016), which is based on PHOX (Biffi et al., 2013), by assuming an input emission model where the hot X-ray emitting gas is in collisional ionization equilibrium. The X-ray emissivity, ϵ, in turn depends on the gas mass density ρ, temperature T and the metallicity of the gas $Z_{\rm met}$ as follows (Lovisari et al., 2021),

$$\epsilon = n_{\rm e} n_{\rm p} \Lambda(T, Z_{\rm met}), \tag{4.1}$$

where n_e and n_p are the number densities of the electron and protons, which are related to the gas mass density $\rho = \mu m_{\rm p}(n_{\rm e} + n_{\rm p})$. Here, μ and $m_{\rm p}$ are the mean molecular weight and the proton mass, respectively. $\Lambda(T, Z_{\rm met})$ is the cooling function of the hot gas, which depends on the emission mechanism in the considered energy window[3]. The spectral model computations of hot plasma use the Astrophysical Plasma Emission Code, APEC[4] code (Smith et al., 2001) with atomic data from ATOMDB v3.0.9 (Foster et al., 2012) and solar abundance values from Anders & Grevesse (1989). This model uses the plasma temperature of the gas cells (in keV), the redshift z and metallicity. In this Chapter, we have improved the mock X-ray generation from Shreeram et al. (2025c), where we assumed a constant metallicity of 0.3 $Z_\odot$, to include the intrinsic TNG gas cell metallicity. This is a key improvement as it allows a more accurate and self-consistent estimate of the X-ray emission at the gas cell level throughout the lightcone.

The events are generated by assuming a telescope with an energy-independent collecting area of 1000 cm^2 and an exposure time of 1000 ks. The photon list is generated in the observed frame of the X-ray emitting gas cells and is corrected to rest frame energies. Finally, the photons generated by the gas cells are projected onto the sky. We use the projected central galaxy positions and obtain the XSB profiles in the 0.5 – 2.0 keV band. We select the X-ray events within $R_{\rm 200m}$[5] of the parent halo for obtaining the XSB profiles and we define these profiles as the intrinsic hot

[3] these could be free-free, recombination, or line cooling; see Böhringer & Werner (2010) for a review.

[4] APEC link `https://heasarc.gsfc.nasa.gov/xanadu/xspec/manual/node134.html`

[5] $R_{\rm 200m}$ and $M_{\rm 200m}$ is the radius and mass at which the density of the halo is 200× the mean matter density (cold dark matter and baryons).

gas emission profiles. In this work, we present the impact of the CGM environment on the XSB profiles. For this purpose, we classify the cosmic web in the LC-TNGX into different LSEs, shown in the top panel of Fig. 4.1, as further described in the following sections. We also show the distribution of X-ray events in the bottom panel of Fig. 4.1.

4.3.2 Extracting cosmic filaments in LC-TNGX using DisPerSE

The theoretical background of DisPerSE is provided in Sousbie (2011); Sousbie et al. (2011)[6]; here we summarise the most important details. DisPerSE deals with discrete datasets and provides the user with a geometric three-dimensional ridge, allowing for the classification of the LSS based on its topology. It is built on Morse and persistence theories, and it functions by first estimating the underlying density field, given an input galaxy distribution, using the Delaunay tessellation field estimator (DTFE; Schaap & Van De Weygaert 2000; Cautun & van de Weygaert 2011). The Delaunay tessellation is a triangulated space representing a geometric assembly of cells, faces, edges and vertices mapping the entire volume of the galaxy distribution. The gradients of the DTFE density field, $\rho_{\rm DTFE}$, provide the critical points: maxima, minima and saddles, which are connected by field lines tangent to the gradient of $\rho_{\rm DTFE}$. The filaments comprise connecting segments between the maxima of the density field, also called CPmax or peaks, to the saddle points.

The significance of a filament, or the persistence threshold, is estimated by the density contrast of the critical pair chosen to pass a certain signal-to-noise threshold. For a filament, this critical pair is between a CPmax and the saddle point. The noise level is defined relative to the root mean square of the significance values obtained from random sets of points. This thresholding eliminates less significant filaments, simplifying the Morse complex and retaining its most topologically robust features. The skeletons generated in this work use the 3σ persistence thresholds, following the careful calibration method presented in Galárraga-Espinosa et al. (2024). The galaxies above $M_\star > 10^9$ $\mathrm{M}_\odot$ (83,297 galaxies) were used to build the skeleton, shown in Fig. 4.1. This mass choice is motivated to match typical galaxy mass limits in current observation surveys, and the resolution of the simulation used to build the lightcone. We highlight that while the filament skeleton is constructed from DisPerSE, using the galaxy distribution, as shown by the top panel of Fig. 4.1, we find that the hot gas, as probed by the X-rays, also traces the cosmic web as shown in the bottom panel of Fig. 4.1. This alignment provides a compelling validation of the full pipeline used in this work, from the construction of the lightcone and the generation of X-ray maps to the identification of the filamentary network.

4.3.3 Classification of halos in LC-TNGX into different cosmic web environments

Given the skeleton from DisPerSE, the central galaxies in the LC-TNGX are divided into five mutually exclusive categories in a similar fashion as in Galárraga-Espinosa et al. (2023), also depicted in Fig. 4.1. We summarise the fraction of galaxies in each of these distinct LSE categories

[6] http://www2.iap.fr/users/sousbie/web/html/indexd41d.html

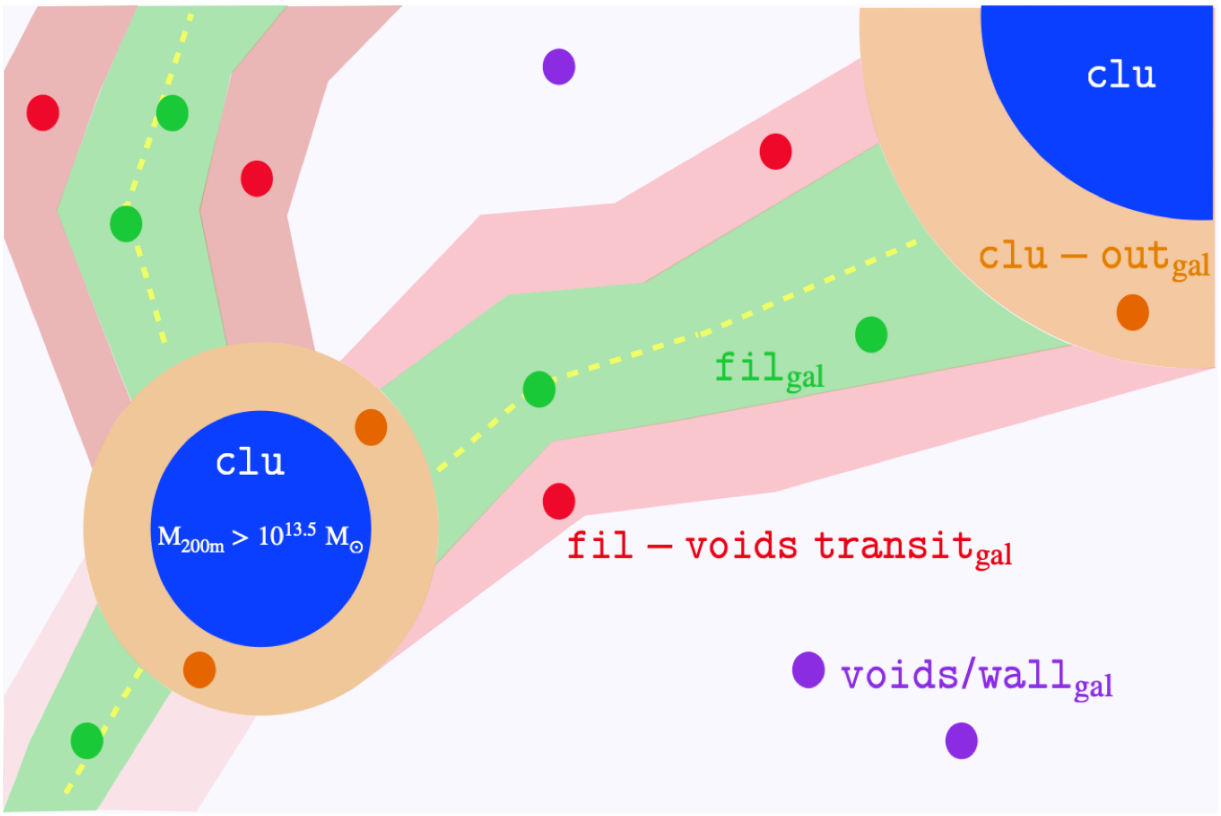

Figure 4.2: Illustration of the classification of galaxies into different LSE categories within the LC-TNGX. The filament spines (yellow dashed lines) are extracted using the DisPerSe algorithm. The clusters, representing the nodes of the cosmic web, are defined as halos with masses $M_{200\mathrm{m}} > 10^{13.5}$ $\mathrm{M}_{\odot}$. The dots represent central galaxies in different LSE, such as cluster outskirts (orange), filaments (green), filament-void transition region (red), and voids/walls (purple).

Table 4.1: Fraction of galaxies in each halo mass bin for each large-scale environment classification. For every halo mass bin, we present the percentage of objects in cluster outskirts (orange), filaments (green), filament-void transition region (red), and voids/walls (purple) within LC-TNGX (detailed in Sec. 4.3.3). The $M_{200\mathrm{m}} > 10^{13.5} M_{\odot}$ halos, of which there are 551, are defined as massive groups and clusters.

Color	LSS classifications	$\mathrm{M}_{200\mathrm{m}} \in 10^{11.5-12}\mathrm{M}_{\odot}$ 28,492 halos	$\mathrm{M}_{200\mathrm{m}} \in 10^{12-12.5}\mathrm{M}_{\odot}$ 11,094 halos	$\mathrm{M}_{200\mathrm{m}} \in 10^{12.5-13}\mathrm{M}_{\odot}$ 3,677 halos	$\mathrm{M}_{200\mathrm{m}} \in 10^{13-13.5}\mathrm{M}_{\odot}$ 1,113 halos	All $\mathrm{M}_{200\mathrm{m}} \in 10^{11.5-13.5}\mathrm{M}_{\odot}$ 44,376 halos
■	Cluster outskirts	3% (975)	3% (304)	3% (113)	2% (25)	3% (1417)
■	Filaments	12% (3,470)	10% (1,139)	13% (465)	20% (221)	12% (5,295)
■	Filament-void transition	23% (6,627)	22% (2,391)	22% (801)	22% (242)	23% (10,061)
■	Voids/Walls	61% (17,420)	65% (7,260)	63% (2,298)	56% (625)	62% (27,603)

in Tab. 4.1, and we also illustrate the LSE classification of galaxies in Fig. 4.2, which are defined as follows.

1. Clusters and massive groups: The galaxy clusters and massive groups are defined as halos with $M_{200\mathrm{m}} > 10^{13.5}$ $\mathrm{M}_{\odot}$, with a radius $R_{200\mathrm{m}}$, centred on the positions of the FoF halos. As

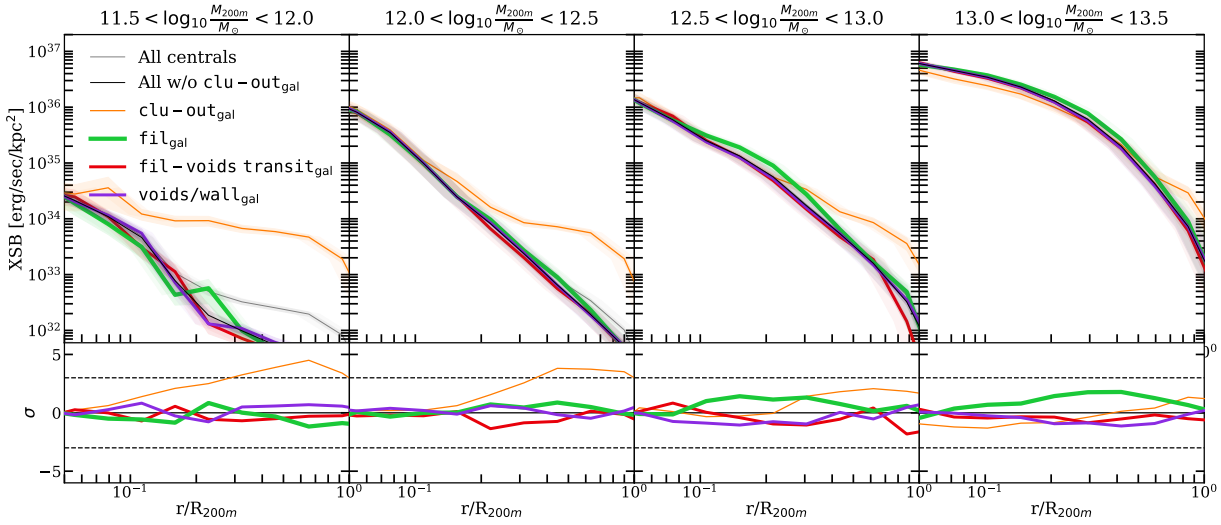

Figure 4.3: The X-ray surface brightness profiles (XSB) of halos located in different cosmic web environments in increasing halo mass bins from left to right. The fraction of central galaxies in each mass bin (and each LSE category) is shown in Tab. 4.1. The bottom panel shows the significance (see Eq. 4.2) of the difference in the XSB in a given cosmic environment with respect to the others (see text for details). The shaded regions around each curve correspond to the uncertainty in the mean profile obtained by bootstrapping.

the X-ray emission around these objects probes the hot gas in the well-studied intracluster medium (ICM; see e.g, Fabbiano 1996) and introgroup medium (IGrM; e.g., Lovisari & Ettori 2021), these objects are excluded from further analysis.

2. Galaxies in cluster and group outskirts ($\texttt{clu-out}_{\rm gal}$): This category comprises galaxies located $(1-3)\times R_{\rm 200m}$ from a cluster center. This radial range is motivated by Aung et al. (2023), who demonstrated that the gas accretion shock is located at approximately $(1.5-3)\times R_{\rm 200m}$. This accretion shock leads to the onset of the galaxy quenched fraction, influenced by ram pressure and tidal stripping due to clusters, approaching the average value (e.g., Cen et al. 2014).

3. Galaxies in filaments ($\texttt{fil}_{\rm gal}$): The cosmic filaments that are extracted by DisPerSe are defined as cylinders, with a radius of 1 cMpc (Wang et al., 2024), aligned along the spine of the filament skeleton identified by DisPerSe (Sec. 4.3.2). The central galaxies that are within the 1 cMpc cylinder of the filament spine are defined as galaxies in filaments.

4. Galaxies in the filament-voids/walls transition region ($\texttt{fil-voids transit}_{\rm gal}$): The central galaxies that are $1-3$ cMpc away from the filament spine are categorised as galaxies in the environments lying between filaments and voids. This category is primarily constructed to define a smooth transition between the galaxies located in filament outskirts to those in voids. For brevity, we also call this group of galaxies the transition galaxies.

5. Galaxies in voids and walls ($\texttt{voids/wall}_{\rm gal}$): This category encompasses all the galaxies

that do not fall in any of the above categories. These galaxies are also called "field" galaxies. The galaxies in voids and walls are combined due to the lack of information about the void or wall size, which is required to associate galaxies in these distinct categories.

We present the fraction of central galaxies in each of these distinct categories in Tab. 4.1; within LC-TNGX, of the 44,376 halos with $M_{200m} \in 10^{11.5-13.5} M_\odot$, 3%, 12%, 23%, and 62% of the halos are located in cluster outskirts, filaments, filament-void transition region and voids/walls, respectively.

We compare our findings on the fraction of filament galaxies with other literature works. Ganeshaiah Veena et al. (2019) find that 63% of central galaxies are hosted by filaments in the EAGLE simulation based on the Bisous filament finder. Using the TheThreeHundred project, Kuchner et al. (2022) find that 45% of the galaxies in filaments are feeding clusters (independent of the distance to the cluster). Navdha et al. (2025), using the Millennium simulation, to show that 26% of the galaxies reside in the cosmic web at a halo mass of $10^{11} M_\odot$, going up to 50% at $10^{12.7} M_\odot$. However, these fractions include both central and satellite galaxies, and they define the cosmic web differently. We draw extreme caution when directly comparing these values with the 12% of filament galaxies found in our work. As also highlighted by these works (Ganeshaiah Veena et al., 2019; Kuchner et al., 2022; Navdha et al., 2025), the fraction of filament galaxies is affected by the following: (1) the box size and the volume of the simulation, in turn affecting the number of massive clusters in the LSS, which are different across the simulations discussed here; (2) different filament finding techniques (see e.g., Cautun et al. 2013; Leclercq et al. 2016; Libeskind et al. 2018; Rost et al. 2020, for comparisons between different cosmic web identification methods); and (3) different cosmic web definitions, affecting in turn the resulting fraction of galaxies considered to be in filaments. More so, we are for the first time performing such a categorisation of galaxies in a lightcone configuration (ranging across $0.03 \leq z \leq 0.3$), which could show further deviations from a galaxy categorisation in a cubic snapshot at a fixed redshift.

4.4 Effect of the environment on the simulated X-ray surface brightness profiles of halos

The hot CGM emits in X-rays due to infalling gas within halos, which is shock-heated up to the virial temperatures, $T_{vir} \gtrsim 5 \times 10^5$ K (White & Rees, 1978). We present the projected X-ray surface brightness profiles of halos for varying halo masses and cosmic web environments in Fig. 4.3. The increasing halo mass bins (left to right) result in brighter XSB profiles, given that the gas is heated to higher virial temperatures (e.g., Comparat et al. 2022; Zhang et al. 2024a).

We separate galaxies into the following different bins of halo mass: $M_{200m} \in 10^{11.5-12}$ $M_\odot$, $M_{200m} \in 10^{12-12.5}$ $M_\odot$, $M_{200m} \in 10^{12.5-13}$ $M_\odot$ and $M_{200m} \in 10^{13-13.5}$ $M_\odot$. These are hereafter referred to as the lowest, low, medium, and highest mass bins, respectively. For the lowest halo mass bin (leftmost panel), the peak temperature of the gas within the halo is 0.03 – 0.09 keV (also shown later in Fig. 4.5), which is well below the 0.5 – 2 keV soft X-ray band considered here for measuring the XSB profiles. Therefore, the results of the XSB profiles corresponding to

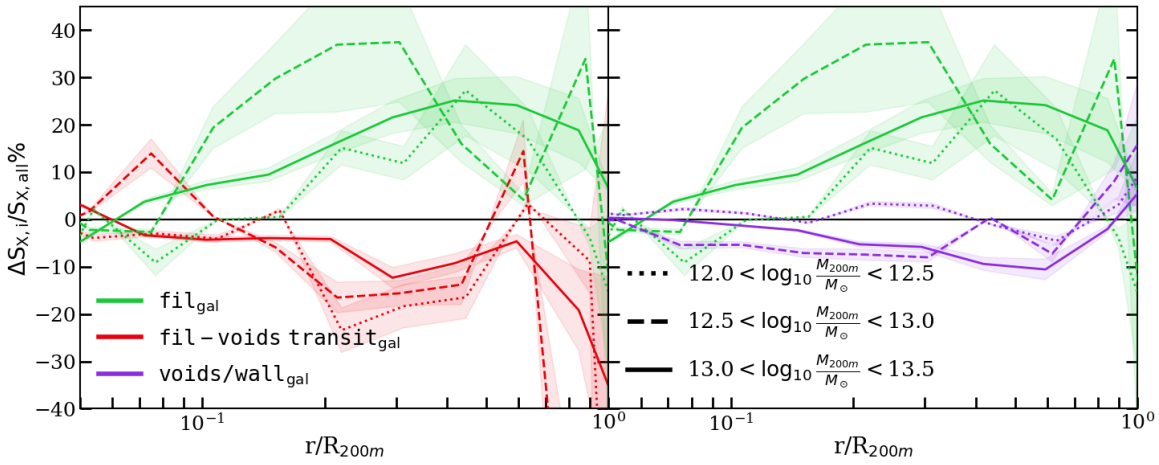

Figure 4.4: The percentage deviations of the XSB profiles of halos located in filaments (green), compared to those in the filament-void transition region (left panel; red lines) and in voids/walls (right; purple lines). We also consider galaxies in different halo mass bins, where the dotted lines represent the $M_{200\mathrm{m}} \in 10^{12-12.5}$ M$_\odot$ halos, whereas the dashed and solid lines represent the $M_{200\mathrm{m}} \in 10^{12.5-13}$ M$_\odot$ and $M_{200\mathrm{m}} \in 10^{13-13.5}$ M$_\odot$ bins, respectively. The shaded regions around each curve correspond to the uncertainty in the mean profile obtained by bootstrapping. We find that the XSB profiles of fil$_{\mathrm{gal}}$ are X-ray brighter in the range $\sim (0.3 - 0.5) \times R_{200\mathrm{m}}$ by $20 - 45\%$ with respect to the the fil-voids transit$_{\mathrm{gal}}$ and voids/wall$_{\mathrm{gal}}$ populations.

this lowest mass bin are only probing the high-temperature end of the lowest halo mass bin halos in the XSB profiles presented here, thereby explaining their weak signal.

The different LSE considered here are as follows, as also shown in Fig. 4.3 are cluster outskirts (orange), filaments (green), filament-void transition region (red) and voids/walls (purple). The bottom panel of Fig. 4.3 shows the significance of the deviation of a given XSB profile, $S_{X,i}$, in a defined LSE category with respect to all the other categories, $\tilde{S}_{X,i}$. Here, the subscript i signifies one among the five LSE categories defined in Sec. 4.3.3 (also shown by the colored lines in Fig. 4.3), while $\tilde{S}_X$,with a tilde, is the XSB profile obtained by averaging over all the galaxies in the other LSE categories. The significance, σ, is defined as

$$\sigma = \frac{S_{X,i} - \tilde{S}_X}{\sqrt{\tilde{\delta}^2 + \delta_i^2}}, \tag{4.2}$$

where δ_i and $\tilde{\delta}$ are the uncertainties in the mean XSB profiles obtained from bootstrapping. A positive significance implies that a given $S_{X,i}$ is brighter at a given scale compared to its counterparts in other LSE, while the negative significance represents steeper or X-ray fainter profiles.

The following sections detail the trends observed in the XSB profiles in the different LSE categories, where we present the effect of the LSE on the XSB profiles of halos in cluster outskirts in Sec. 4.4.1 and in filaments and voids/walls in Sec. 4.4.2.

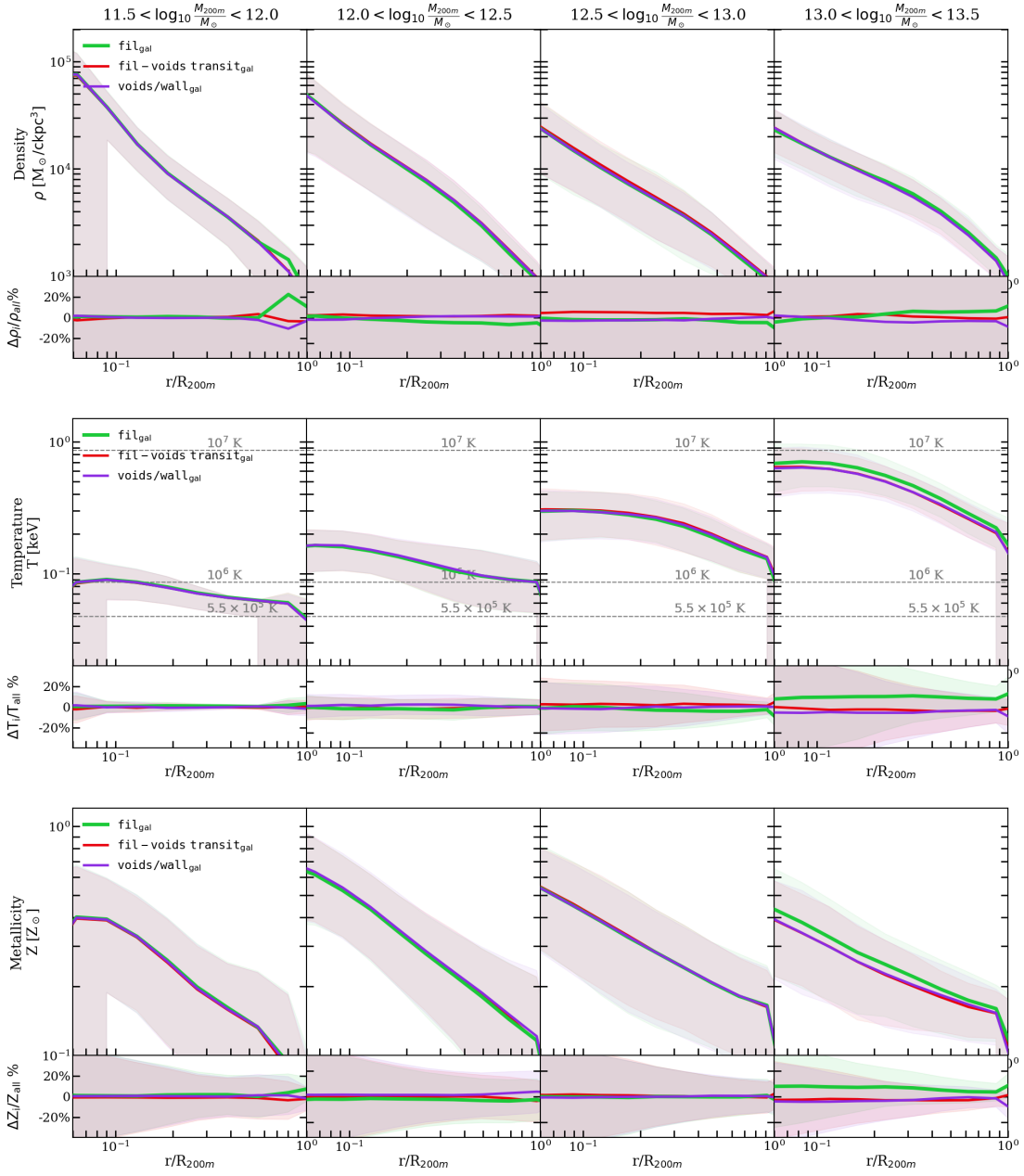

Figure 4.5: The volume weighted gas mass density (top panel), temperature (middle panel) and metallicity (bottom panels) profiles together with their percentage deviations (corresponding bottom rows) of halos located in different LSE in increasing halo mass bins from left to right. The different cosmic environments considered here are filaments (green), filament-void transition region (red), and voids/walls (purple). The shaded regions show the $16^{th} - 84^{th}$ percentile distribution.

4.4.1 Galaxies in cluster outskirts

The $\texttt{clu-out}_{\rm gal}$ galaxy population probes the XSB profile of the halos located physically close to a cluster, shown by the orange lines in Fig. 4.3. Across all halo mass bins (left to right), although notably more prominent at the lowest and low halo mass bins, the XSB profiles from $\texttt{clu-out}_{\rm gal}$ are significantly brighter than the mean XSB profile (without categorising halos by their LSE). We attribute this striking feature of XSB profiles from $\texttt{clu-out}_{\rm gal}$ to its close proximity to a cluster, where the emission from the ICM in the cluster outskirts begins to dominate the profile at these radii. We further quantify this effect in the significance plots in the bottom panel of Fig. 4.3. We show that the halos in the least-massive bin are 3σ brighter at 0.2 $R_{\rm 200m}$ and 5σ brighter at 0.7 $R_{\rm 200m}$. The significance reduces to 3σ at 0.7 $R_{\rm 200m}$ for the low halo mass bin. For the medium and highest halo mass bins considered here, the significance of the XSB profiles from $\texttt{clu-out}_{\rm gal}$ being brighter than their counterparts in other LSE is $< 3\sigma$ significant at all radii. We interpret the lower significance of the highest halo mass bins by the fact that more massive halos have comparable intrinsic X-ray brightness to their neighbouring cluster. Therefore, the cluster emission only dominates at large radii. Our results show that the X-ray contamination from the cluster is an important effect to consider when studying the galaxies in the cluster outskirts in X-ray stacking experiments.

Cluster and group outskirts are special regions, where, due to gas stripping processes, the gas in the galaxies in cluster outskirts is depleted, as shown by simulations (e.g., Bahé et al. 2013; Cen et al. 2014) and observations (e.g., Tanaka et al. 2004; Catinella et al. 2013; Cortese et al. 2011). However, in order to measure the impact of such stripping processes on the average XSB profiles obtained in stacking experiments, one must accurately model out the cluster XSB contribution. We leave such a modelling analysis to recover the XSB of galaxies in cluster outskirts from the contamination of the nearby cluster emission for future work. The following sections focus on the other LSE categories that are unaffected by cluster emission, as they are located far ($> 3R_{\rm 200m}$) from the cluster and group centres.

4.4.2 Galaxies in filaments and voids

We now focus on the galaxies far away from clusters and massive groups, which are located in filaments, voids/walls and the transition region in between them. The $\texttt{fil}_{\rm gal}$, $\texttt{fil-voids transit}_{\rm gal}$, and $\texttt{voids/wall}_{\rm gal}$ population are shown by the green, red, and purple lines in Fig. 4.3, respectively, with the bottom panel showing the significance of deviation compared to other LSE. We further study these three categories in Fig. 4.4, showing the absolute deviation in the XSB profiles in the low, medium and highest halo mass bins. We exclude the lowest halo mass bin, $M_{\rm 200m} \in 10^{11.5-12}$ $\rm M_\odot$, in this comparison as there is no observable trend due to the high scatter in the measured XSB profiles. We quantify the deviation of the filament galaxies with respect to transition galaxies (left panel), and the voids/walls galaxies (right panel).

We find that for all the halo mass bins considered, the XSB profiles of $\texttt{fil}_{\rm gal}$ are X-ray brighter than the mean population between $\sim (0.3 - 0.5) \times R_{\rm 200m}$ by $20 - 45\%$. More precisely, Fig. 4.4 shows that the filament galaxies in the low, medium and highest halo mass bins are brighter than the mean XSB profile at different fractions of $R_{\rm 200m}$. For the low halo mass bin,

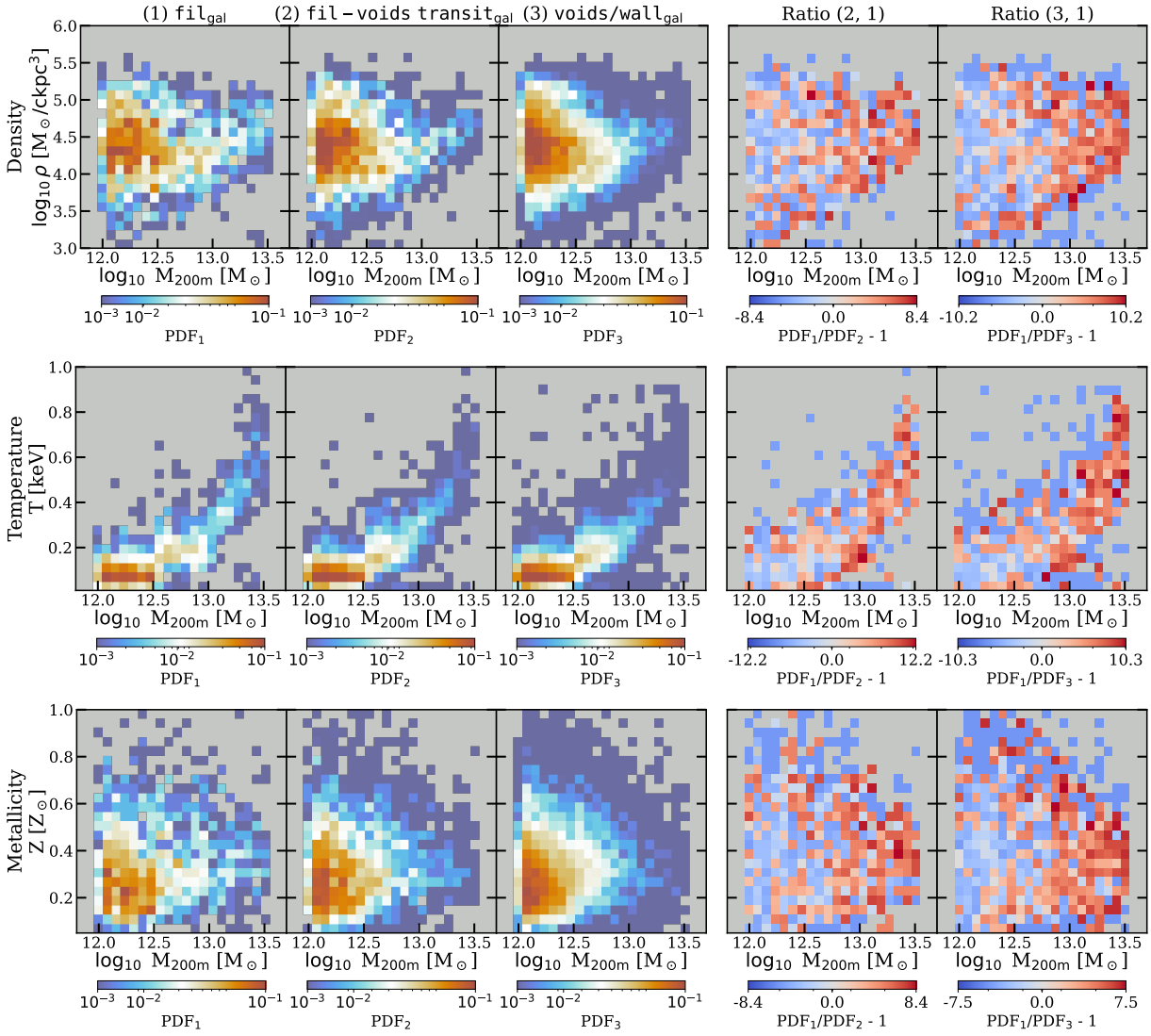

Figure 4.6: The normalised probability distribution functions of gas mass density, ρ (top row), temperature, T (middle row), metallicity $Z_{\rm met}$ (bottom row) as a function of the halo mass. The population of galaxies in filaments (1, 825), filament-void transition region (3, 434), and voids/walls (10, 183) is shown in the first three columns, respectively. The last two columns show the ratios of the `fil-voids transit`$_{\rm gal}$ and the `voids/wall`$_{\rm gal}$ to the `fil`$_{\rm gal}$ population. The colour bars in the ratio panels indicate the relative suppression (blue) or enhancement (red) of the thermodynamic quantity of the filament galaxies with respect to transition or voids/walls galaxies. We find that the overdense intrafilamentary environments hosting the `fil`$_{\rm gal}$ population show up to a factor of 10× higher gas densities, 12× higher temperatures, and 8× higher metallicities compared to both the transitional and voids/walls populations.

the maximum mean deviation is 20% at $\sim 0.45 \times R_{\rm 200m}$, whereas for medium and highest halo mass bins, the maximum mean deviation of 40% and 25% is at $\sim 0.3R_{\rm 200m}$ and $\sim 0.5R_{\rm 200m}$, respectively.

Interestingly, we also find that the voids/walls and the transition galaxies are X-ray fainter than the mean XSB profiles. In the `fil-voids transit`$_{\rm gal}$ case, for all halo mass bins, the maximum mean deviation is between $-(10-20)\%$ at $\sim (0.2-0.3)\times R_{\rm 200m}$. This trend becomes weaker for the `voids/wall`$_{\rm gal}$ populations, where all the XSB profiles are fainter than the mean profiles by less than 10% across all halo mass bins.

We delve deeper into understanding the non-negligible XSB excess in the filamentary galaxies with respect to those in voids/walls and the transition galaxies by exploring the primary quantities affecting the X-ray emission, which are the underlying thermodynamic quantities, as further detailed in the following section.

4.5 Thermodynamic properties of the simulated CGM

We investigate the thermodynamic properties of the hot gas ($T > 5\times10^5$ K)[7] around galaxies, given the dependence of X-ray emission on the gas density, ρ, temperature, T, and metallicity, $Z_{\rm met}$, as shown in Eq. 4.1.

In Fig. 4.5, we present the radial profiles of ρ (top panel), T (middle panel), and $Z_{\rm met}$ (bottom panel) for galaxies in filaments, voids/walls, and the transitional region, for increasing halo mass bins (left to right columns). These profiles are computed in 3D using volume-weighted averages of gas cell properties, which account for the moving-mesh refinement criterion of the AREPO code. Since AREPO employs a fixed mass threshold for gas cells (Weinberger et al., 2020), resulting in a wide range of cell volumes, volume-weighting ensures that our results are not biased by irregular Voronoi cell sizes, unlike mass-weighted profiles.

For the highest halo mass bin, the mean radial T and $Z_{\rm met}$ profiles are approximately 10% higher in filament galaxies than in voids/walls or the transition population, while mean density profiles show a modest enhancement at $r > 0.2\,R_{\rm 200m}$. However, significant scatter exists around the mean profiles across environments (see also Fig. 5 in Truong et al. 2023). To capture the full distribution of thermodynamic properties beyond averages, we compute probability distribution functions (PDFs).

Using the radial profiles in Fig. 4.5, we calculate the average ρ, T, and $Z_{\rm met}$ within $R_{\rm 200m}$ for each galaxy. Figure 4.6 shows the resulting normalised PDFs as a function of halo mass. The top, middle, and bottom rows display ρ–$M_{\rm 200m}$, T–$M_{\rm 200m}$, and $Z_{\rm met}$–$M_{\rm 200m}$, respectively. The first three columns correspond to galaxies in filaments (left), the filament–void transition region (middle), and voids/walls (right). The last two columns show fractional differences with respect to filaments: transition vs. filaments (column four) and voids/walls vs. filaments (column five). The colour bars in the ratio panels indicate the relative suppression (blue) or enhancement (red) with respect to the filament galaxies. Across all three thermodynamic quantities, filament galaxies exhibit systematic enhancements compared to other large-scale environments. More specifically, galaxies in filaments are up to a factor of 10× more likely to have higher gas densities, 12× more

[7] To ensure that we only include gas cells that physically emit in X-rays, we exclude star-forming gas cells and gas cells with densities above 10^{-25} g/cm^3 (see Shreeram et al. 2025c, Sec. 3.1 and Truong et al. 2020, Appendix B-C).

likely to have higher temperatures, and 8× more likely to have higher metallicities than galaxies in transition regions or voids/walls.

4.6 Discussion on filament galaxies being X-ray brighter than the galaxies in voids/walls

We now interpret these results in the context of their physical origin and implications for X-ray emission. From Fig. 4.6, we find systematic enhancements of thermodynamic properties in filament galaxies compared to galaxies in transition regions or voids/walls.

The environmental contrasts in the thermodynamic quantities are strongest for halos in the intermediate-to-high mass range ($10^{12.5}$ $M_\odot$ < M_{200m} < $10^{13.5}$ $M_\odot$), where the PDF ratios of filament galaxies relative to voids/walls or transition regions exceed them by 50–70% across all three thermodynamic quantities. Because density, temperature, and metallicity directly determine X-ray emissivity (Eq. 4.1), these results provide a possible physical explanation for the enhanced X-ray emission in filament galaxies observed in Fig. 4.4. Specifically, galaxies in filaments statistically inhabit halos with hotter, denser, and more metal-enriched circumgalactic media, making them more X-ray luminous than comparable galaxies in transition regions or voids/walls.

It is important to emphasise that the trends reported here are specific to the IllustrisTNG framework developed in this chapter and in Chapt. 2. While the TNG simulations provide state-of-the-art models for galaxy formation and the CGM, the quantitative results may depend on the underlying subgrid physics and feedback prescriptions implemented in this particular simulation. A natural extension of this work will be to test the robustness of our conclusions against other hydrodynamical suites (e.g., see Sec. 1.4.1), in order to establish whether the environmental dependencies identified here represent generic physical behaviour or are model-specific features.

In the following, we briefly discuss other quantities that may impact X-ray emission. Another possibility for the $\texttt{fil}_{\rm gal}$ population being X-ray brighter could be higher hot gas fractions. The importance of higher hot gas fractions on the X-ray brightness (and their detectability) of galaxy groups (> 10^{13} $M_\odot$) in Magneticum is discussed in Marini et al. (2025), where they show that X-ray bright groups are driven by higher hot gas fractions, alongside a steady accretion history and are located in overdense environments. Future work could jointly explore the impact of the assembly history on the hot gas fractions of the galaxies in different environments.

Finally, another possibility for enhanced X-ray emission from the $\texttt{fil}_{\rm gal}$ population, given their denser environment than void galaxies, could be from gas clumping (Nagai & Lau, 2011)[8] or from penetrating gas streams (van de Voort & Schaye, 2012; Zinger et al., 2016). Particularly, the energy that is carried by infalling hot gas is dissipated and eventually radiated in X-rays at $r \gtrsim 70$ kpc (e.g., see Fig. 14 in Nuza et al. 2014); thereby affecting the XSB in the low-redshift universe. Another way to probe the past and present gas accretion activity of a galaxy can be tested using galaxy connectivity as a proxy (Kraljic et al., 2020). Precisely, Galárraga-Espinosa

[8]While Nagai & Lau (2011) demonstrate gas clumping to be important in cluster outskirts, this could also play a role for intrafilamentary environments.

et al. (2023) demonstrate that galaxy connectivity is impacted by the large-scale environment, galaxy mass, and the local density, which they show to impact the star-formation rate of the galaxy. A future work that studies the contributions to the X-ray emission from infalling streams, as probed by galaxy connectivity, gas accretion rate, and gas clumping for the filament vs void galaxies, could illuminate whether these play an additional role in enhancing the X-ray emission in filament galaxies.

4.7 Conclusions and summary

In this chapter, we use an IllustrisTNG-based lightcone, LC-TNGX, to study the impact of the LSE on the hot gas properties of galaxies. We self-consistently generate mock X-ray observations within the LC-TNGX (Shreeram et al. 2025c and Chapt. 2). We apply DisPerSe on the galaxy distribution to identify the cosmic filaments within LC-TNGX and thereby classify the central galaxies into different LSE. These are as follows: galaxies in cluster and group outskirts ($\texttt{clu-out}_{\rm gal}$), galaxies in filaments ($\texttt{fil}_{\rm gal}$), galaxies in the filament-void transition region ($\texttt{fil-voids transit}_{\rm gal}$), and galaxies in voids and walls ($\texttt{voids/wall}_{\rm gal}$). We also study the effect of LSE in different halo mass bins. The main findings of this work are summarised below.

1. We show that the galaxies in cluster-outskirts are $\gtrsim 3\sigma$ brighter than the other populations at $\gtrsim 0.7R_{\rm 200m}$ at lower halo masses ($M_{\rm 200m} < 10^{12.5}$ M$_\odot$). Although this trend is $\lesssim 3\sigma$ significant for higher halo masses ($M_{\rm 200m} > 10^{12.5}$M$_\odot$), we find that the trend of cluster outskirts being brighter than their counterparts at large radii persists (Fig. 4.3). This striking feature of XSB profiles from galaxies in cluster outskirts being brighter is attributed to their close proximity to a cluster, where the emission from the ICM in the cluster outskirts begins to dominate the profile at these radii. We highlight the importance of this effect when studying the population of halos near clusters in X-ray stacking experiments.

2. We find that the filament galaxies are X-ray brighter than the galaxies in voids/walls and in the transitional region between them. More precisely, independent of the halo mass bins considered here, the XSB profiles of filament galaxies are X-ray brighter between $\sim (0.3 - 0.5) \times R_{\rm 200m}$ by $20 - 45\%$ (Fig. 4.4). We investigate the source of this brightness by exploring the thermodynamic properties (ρ, T, and Z) of the hot gas in these galaxies in these different environments. We find that the filament galaxies show significantly enhanced thermodynamic properties compared to those in transition regions or voids/walls, providing a possible physical explanation for the enhanced X-ray emission in filament galaxies. They are up to $10\times$ more likely to exhibit higher gas densities, $12\times$ more likely to have higher temperatures, and $8\times$ more likely to show elevated metallicities. These differences peak in the $10^{12.5}$ M$_\odot$ $< M_{\rm 200m} <$ $10^{13.5}$ M$_\odot$ range, where ratios of the probability density functions across all quantities are consistently 50−70% higher for filament galaxies.

Our findings highlight the importance of environmental effects in interpreting the hot CGM in X-rays. The framework developed here opens several promising avenues for future work. On

the observational side, with improved spectral resolution from ongoing/upcoming missions like *XRISM* (Tashiro et al., 2020) and *NewAthena* (Barret et al., 2020; Cruise et al., 2025), and the already available depth of *eROSITA* data (Merloni et al., 2024), it is feasible to search for an X-ray excess in filament galaxies using stacking techniques (e.g., Zhang et al. 2024a) by including LSE classification with ongoing/upcoming stage-4 surveys (e.g. Euclid, 4MOST, DESI, PFS). Additionally, future work should explore the energy dependence of the XSB profiles in the soft X-ray regime (0.2–1 keV), particularly for halos with $M_{200\mathrm{m}} < 10^{12}$ $\mathrm{M}_{\odot}$, to better probe the impact of the LSE on lower mass halos in X-rays. On the theoretical side, future studies exploring the effects of gas clumping (Nagai & Lau, 2011; Zhuravleva et al., 2013; Avestruz et al., 2016), infalling hot streams (Zinger et al., 2016), mass assembly history (Marini et al., 2025), galaxy connectivity (Galárraga-Espinosa et al., 2023), and impact of filament morphology (Galárraga-Espinosa et al., 2024; Yu et al., 2025) on filament galaxies could further elucidate the mechanisms driving enhanced X-ray emission in filaments. The work developed here lays the groundwork for jointly constraining CGM properties with the impacts of the cosmic web, key for understanding galaxy formation in a cosmological context.

Chapter 5

Conclusions and Outlook

The hot circumgalactic medium, as probed by X-ray observations, is the most massive and volume-filling phase in halos above $10^{11.5}$ $M_\odot$. The eROSITA X-ray telescope provides the highest signal-to-noise view of the hot CGM to date, where large-area overlapping optical surveys combined with X-ray stacking experiments allow us to detect the hot CGM emission out to the virial radius around Milky Way– and M31-like galaxies (Zhang et al., 2024a,b). Although X-ray stacking represents one of the most sensitive methods for probing the hot CGM currently, these measurements are affected by observational and projection effects that need to be better understood. This motivates the need for forward modelling the hot CGM with large statistics to disentangle intrinsic CGM signals from observational biases, which is one of the primary goals achieved in this thesis.

In this thesis, we have developed and implemented a forward-modelling framework to interpret the extended X-ray emission from the hot CGM around galaxies. We model the hot CGM gas emission using the IllustrisTNG hydrodynamical simulations (Pillepich et al., 2018b; Marinacci et al., 2018; Naiman et al., 2018; Nelson et al., 2015; Springel et al., 2018), with a box of side length 302.6 Mpc; this provides us a large enough box size to encompass the effects of the cosmological large-scale structure (LSS) and also accounts for the complexities introduced by feedback and cooling, inherent to the hot CGM on small scales. Using TNG300, we construct a lightcone, for which we developed the publicly available `LightGen` code, and generate mock X-ray observations, so-called LC-TNGX, as presented in Chapt. 2 and applied to eROSITA data in Chapt. 3. LC-TNGX is constructed with the box remap technique (Carlson & White, 2010), and spans across redshifts $0.03 \lesssim z \lesssim 0.3$, motivated by hot CGM observations in the local Universe (e.g. Comparat et al. 2022; Chadayammuri et al. 2022; Zhang et al. 2024a). It goes out to 1231 comoving Mpc (cMpc) along the x-axis, subtending an area of 47.28 deg^2 on the sky in the y-z plane. The LC-TNGX is a novel tool that forms the basis for the various aspects of the hot CGM studied in this thesis. Using LC-TNGX, we map the hot CGM around a wide range of halo masses embedded in the LSS.

The Chapt. 2, 3, and 4 presented in this thesis, alongside accompanying works Shreeram et al. (2025c,a,b), analyse the average X-ray surface brightness (XSB) profiles of central and satellite galaxies across different stellar and halo mass bins using LC-TNGX. The X-ray information is self-consistently generated within the LC-TNGX lightcone in the 0.5–2.0 keV band using

`pyXsim`, assuming a hot gas emission model in collisional ionization equilibrium. This enables a self-consistent estimate of X-ray emission at the gas cell level, which is done for the first time in a lightcone configuration. The photons are projected onto the sky, and intrinsic XSB profiles are measured within $R_{200\mathrm{m}}$ of each halo, centred on the projected galaxy positions; this way, we mimic the observationally implemented stacking strategy to get average XSB profiles within a given stellar/halo mass and redshift range.

In Chapt. 2, we address the following question. *How do projection effects impact the hot CGM as measured in X-rays?* The motivations for answering this question are as follows. To test theoretical predictions of the hot CGM against X-ray observations requires accounting for several projection effects that contaminate stacking analyses. Key effects include X-ray emission from the locally correlated large-scale structure (LSS), misclassification of satellite galaxies as centrals due to redshift uncertainties, offsets between the X-ray centre and the halo potential minimum, and line-of-sight contamination from uncorrelated foreground and background structures. Chapter 2 investigates these effects in detail using the LC-TNGX simulation to enable a robust interpretation of hot CGM X-ray measurements. The main conclusions from this chapter are summarised as follows.

1. We present an analytical model (Eq. 2.7) that well-describes the intrinsic S_X-profile in LC-TNG300 across the stellar mass bins $10^{10.5-11}\mathrm{M}_\odot$, $10^{11-11.25}\mathrm{M}_\odot$, and $10^{11.25-11.5}\mathrm{M}_\odot$ and halo mass bins of $10^{12.5-13}\mathrm{M}_\odot$, $10^{13-13.5}\mathrm{M}_\odot$, and $10^{13.5-14}\mathrm{M}_\odot$. We provide the best-fitting parameters for the analytical model in Tab. 3.1 and Tab. 2.4 for the stellar and halo mass bins explored in this work.

2. We carry forward the current state-of-the-art modelling analysis presented in Oppenheimer et al. (2020) by also showing the impact of the locally correlated environment on the measured X-ray surface brightness profiles.

3. We present, for the first time, the effect of misclassified centrals in stacking experiments for three stellar mass bins: $10^{10.5-11}\mathrm{M}_\odot$, $10^{11-11.25}\mathrm{M}_\odot$, and $10^{11.25-11.5}\mathrm{M}_\odot$. We find that the contaminating effect of the misclassified centrals on the stacked profiles increases when the stellar mass decreases.

4. For the MW-like galaxies, we conclude that the contribution of satellites (or misclassified centrals) can not be neglected in stacking analysis (see Fig. 2.10). In cases where 30%, 10%, or 1% of the satellites contribute to the total emission of MW-like galaxies, we have shown that they dominate the measured total S_X profile at radii $\geq 0.11 \times R_{500c}$, $\geq 0.24 \times R_{500c}$, and $\geq 1.04 \times R_{500c}$, respectively.

5. We report the mean offset between the centre of the halo defined using the X-ray peak, and that obtained from the minimum of the halo potential is 70 kpc.

In Chapt. 3, we address the following question. *Can we recover hot CGM physics from eROSITA X-ray stacks?* With our understanding of projection effects from Chapt.2, we develop in Chapt.3 a forward model for the stacked X-ray radial surface brightness profiles around MW-mass galaxies in eROSITA data. Our model includes two emitting components: hot gas (from

both central galaxies and satellites in more massive halos) and X-ray point sources (X-ray binaries and AGN). We show that, for a fixed mean stellar mass, doubling the mean halo mass leads to a $\sim 4\times$ increase in the stacked X-ray luminosity of the hot CGM, highlighting the tight correlation between the gas physics shaping the observed hot CGM and the underlying halo mass distribution in stellar-mass-selected stacking experiments. This work provides a novel technique to jointly constrain the mean AGN X-ray luminosity and the radial hot CGM gas distribution within halos, using X-ray stacking measurements as a new benchmark. Alongside advances in understanding how different stellar and AGN feedback prescriptions impact hot CGM properties (Lau et al., 2024; Medlock et al., 2025), we emphasise the crucial role of the halo mass distributions in shaping the hot CGM probed in X-ray observations. The detailed conclusions from Chapt. 3 are are summarized as follows:

1. We test the impact of the underlying halo mass distribution on the TNG-based prediction for corresponding X-ray surface brightness profiles. We do so by generating multiple mock galaxy catalogues using LC-TNG300, matched in stellar mass and redshift to the $\text{Full}_{\text{phot}}$ galaxy catalogue, however, with different underlying halo mass distributions (Sec. 3.4.3; Fig. 3.1). Namely, the three models obtained by varying the halo mass distribution are as follows: model 1 leaves the LC-TNG300 halo mass distribution unchanged, model 2 and 3 change the underlying halo distribution by excluding the 10% and 30% most massive halos from the original LC-TNG300 halo mass distribution, respectively. We show that the shape and normalization of the hot CGM X-ray surface brightness profiles are impacted by varying the halo mass distributions, where discarding the most massive halos from the underlying halo distribution results in steeper profiles with lower normalization. More precisely, we find that a factor $\sim 2\times$ increase in the mean value of the underlying halo mass distribution results in $\sim 4\times$ increase in the X-ray luminosity from the hot CGM.

2. We fit for the stacked X-ray radial surface brightness profile by eROSITA around MW-mass galaxies from Zhang et al. (2024a) with our forward models. Our model contains two emitting components (Eq. 3.1-3.3): hot gas (around central galaxies and around satellite galaxies hosted by more massive halos) and X-ray point sources (X-ray binaries and Active Galactic Nuclei). For three forward models, we compute the X-ray luminosity from point sources, $L_{X,\,\text{PS}}$, and CGM (see results in Tab. 3.1). Using the empirical estimates for the expected luminosity from XRB (Sec. 3.5.1) and AGN (Sec. 3.5.2) for MW-mass galaxies, we put constraints on the permissible values of $L_{X,\,\text{PS}}$ contribution to the X-ray stack (see Fig. 3.1). This analysis favours model three, which has a mean $M_{200\text{m}} = 3.5 \times 10^{12}\ \text{M}_\odot$, implying that the hot CGM component allows for a point source component with a mean AGN luminosity that agrees with empirical estimates from the low redshift universe. We focus our results on model three for all the following discussions of the hot CGM.

3. By integrating the area under the mean X-ray surface brightness profile from the

central galaxy hot CGM component within R_{500c}, we obtain an X-ray luminosity, $L_{X,\,\mathrm{CGM}} = 1.69^{+0.28}_{-0.91} \times 10^{40}$ ergs/s. We also show the residual plot of the per cent deviation of the data from our model, where the discrepancies within the 50 – 105 kpc range are within 15% (Fig. 3.3). We find that at $\lesssim$ 40 kpc, the hot CGM from central galaxies and the X-ray point sources emission from XRB and AGN each account for 40 – 50% of the total X-ray emission budget, respectively (Fig. 3.5). At larger radii > 40 kpc, the contribution from the emission around satellites dominates the total X-ray emission, thereby explaining the overall flattening in the measurements.

4. We compare our results with the other hot CGM measurements presented in Zhang et al. (2024a), based on a different optical galaxy catalogue, namely from the SDSS spectroscopic survey (see comparison in Fig. 3.6). Our TNG-based forward model of the hot CGM prediction broadly agrees with the hot CGM measurement from Zhang et al. (2024a). The $L_{X,\,\mathrm{CGM}}$ measured between the two works is consistent. We note that the halo mass distributions of the two samples are similar mean values, where the mean $M_{200\mathrm{m}} = 3.5 \times 10^{12}$ M$_\odot$ for our forward model 3 and the mean $M^{\mathrm{CEN}}_{200\mathrm{m}} \sim 3 \times 10^{12}$ M$_\odot$. This result further emphasises the importance of the underlying halo mass distribution when comparing hot CGM profiles across different observations and simulation-based models.

Finally, in the final Chapt. 4, we address the following question. *How does the large-scale cosmic web impact the X-ray emitting CGM?* While key physical processes shaping the hot CGM have been widely studied, the influence of a galaxy's large-scale cosmic environment on the hot gas content remains less explored. In Chapt.4, we investigate how the large-scale cosmic web affects the X-ray surface brightness (XSB) profiles of galaxies using the IllustrisTNG-based lightcone, LC-TNGX, first developed in Chapt.2. We apply the filament finder DisPerSE to the galaxy distribution within LC-TNGX to identify cosmic filaments and classify central galaxies into five large-scale environment (LSE) categories: clusters and massive groups, cluster outskirts, filaments, filament-void transition regions, and voids/walls. The main findings from this work are as follows:

1. We show that the galaxies in cluster-outskirts are $\gtrsim 3\sigma$ brighter than the other populations at $\gtrsim 0.7R_{200\mathrm{m}}$ at lower halo masses ($M_{200\mathrm{m}} < 10^{12.5}$ M$_\odot$). Although this trend is $\lesssim 3\sigma$ significant for higher halo masses ($M_{200\mathrm{m}} > 10^{12.5}M_\odot$), we find that the trend of cluster outskirts being brighter than their counterparts at large radii persists (Fig. 4.3). This striking feature of XSB profiles from galaxies in cluster outskirts being brighter is attributed to their close proximity to a cluster, where the cluster outskirt begins to dominate the profile at these radii. We highlight the importance of this effect when studying the population of halos near clusters in X-ray stacking experiments.

2. We find that the filament galaxies are X-ray brighter than the galaxies in voids/walls and in the transitional region between them. More precisely, independent of the halo mass bins considered here, the XSB profiles of filament galaxies are X-ray brighter between

$\sim (0.3 - 0.5) \times R_{200m}$ by $20 - 45\%$ (Fig. 4.4). We investigate the source of this brightness by exploring the thermodynamic properties (ρ, T, and Z) of the hot gas in these galaxies in these different environments. We find that the filament galaxies show significantly enhanced thermodynamic properties compared to those in transition regions or voids/walls. They are up to 10× more likely to exhibit higher gas densities, 12× more likely to have higher temperatures, and 8× more likely to show elevated metallicities. These differences peak in the $10^{12.5}$ $M_\odot < M_{200m} < 10^{13.5}$ $M_\odot$ range, where ratios of the probability density functions across all quantities are consistently 50–70% higher for filament galaxies.

Taken together, the investigations presented in Chapt. 2, Chapt. 3, and Chapt. 4 provide a comprehensive framework for interpreting the X-ray emission from the hot CGM in the era of wide-area surveys like eROSITA. In Chapt. 2, we quantify crucial projection effects—such as contamination from correlated LSS, misclassified centrals, which must be accounted for when connecting simulations to stacked X-ray observations. Building on this understanding, Chapt. 3 demonstrates that the X-ray luminosity of the hot CGM is highly sensitive to the underlying halo mass distribution in stellar-mass-selected samples, and develops a forward modelling framework that jointly constrains both hot gas properties and AGN contributions. Finally, Chapt. 4 extends the analysis to the cosmic web, revealing that the large-scale environment imprints measurable signatures on the X-ray profiles of galaxies, with galaxies in filament environments producing significantly enhanced X-ray emission and thermodynamic properties. Altogether, these works highlight the intricate interplay between baryonic physics, halo demographics, and the cosmic environment, offering new pathways to leverage X-ray stacking analyses as precise probes of the diffuse hot CGM in galaxy halos.

5.1 Outlook

Modelling observed CGM profiles and comparing them with simulations is an active field that has been attracting increasing interest in recent years (Oppenheimer et al., 2020; Truong et al., 2023; Vladutescu-Zopp et al., 2024; Marini et al., 2024; Shreeram et al., 2025c,a,b; Grayson et al., 2025). This is due to its crucial role in constraining galaxy formation models and improving our understanding of how feedback and physics prescriptions affect the hot CGM and the baryon cycle (Péroux & Howk, 2020). Current state-of-the-art cosmological hydrodynamical simulations, calibrated to reproduce the galaxy stellar mass functions, successfully produce realistic galaxy populations. Yet differences persist in the prediction of the gas properties at MW-mass to galaxy group-mass scales, see e.g, Davies et al. (2020b); Truong et al. (2023); Khrykin et al. (2024); Wright et al. (2024); Popesso et al. (2024c); Lau et al. (2024); Medlock et al. (2024) as observed in the CGM at Milky Way masses, due to variations in feedback and baryonic physics implementations across different simulations. The hot CGM, probed by X-ray observations, provides a powerful benchmark to inform simulations (Zhang et al., 2024a,b). Alongside the progress in our understanding of how various stellar and AGN feedback prescriptions impact the hot CGM's properties, our work (Shreeram et al., 2025a) highlights another vital ingredient when comparing simulations with X-ray observations: the sensitivity of the X-ray CGM properties to the underlying halo mass distribution, stellar mass and redshift. The model and methodology developed

in this thesis provide the machinery for systematic comparisons of hot CGM profiles with data and across simulations. Future work applying the data-comparison framework established here to other state-of-the-art cosmological hydrodynamical simulations (e.g., EAGLE (Crain et al., 2015; Schaye et al., 2015), FLAMINGO (Schaye et al., 2023b), Magneticum (Dolag et al., 2005; Beck et al., 2016), SIMBA (Davé et al., 2019)) is required to self-consistently test the impact of different baryonic physics implementations across simulations.

On the observational side, going beyond current X-ray stacking measurements from e.g., Zhang et al. (2024a); Popesso et al. (2024c), upcoming X-ray missions like NewAthena (Nandra et al., 2013; Barret et al., 2020; Cruise et al., 2025), and HUBS (Cui et al., 2020) will extend detection limits, delivering higher spatial and spectral resolution, better point-source contamination control, and the sensitivity to detect fainter surface brightness levels. These capabilities will improve measurements of the hot CGM at higher redshifts and enable more precise comparisons with simulated spatially resolved hot gas distributions around MW-mass galaxies. The knowledge of projection effects (i.e., misclassified centrals, the local environment, emission from X-ray point sources; Chapt. 2 and Shreeram et al. 2025c) quantified in this thesis is a step toward fully exploiting these current and upcoming datasets, aiming to better interpret the hot X-ray CGM measurements in stacking experiments.

One of the outstanding challenges in the current paradigm of galaxy formation and evolution models implemented in hydrodynamical simulations is to jointly constrain the microscopic scales (e.g., subgrid model physics) and their impact on the diffuse gas within the halo (Crain & van de Voort, 2023). Our work in Chapt. 3 and accompanying paper Shreeram et al. (2025a) provides a new and novel technique to constrain the mean AGN X-ray luminosity of a galaxy sample jointly with the radial hot CGM gas distribution within the halo using the X-ray hot CGM (stacking) measurements as a new benchmark. Our forward model comparison with data opens a new perspective to constrain AGN feedback mechanisms using observationally motivated limits on allowed X-ray AGN luminosities at MW-mass scales. Future work on testing AGN feedback models in simulations with observationally permitted AGN X-ray luminosities offers a new avenue for refining sub-grid AGN physics (see e.g. Alexander & Hickox, 2012).

Our findings on the importance of environmental effects studied in Chapt. 4 for interpreting the hot CGM in X-rays open several promising directions. With the improved spectral resolution from missions like *XRISM* (Tashiro et al., 2020), *NewAthena* (Barret et al., 2020; Cruise et al., 2025), and the depth of *eROSITA* data (Merloni et al., 2024), it becomes feasible to search for X-ray excesses in filament galaxies using stacking techniques (e.g. Zhang et al., 2024a) combined with LSE classification from stage-4 surveys such as Euclid, 4MOST, DESI, and PFS. Future work should also explore the energy dependence of X-ray surface brightness profiles in the soft band (0.2–1keV), particularly for halos below 10^{12} $M_{\odot}$, to better probe the influence of large-scale structure on low-mass systems. On the theoretical side, further studies of gas clumping (Nagai & Lau, 2011; Zhuravleva et al., 2013; Avestruz et al., 2016), infalling hot streams (Zinger et al., 2016), mass assembly history (Marini et al., 2025), galaxy connectivity (Galárraga-Espinosa et al., 2023), and filament morphology (Galárraga-Espinosa et al., 2024; Yu et al., 2025) can help elucidate mechanisms driving enhanced X-ray emission in filaments. The tools and insights developed in this thesis lay the groundwork for jointly constraining CGM properties alongside the influence of the cosmic web, which is fundamental for understanding

galaxy formation within its cosmological context.

Taken together, the progress outlined in this thesis underscores that fully understanding the hot CGM requires an integrated approach, combining X-ray observations, careful modelling of projection and environmental effects, and robust and cautious comparisons across multiple hydrodynamical simulations. The methods and models developed here provide a critical framework for interpreting current and future X-ray surveys, enabling us to disentangle the complex interplay of baryonic physics, AGN feedback, halo demographics, and the cosmic web in shaping the hot gas around galaxies. As new data arrive from next-generation missions, alongside increasingly sophisticated simulations, we stand at the threshold of using the hot CGM as a precise cosmological and astrophysical probe. The challenges ahead in linking microphysical feedback processes to large-scale observables, quantifying environmental impacts, and constraining the diverse mechanisms governing baryon cycles offer an exciting frontier where theory and observation converge to refine our models of galaxy formation and evolution.

Bibliography

Aarseth S. J., 2003, Gravitational N-Body Simulations

Abazajian K. N., et al., 2009, The Astrophysical Journal Supplement Series, 182, 543

Abel T., Bryan G. L., Norman M. L., 2002, science, 295, 93

Ade P. A., et al., 2016, A&A, 594, A13

Agertz O., Kravtsov A. V., 2016, The Astrophysical Journal, 824, 79

Aird J., et al., 2013, The Astrophysical Journal, 775, 41

Aird J., Coil A. L., Georgakakis A., Nandra K., Barro G., Pérez-González P. G., 2015, MNRAS, 451, 1892

Aird J., Coil A. L., Georgakakis A., 2017, MNRAS, 465, 3390

Alam S., et al., 2021, Physical Review D, 103, 083533

Alexander D. M., Hickox R. C., 2012, New Astronomy Reviews, 56, 93

Alpaslan M., et al., 2015, MNRAS, 451, 3249

Anand A., Nelson D., Kauffmann G., 2021, Monthly Notices of the Royal Astronomical Society, 504, 65

Anders E., Grevesse N., 1989, Geochimica et Cosmochimica acta, 53, 197

Anderson M. E., Gaspari M., White S. D., Wang W., Dai X., 2015, MNRAS, 449, 3806

Anderson M. E., Churazov E., Bregman J. N., 2016, MNRAS, 455, 227

Angulo R. E., Springel V., White S. D. M., Jenkins A., Baugh C. M., Frenk C. S., 2012, MNRAS, 426, 2046

Arbey A., Mahmoudi F., 2021, Progress in Particle and Nuclear Physics, 119, 103865

Arthur J., et al., 2019, Monthly Notices of the Royal Astronomical Society, 484, 3968

Asari N. V., et al., 2007, Monthly Notices of the Royal Astronomical Society, 381, 263

Aung H., et al., 2023, MNRAS, 519, 1648

Avestruz C., Nagai D., Lau E. T., 2016, ApJ, 833, 227

Ayromlou M., Nelson D., Yates R. M., Kauffmann G., Renneby M., White S. D., 2021a, Monthly Notices of the Royal Astronomical Society, 502, 1051

Ayromlou M., Kauffmann G., Yates R. M., Nelson D., White S. D., 2021b, Monthly Notices of the Royal Astronomical Society, 505, 492

Ayromlou M., Nelson D., Pillepich A., 2023, MNRAS, 524, 5391

Bahé Y. M., McCarthy I. G., Balogh M. L., Font A. S., 2013, MNRAS, 430, 3017

Bahé Y. M., et al., 2017, Monthly Notices of the Royal Astronomical Society, 470, 4186

Baldry I. K., Glazebrook K., Brinkmann J., Ivezić Ž., Lupton R. H., Nichol R. C., Szalay A. S., 2004, The Astrophysical Journal, 600, 681

Baldry I. K., Glazebrook K., Driver S. P., 2008, Monthly Notices of the Royal Astronomical Society, 388, 945

Baldry I. K., et al., 2012, Monthly Notices of the Royal Astronomical Society, 421, 621

Barret D., Decourchelle A., Fabian A., Guainazzi M., Nandra K., Smith R., den Herder J.-W., 2020, Astronomische Nachrichten, 341, 224

Barrow J. D., Matzner R. A., 1977, Monthly Notices of the Royal Astronomical Society, 181, 719

Beck R., 2009, Astrophysics and Space Sciences Transactions (ASTRA), 5, 43

Beck A. M., et al., 2016, MNRAS, 455, 2110

Begelman M. C., Fabian A., 1990, Monthly Notices of the Royal Astronomical Society (ISSN 0035-8711), vol. 244, May 15, 1990, p. 26P-29P. Research supported by the Alfred P. Sloan Foundation and Royal Society., 244, 26P

Behroozi P. S., Wechsler R. H., Conroy C., 2013, The Astrophysical Journal, 770, 57

Behroozi P., Wechsler R. H., Hearin A. P., Conroy C., 2019, MNRAS, 488, 3143

Bell E. F., de Jong R. S., 2001, The Astrophysical Journal, 550, 212

Bell E. F., et al., 2004, The Astrophysical Journal, 608, 752

Benítez-Llambay A., Navarro J. F., Abadi M. G., Gottlöber S., Yepes G., Hoffman Y., Steinmetz M., 2013, ApJ Letters, 763, L41

Benson A. J., Bower R. G., Frenk C. S., Lacey C. G., Baugh C. M., Cole S., 2003, ApJ, 599, 38

Berger M. J., Oliger J., 1984, Journal of computational Physics, 53, 484

Berlind A. A., Weinberg D. H., 2002, The Astrophysical Journal, 575, 587

Berlok T., Pfrommer C., 2019, Monthly Notices of the Royal Astronomical Society, 489, 3368

Bertone S., Schaye J., Dalla Vecchia C., Booth C. M., Theuns T., Wiersma R. P. C., 2010, MNRAS, 407, 544

Bhandari S., Flynn C., 2021, Universe, 7, 85

Bhattacharyya J., Das S., Gupta A., Mathur S., Krongold Y., 2023, The Astrophysical Journal, 952, 41

Biffi V., Dolag K., Böhringer H., 2013, MNRAS, 428, 1395

Biffi V., Planelles S., Borgani S., Rasia E., Murante G., Fabjan D., Gaspari M., 2018a, MNRAS, 476, 2689

Biffi V., Dolag K., Merloni A., 2018b, MNRAS, 481, 2213

Binggeli B., Sandage A., Tammann G. A., 1988, ARA&A, 26, 509

Birnboim Y., Dekel A., 2003, Monthly Notices of the Royal Astronomical Society, 345, 349

Blanton M. R., Moustakas J., 2009, Annual Review of Astronomy and Astrophysics, 47, 159

Blanton M. R., et al., 2003, The Astrophysical Journal, 592, 819

Blanton M. R., Eisenstein D., Hogg D. W., Schlegel D. J., Brinkmann J., 2005, ApJ, 629, 143

Blumenthal G. R., Faber S., Primack J. R., Rees M. J., 1984, Nature, 311, 517

Bocquet S., et al., 2019, The Astrophysical Journal, 878, 55

Bogdán Á., et al., 2013a, The Astrophysical Journal, 772, 97

Bogdán Á., Forman W. R., Kraft R. P., Jones C., 2013b, The Astrophysical Journal, 772, 98

Bogdán Á., Bourdin H., Forman W. R., Kraft R. P., Vogelsberger M., Hernquist L., Springel V., 2017, The Astrophysical Journal, 850, 98

Bogdán Á., et al., 2023, The Astrophysical Journal, 953, 42

Böhringer H., Werner N., 2010, The Astronomy and Astrophysics Review, 18, 127

Bond J. R., Kofman L., Pogosyan D., 1996, Nature, 380, 603

Bonjean V., Aghanim N., Douspis M., Malavasi N., Tanimura H., 2020, Astronomy & Astrophysics, 638, A75

Bordoloi R., et al., 2014, The Astrophysical Journal, 796, 136

Boroson B., Kim D.-W., Fabbiano G., 2011, The Astrophysical Journal, 729, 12

Bowen D. V., Chelouche D., Jenkins E. B., Tripp T. M., Pettini M., York D. G., Frye B. L., 2016, The Astrophysical Journal, 826, 50

Brandt W., Alexander D., 2015, The Astronomy and Astrophysics Review, 23, 1

Bregman J. N., Anderson M. E., Miller M. J., Hodges-Kluck E., Dai X., Li J.-T., Li Y., Qu Z., 2018, The Astrophysical Journal, 862, 3

Bregman J. N., Hodges-Kluck E., Qu Z., Pratt C., Li J.-T., Yun Y., 2022, The Astrophysical Journal, 928, 14

Brinchmann J., Charlot S., White S. D., Tremonti C., Kauffmann G., Heckman T., Brinkmann J., 2004, Monthly notices of the royal astronomical society, 351, 1151

Bromm V., Larson R. B., 2004, Annu. Rev. Astron. Astrophys., 42, 79

Bryan G. L., et al., 2014, The Astrophysical Journal Supplement Series, 211, 19

Buchner J., Bauer F. E., 2017, MNRAS, 465, 4348

Buchner J., et al., 2015, The Astrophysical Journal, 802, 89

Buchner J., et al., 2024, A&A, 692, A161

Buck T., Pfrommer C., Pakmor R., Grand R. J., Springel V., 2020, Monthly Notices of the Royal Astronomical Society, 497, 1712

Butcher H., Oemler A., 1984, ApJ, 285, 426

Butsky I. S., Quinn T. R., 2018, The Astrophysical Journal, 868, 108

Butsky I. S., et al., 2022, The Astrophysical Journal, 935, 69

Cantalupo S., Porciani C., Lilly S. J., Miniati F., 2005, The Astrophysical Journal, 628, 61

Cantalupo S., Arrigoni-Battaia F., Prochaska J. X., Hennawi J. F., Madau P., 2014, Nature, 506, 63

Cappelluti N., et al., 2017, The Astrophysical Journal Letters, 847, L11

Carlson J., White M., 2010, The Astrophysical Journal Supplement Series, 190, 311

Carroll S. M., 2001, Living reviews in relativity, 4, 1

Cassisi S., Salaris M., 2013, Old stellar populations: how to study the fossil record of galaxy formation. John Wiley & Sons

Catinella B., et al., 2013, MNRAS, 436, 34

Cautun M. C., van de Weygaert R., 2011, arXiv preprint arXiv:1105.0370

Cautun M., van de Weygaert R., Jones B. J., 2013, MNRAS, 429, 1286

Cautun M., Van De Weygaert R., Jones B. J., Frenk C. S., 2014, Monthly Notices of the Royal Astronomical Society, 441, 2923

Cavaliere A., Fusco-Femiano R., 1976, Astronomy and Astrophysics, vol. 49, no. 1, May 1976, p. 137-144., 49, 137

Cen R., Ostriker J., 1992, Astrophysical Journal, Part 1 (ISSN 0004-637X), vol. 393, no. 1, July 1, 1992, p. 22-41., 393, 22

Cen R., Ostriker J. P., 1999, The Astrophysical Journal, 514, 1

Cen R., Pop A. R., Bahcall N. A., 2014, PNAS, 111, 7914

Ceverino D., Klypin A., 2009, The Astrophysical Journal, 695, 292

Chadayammuri U., Bogdán Á., Oppenheimer B. D., Kraft R. P., Forman W. R., Jones C., 2022, ApJ, 936, L15

Chan T., Kereš D., Gurvich A. B., Hopkins P. F., Trapp C., Ji S., Faucher-Giguère C.-A., 2022, Monthly Notices of the Royal Astronomical Society, 517, 597

Chiosi C., Carraro G., 2002, Monthly Notices of the Royal Astronomical Society, 335, 335

Choi E., Ostriker J. P., Naab T., Oser L., Moster B. P., 2015, Monthly Notices of the Royal Astronomical Society, 449, 4105

Churchill C. W., Vander Vliet J. R., Trujillo-Gomez S., Kacprzak G. G., Klypin A., 2015, The Astrophysical Journal, 802, 10

Cole S., Lacey C. G., Baugh C. M., Frenk C. S., 2000, Monthly Notices of the Royal Astronomical Society, 319, 168

Cole S., et al., 2005, Monthly Notices of the Royal Astronomical Society, 362, 505

Colless M., et al., 2001, MNRAS, 328, 1039

Collin S., Boisson C., Mouchet M., Dumont A.-M., Coupé S., Porquet D., Rokaki E., 2002, A&A, 388, 771

Comparat J., et al., 2017, arXiv e-prints, p. arXiv:1711.06575

Comparat J., et al., 2019, MNRAS, 487, 2005

Comparat J., et al., 2020, The Open Journal of Astrophysics, 3, 13

Comparat J., et al., 2022, A&A, 666, A156

Comparat J., et al., 2025, A&A, 697, A173

Conroy C., 2013, Annual Review of Astronomy and Astrophysics, 51, 393

Conselice C. J., 2014, Annual Review of Astronomy and Astrophysics, 52, 291

Cooke R. J., Pettini M., Jorgenson R. A., Murphy M. T., Steidel C. C., 2014, The Astrophysical Journal, 781, 31

Cooray A., Sheth R., 2002, Phys. Rep., 372, 1

Cortese L., Catinella B., Boissier S., Boselli A., Heinis S., 2011, MNRAS, 415, 1797

Coupon J., et al., 2015, MNRAS, 449, 1352

Cowie L. L., Songaila A., Hu E. M., Cohen J., 1996, arXiv preprint astro-ph/9606079

Crain R. A., van de Voort F., 2023, Annual Review of Astronomy and Astrophysics, 61, 473

Crain R. A., et al., 2015, MNRAS, 450, 1937

Croton D. J., et al., 2006, Monthly Notices of the Royal Astronomical Society, 365, 11

Cruise M., et al., 2025, Nat. Astron., 9, 36

Cui W., et al., 2016, MNRAS, 456, 2566

Cui W., Knebe A., Yepes G., Yang X., Borgani S., Kang X., Power C., Staveley-Smith L., 2018a, MNRAS, 473, 68

Cui W., et al., 2018b, Monthly Notices of the Royal Astronomical Society, 480, 2898

Cui W., et al., 2020, Journal of Low Temperature Physics, 199, 502

Curti M., Mannucci F., Cresci G., Maiolino R., 2020, Monthly Notices of the Royal Astronomical Society, 491, 944

Cyburt R. H., Fields B. D., Olive K. A., Yeh T.-H., 2016, Reviews of Modern Physics, 88, 015004

DES Collaboration Abbott T., et al., 2025, arXiv preprint arXiv:2503.13632

Das S., Mathur S., Gupta A., Nicastro F., Krongold Y., Null C., 2019, The Astrophysical Journal, 885, 108

Das S., Chiang Y.-K., Mathur S., 2023, arXiv e-prints, p. arXiv:2305.12353

Davé R., Thompson R., Hopkins P. F., 2016, Monthly Notices of the Royal Astronomical Society, 462, 3265

Davé R., Anglés-Alcázar D., Narayanan D., Li Q., Rafieferantsoa M. H., Appleby S., 2019, MNRAS, 486, 2827

Davies J. J., Crain R. A., Oppenheimer B. D., Schaye J., 2020b, MNRAS, 491, 4462

Davies J. J., Crain R. A., Oppenheimer B. D., Schaye J., 2020a, MNRAS, 491, 4462

De Jong R. S., Simard L., Davies R. L., Saglia R., Burstein D., Colless M., McMahan R., Wegner G., 2004, Monthly Notices of the Royal Astronomical Society, 355, 1155

De Jong R. S., et al., 2012, in Ground-based and airborne instrumentation for astronomy IV. pp 252–266

De Lapparent V., Geller M. J., Huchra J. P., 1986, ApJ, Part 2-Letters to the Editor (ISSN 0004-637X), vol. 302, March 1, 1986, p. L1-L5. Research supported by the Smithsonian Institution., 302, L1

De Luca A., Molendi S., 2004, A&A, 419, 837

De Vaucouleurs G., 1959, in , Astrophysik iv: Sternsysteme/astrophysics iv: Stellar systems. Springer, pp 275–310

Dekel A., Birnboim Y., 2006, Monthly notices of the royal astronomical society, 368, 2

Dekel A., Silk J., 1986, Astrophysical Journal, Part 1 (ISSN 0004-637X), vol. 303, April 1, 1986, p. 39-55., 303, 39

Dekel A., Woo J., 2003, MNRAS, 344, 1131

Dekel A., Sari R., Ceverino D., 2009, The Astrophysical Journal, 703, 785

Dey A., et al., 2019, The Astronomical Journal, 157, 168

Di Mascolo L., et al., 2024, arXiv preprint arXiv:2403.00909

Di Matteo T., Springel V., Hernquist L., 2005, nature, 433, 604

Diemer B., Mansfield P., Kravtsov A. V., More S., 2017, The Astrophysical Journal, 843, 140

Dijkstra M., 2014, Publications of the Astronomical Society of Australia, 31, e040

Dolag K., 2015, IAU General Assembly, 29, 2250156

Dolag K., Grasso D., Springel V., Tkachev I., 2005, J. Cosmology Astropart. Phys., 2005, 009

Dolag K., Borgani S., Murante G., Springel V., 2009, MNRAS, 399, 497

Dolag K., et al., 2025, arXiv preprint arXiv:2504.01061

Donahue M., Voit G. M., 2022, Physics Reports, 973, 1

Donnari M., et al., 2019, MNRAS, 485, 4817

Donnari M., Pillepich A., Nelson D., Marinacci F., Vogelsberger M., Hernquist L., 2021, MNRAS, 506, 4760

Dressler A., 1980, ApJ, Part 1, vol. 236, Mar. 1, 1980, p. 351-365., 236, 351

Dressler A., et al., 1997, ApJ, 490, 577

Driver S. P., et al., 2011, MNRAS, 413, 971

Driver S. P., et al., 2022, MNRAS, 513, 439

Dubois Y., et al., 2014, Monthly Notices of the Royal Astronomical Society, 444, 1453

Duras F., et al., 2020, A&A, 636, A73

Eckert D., Gaspari M., Gastaldello F., Le Brun A. M., O'Sullivan E., 2021, Universe, 7, 142

Einasto M., et al., 2018, Astronomy & Astrophysics, 620, A149

Einstein A., 1915, Sitzungsberichte der Königlich Preußischen Akademie der Wissenschaften, pp 844–847

Eisenstein D. J., et al., 2005, The Astrophysical Journal, 633, 560

Ellis G., Harrison E., 1974, Comments on Astrophysics and Space Physics, Vol. 6, p. 23-27, 6, 23

Elmegreen D. M., Elmegreen B. G., 1987, Astrophysical Journal, Part 1 (ISSN 0004-637X), vol. 314, March 1, 1987, p. 3-9., 314, 3

Erb D. K., Shapley A. E., Pettini M., Steidel C. C., Reddy N. A., Adelberger K. L., 2006, The Astrophysical Journal, 644, 813

Fabbiano G., 1996, in Röntgenstrahlung from the Universe. pp 347–356

Fabbiano G., 2006, Annu. Rev. Astron. Astrophys., 44, 323

Fabian A. C., 2012, ARA&A, 50, 455

Faerman Y., Werk J. K., 2023, ApJ, 956, 92

Faerman Y., Sternberg A., McKee C. F., 2017, ApJ, 835, 52

Faerman Y., Sternberg A., McKee C. F., 2020, The Astrophysical Journal, 893, 82

Faerman Y., Pandya V., Somerville R. S., Sternberg A., 2022, The Astrophysical Journal, 928, 37

Falcón-Barroso J., Knapen J. H., 2013, Secular Evolution of Galaxies. Vol. 23, Cambridge University Press

Fall S. M., Efstathiou G., 1980, Monthly Notices of the Royal Astronomical Society, 193, 189

Fardal M. A., Katz N., Gardner J. P., Hernquist L., Weinberg D. H., Davé R., 2001, The Astrophysical Journal, 562, 605

Farina E. P., et al., 2019, The Astrophysical Journal, 887, 196

Faucher-Giguère C.-A., Oh S. P., 2023, Annual Review of Astronomy and Astrophysics, 61, 131

Faucher-Giguère C.-A., Quataert E., 2012, Monthly Notices of the Royal Astronomical Society, 425, 605

Faucher-Giguère C.-A., Kereš D., Ma C.-P., 2011, Monthly Notices of the Royal Astronomical Society, 417, 2982

Feng Y., Di-Matteo T., Croft R. A., Bird S., Battaglia N., Wilkins S., 2016, Monthly Notices of the Royal Astronomical Society, 455, 2778

Field G. B., 1965, Astrophysical Journal, vol. 142, p. 531, 142, 531

Fielding D., Quataert E., McCourt M., Thompson T. A., 2017, MNRAS, 466, 3810

Finlator K., Davé R., 2008, Monthly Notices of the Royal Astronomical Society, 385, 2181

Fontanot F., De Lucia G., Monaco P., Somerville R. S., Santini P., 2009, Monthly Notices of the Royal Astronomical Society, 397, 1776

Foreman-Mackey D., Hogg D. W., Lang D., Goodman J., 2013, Publications of the Astronomical Society of the Pacific, 125, 306

Foster A., Ji L., Smith R., Brickhouse N., 2012, The Astrophysical Journal, 756, 128

Fox A., Davé R., eds, 2017, Gas Accretion onto Galaxies Astrophysics and Space Science Library Vol. 430, doi:10.1007/978-3-319-52512-9.

Fukugita M., Peebles P. J. E., 2004, The Astrophysical Journal, 616, 643

Fumagalli M., 2024, arXiv preprint arXiv:2409.00174

Galárraga-Espinosa D., Aghanim N., Langer M., Tanimura H., 2021, A&A, 649, A117

Galárraga-Espinosa D., Garaldi E., Kauffmann G., 2023, A&A, 671, A160

Galárraga-Espinosa D., et al., 2024, A&A, 684, A63

Galeazzi M., Gupta A., Covey K., Ursino E., 2007, The Astrophysical Journal, 658, 1081

Ganeshaiah Veena P., Cautun M., Tempel E., van de Weygaert R., Frenk C. S., 2019, MNRAS, 487, 1607

Garrel C., et al., 2022, Astronomy & Astrophysics, 663, A3

Gebhardt M., et al., 2024, MNRAS, 529, 4896

Genel S., et al., 2014, Monthly Notices of the Royal Astronomical Society, 445, 175

Ghirardini V., et al., 2024, Astronomy & Astrophysics, 689, A298

Gilfanov M., 2004, MNRAS, 349, 146

Gilli R., Comastri A., Hasinger G., 2007, A&A, 463, 79

Gilmore G., Reid N., 1983, Monthly Notices of the Royal Astronomical Society, 202, 1025

Girelli G., Pozzetti L., Bolzonella M., Giocoli C., Marulli F., Baldi M., 2020, A&A, 634, A135

Giri S. K., Schneider A., 2021, Journal of Cosmology and Astroparticle Physics, 2021, 046

Girichidis P., Werhahn M., Pfrommer C., Pakmor R., Springel V., 2024, Monthly Notices of the Royal Astronomical Society, 527, 10897

Gouin C., Aghanim N., Bonjean V., Douspis M., 2020, Astronomy & Astrophysics, 635, A195

Governato F., et al., 2010, Nature, 463, 203

Grand R. J., et al., 2017, Monthly Notices of the Royal Astronomical Society, 467, 179

Graves G. J., Faber S., Schiavon R. P., 2009, The Astrophysical Journal, 693, 486

Grayson S., Scannapieco E., Comparat J., ZuHone J. A., Zhang Y., Shreeram S., Bruggen M., Bulbul E., 2025, arXiv e-prints, p. arXiv:2506.09123

Grimm H. J., Gilfanov M., Sunyaev R., 2003, MNRAS, 339, 793

Guedes J., Callegari S., Madau P., Mayer L., 2011, The Astrophysical Journal, 742, 76

Gunn J. E., Gott III J. R., 1972, ApJ, 176, 1

Guo Q., et al., 2011, Monthly Notices of the Royal Astronomical Society, 413, 101

Gupta A., Mathur S., Kingsbury J., Das S., Krongold Y., 2023, Nature Astronomy, 7, 799

Guzzo L., et al., 2014, A&A, 566, A108

Habib S., et al., 2012, arXiv e-prints, p. arXiv:1211.4864

Habib S., et al., 2016, New Astronomy, 42, 49

Habouzit M., et al., 2019, MNRAS, 484, 4413

Hahn O., Porciani C., Carollo C. M., Dekel A., 2007, MNRAS, 375, 489

Hallinan G., et al., 2019, arXiv preprint arXiv:1907.07648

Harrison C. M., Ramos Almeida C., 2024, Galaxies, 12, 17

Hasinger G., 2008, A&A, 490, 905

Hastings W. K., 1970, Biometrika, 57, 97

Hayes M., Melinder J., Östlin G., Scarlata C., Lehnert M. D., Mannerström-Jansson G., 2016, ApJ, 828, 49

Heckman T. M., Best P. N., 2014, Annual Review of Astronomy and Astrophysics, 52, 589

Henden N. A., Puchwein E., Shen S., Sijacki D., 2018, Monthly Notices of the Royal Astronomical Society, 479, 5385

Henley D. B., Shelton R. L., 2010, The Astrophysical Journal Supplement Series, 187, 388

Henley D. B., Shelton R. L., 2012, The Astrophysical Journal Supplement Series, 202, 14

Henley D. B., Shelton R. L., 2013, The Astrophysical Journal, 773, 92

Hennawi J. F., Prochaska J. X., 2013, The Astrophysical Journal, 766, 58

Henriques B. M., White S. D., Thomas P. A., Angulo R., Guo Q., Lemson G., Springel V., Overzier R., 2015, Monthly Notices of the Royal Astronomical Society, 451, 2663

Hernández-Aguayo C., et al., 2023, MNRAS, 524, 2556

Hernquist L., Katz N., Weinberg D. H., Miralda-Escude J., 1996, The Astrophysical Journal, 457, L51

Hikage C., Mandelbaum R., Leauthaud A., Rozo E., Rykoff E. S., 2018, MNRAS, 480, 2689

Hinshaw G., et al., 2013, ApJS, 208, 19

Hirschmann M., De Lucia G., Fontanot F., 2016, Monthly Notices of the Royal Astronomical Society, 461, 1760

Hoekstra H., Jain B., 2008, Annual Review of Nuclear and Particle Science, 58, 99

Holmberg E., 1941, ApJ, 94, 385

Hoosain M., et al., 2024, MNRAS, 528, 4139

Hopkins P. F., 2015, Monthly Notices of the Royal Astronomical Society, 450, 53

Hopkins P. F., Elvis M., 2010, Monthly Notices of the Royal Astronomical Society, 401, 7

Hopkins P. F., Quataert E., Murray N., 2012, Monthly Notices of the Royal Astronomical Society, 421, 3522

Hopkins P. F., Kereš D., Oñorbe J., Faucher-Giguère C.-A., Quataert E., Murray N., Bullock J. S., 2014, Monthly Notices of the Royal Astronomical Society, 445, 581

Hopkins P. F., et al., 2018, Monthly Notices of the Royal Astronomical Society, 480, 800

Hoshino H., et al., 2015, MNRAS, 452, 998

Hubble E., 1929, Proceedings of the national academy of sciences, 15, 168

Huchra J. P., et al., 2012, ApJ Supplement Series, 199, 26

Ider Chitham J., et al., 2020, Monthly Notices of the Royal Astronomical Society, 499, 4768

Ishiyama T., et al., 2021, MNRAS, 506, 4210

Jetley P., Gioachin F., Mendes C., Kale L. V., Quinn T., 2008, in 2008 IEEE International Symposium on Parallel and Distributed Processing. pp 1–12

Ji S., et al., 2020, Monthly Notices of the Royal Astronomical Society, 496, 4221

Jing Y., Zhang P., Lin W., Gao L., Springel V., 2006, The Astrophysical Journal, 640, L119

Jones D. H., et al., 2009, MNRAS, 399, 683

Kaaret P., et al., 2020, Nature Astronomy, 4, 1072

Kakoly A., Stern J., Faucher-Giguère C.-A., Fielding D. B., Goldner R., Sun G., Hummels C. B., 2025, arXiv preprint arXiv:2504.17001

Katz H., Rey M. P., Cadiou C., Kimm T., Agertz O., 2024, arXiv preprint arXiv:2411.07282

Kauffmann G., et al., 2003, Monthly Notices of the Royal Astronomical Society, 341, 33

Kaviraj S., et al., 2017, Monthly Notices of the Royal Astronomical Society, 467, 4739

Kay S. T., Pearce F. R., Frenk C. S., Jenkins A., 2002, Monthly Notices of the Royal Astronomical Society, 330, 113

Kennicutt Jr R. C., 1998, Annual Review of Astronomy and Astrophysics, 36, 189

Kereš D., Katz N., Weinberg D. H., Davé R., 2005, Monthly Notices of the Royal Astronomical Society, 363, 2

Kereš D., Katz N., Fardal M., Davé R., Weinberg D. H., 2009, Monthly Notices of the Royal Astronomical Society, 395, 160

Khandai N., Di Matteo T., Croft R., Wilkins S., Feng Y., Tucker E., DeGraf C., Liu M.-S., 2015, Monthly Notices of the Royal Astronomical Society, 450, 1349

Khrykin I. S., Sorini D., Lee K.-G., Davé R., 2024, MNRAS, 529, 537

Kilbinger M., 2015, Reports on Progress in Physics, 78, 086901

Kleiner D., Pimbblet K. A., Jones D. H., Koribalski B. S., Serra P., 2017, MNRAS, 466, 4692

Klypin A. A., Shandarin S. F., 1983, Monthly Notices of the Royal Astronomical Society, 204, 891

Knobel C., 2012, arXiv preprint arXiv:1208.5931

Kofman L. A., Gnedin N. Y., Bahcall N. A., 1993, Astrophysical Journal, Part 1 (ISSN 0004-637X), vol. 413, no. 1, p. 1-9., 413, 1

Kollmeier J. A., et al., 2014, The Astrophysical Journal Letters, 789, L32

Köppen J., Weidner C., Kroupa P., 2007, Monthly Notices of the Royal Astronomical Society, 375, 673

Kormendy J., Ho L. C., 2013, Annual Review of Astronomy and Astrophysics, 51, 511

Kormendy J., Kennicutt Jr R. C., 2004, Annu. Rev. Astron. Astrophys., 42, 603

Koutroumpa D., Acero F., Lallement R., Ballet J., Kharchenko V., 2007, A&A, 475, 901

Kraljic K., et al., 2020, MNRAS, 491, 4294

Kravtsov A. V., Klypin A. A., Khokhlov A. M., 1997, The Astrophysical Journal Supplement Series, 111, 73

Kravtsov A. V., Berlind A. A., Wechsler R. H., Klypin A. A., Gottlöber S., Allgood B., Primack J. R., 2004, The Astrophysical Journal, 609, 35

Kriek M., et al., 2006, The Astrophysical Journal, 645, 44

Kuchner U., et al., 2022, MNRAS, 510, 581

Lacey C., Silk J., 1991, Astrophysical Journal, Part 1 (ISSN 0004-637X), vol. 381, Nov. 1, 1991, p. 14-32., 381, 14

Lagos C. d. P., Tobar R. J., Robotham A. S., Obreschkow D., Mitchell P. D., Power C., Elahi P. J., 2018, Monthly Notices of the Royal Astronomical Society, 481, 3573

Laigle C., et al., 2018, MNRAS, 474, 5437

Lan T.-W., 2020, The Astrophysical Journal, 897, 97

Lan T.-W., Mo H., 2018, The Astrophysical Journal, 866, 36

Lau E. T., et al., 2024, arXiv preprint arXiv:2412.04559

Lauer T. R., Postman M., Strauss M. A., Graves G. J., Chisari N. E., 2014, The Astrophysical Journal, 797, 82

Laureijs R., et al., 2011, arXiv preprint arXiv:1110.3193

Laurent P., et al., 2016, Journal of Cosmology and Astroparticle Physics, 2016, 060

Le Brun A. M., McCarthy I. G., Schaye J., Ponman T. J., 2014, MNRAS, 441, 1270

Leauthaud A., et al., 2012, ApJ, 744, 159

Leclercq F., Lavaux G., Jasche J., Wandelt B., 2016, Journal of Cosmology and Astroparticle Physics, 2016, 027

Leclercq F., et al., 2020, Astronomy & Astrophysics, 635, A82

Lee K.-G., Ata M., Khrykin I. S., Huang Y., Prochaska J. X., Cooke J., Zhang J., Batten A., 2022, The Astrophysical Journal, 928, 9

Lehmer B., et al., 2016, The Astrophysical Journal, 825, 7

Lehmer B. D., et al., 2019, The Astrophysical Journal Supplement Series, 243, 3

Lehner N., Howk J. C., Wakker B. P., 2015, The Astrophysical Journal, 804, 79

Lehner N., et al., 2022, The Astrophysical Journal, 936, 156

Leung C., et al., 2021, The Astronomical Journal, 161, 81

Lewis I., et al., 2002, MNRAS, 334, 673

Li Y., Bregman J., 2017, The Astrophysical Journal, 849, 105

Li J.-T., Bregman J. N., Wang Q. D., Crain R. A., Anderson M. E., Zhang S., 2017, The Astrophysical Journal Supplement Series, 233, 20

Li J. S., et al., 2023, The Astrophysical Journal, 952, 137

Liao S., Gao L., 2019, Monthly Notices of the Royal Astronomical Society, 485, 464

Libeskind N. I., et al., 2018, MNRAS, 473, 1195

Lilly S. J., Carollo C. M., Pipino A., Renzini A., Peng Y., 2013, The Astrophysical Journal, 772, 119

Lim S., Mo H., Li R., Liu Y., Ma Y.-Z., Wang H., Yang X., 2018, The Astrophysical Journal, 854, 181

Lim S., Barnes D., Vogelsberger M., Mo H., Nelson D., Pillepich A., Dolag K., Marinacci F., 2021, MNRAS, 504, 5131

Locatelli N., et al., 2024, A&A, 681, A78

Lochhaas C., Bryan G. L., Li Y., Li M., Fielding D., 2020, Monthly Notices of the Royal Astronomical Society, 493, 1461

Lovell C. C., Vijayan A. P., Thomas P. A., Wilkins S. M., Barnes D. J., Irodotou D., Roper W., 2021, Monthly Notices of the Royal Astronomical Society, 500, 2127

Lovisari L., Ettori S., 2021, The Physical Properties of the Groups of Galaxies

Lovisari L., Ettori S., Gaspari M., Giles P. A., 2021, Universe, 7, 139

Luo B., et al., 2016, The Astrophysical Journal Supplement Series, 228, 2

Lyskova N., Churazov E., Khabibullin I., Burenin R., Starobinsky A., Sunyaev R., 2023, MNRAS, 525, 898

Macquart J.-P., et al., 2020, Nature, 581, 391

Maiolino R., Mannucci F., 2019, The Astronomy and Astrophysics Review, 27, 3

Malavasi N., et al., 2017, MNRAS, 465, 3817

Maller A. H., Bullock J. S., 2004, Monthly Notices of the Royal Astronomical Society, 355, 694

Mantz A. B., et al., 2015, Monthly Notices of the Royal Astronomical Society, 446, 2205

Marconi A., Hunt L. K., 2003, The Astrophysical Journal, 589, L21

Marinacci F., et al., 2018, MNRAS, 480, 5113

Marini I., et al., 2024, A&A, 689, A7

Marini I., et al., 2025, arXiv preprint arXiv:2503.19121

Marra R., Churchill C. W., Doughty C., Kacprzak G. G., Charlton J., Nielsen N. M., Ceverino D., Trujillo-Gomez S., 2021, Monthly Notices of the Royal Astronomical Society, 508, 4938

Martel H., Robichaud F., Barai P., 2014, The Astrophysical Journal, 786, 79

Martin G., Kaviraj S., Devriendt J., Dubois Y., Pichon C., 2018, Monthly Notices of the Royal Astronomical Society, 480, 2266

Martínez H. J., Muriel H., Coenda V., 2016, Monthly Notices of the Royal Astronomical Society, 455, 127

Martizzi D., et al., 2019, Monthly Notices of the Royal Astronomical Society, 486, 3766

Mashchenko S., Couchman H. M. P., Wadsley J., 2006, Nature, 442, 539

Mashchenko S., Wadsley J., Couchman H. M. P., 2008, Science, 319, 174

Mathur S., Das S., Gupta A., Krongold Y., 2023, MNRAS: Letters, 525, L11

McCarthy I. G., Schaye J., Bird S., Le Brun A. M. C., 2016, Monthly Notices of the Royal Astronomical Society, p. stw2792

McCourt M., Parrish I. J., Sharma P., Quataert E., 2011, Monthly Notices of the Royal Astronomical Society, 413, 1295

McCourt M., Sharma P., Quataert E., Parrish I. J., 2012, Monthly Notices of the Royal Astronomical Society, 419, 3319

McKee C. F., Ostriker J. P., 1977, The Astrophysical Journal, 218, 148

McNamara B., Nulsen P., 2007, Annu. Rev. Astron. Astrophys., 45, 117

McQuinn M., 2013, The Astrophysical Journal Letters, 780, L33

Medlock I., Nagai D., Singh P., Oppenheimer B., Anglés-Alcázar D., Villaescusa-Navarro F., 2024, The Astrophysical Journal, 967, 32

Medlock I., et al., 2025, The Astrophysical Journal, 980, 61

Mellier Y., 1999, Annual Review of Astronomy and Astrophysics, 37, 127

Merloni A., et al., 2024, A&A, 682, A34

Merritt D., 1999, Publications of the Astronomical Society of the Pacific, 111, 129

Merson A. I., et al., 2013, MNRAS, 429, 556

Miller M. J., Bregman J. N., 2015, The Astrophysical Journal, 800, 14

Mineo S., Gilfanov M., Sunyaev R., 2012, MNRAS, 419, 2095

Mitchell P. D., et al., 2018, Monthly Notices of the Royal Astronomical Society, 474, 492

Mo H., Miralda-Escudé J., 1996, arXiv preprint astro-ph/9603027

Mo H., Mao S., White S. D., 1998, Monthly Notices of the Royal Astronomical Society, 295, 319

Mo H., Van den Bosch F., White S., 2010, Galaxy formation and evolution. Cambridge University Press

Moster B. P., Somerville R. S., Maulbetsch C., Van Den Bosch F. C., Macciò A. V., Naab T., Oser L., 2010, The Astrophysical Journal, 710, 903

Moster B. P., Naab T., White S. D., 2013, Monthly Notices of the Royal Astronomical Society, 428, 3121

Moster B. P., Naab T., White S. D. M., 2020, MNRAS, 499, 4748

Mostoghiu R., et al., 2021, Monthly Notices of the Royal Astronomical Society, 501, 5029

Muñoz J. B., Loeb A., 2018, Physical Review D, 98, 103518

Munshi D., Valageas P., Van Waerbeke L., Heavens A., 2008, Physics Reports, 462, 67

Muratov A. L., Kereš D., Faucher-Giguère C.-A., Hopkins P. F., Quataert E., Murray N., 2015, Monthly Notices of the Royal Astronomical Society, 454, 2691

Mushotzky R. F., et al., 2019, arXiv preprint arXiv:1903.04083

Naab T., Ostriker J. P., 2017, Annual review of astronomy and astrophysics, 55, 59

Nagai D., Lau E. T., 2011, ApJ, 731, L10

Naiman J. P., et al., 2018, MNRAS, 477, 1206

Nakashima S., Inoue Y., Yamasaki N., Sofue Y., Kataoka J., Sakai K., 2018, ApJ, 862, 34

Nandra K., et al., 2013, arXiv preprint arXiv:1306.2307

Navdha Busch P., White S. D. M., 2025, MNRAS, 539, 1248

Neistein E., Van Den Bosch F. C., Dekel A., 2006, Monthly Notices of the Royal Astronomical Society, 372, 933

Nelson D., et al., 2015, Astronomy and Computing, 13, 12

Nelson D., et al., 2018, MNRAS, 475, 624

Nelson D., et al., 2019, Computational Astrophysics and Cosmology, 6, 1

Nelson D., et al., 2020, Monthly Notices of the Royal Astronomical Society, 498, 2391

Nelson D., et al., 2023, MNRAS, 522, 3665

Ng Y. V., et al., 2025, arXiv preprint arXiv:2503.11139

Nicastro F., et al., 2005, Nature, 433, 495

Noeske K., et al., 2007, The Astrophysical Journal, 660, L43

Nuza S. E., Parisi F., Scannapieco C., Richter P., Gottlöber S., Steinmetz M., 2014, MNRAS, 441, 2593

Ocker S. K., Chen M., Oh S. P., Sharma P., 2025, arXiv preprint arXiv:2503.02329

Ocvirk P., Pichon C., Teyssier R., 2008, Monthly Notices of the Royal Astronomical Society, 390, 1326

Odekon M. C., Hallenbeck G., Haynes M. P., Koopmann R. A., Phi A., Wolfe P.-F., 2018, ApJ, 852, 142

Oguri M., Takada M., 2011, Phys. Rev. D, 83, 023008

Oguri M., et al., 2018, Publications of the Astronomical Society of Japan, 70, S20

Okamoto T., Eke V. R., Frenk C. S., Jenkins A., 2005, MNRAS, 363, 1299

Oks E., 2021, New Astronomy Reviews, 93, 101632

Oppenheimer B. D., Davé R., Katz N., Kollmeier J. A., Weinberg D. H., 2012, Monthly Notices of the Royal Astronomical Society, 420, 829

Oppenheimer B. D., et al., 2020, The Astrophysical Journal Letters, 893, L24

Oppenheimer B. D., Babul A., Bahé Y., Butsky I. S., McCarthy I. G., 2021, Universe, 7, 209

Oren Y., Sternberg A., McKee C. F., Faerman Y., Genel S., 2024, arXiv e-prints, p. arXiv:2403.09476

Osato K., Nagai D., 2023, Monthly Notices of the Royal Astronomical Society, 519, 2069

Ostriker E. C., Shetty R., 2011, The Astrophysical Journal, 731, 41

Owen E. R., Wu K., Inoue Y., Yang H.-Y. K., Mitchell A. M., 2023, Galaxies, 11, 86

O'Kane C. J., Kuchner U., Gray M. E., Aragón-Salamanca A., 2024, MNRAS, 534, 1682

Padmanabhan T., 2002, Theoretical Astrophysics - Volume 3, Galaxies and Cosmology. Vol. 3, Cambridge University Press, doi:10.2277/0521562422

Padmanabhan T., 2003, Physics reports, 380, 235

Pakmor R., Springel V., 2013, Monthly Notices of the Royal Astronomical Society, 432, 176

Pakmor R., Marinacci F., Springel V., 2014, The Astrophysical Journal Letters, 783, L20

Pakmor R., et al., 2020, Monthly Notices of the Royal Astronomical Society, 498, 3125

Pakmor R., et al., 2023, MNRAS, 524, 2539

Pal Choudhury P., Sharma P., Quataert E., 2019, MNRAS, 488, 3195

Pan Z., Qu Z., Bregman J. N., Liu J., 2024, ApJS, 271, 62

Pandya V., et al., 2023, The Astrophysical Journal, 956, 118

Pasquali A., Nachname V., 2015, Astronomische Nachrichten, 336, 505

Peebles P. J. E., 2020, Cosmology's Century: An Inside History of our Modern Understanding of the Universe, doi:10.1515/9780691201665.

Peebles P. J. E., Ratra B., 2003, Reviews of modern physics, 75, 559

Peeples M. S., et al., 2019, The Astrophysical Journal, 873, 129

Peletier R., Balcells M., 1996, arXiv preprint astro-ph/9602088

Peng Y.-j., et al., 2010, The Astrophysical Journal, 721, 193

Penzias A. A., Wilson R. W., 1979, in , A Source Book in Astronomy and Astrophysics, 1900–1975. Harvard University Press, pp 873–876

Percival W. J., Cole S., Eisenstein D. J., Nichol R. C., Peacock J. A., Pope A. C., Szalay A. S., 2007, Monthly Notices of the Royal Astronomical Society, 381, 1053

Perlmutter S., et al., 1999, The Astrophysical Journal, 517, 565

Péroux C., Howk J. C., 2020, Annual Review of Astronomy and Astrophysics, 58, 363

Petroff E., Hessels J., Lorimer D., 2019, The Astronomy and Astrophysics Review, 27, 4

Pillepich A., et al., 2018a, MNRAS, 473, 4077

Pillepich A., et al., 2018b, MNRAS, 475, 648

Pillepich A., et al., 2021, in Nagel W. E., Kröner D. H., Resch M. M., eds, High Performance Computing in Science and Engineering '19. Springer International Publishing, Cham, pp 5–22

Planck Collaboration Ade P., et al., 2013, Astronomy & Astrophysics, 557, A52

Planck Collaboration et al., 2020, A&A, 641, A6

Ponnada S. B., et al., 2022, Monthly Notices of the Royal Astronomical Society, 516, 4417

Ponnada S. B., et al., 2024, Monthly Notices of the Royal Astronomical Society, 527, 11707

Ponti G., et al., 2023a, A&A, 674, A195

Ponti G., et al., 2023b, A&A, 674, A195

Pontzen A., Governato F., 2012, Monthly Notices of the Royal Astronomical Society, 421, 3464

Poole G. B., et al., 2015, MNRAS, 449, 1454

Popesso P., et al., 2024a, arXiv preprint arXiv:2411.16546

Popesso P., et al., 2024b, arXiv e-prints, p. arXiv:2411.16555

Popesso P., et al., 2024c, arXiv e-prints, p. arXiv:2411.17120

Popping A., Davé R., Braun R., Oppenheimer B. D., 2009, A&A, 504, 15

Potter D., Stadel J., Teyssier R., 2017, Computational Astrophysics and Cosmology, 4, 2

Predehl P., et al., 2010, in AIP Conference Proceedings. pp 543–548

Prescott M. K., Martin C. L., Dey A., 2015, The Astrophysical Journal, 799, 62

Primack J. R., 2024, Annual Review of Nuclear and Particle Science, 74, 173

Prochaska J. X., Zheng Y., 2019, Monthly Notices of the Royal Astronomical Society, 485, 648

Prochaska J. X., Weiner B., Chen H.-W., Mulchaey J., Cooksey K., 2011, The Astrophysical Journal, 740, 91

Prochaska J. X., et al., 2019, Science, 366, 231

Putman M., Peek J., Joung M., 2012, Annual Review of Astronomy and Astrophysics, 50, 491

Rahmati A., Schaye J., Crain R. A., Oppenheimer B. D., Schaller M., Theuns T., 2016, MNRAS, 459, 310

Ramesh R., Nelson D., Heesen V., Brüggen M., 2023a, arXiv e-prints, p. arXiv:2305.11214

Ramesh R., Nelson D., Pillepich A., 2023b, Monthly Notices of the Royal Astronomical Society, 518, 5754

Rauch M., Haehnelt M. G., 2011, Monthly Notices of the Royal Astronomical Society: Letters, 412, L55

Ravi V., et al., 2019, BAAS, 51, 1903

Rees M. J., Ostriker J., 1977, Monthly Notices of the Royal Astronomical Society, 179, 541

Renzini A., 2006, Annu. Rev. Astron. Astrophys., 44, 141

Ricci C., et al., 2017, Nature, 549, 488

Rieder M., Teyssier R., 2016, Monthly Notices of the Royal Astronomical Society, 457, 1722

Riess A. G., et al., 1998, The astronomical journal, 116, 1009

Riess A. G., Casertano S., Yuan W., Macri L. M., Scolnic D., 2019, The Astrophysical Journal, 876, 85

Riess A. G., Casertano S., Yuan W., Bowers J. B., Macri L., Zinn J. C., Scolnic D., 2021, The Astrophysical Journal Letters, 908, L6

Rodríguez-Medrano A. M., Springel V., Stasyszyn F. A., Paz D. J., 2024, MNRAS, 528, 2822

Rohr E., Pillepich A., Nelson D., Ayromlou M., Zinger E., 2024, A&A, 686, A86

Rosas-Guevara Y., Bower R. G., Schaye J., McAlpine S., Dalla Vecchia C., Frenk C. S., Schaller M., Theuns T., 2016, MNRAS, 462, 190

Rost A., Stasyszyn F., Pereyra L., Martínez H. J., 2020, MNRAS, 493, 1936

Rubin K. H., 2017, Gas Accretion onto Galaxies, pp 95–115

Rubin V. C., Ford Jr W. K., Thonnard N., 1980, Astrophysical Journal, Part 1, vol. 238, June 1, 1980, p. 471-487., 238, 471

Rudd D. H., Zentner A. R., Kravtsov A. V., 2008, The Astrophysical Journal, 672, 19

Ruszkowski M., Pfrommer C., 2023, The Astronomy and Astrophysics Review, 31, 4

Sahni V., 2004, The Physics of the Early Universe, pp 141–179

Salem M., Bryan G. L., Corlies L., 2016, Monthly Notices of the Royal Astronomical Society, 456, 582

Salerno J. M., Martínez H. J., Muriel H., 2019, Monthly Notices of the Royal Astronomical Society, 484, 2

Sampaio V., De Carvalho R., Ferreras I., Aragón-Salamanca A., Parker L., 2022, Monthly Notices of the Royal Astronomical Society, 509, 567

Sandage A., 2005, Annu. Rev. Astron. Astrophys., 43, 581

Sanders R. L., et al., 2021, The Astrophysical Journal, 914, 19

Saro A., et al., 2015, MNRAS, 454, 2305

Sarron F., Adami C., Durret F., Laigle C., 2019, Astronomy & Astrophysics, 632, A49

Sawala T., et al., 2016, Monthly Notices of the Royal Astronomical Society, 457, 1931

Schaan E., et al., 2021, Physical Review D, 103, 063513

Schaap W., Van De Weygaert R., 2000, arXiv preprint astro-ph/0011007

Schaller M., et al., 2024, MNRAS, 530, 2378

Schaye J., Dalla Vecchia C., 2008, Monthly Notices of the Royal Astronomical Society, 383, 1210

Schaye J., et al., 2010, MNRAS, 402, 1536

Schaye J., et al., 2015, MNRAS, 446, 521

Schaye J., et al., 2023a, arXiv e-prints, p. arXiv:2306.04024

Schaye J., et al., 2023b, MNRAS, 526, 4978

Schechter P., 1976, Astrophysical Journal, Vol. 203, p. 297-306, 203, 297

Schellenberger G., et al., 2024, The Astrophysical Journal, 969, 85

Schmidt W., Schmidt J., Grete P., 2021, Astronomy & Astrophysics, 654, A115

Scoville N., et al., 2007, ApJ Supplement Series, 172, 150

Seppi R., et al., 2023, A&A, 671, A57

Sheth R. K., Van De Weygaert R., 2004, Monthly Notices of the Royal Astronomical Society, 350, 517

Shimakawa R., Tanaka T. S., Toshikage S., Tanaka M., 2021, PASJ, 73, 1575

Shreeram S., et al., 2025a, arXiv preprint arXiv:2504.03840

Shreeram S., et al., 2025b, arXiv preprint arXiv:2506.17222

Shreeram S., et al., 2025c, A&A, 697, A22

Shtykovskiy P., Gilfanov M., 2005, MNRAS, 362, 879

Shuntov M., et al., 2022, A&A, 664, A61

Sijacki D., Vogelsberger M., Genel S., Springel V., Torrey P., Snyder G. F., Nelson D., Hernquist L., 2015, MNRAS, 452, 575

Silk J., 1977, Astronomy and Astrophysics, vol. 59, no. 1, July 1977, p. 53-58., 59, 53

Silk J., Rees M. J., 1998, A&A, 331, L1

Singh A., Mahajan S., Bagla J. S., 2020, Monthly Notices of the Royal Astronomical Society, 497, 2265

Singh P., Voit G., Nath B. B., 2021, MNRAS, 501, 2467

Singh P., Lau E. T., Faerman Y., Stern J., Nagai D., 2024, arXiv preprint arXiv:2407.06555

Skibba R. A., van den Bosch F. C., Yang X., More S., Mo H., Fontanot F., 2011, MNRAS, 410, 417

Smith R. K., Brickhouse N. S., Liedahl D. A., Raymond J. C., 2001, The Astrophysical Journal, 556, L91

Somerville R. S., Davé R., 2015, Annual Review of Astronomy and Astrophysics, 53, 51

Somerville R. S., Primack J. R., 1999, Monthly Notices of the Royal Astronomical Society, 310, 1087

Sorini D., Davé R., Cui W., Appleby S., 2022, MNRAS, 516, 883

Sorini D., Bose S., Davé R., Alcázar D. A., 2024, arXiv preprint arXiv:2409.05815

Sousbie T., 2011, MNRAS, 414, 350

Sousbie T., Pichon C., Kawahara H., 2011, MNRAS, 414, 384

Sparre M., Pfrommer C., Ehlert K., 2020, Monthly Notices of the Royal Astronomical Society, 499, 4261

Speagle J. S., Steinhardt C. L., Capak P. L., Silverman J. D., 2014, The Astrophysical Journal Supplement Series, 214, 15

Springel V., 2005, Monthly notices of the royal astronomical society, 364, 1105

Springel V., 2010a, Annual Review of Astronomy and Astrophysics, 48, 391

Springel V., 2010b, Monthly Notices of the Royal Astronomical Society, 401, 791

Springel V., Hernquist L., 2003, MNRAS, 339, 289

Springel V., Hernquist L., 2005, The Astrophysical Journal, 622, L9

Springel V., White S. D., Tormen G., Kauffmann G., 2001, Monthly Notices of the Royal Astronomical Society, 328, 726

Springel V., et al., 2005a, arXiv preprint astro-ph/0504097

Springel V., Di Matteo T., Hernquist L., 2005b, ApJ, 620, L79

Springel V., Frenk C. S., White S. D., 2006, nature, 440, 1137

Springel V., et al., 2008, Monthly Notices of the Royal Astronomical Society, 391, 1685

Springel V., et al., 2018, MNRAS, 475, 676

Stern J., Fielding D., Faucher-Giguère C.-A., Quataert E., 2019, Monthly Notices of the Royal Astronomical Society, 488, 2549

Stern J., Fielding D., Hafen Z., Su K.-Y., Naor N., Faucher-Giguère C.-A., Quataert E., Bullock J., 2024, MNRAS, 530, 1711

Stinson G. S., Brook C., Macciò A. V., Wadsley J., Quinn T. R., Couchman H. M. P., 2013, MNRAS, 428, 129

Strateva I., et al., 2001, The Astronomical Journal, 122, 1861

Strauss M. A., et al., 2002, The Astronomical Journal, 124, 1810

Strickland D. K., Heckman T. M., 2009, The Astrophysical Journal, 697, 2030

Su K.-Y., Hopkins P. F., Hayward C. C., Faucher-Giguère C.-A., Kereš D., Ma X., Robles V. H., 2017, Monthly Notices of the Royal Astronomical Society, 471, 144

Sultan I., Faucher-Giguère C.-A., Stern J., Rotshtein S., Byrne L., Wijers N., 2025, Monthly Notices of the Royal Astronomical Society, 540, 1017

Sunyaev R., Zeldovich Y. B., 1972, Astronomy and Astrophysics, Vol. 20, p. 189 (1972), 20, 189

Sutherland R. S., Dopita M. A., 1993, Astrophysical Journal Supplement Series (ISSN 0067-0049), vol. 88, no. 1, p. 253-327., 88, 253

Swinbank A., et al., 2015, Monthly Notices of the Royal Astronomical Society, 449, 1298

Tacchella S., et al., 2022, Monthly Notices of the Royal Astronomical Society, 513, 2904

Takada M., et al., 2014, PASJ, 66, R1

Tanaka M., Goto T., Okamura S., Shimasaku K., Brinkmann J., 2004, AJ, 128, 2677

Tashiro M., et al., 2020, in Space Telescopes and Instrumentation 2020: Ultraviolet to Gamma Ray. pp 293–303

Taylor E. N., et al., 2020, MNRAS, 499, 2896

Tegmark M., Silk J., Rees M. J., Blanchard A., Abel T., Palla F., 1997, The Astrophysical Journal, 474, 1

Terrazas B. A., et al., 2020, MNRAS, 493, 1888

Teyssier R., 2002, Astronomy & Astrophysics, 385, 337

Thompson T. A., Quataert E., Zhang D., Weinberg D. H., 2016, MNRAS, 455, 1830

Tinker J. L., 2021, The Astrophysical Journal, 923, 154

Tinker J., Wetzel A., Conroy C., 2011, arXiv e-prints, p. arXiv:1107.5046

To C., et al., 2021, Physical review letters, 126, 141301

Tojeiro R., et al., 2013, Monthly Notices of the Royal Astronomical Society, 432, 359

Toomre A., Toomre J., 1972, ApJ, 178, 623

Trapp C. W., et al., 2022, Monthly Notices of the Royal Astronomical Society, 509, 4149

Tremmel M., Karcher M., Governato F., Volonteri M., Quinn T., Pontzen A., Anderson L., Bellovary J., 2017, Monthly Notices of the Royal Astronomical Society, 470, 1121

Tremonti C. A., et al., 2004, The Astrophysical Journal, 613, 898

Truong N., et al., 2020, MNRAS, 494, 549

Truong N., Pillepich A., Werner N., 2021a, MNRAS, 501, 2210

Truong N., Pillepich A., Nelson D., Werner N., Hernquist L., 2021b, MNRAS, 508, 1563

Truong N., et al., 2023, MNRAS, 525, 1976

Tumlinson J., et al., 2013, The Astrophysical Journal, 777, 59

Tumlinson J., Peeples M. S., Werk J. K., 2017, Annual Review of Astronomy and Astrophysics, 55, 389

Ueda Y., Akiyama M., Hasinger G., Miyaji T., Watson M. G., 2014, The Astrophysical Journal, 786, 104

Van Den Bosch F. C., Aquino D., Yang X., Mo H., Pasquali A., McIntosh D. H., Weinmann S. M., Kang X., 2008, Monthly Notices of the Royal Astronomical Society, 387, 79

Van den Bergh S., 2009, The Astrophysical Journal, 702, 1502

Vanderlinde K., Liu A., Gaensler B., et al., 2019, LRP2020,[accessed date 9th November 2022], 10

Vani A., Ayromlou M., Kauffmann G., Springel V., 2025, Monthly Notices of the Royal Astronomical Society, 536, 777

Velliscig M., van Daalen M. P., Schaye J., McCarthy I. G., Cacciato M., Le Brun A. M., Vecchia C. D., 2014, Monthly Notices of the Royal Astronomical Society, 442, 2641

Vikhlinin A., Kravtsov A., Forman W., Jones C., Markevitch M., Murray S., Van Speybroeck L., 2006, The Astrophysical Journal, 640, 691

Vikram V., Lidz A., Jain B., 2017, MNRAS, 467, 2315

Villaescusa-Navarro F., et al., 2021a, The Astrophysical Journal, 915, 71

Villaescusa-Navarro F., et al., 2021b, ApJ, 915, 71

Vladutescu-Zopp S., Biffi V., Dolag K., 2023, A&A, 669, A34

Vladutescu-Zopp S., Biffi V., Dolag K., 2024, arXiv preprint arXiv:2406.02686

Vogelsberger M., et al., 2014, MNRAS, 444, 1518

Vogelsberger M., Marinacci F., Torrey P., Puchwein E., 2020, Nature Reviews Physics, 2, 42

Voit G. M., 2021, The Astrophysical Journal Letters, 908, L16

Voit G. M., Meece G., Li Y., O'Shea B. W., Bryan G. L., Donahue M., 2017, The Astrophysical Journal, 845, 80

Voit G. M., Ma C., Greene J., Goulding A., Pandya V., Donahue M., Sun M., 2018, The Astrophysical Journal, 853, 78

Voit G. M., Donahue M., Zahedy F., Chen H.-W., Werk J., Bryan G. L., O'Shea B. W., 2019, The Astrophysical Journal Letters, 879, L1

Volonteri M., Dubois Y., Pichon C., Devriendt J., 2016, MNRAS, 460, 2979

Vulcani B., Poggianti B. M., Fritz J., Fasano G., Moretti A., Calvi R., Paccagnella A., 2014, The Astrophysical Journal, 798, 52

Wadsley J. W., Keller B. W., Quinn T. R., 2017, Monthly Notices of the Royal Astronomical Society, 471, 2357

Wakker B., van Woerden H., 1997, Annual Review of Astronomy and Astrophysics, 35, 217

Wang Q. D., et al., 2005, The Astrophysical Journal, 635, 386

Wang L., Dutton A. A., Stinson G. S., Macciò A. V., Penzo C., Kang X., Keller B. W., Wadsley J., 2015, MNRAS, 454, 83

Wang E., et al., 2018, ApJ, 860, 102

Wang S., Xu D., Lu S., Cai Z., Xiang M., Mao S., Springel V., Hernquist L., 2022, MNRAS, 509, 3148

Wang W., et al., 2024, MNRAS, 532, 4604

Wechsler R. H., Tinker J. L., 2018, ARA&A, 56, 435

Weinberg S., 1989, Reviews of modern physics, 61, 1

Weinberger R., et al., 2016, MNRAS, 465, 3291

Weinberger R., et al., 2018, MNRAS, 479, 4056

Weinberger R., Springel V., Pakmor R., 2020, The Astrophysical Journal Supplement Series, 248, 32

Weng S., Péroux C., Ramesh R., Nelson D., Sadler E. M., Zwaan M., Bollo V., Casavecchia B., 2024, MNRAS, 527, 3494

Werhahn M., Pfrommer C., Girichidis P., Puchwein E., Pakmor R., 2021, Monthly Notices of the Royal Astronomical Society, 505, 3273

Werk J. K., et al., 2014, The Astrophysical Journal, 792, 8

Whitaker K. E., Van Dokkum P. G., Brammer G., Franx M., 2012, The Astrophysical Journal Letters, 754, L29

White S. D., Frenk C. S., 1991, Astrophysical Journal, Part 1 (ISSN 0004-637X), vol. 379, Sept. 20, 1991, p. 52-79. Research supported by NASA, NSF, and SERC., 379, 52

White S. D., Rees M. J., 1978, MNRAS, 183, 341

Wiersma R. P., Schaye J., Smith B. D., 2009, Monthly Notices of the Royal Astronomical Society, 393, 99

Wijers N. A., 2022, MNRAS, 514, 5214

Wijers N. A., Schaye J., Oppenheimer B. D., Crain R. A., Nicastro F., 2019, MNRAS, 488, 2947

Wijers N. A., Schaye J., Oppenheimer B. D., 2020, MNRAS, 498, 574

Williams R. J., Quadri R. F., Franx M., Van Dokkum P., Labbé I., 2009, The Astrophysical Journal, 691, 1879

Winkel N., Pasquali A., Kraljic K., Smith R., Gallazzi A., Jackson T. M., 2021, MNRAS, 505, 4920

Wisotzki L., et al., 2018, Nature, 562, 229

Wright R. J., Somerville R. S., Lagos C. d. P., Schaller M., Davé R., Anglés-Alcázar D., Genel S., 2024, Monthly Notices of the Royal Astronomical Society, 532, 3417

Wu X., McQuinn M., 2023, The Astrophysical Journal, 945, 87

Wu Y.-Z., Zhang S.-N., Zhao Y.-H., Zhang W., 2016, Monthly Notices of the Royal Astronomical Society, 457, 2929

Wu P.-F., et al., 2018, The Astrophysical Journal, 855, 85

Wu X., et al., 2025, The Astrophysical Journal, 983, 186

Yang Y., Ji S., 2023, Monthly Notices of the Royal Astronomical Society, 520, 2148

Yang X., Mo H., van den Bosch F. C., 2009, The Astrophysical Journal, 695, 900

Yates R. M., Hendriks D., Vijayan A. P., Izzard R. G., Thomas P. A., Das P., 2024, MNRAS, 527, 6292

Yeung M. C., et al., 2024, A&A, 690, A399

York D. G., et al., 2000, AJ, 120, 1579

Yu G., Zhu W., Yang Q.-R., Mo J.-F., Luan T.-C., Feng L.-L., 2025, arXiv preprint arXiv:2504.01245

Zahid H. J., Dima G. I., Kudritzki R.-P., Kewley L. J., Geller M. J., Hwang H. S., Silverman J. D., Kashino D., 2014, The Astrophysical Journal, 791, 130

Zhang B., 2023, Reviews of Modern Physics, 95, 035005

Zhang H., Zaritsky D., 2024, Science Advances, 10, eadp8629

Zhang Y., Anninos P., Norman M. L., 1995, The Astrophysical Journal, 453, L57

Zhang Z., Gilfanov M., Bogdán Á., 2012, A&A, 546, A36

Zhang H., Zaritsky D., Zhu G., Ménard B., Hogg D. W., 2016, The Astrophysical Journal, 833, 276

Zhang H., Zaritsky D., Behroozi P., 2018, ApJ, 861, 34

Zhang Y., et al., 2019, MNRAS, 487, 2578

Zhang H., Yang X., Zaritsky D., Behroozi P., Werk J., 2020, The Astrophysical Journal, 888, 33

Zhang Y., et al., 2024a, arXiv preprint arXiv:2401.17308

Zhang Y., et al., 2024b, arXiv preprint arXiv:2401.17309

Zheng X., et al., 2024a, arXiv e-prints, p. arXiv:2401.17310

Zheng X., et al., 2024b, A&A, 689, A328

Zhu G., Ménard B., 2013, The Astrophysical Journal, 770, 130

Zhuravleva I., Churazov E., Kravtsov A., Lau E. T., Nagai D., Sunyaev R., 2013, MNRAS, 428, 3274

Zinger E., Dekel A., Birnboim Y., Kravtsov A., Nagai D., 2016, MNRAS, 461, 412

Zinger E., et al., 2020, Monthly Notices of the Royal Astronomical Society, 499, 768

Zitrin A., Bartelmann M., Umetsu K., Oguri M., Broadhurst T., 2012, Monthly Notices of the Royal Astronomical Society, 426, 2944

Zou H., Gao J., Zhou X., Kong X., 2019, The Astrophysical Journal Supplement Series, 242, 8

Zou H., et al., 2022, Research in Astronomy and Astrophysics, 22, 065001

ZuHone J. A., Hallman E. J., 2016, Astrophysics Source Code Library, pp ascl–1608

ZuHone J. A., et al., 2024, The Astrophysical Journal, 967, 49

Zwicky F., 1933, Helvetica Physica Acta, Vol. 6, p. 110-127, 6, 110

van Daalen M. P., Schaye J., McCarthy I. G., Booth C., Vecchia C. D., 2014, Monthly Notices of the Royal Astronomical Society, 440, 2997

van Daalen M. P., McCarthy I. G., Schaye J., 2020, Monthly Notices of the Royal Astronomical Society, 491, 2424

van de Voort F., 2013, MNRAS, 430, 2688

van de Voort F., Schaye J., 2012, MNRAS, 423, 2991

van de Voort F., Schaye J., Booth C., Haas M. R., Dalla Vecchia C., 2011, Monthly Notices of the Royal Astronomical Society, 414, 2458

van de Voort F., Bieri R., Pakmor R., Gómez F. A., Grand R. J. J., Marinacci F., 2021, MNRAS, 501, 4888

van den Bergh S., 1976, Astrophysical Journal, vol. 206, June 15, 1976, pt. 1, p. 883-887. Research supported by the National Research Council of Canada., 206, 883

Acknowledgements

To call this PhD challenging alone would be far from an understatement. With a difficult beginning and a highly time-constrained end, I have a multitude of people to thank for being able to see this day. Most importantly, Johan Comparat, my supervisor for this thesis. Quite literally, he saved my PhD by adopting me as his new student almost midway through the 2nd year. While the time for finishing the PhD despite the change stayed the same, he nevertheless undertook this challenge together, with me starting off on a completely new topic, to make this a successful thesis. He helped me grow into the independent scientist of today, always believing and encouraging me that I could achieve more than I knew myself. I sincerely thank him for mentoring me, and needless to say, it is also his success as a supervisor that is leading me to accomplish this PhD.

I would like to thank my mentors and collaborators whom I met along the way during my time here at MPE. Andrea, for always being available with your open door and for the many engaging scientific discussions. I'd like to thank Jochen Weller for being so supportive throughout my PhD, and Paul for his support and all the detailed comments on this thesis. Thanks to Yi, Gabriele, and Ilaria for the collaborations. Special thanks also to Birgit for being a supportive secretary in the most crucial moments and to Caroline Echer for helping me with all the visa application procedures. Mara, who always uplifted and believed in me, far before the end seemed near, thank you. Daniela, you've been so much fun to work with, and while I knew this already when working with you in my first cosmic-filament project of my PhD, I'm glad we could reunite to work together at the very end! You've helped me become a better scientist, and doing the last project in under three months would've been far from possible without your support, reassurance, and constant encouragement.

The next set of acknowledgments goes to my support system, without whom I could not see the end of this PhD. Fulvio and Antonia, who have been my closest family in Munich and helped me without a blink of hesitation in some of the toughest moments in these last years; Emre, for the high-quality company making those unavoidable late work evenings even fun; Sophia, for being a backbone of support especially during my craziest moving in Munich; Bob, for always cheering me at bouldering (the effort of the climb has always been 60/40); Matti, for all the cozy evenings watching tv series; Toska, for the uncountable laughs and memorable trips; Ricky, for being so inspiring and always bringing people together; Francis, for cooking us so many amazing meals, and the sacrificers: Antonia, Bob, and Jed, for all the time together, especially the lovely painting and wine evenings; thank you all for your support and precious friendships. I would like to especially thank my dearest Not So Secret Santa friends: Sophia, Emre, Ricky, Francis,

Fulvio, and James. Such a lovely time I've had with you all, the many lunches, dinners, trips, and hikes make some of the most cherishable memories of my PhD, and I've missed having you all immensely in the last year.

I would like to thank my dearest bouldering crew: Antonia, Bob, Toska, Matteo E, Marina, Jed, Luki, Markus, Yun-Hsin, and the many other people who joined us over the last four years. All those weekly adventures that started as a reason for doing a sport turned into a wonderful friendship that I will cherish for the rest of my life. You have been crucial, and I am grateful for every one of those (very late) evenings we shared together, whether at Satluj or Esco bar, all your laughs with ein hellas for sure, and some good food have been some of the most beautiful weekly adventures in these years. Thank you to my musical friends: Fulvio, James, Toska, Laz, Damien, Nico, Mrinal, and my drum teacher, Christos, with whom I've had the privilege to learn from and play the drums together. Also, a special thanks to Gauri.

I've had the privilege to share the office for most of my PhD with some very beautiful souls, Sophia, Zsofi, and later Ania and Luisa. In some of the toughest moments, Sophia and Zsofi have been a shoulder to rely on. I've had so much fun with our many long chats and heart-to-heart laughs. Thank you, Sophia and Zsofi, for creating such a nice office environment (Sophia, be it carrying a second-hand Yucca palm tree all the way from Trudering; and Zso, for always feeding me with snacks in my pangs of hunger and for motivating each other in this last sprint). I look back on all our times together very fondly!

I'd like to thank the vibrant community of PhDs I've met over these last years. It's been a great opportunity being an IMPRS student representative, and it has made me admire how beautifully all the students support each other to survive the many challenges of a PhD. Being part of organizing the cineclub, yoga, and IMRPS events has been so rewarding. I'd like to thank the people I met as part of the High-Energy group: Chris G., Alena, Eve, Manu, Raph, David, Isa, Ana, Safiyee, Caro, Brivael, Pietro, Cata, Martin, Adam, Ricky Arcodio, Jacob, Xueying, Mike, Yi, Damien, and so many more. I'd also like to thank the many other lovely souls, with whom I've shared the many Friday WAW beer evenings or other PhD adventures around Munich: Laz, Stavroula, Matteo G, Laura, Benny, Abinaya, Hitesh, Anshuman, Arghyadeep, Chris D., Anna G., Enrico, Mrinal, Nico, Melika, Ruggero, Geza, Maria W., Aniket, Ivana, Capucine and the Carbonaras. I'm so sorry for the kind friends whose names I forgot to include in this acknowledgment as I wrote it. While I regret not writing your name when I see you next time, I would like to thank you for being part of this journey.

To all dear friends whom I've met in my last years in Europe before coming to Munich. Even though we are today scattered across Europe, they've kept me lovely company with fun trips, visits, and many calls over these last years. Irene, my yoga-buddy and my star, for her unwavering support during some tough moments in these last years. You've been so precious. Roke, for always rooting for me and introducing me to the many first-time experiences with adventurous hiking/snorkelling trips over these last years. I'd also like to thank Sona, Célia, and Oana for the warmth you've brought by being there with your visits and phone calls. It's been a pleasure growing together over these last years. I am also very grateful to Silvi for always being so welcoming during all my trips to Sicily.

To my dear friends from home, Vruddhi, Evi, Apoorva, Simran, Toshavi, Raj, Riya, and Anushka, for always welcoming me back with love and for always making my visits home lots

of fun, sharing many adventures and conversations; what a pleasure it is to see how we've all grown up since school! My gratitude goes to Fulvio's family, who have welcomed me with great love and joy every time I have been in Sicily. Special thanks to Silvana, for all her support and inspiration. I could not have survived this PhD without my family. I'd like to thank my brother-in-law, Varun, for all the fun times together; our dear dog, Bubbly, whose calm and cheerfulness always fills my heart with joy; Manoj and Swathi, for always sharing their love and support; Prakash periappa and Sarita periamma, for always believing in me; and my grandparents, who've been my steadfast well-wishers all along, especially Tatha, who would've loved to witness this day. To my dad, his support from the beginning has been crucial for me on this journey to be an astrophysicist. My sister, Kashmira, has been a constant source of strength and reason throughout my journey. Most importantly, I would like to thank Amma for coming all the way to Munich to support me in the toughest moments of the PhD, and for always being available and supportive. I could not have made it here today without her. Last but not least, a huge thank you to Fulvio. What a journey it has been over the last four years, and I feel privileged to have had your steadfast support and company at every moment. Meeting you and sharing this experience together has definitely been among the best gifts of this PhD journey.